

**UCLA**

**UCLA Electronic Theses and Dissertations**

**Title**

Electro-Optical Properties of Quantum Dots with Copper Impurities

**Permalink**

<https://escholarship.org/uc/item/6nv1g453>

**Author**

Fuhr, Addis

**Publication Date**

2019

Peer reviewed|Thesis/dissertation

UNIVERSITY OF CALIFORNIA

LOS ANGELES

**Electro-Optical Properties of Quantum Dots with Copper Impurities**

A dissertation submitted in partial satisfaction of the requirements for the degree Doctor  
of Philosophy in Chemical Engineering

By

Addis Sidney Fuhr

2019

© Copyright by

Addis Fuhr

2019

## ABSTRACT OF THE DISSERTATION

*Electro-Optical Properties of Quantum Dots with Copper Impurities*

by

Addis Fuhr

Doctor of Philosophy in Chemical Engineering

University of California, Los Angeles, 2019

Professor Philippe Sautet, Chair

In this work, I focus on understanding the single exciton absorption/emission mechanisms, multicarrier interactions, and charge transport mechanisms for quantum dots (QDs) containing Cu cations with a particular emphasis on  $\text{Cu}_x\text{In}_{2-x}\text{Se}_y\text{S}_{2-y}$  (CISeS) QDs. Specifically, I combine theory with experiment to determine the origin of their large Stokes shifts, broad absorption and emission spectral linewidths, long radiative lifetimes, reveal their multicarrier (*e.g.* trions and biexciton) interactions, and charge transport mechanisms. My theoretical toolkit predominantly utilizes density functional theory (DFT) calculations in which I predict that most of the physical properties in these systems are due to Cu impurities such as native defects (*e.g.* anti-site defects), or extrinsic dopants

(e.g. substitution of  $\text{Zn}^{2+}$  cations in ZnSe with  $\text{Cu}^{1+}$ , or  $\text{Cu}^{2+}$  cations). Each of these predictions are then experimentally tested using a combination of ultra-fast spectroscopy, magneto-optical spectroscopy, single-particle spectroscopy, and *in-situ* spectral electrochemistry measurements. And, in some cases, device studies are compared to theoretical/experimental predictions to further confirm my findings.

My studies conclude that the single- and multi-exciton absorption and emission mechanisms are dominated by three basic pathways: band-edge,  $\text{Cu}^{1+}$  defect, and  $\text{Cu}^{2+}$  defect excitation and recombination. Band-edge optical processes (both single and multi-exciton) for CISES QDs match the general trends predicted for “typical” II-VI QDs such as sharp absorption, narrow emission, fast radiative lifetimes and Auger decay, and adherence to “universal volume scaling” relationships. The origin of these effects are small subensembles of CISES QDs in experimental batches that have no defects, and correspondingly can be described by delocalized (valence band-to-conduction band) excitonic interactions.  $\text{Cu}^{1+}$  defects stem from anti-site swapping of  $\text{Cu}^{1+}$  and  $\text{In}^{3+}$  atoms into charge-balanced  $\text{Cu}_{\text{In}}^{\bullet} + \text{In}_{\text{Cu}}^{\bullet\bullet}$  defect pairs, and result in intra-gap “occupied”  $\text{Cu}_{\text{In}}^{\bullet}$  defect states with the  $[\text{Ar}]3d^{10}$  electron configuration. In order to emit, these defects need to localize a hole either by trapping valence band (VB) carriers, or direct intra-gap excitation. This leads to a small nuclear reorganization and Franck-Condon shift prior to emission referred to as the “real Stokes shift,” or the energy difference between absorptive  $\text{Cu}_{\text{In}}^{\bullet}$  defects and emissive  $\text{Cu}^{2+}$  defects. These  $\text{Cu}^{2+}$  defects have a hole in their electronic configuration ( $[\text{Ar}]3d^9$ ), which are thereby expected to lead to strong Jahn-Teller distortions, and shift the energy of the  $\text{Cu}^x$  impurity state (where  $x=1+$  or  $2+$ ). This new, emissive  $\text{Cu}^{2+}$  state also has an “apparent Stokes shift” defined by the energy

difference between  $\text{Cu}^{2+}$  emission and band-edge absorption.  $\text{Cu}^{2+}$  defects can also occur in the ground-state by charge-compensation of copper vacancies in  $V_{\text{Cu}}' + \text{Cu}_{\text{Cu}}\cdot$  defect pairs. In this case, the  $\text{Cu}^{2+}$ , or  $\text{Cu}_{\text{Cu}}\cdot$  impurities are “emission ready,” do not require localization of VB holes, and only the apparent Stokes shift is observed. Instead, VB holes are removed by non-emissive traps (e.g. dangling bonds), which block the faster band edge transition. However, considering that the hole removal rate for QDs with  $\text{Cu}_{\text{Cu}}\cdot$  defects occurs at a slower rate than hole localization for QDs with  $\text{Cu}_{\text{In}}''$  defects, or biexciton decay for defect-free QDs, at the multi-exciton level QDs with  $\text{Cu}_{\text{Cu}}\cdot$  defects exhibit Auger dynamics that are indistinguishable from defect-free QDs.

For each of these described single exciton and multiexciton interactions, ensemble spectral measurements usually represent the average of *all* of the described subensembles. However, subensembles with  $\text{Cu}^{2+}$  defects are more prevalent in highly Cu-deficient QDs due to an excess of Cu vacancies, or when the Fermi-level is below the  $\text{Cu}^x$  state. On the other hand,  $\text{Cu}^{1+}$  defects are more common in subensembles where the Fermi-level is above the  $\text{Cu}^x$  state, or in (near)-stoichiometric, or Cu-rich conditions where the concentration of  $\text{Cu}^{1+}$  and  $\text{In}^{3+}$  cations are comparable. As expected by this description, the relative population of each of these subensembles can thereby be controlled by altering chemical process conditions with the clearest process control parameters focusing on either Fermi-level modulation, or Cu:In ratios. In addition to each of these effects, regardless of the oxidation state of  $\text{Cu}^x$  impurities, their local chemical bonding environment significantly alters their ground state energy. This is due to the high covalency of Cu-X (where X=S, or Se) bonds in which local variations in electrostatics and bond geometry alter their crystal field splitting energy. Hence, spectral linewidths at

the single particle level are *intrinsically* narrow, but ensemble spectra is broadened by the lack of positional control of  $\text{Cu}^x$  defects during QD synthesis. This leads to large variations in the emission energy at the single particle level, which average to the broad spectra observed in ensemble measurements. This finding indicates that while electron-phonon coupling may be stronger in these systems than “typical” II-VI structures, there are no fundamental limits to achieving narrow ensemble spectra. Hence, if synthesis, or device fabrication conditions are altered to control heterogeneity, narrow ensemble spectra can be achieved.

Finally, I conclude that  $\text{Cu}^x$  defects lead to “self-doped” structures, and correspondingly *p*-type transport in QD films with inert substrates (e.g. Au). However, In-related defects (e.g.  $\text{In}_{\text{Cu}}^{2+}$ ) lead to *n*-type transport, and heating in the presence of In substrates can alter the charge polarity from *p*- to *n*-type. Regardless of the charge polarity, much like the optical properties for CISES QDs, charge transport can be described by delocalized band-edge carriers and localized impurity carriers. Delocalized carriers lead to “high mobility” states whereas localized carriers lead to “low mobility states.” For charge transport, delocalized/localized pathways are thermally coupled, and higher conductivity films can be realized by minimizing the energy separation between impurity and band-edge states, which allows for carriers to be thermally promoted from low-to-high mobility states, and increases the contribution of high mobility states to transport. In this case, the Cu/In ratio is of less importance than the Se/S ratio where a higher Se concentration shifts the band-edges closer to the impurity states, and leads to stronger thermal coupling between the low and high mobility states.

This dissertation of Addis Fuhr is approved.

Dante A. Simonetti

Anastassia N. Alexandrova

Victor I. Klimov

Philippe Sautet, Committee Chair

University of California, Los Angeles

2019

*To everyone who's love and support helped me mine for my gold, Timshel*

## TABLE OF CONTENTS

List of Figures .....	xi
Acknowledgments .....	xxxix
Vita .....	xxxviii
Publications & Patents .....	xxxix
<b>Chapter 1: Motivation &amp; Interest in Quantum Dots with Copper Impurities .....</b>	<b>1</b>
1.1. <i>Introduction: Climate Change &amp; Quantum Dots</i> .....	2
1.2. <i>Nanocrystal Quantum Dots: Materials Chemistry &amp; Device Physics</i> .....	5
1.2.1. Unique Properties Arising from Quantum Confinement .....	5
1.2.2. Quantum Dot Photonic Devices: Prospects & Challenges for Lowering Carbon Emissions....	10
1.3. <i>I-III-VI<sub>2</sub> Quantum Dots</i> .....	17
1.4. <i>Thesis Objectives</i> .....	20
1.5. <i>References</i> .....	21
<b>Chapter 2: Photoluminescence &amp; Magnetic Exchange from Native Defects.....</b>	<b>27</b>
2.1. <i>Light Emission Mechanisms in CuInS<sub>2</sub> Quantum Dots Evaluated by Spectral Electrochemistry</i> .....	28
2.1.1. Introduction.....	28
2.1.2. Results and Discussion .....	30
2.1.3. Conclusions.....	49
2.1.4. Methods.....	51
2.1.5. References .....	53
2.2. <i>Defect-Controllable Magneto-Optical Properties in Cu<sub>x</sub>In<sub>2-x</sub>S<sub>y</sub> Quantum Dots</i> .....	64
2.2.1. Introduction & Low-Temperature Spectra .....	64
2.2.2. Magneto-Optical Spectroscopy & Density Functional Theory .....	67
2.2.3. Conclusions.....	74
2.2.4. Methods.....	75
2.2.5. References .....	77
<b>Chapter 3: Compositional Heterogeneity &amp; Types of Stokes Shifts: Low Photon Flux Spectral Broadening Mechanisms .....</b>	<b>85</b>

3.1. <i>Effect of Stoichiometry on Reabsorption in <math>Cu_xIn_{2-x}S_y</math> Quantum Dots: Determining the “Real” vs. “Apparent” Stokes Shift</i> .....	86
3.1.1. Introduction.....	86
3.1.2. Results and Discussion .....	90
3.1.3. Conclusions.....	109
3.1.4. Methods.....	111
3.1.5. References .....	111
3.2. <i>Heterogeneity in Local Chemical Bonding Explains Spectral Broadening in Quantum Dots with Cu Impurities</i> .....	118
3.2.1. Introduction.....	118
3.2.2. Results and Discussion .....	120
3.2.3. Conclusions .....	137
3.2.4. Methods.....	138
3.2.5. References .....	139
3.3. <i>Distinguishing between Homogeneous &amp; Inhomogeneous Spectral Broadening: Single Particle &amp; Temperature-Dependent Ensemble Spectroscopy of <math>Cu_xIn_{2-x}S_y</math> Quantum Dots</i> ...	147
3.3.1. Introduction.....	147
3.3.2. Results and Discussion .....	148
3.3.3. Conclusions .....	154
3.3.4. Methods.....	154
3.3.5. References .....	155
<b>Chapter 4: Multicarrier Interactions for Quantum Dots with Cu Impurities</b> .....	<b>160</b>
4.1. <i>Localized &amp; Delocalized Auger Interactions in Quantum Dots with Native Defects</i> .....	161
4.1.1. Introduction.....	161
4.1.2. Results and Discussion .....	163
4.1.3. Conclusions .....	186
4.1.4. Methods.....	187
4.1.5. References .....	189
<b>Chapter 5: Charge Transport Mechanisms in Quantum Dots with Cu Impurities</b> .....	<b>196</b>
5.1. <i>Charge Transport Mechanisms in <math>CuInSe_xS_{2-x}</math> Quantum Dot Films</i> .....	197
5.1.1. Introduction.....	197
5.1.2. Results and Discussion .....	199
5.1.3. Conclusions .....	214
5.1.4. Methods.....	215
5.1.5. References .....	219
<b>Appendix</b> .....	<b>227</b>
6.1. <i>Supporting Information for Chapter 2, Section 2.1</i> .....	227
6.2. <i>Supporting Information for Chapter 2, Section 2.2</i> .....	232

6.3. <i>Supporting Information for Chapter 3, Section 3.1</i> .....	234
6.4. <i>Supporting Information for Chapter 3, Section 3.2</i> .....	237
6.5. <i>Supporting Information for Chapter 4</i> .....	244
6.6. <i>Supporting Information for Chapter 5</i> .....	248

## LIST OF FIGURES

**Figure 1.2.1.1:** Idealized comparison of the energy bands for a bulk semiconductor (left) and spherical QD (right) made of the same material. Bulk semiconductors show a parabolic dispersion of the carrier kinetic energies, which then transform to discrete atomic-like energy levels in QDs. VB and CB refer to the valence and conduction bands, respectively. The band gap is represented by  $E_g$ .

**Figure 1.2.1.2:** Auger recombination pathways normally observed in QDs: (a) negative trion ( $X^-$ ), (b) a positive trion ( $X^+$ ), (c) a biexciton ( $2X$ ), and (d,e) a triexciton ( $3X$ ) where  $X$  refers to the number of e-h pairs. Trions represent the case where the energy released during recombination is transferred to a CB electron ( $X^-$ ) or VB hole ( $X^+$ ). Biexcitons describe two excitons and triexcitons three excitons where Auger recombination can occur *via*  $X^+$  or  $X^-$  pathways. For triexcitons, there are symmetric (d) and asymmetric (e) pathways where symmetric refers to the case where all charge carriers are in the 1S (CB or VB) states and asymmetric when there are 2-fold degenerate 1S levels resulting in a third carrier in the 1P state.

**Figure 1.2.2.1:** Schemes for QD-LSC fabrication are shown in (a) and (b). QDs are represented by purple spheres, blue represents the glass or polymer matrix, and the window edges which form the PV cells are shown in silver. A more detailed description of losses are shown in (b): geometric (1), scattering (2), reabsorption followed by emission into the “Escape cone” (3), and reabsorption followed by nonradiative recombination (4). An ideal LSC material is shown in c) where step-like absorption ( $\alpha_1$ ), which overlaps with

most of the solar spectrum (grey lines) is shown by a black line. To limit reabsorption losses, this material would ideally reemit at a much lower energy ( $\alpha_2$ ).

**Figure 1.2.2.2:** Typical device architecture for a QD-LED and the corresponding band diagrams are shown in (a). Electrons and holes are injected into the CB and VB bands after biasing the electrodes. The sharp emission shown in (b), results from recombination of these charge carriers. For (b), spectra for QDs are shown by solid lines and organic emitters in dotted lines. Clearly, the emission linewidth is much narrower for QDs, which leads to higher color purity.

**Figure 1.3.1:** The multiple mechanisms purported to explain CIS emission: (a) Splitting of the band-edge states due to symmetry breaking (b) electron-phonon coupling, (c) an electron localized at an In defect, and (d) a hole localized at a Cu defect.

**Figure 2.1.2.1.** (a) Optical measurements for stoichiometric core-only CIS QDs of four different sizes. The blue solid lines represent the absorption spectra, blue dotted lines are the second derivative of the absorption spectra, and the solid red lines are the emission spectra. (b) The Cu-defect related mechanisms for intra-gap emission from CIS QDs. Top: the QD absorption is due primarily to the VB-CB transitions, while the emission is due to radiative recombination of the CB electron with a hole residing in an intra-gap  $\text{Cu}^x$  state ( $x = 1+ \text{ or } 2+$ ). Bottom-left: The  $\text{Cu}^{2+}$  defect contains a pre-existing hole in the ground state, which can directly recombine with the CB electron (process 2). This recombination channel, however, is fairly slow (hundreds of nanoseconds time scales), therefore, in order for it to dominate emission, the photogenerated hole must be quickly removed from the VB state *via* capture by another hole trap (process 1) such as a Cu vacancy (denoted

as  $V_{Cu}$ ) forming a charge-compensated pair with the  $Cu^{2+}$  defect. The recombination cycle is completed after the electron captured radiatively by the Cu-center recombines with the trapped hole (process 3), which restores the original 2+ oxidation state of the Cu defect. Bottom right: To become PL-active, the  $Cu^{1+}$  state must first capture a VB hole (process 1); this leads to formation of the  $Cu^{2+}$ -like state, which then radiatively recombines with the CB electron (process 2) to restore the original 1+ oxidation state.

**Figure 2.1.2.2.** (a) CV measurements of CIS QDs conducted with a scan rate of 0.1 V/s (sample C from **Figure 2.1.2.1**). The black circle corresponds to the starting EC potential ( $V_{EC} = 0$  V). “Forward scans” refer to ramping the potential from 0 V to more positive values (labeled “F”) and “reverse scans” refer to scanning to more negative  $V_{EC}$  (labeled “R”). A clear intra-gap oxidation (forward) and reduction (reverse) reactions are observed at potentials of 0.65 V and 0.45 V, respectively. A weak shoulder, which appears at negative  $V_{EC}$  at -0.33 V on the reverse scans, may represent an unoccupied intra-gap trap (denoted  $T_C$ ). The VB-edge and  $Cu^x$  positions are derived from the onset potential for CIS QD (or  $Cu^x$ ) oxidation on the forward scans using linear fits (dotted red lines), while the  $T_C$  position is determined by the onset potential for the reduction current on the reverse scans. “E” denotes the parasitic electrolyte background current, which makes the CB position difficult to observe in the CV measurements. (b) The CB (red solid circles) and VB (blue solid circles) edge positions for stoichiometric CIS QDs based on combined CV and optical measurements. Green solid circles correspond to the measured redox potentials of the intra-gap feature assigned to the  $Cu^{1+/2+}$  state, while open turquoise circles correspond to the energy of the intra-gap state obtained based on the apparent Stokes shift from the optical PL and absorption measurements. Open blue and red

diamonds correspond, respectively, to the VB and CB edges of Cu-deficient CIS QDs ( $\text{Cu}_{0.56}\text{In}_{1.44}\text{S}_2$ ) obtained from optical measurements (the VB data are placed along the trend line derived from the CV measurements of stoichiometric CIS QDs). The Stokes shifts for these samples are represented by open turquoise diamonds as measured from the PL spectrum. Bulk CIS (closed triangles) band positions are based on **refs. 3 and 36**. The solid horizontal line shows the standard  $\text{Cu}^{1+/2+}$  redox potential from literature, while the dashed line shows the average  $\text{Cu}^{1+/2+}$  redox potential for CIS QDs as measured here.

**Figure 2.1.2.3.** (a) LSV measurements of stoichiometric CIS QDs (sample C from **Figure 2.1.2.1a**) without (solid blue line) and with (dotted blue line) continuous wave illumination with low-intensity 532 nm light. The intra-gap  $\text{Cu}^x$  oxidation feature becomes significantly less prominent after 30 minutes of continuous illumination, likely due to photoconversion of  $\text{Cu}^{1+}$  to  $\text{Cu}^{2+}$ . Notably, this feature also disappears in the dark current for  $\text{Cu}_{0.44}\text{In}_{1.56}\text{S}_2$  QDs (solid red line), indicating  $\text{Cu}^{2+}$  defects are more prevalent than  $\text{Cu}^{1+}$  defects. Inset: A possible mechanisms of  $\text{Cu}^{1+}$ -to- $\text{Cu}^{2+}$  photonversion (see text for details);  $\text{LT}_e$  is a long-lived electron trap. (b) SEC measurements of PL intensity (measured at the peak) as a function of applied bias for core-only stoichiometric CIS QDs (purple solid circles), Cu-deficient CIS QDs ( $\text{Cu}_{0.56}\text{In}_{1.44}\text{S}_2$  and  $\text{Cu}_{0.44}\text{In}_{1.56}\text{S}_2$ ; green squares and blue triangles, respectively), and stoichiometric CIS with a ZnS shell (red diamonds); the data are normalized to the PL intensity observed with  $V_{EC} = 0$ . Band-edges for the  $\text{Cu}_{0.44}\text{In}_{1.56}\text{S}_2$  QDs (roughly equivalent to the band positions for  $\text{Cu}_{0.56}\text{In}_{1.44}\text{S}_2$ ) are shown as vertical dotted green lines, stoichiometric QDs as dotted purple lines, and  $\text{Cu}^x$  by the solid yellow line. (c) The full  $V_{EC}$ -dependent PL spectra for stoichiometric CIS QDs (left panel),  $\text{Cu}_{0.44}\text{In}_{1.56}\text{S}_2$  QDs (middle panel), and stoichiometric CIS/ZnS core-shell QDs (right

panel). These experiments were done using the same EC setup as the CV/LSV measurements, but holding each potential for 3 minutes before collecting the spectra. Spectra were measured under low-intensity excitation at 500 nm using a Xe lamp. (d) Schematic depictions of relaxation processes in stoichiometric (left) and Cu-deficient (middle) core-only CIS QDs, and stoichiometric CIS/ZnS core/shell samples (right). The results of SEC measurements suggest that the stoichiometric QDs exhibit two trap bands associated with surface defects; one is located near the CB edge ( $T_C$ ) and the other, near the VB edge ( $T_V$ ). The position of the Fermi level ( $E_F$ ), controlled by  $V_{EC}$ , and determines the degree of filling of the trap bands. The occupied states (below  $E_F$ ) serve as hole traps, while unoccupied states (above  $E_F$ ) serve as electron traps. The radiative transition (red wavy arrow) can be quenched by either electron or hole trapping (black arrows). The vertical double-sided arrows show the span of the surface-trap-free region (denoted as the "T-free" region), which manifests in SEC measurements as the range of EC potentials wherein the change in  $V_{EC}$  does not affect the PL intensity.

**Figure 2.2.1.1:** (a) Absorption/emission mechanism for CIS QDs (top panel). For Cu-rich, stoichiometric, or near-stoichiometric QDs (bottom left panel) there is an additional absorption band from  $Cu^{1+}$  defects (dashed blue line), which require "photoactivation" prior to  $Cu^x$  emission. For far-off stoichiometry, Cu-deficient QDs (right bottom panel) Cu defects are predominantly in the 2+ oxidation state and are therefore "emission ready." Hence, the band-edge hole is trapped (dashed black lines) at a separate state labeled  $T_h$ . (b) Low-temperature (15 K) absorption (solid colored lines) and emission (dotted colored lines) spectra for CIS QDs with two different Cu:In ratios. Solid black lines represent Gaussian fits.

**Figure 2.2.1.2:** (a) Magnetic field- ( $T = 3$  K, top panel) and temperature-dependent ( $H = 6$  T, bottom panel) MCD measurements for  $\text{Cu}_{0.47}\text{In}_1\text{S}_y$ . The linear absorption spectra (3 K, dashed black lines) is also shown. (b,c) The H- (b) and T-dependent (c) Zeeman splitting energies ( $\Delta E_Z$ ). Red circles represent  $\text{Cu}_{0.47}\text{In}_1\text{S}_y$  and green circles indicate  $\text{Cu}_{0.85}\text{In}_1\text{S}_y$ . The solid lines in (b) represent fits to the experimental data using equation 1, while the dashed lines in (c) are simply a visual guide for the data. (d) The stoichiometry-dependent  $\Delta E_{spd}$  where “x” refers to the Cu/In ratio.

**Figure 2.2.1.3.** (a) Defect formation energy as a function of spatial separation between defects. (b,c) The formation energies of anti-site defects are lower than intermediate defects required for “self-purification.” Hence, defects in CIS are kinetically trapped during synthesis.

**Figure 2.2.1.4:** (a) DOS for anti-site defects on a model QD with two different defect pair separation distances (7 Å and 11 Å for the left and right panel, respectively). Solid black lines mark the band-edges, dashed black lines the Fermi level, and black squares trap-like surface states (labeled  $S_{St}$ ). The charge density for each labeled state is depicted in (b) for  $(\text{Cu}_{In} + \text{In}_{Cu})_{11\text{Å}}$  using purple (occupied) and green (unoccupied) iso-surfaces. (c,d) The same analysis is used for QDs with a single copper vacancy. For (c), calculations were spin-polarized due to the paramagnetism of  $\text{Cu}^{2+}$ ; and the two columns represent different electron spins. In both (b) and (d), the bottom center panel shows a second, zoomed-in image of the  $\text{Cu}^x$  defect for clarity.

**Figure 3.1.2.1:** (a) Scheme distinguishing between the two Stokes shifts in CIS QDs. Cu-rich, stoichiometric, and near-stoichiometric QDs have a larger concentration of

subensembles with  $\text{Cu}^{1+}$ , or anti-site defects, which have a filled  $d$  shell that requires “photoactivation” *via* either intra-gap absorption or hole localization from the VB (left panel). Cu-deficient QDs (right panel), on the other hand, have larger subensembles of  $\text{Cu}^{2+}$  defects, which are “emission ready” due to a pre-existing hole in its  $d$  shell and do not undergo this photoconversion process. Correspondingly, *both* subensembles have an apparent Stokes shift ( $\Delta_{S,A}$ , both panels) represented by the energy difference between  $\text{Cu}^{2+}$  defect (ground-state or photogenerated) emission and band-edge absorption. However, only subensembles with  $\text{Cu}^{1+}$  defects have a “real Stokes shift,” which represents the energy difference between  $\text{Cu}^{1+}$  defect absorption, and photogenerated  $\text{Cu}^{2+}$  defect emission. This energy separation is due to the vibronically coupled Franck-Condon shift in  $\text{Cu}^x$  defect energy during the photoconversion process. (b) The linear absorption spectra (solid colored lines) are compared to the transient absorption spectra (grey scatter plots) fitted to Gaussian peaks (solid black lines for all samples with grey infilling for Cu-rich and slightly Cu-deficient QDs, purple infilling for excitonic absorption and orange infilling for weak  $\text{Cu}^{1+}$  defect absorption in highly Cu-deficient QDs), and the PL spectra (dashed colored lines). (c) The second derivatives of the two Cu-deficient QDs show near-identical band gaps, but highly Cu-deficient QDs have significantly narrower absorption spectra due to the removal of  $\text{Cu}^{1+}$  defects. The figure inset shows the “subtraction spectrum” where the linear absorption spectrum of  $\text{Cu}_{0.85}\text{In}_1\text{S}_y$  is subtracted from  $\text{Cu}_{0.47}\text{In}_1\text{S}_y$ . The negative peak represents a decrease in the relative intensity of the band-edge transition whereas the positive peak represents an increase in the intensity of Cu-defect absorption as QDs become closer to stoichiometric, or Cu-rich. (d) Comparison of the PL and TA FWHM (right axis for both cases) as determined from the high energy

peak of the Bi-Gaussian fit for the TA bleach of  $\text{Cu}_{0.47}\text{In}_1\text{S}_y$ , and the only peak of the single Gaussian fit for the TA bleach of all other samples (purple closed circles). For PL, a single Gaussian fit was used for all samples (orange closed triangles). Since highly Cu-deficient QDs have two bands in the TA spectrum, an additional point is shown for the  $\text{Cu}^{1+}$  defect absorption shoulder (purple open circle). Both data sets are compared to the QY for the same samples (turquoise closed squares and left axis).

**Figure 3.1.2.2:** 3D-PLE measurements for CIS QDs. (a) Excitation energy-dependent PL for  $\text{Cu}_{0.85}\text{In}_1\text{S}_y$ . We observe little change in the spectral shape for above band gap (2.9 to 2.3 eV), resonant (2.3 eV), or shallow intra-gap excitation (2.3 eV to 2.1 eV). This is expected since the proposed energy of the absorptive intra-gap  $\text{Cu}^{1+}$  defects is  $\sim 2.05$  eV. However, for deep intra-gap excitation (2.1 eV, or lower in energy) the PL peak red-shifts due to QD size selection for both samples (for sample  $\text{Cu}_{0.85}\text{In}_1\text{S}_y$  see Figure S6.3.3). (b) PL excitation energy (PLE) measurements resonant with the PL energies marked by colored arrows with corresponding colors in (a) for  $\text{Cu}_{0.85}\text{In}_1\text{S}_y$  (c) The same measurements shown in (b) are repeated for  $\text{Cu}_{0.47}\text{In}_1\text{S}_y$ . The black lines for both (b) and (c) mark the peak of the PLE second derivative, and is used as an indicator of the absorptive transition responsible for PL emission at the marked probe energies. The TA measurements shown in Figure 3.1.2.1 are superimposed with these measurements for comparison. (d) The data from (a,b,c) is summarized and compared with  $\text{Cu}_{0.85}\text{In}_1\text{S}_y$  being represented by green squares and  $\text{Cu}_{0.47}\text{In}_1\text{S}_y$  represented by red circles. In each case, the PL peak energy is marked by solid symbols and the second derivative of the resonant PLE is marked with open symbols. (e) The PLE probe energy-dependent Stokes shift is measured by calculating energy difference between the peak of the PLE second

derivative and the probe energy at which it was collected. The dashed lines indicate the Stokes shift as predicted by the absorptive transition energies from the TA and PL measurements. The large variations in Stokes shift cannot be explained by size dispersion, and is in agreement with our proposed emission mechanism where the absorptive transitions responsible for PL arise from two distinct absorptive states: band-edges and  $\text{Cu}^{1+}$  defects.

**Figure 3.1.2.3:** (a) Femtosecond spectrally resolved transient absorption measurements: blue represents the spectra in the first 1 ps, green at 10 ps, and red at 100 ps. (b,c) The decay curves for the probe energies marked with the same colors in (a) where (b) is the raw data and (c) is the measurement normalized to the peak TA intensity. For each case, the panels are in the same order as in (a) where the Cu-rich QDs are in the bottom panel, and the most Cu-deficient in the top panel. (d-f) The decay curve at the TA peak (purple) is compared to the decay curve at the reddest probe energy (orange). For the (near)-stoichiometric QDs (e,f) there is no significant difference between the decay rates at different probe energies (with a small difference in the relative amplitude of the decays in Cu-rich QDs due to excessive electron trapping). For highly Cu-deficient QDs, the decay curve at the TA peak has to be fitted with a tri-exponential function (dashed red lines) whereas only a bi-exponential (dashed black lines) is needed for the decay on the red side. The additional component in the TA fit most likely represents hole localization, and its time constant is  $\sim 745$  fs.

**Figure 3.1.2.4:** (a) DOS for CIS supercells with two different defect pairs. The left panel represents anti-site “ $\text{Cu}^{1+}$  defects” whereas the right panel represents copper vacancies. For the right panel, copper vacancies result in an unoccupied state above the Fermi level,

which is spin-polarized due to the removal of an electron from  $\text{Cu}^x$ . Hence, the DOS for both spins are represented, and the intra-gap state is referred to as a “ $\text{Cu}^{2+}$  defect” due to its partially filled d shell. (b) Scheme representing the two defect pairs calculated in (a).  $\text{Cu}^{1+}$  defects form after anti-site swapping with  $\text{In}^{3+}$  to make charge-balanced defect pairs. For copper vacancies, the negative charge associated with the removal of a copper atom is charge-compensated by the oxidation of a second copper atom. As a result, we expect  $\text{Cu}^{2+}$  defects to occur in higher concentrations in QD ensembles that are highly Cu-deficient due to the increased prevalence of copper vacancies. (c) The computed linear absorption based on the DOS shown in (a), which indicates that the absorption of a photon promotes an electron from  $\text{Cu}^{1+}$ , or anti-site  $\text{Cu}_{\text{In}}$  defects to the CB, which leads to a low energy transition that broadens the absorption spectrum.  $\text{Cu}^{2+}$  defects, on the other hand, do not show this transition due to their partially occupied d shell, which leads to sharper spectra and a more distinct  $\text{VB} \rightarrow \text{CB}$  absorption peak.

**Figure 3.2.2.1.** Calculated local minima for 1.5 nm ZnSe QDs doped with  $\text{Cu}^{1+}$  atoms. “Sub” refers to subsurface impurities, “Surf4” and “Surf3” refer to surface impurities with a coordination number of 4 or 3, “Sub/Surf3” refers to QDs with 2 Cu impurities in the “Sub” and “Surf3” positions, and “ $\text{Cu}_4$ ” refers to QDs with 4 Cu atoms doped as a cluster. For Sub and Surf3, additional calculations with  $\text{Cu}^{2+}$  dopants are also described. Zn atoms are depicted in green, Se in blue, Cu in red, and pseudo-hydrogens in grey.

**Figure 3.2.2.2.** (a) DOS for subsurface  $\text{Cu}^{1+}$  doped ZnSe QDs. Band-edges (BE) are marked by solid black lines and the intragap “IG”  $\text{Cu}^{1+}$  impurity state is marked by a dashed line (here, at the Fermi level). Possible optical absorption transitions are marked by colored arrows and the theoretical Stokes shift, or  $\Delta_s$  (energy off-set between IG and

VB) is also labeled. The CB was determined to be the lowest unoccupied delocalized state (b), IG to be the Cu-Se occupied localized state (c), and VB to be the highest occupied delocalized state (d) based on the charge density distributions, which are shown in purple for occupied, and yellow for unoccupied energy levels. All unlabeled states between VB and IG are surface “trap-like” states. (e) The molecular orbital (MO) diagram for the QD, which includes the local tetrahedral coordination environment predicting the orbital hybridization for Cu-Se  $\sigma$  bonds. The BE states for Zn are also shown, and their full description is presented in Figure S3 using bulk ZnSe. The panel on the right of (e) depicts possible optical absorption (grey arrows) and emission (red arrow) transitions corresponding with the MO diagram.

**Figure 3.2.2.3.** (a) Effect of impurity position, coordination environment, and concentration on the DOS. The charge density distribution for each labeled IG state (marked by dashed lines) is depicted in (b-g) along with its orbital contribution to the corresponding DOS. A higher concentration of Cu (1.85%, 3.77%, and 7.84%, respectively) leads to additional absorptive/emissive states. For moderately doped QDs (e-f) the charge density of each labeled state is separately localized on its respective impurity ( $\Delta_{S1}$  on the 3-coordinated surface Cu, and  $\Delta_{S2}$  on the subsurface Cu). At higher impurity concentrations (g) the charge density is localized on all 4 Cu dopants regardless of the IG state energy.

**Figure 3.2.2.4.** Summary of the effects of chemical bonding on the theoretical Stokes shift. The clearest trends emerge in (a-c), which show that the ground state energy of Cu impurities is predominantly determined by coordination geometry and orbital contribution from Cu. IG states with less Cu character and in the distorted trigonal planar geometry

tend to have smaller Stokes shifts. All bond distances and angles are presented as the average between each Cu-Se bond in the coordination sphere, and error bars represent the standard deviation from the average bond angle or distance. (d) There does not appear to be a trend in changes of the ground state energy for surface vs. subsurface Cu impurities.

**Figure 3.2.2.5.** Charge density difference plots and Bader charges for each of the Cu impurity centers. QDs with a single Cu<sup>1+</sup> impurity are shown in (a-c), which represent the Sub, Surf4, and Surf3 systems, respectively. Calculations for Surf3 (d) and Surf4 (Figure S8) were repeated using single Cu<sup>2+</sup> impurities. QDs with multiple Cu<sup>1+</sup> impurities are shown in (e-f) where (e) represents the Sub/Surf3 system and (f) represents the Cu<sub>4</sub> system.

**Figure 3.2.2.6.** Computed absorption spectra for Cu doped ZnSe QDs with different impurity concentrations (left panel). A high Cu content leads to additional absorptive states, and inhomogeneous broadening. Considering that these impurities are also emissive, the same effects should also lead to broadening of emission spectra (right panel). For the scheme, BE absorption is marked by the grey arrow, Cu absorption by black arrows, and Cu emission by red arrows.

**Figure 3.3.2.1.** Examples of single-QD spectroscopic measurements for the UbiQD samples. (a) The PL intensity trajectory shows random fluctuations between the states of low (OFF) and high (ON) emissivities. This behavior is usually referred to as “blinking,” and is generally ascribed to either trapping at surface defects, and/or QD photoionization followed by nonradiative Auger recombination. Based on this measurement, the average

ON-time fraction is ~60%, which allows us to classify these dots as “weakly blinking.” (b) The strong photon antibunching behavior revealed by the second-order PL intensity-correlation function confirms that these measurements are conducted on a single-dot instead of a cluster. (c) A single-dot PL spectrum indicates a linewidth of 67 meV as determined based on the full width at half maximum (FWHM) of a Lorentzian fit (red line) of the experimental spectrum (black line).

**Figure 3.3.2.2.** Statistical analysis of single-particle data in comparison to ensemble measurements. (a) Ensemble absorption (blue line) and emission (red line) spectra exhibit a large Stokes shift (~340 meV) and a broad linewidth (~358 meV) typical of CIS QDs. (b) The Lorentzian fits for several single-particle PL spectra (colored lines) are projected onto the ensemble PL spectrum. As can be seen, the single-particle spectra are significantly narrower than the ensemble spectrum, but have widely varied peak emission energies. (c) The single-dot linewidth vs. peak position does not show any correlations between the two. (d) The histogram of single-QD linewidths. All of the measured QDs show linewidths less than ~100 meV, while the majority of the dots (~70%) have linewidths in the 50-to-70 meV range. The average linewidth is  $71 \pm 16$  meV.

**Figure 3.3.2.3:** Temperature controlled PL spectra for  $\text{Cu}_{0.47}\text{In}_1\text{S}_y$  QDs are shown in (a). The same measurement was repeated with  $\text{Cu}_{0.85}\text{In}_1\text{S}_y$  QDs. The spectrally integrated PL intensity for both measurements are presented as a scatter plot in (b) with  $\text{Cu}_{0.47}\text{In}_1\text{S}_y$  QDs represented by closed red circles, and  $\text{Cu}_{0.85}\text{In}_1\text{S}_y$  QDs represented with closed green squares. In both cases, fits based on equation 1 are shown as black lines (solid for  $\text{Cu}_{0.85}\text{In}_1\text{S}_y$  QDs and dashed for  $\text{Cu}_{0.47}\text{In}_1\text{S}_y$  QDs). In (c), the PL spectra for  $\text{Cu}_{0.47}\text{In}_1\text{S}_y$  QDs is normalized to the peak intensity for each temperature. The same procedure is

repeated for  $\text{Cu}_{0.85}\text{In}_1\text{S}_y$  QDs, and changes in peak position (top panel) and FWHM (bottom panel) are both plotted in (d). In both cases,  $\text{Cu}_{0.47}\text{In}_1\text{S}_y$  QDs are shown as red circles (closed for FWHM and open for peak position) and  $\text{Cu}_{0.85}\text{In}_1\text{S}_y$  QDs are represented as green squares (closed for FWHM and open for peak position).

**Figure 4.1.2.1:** (a) Absorption mechanisms for subensembles of CIS QDs with  $\text{Cu}^x$  defects. VB holes are either localized to the  $\text{Cu}^x$  state ( $x=1+$ ) or to a trap state ( $x=2+$ ). For  $\text{Cu}^{2+}$ , holes are already localized to  $\text{Cu}^x$  in the ground-state. (b) After holes are localized (by either  $\text{Cu}^x$  defect mechanism), emission occurs by recombination between a CB electron and a  $\text{Cu}^x$  hole. DFT calculations show that the  $\text{Cu}^x$  hole is localized to the Cu-S defect tetrahedra, and the CB electron is delocalized. (c) If QDs are defect-free, band-edge recombination occurs. Dissimilar to other reports,<sup>25</sup> we show with DFT that both band-edges are delocalized, and therefore recombination for band-edge carriers is faster than for  $\text{Cu}^x$  due to improved wavefunction overlap. (d) The top panel shows SNSPD measurements ( $\langle N \rangle < 0.1$ ) for CIS/ZnS core/shell QDs with 85% QY. Tri-exponential fits yield:  $\tau_t = 760 \text{ ps}$ ,  $\tau_{BE} = 27 \text{ ns}$ , and  $\tau_{Cu} = 297 \text{ ns}$ . If these measurements are repeated at different probe energies for core-only CIS with 28% QY (middle panel) we obtain nearly identical decay rates from a global tri-exponential fit. The bottom panel shows spectral electrochemistry measurements for the same core-only CIS. Since the dynamics are measured with TCSPC in the SEC measurements, the trapping component is too fast to be observed (resolution  $\sim 1.5 \text{ ns}$ ). However, both the BE and  $\text{Cu}^x$  lifetimes can still be found. As the Fermi level is lowered the oxidation state for  $\text{Cu}^x$  defects can be changed ( $\text{Cu}^{1+} \rightarrow \text{Cu}^{2+}$ ). (e) The relative amplitudes of each of the 3 decays for the middle panel of (d) are plotted, and projected against the steady-state PL spectra in the background

(black lines, grey shading). The “Gaussian-like” shape of the trapping and  $\text{Cu}^x$  components reflect different QY across the ensemble with trapping being weakest, and  $\text{Cu}^x$  emission being strongest at the PL peak. The BE component becomes weaker on the red side as expected by the smaller Stokes shift. (f) SEC measurements in the bottom panel of (d) are summarized. When the Fermi level is below the  $\text{Cu}^x$  state, there is an increase in the concentration of  $\text{Cu}^{2+}$  defects, which do not localize VB holes. Correspondingly, in subensembles without a separate hole trapping state BE recombination becomes competitive with  $\text{Cu}^x$  recombination, and the relative amplitude of the BE component increases.

**Figure 4.1.2.2.** (a) Linear absorption (black) and PL (red) for CIS/ZnS core/shell QDs. TA is measured at non-resonant (blue arrow) and (near)-resonant (green arrow) excitation. (b) Measurement of the absorption cross-sections at different excitation energies, which shows that the ratio of the absorption cross-sections at different excitation energies match the ratios of their optical densities (ODs) in the linear absorption spectra (details in main text). (c) The dynamics at low excitation density for both the non-resonant, and (near)-resonant excitation. Hole localization is faster than carrier cooling, which makes it difficult to resolve hole localization at non-resonant excitation. Hence, later-described Auger dynamics measured at 3.61 eV excitation are expected to be dominated by QD subensembles without hole localizing  $\text{Cu}^{1+}$  defects.

**Figure 4.1.2.3** (a) TA dynamics (CIS/ZnS core/shells with ~85% QY) at (near)-resonant excitation is dominated by hole localization for the subensembles with  $\text{Cu}^{1+}$  defects. Hole localization is ~200 fs, which is faster than the “normal” biexciton lifetime. The 10 ps biexciton lifetime obtained from the biexponential fit represents the small subensemble of

QDs without  $\text{Cu}^{1+}$  defects that undergo “normal” Auger between two delocalized states. (b) After holes are localized, biexcitons occur through delocalized CB and localized  $\text{Cu}^x$  states and have lifetimes more similar to what is expected for 2 trions when measured with SNSPD. (c,d) Hole localization determines whether the subensemble will undergo delocalized, or localized Auger. The left panel for both represents subensembles of QDs with  $\text{Cu}^{1+}$  defects, and explains the optical processes in (a,b). The panels on the right, on the other hand, show Auger properties for QDs without  $\text{Cu}^{1+}$  defects (either defect free or with  $\text{Cu}^{2+}$  defects). In this case, sub-ps hole localization from the VB to the  $\text{Cu}^x$  state does not occur, and TA measurements at non-resonant excitation can be used to obtain the “normal” biexciton lifetime since carrier cooling is slower than hole localization. (e) In this case, mono-exponential fits are used and also show  $\sim 10$  ps biexciton lifetimes. (f) The same measurements are repeated for core-only CIS QDs at high energy excitation. Here, biexponential fits are required due to photocharging, which yields the same biexciton lifetime ( $\sim 10$  ps), but with an additional  $\sim 150$  ps trion lifetime.

**Figure 4.1.2.4:** (a) Poisson statistics fits to the fluence-dependent early- (red) and late-time (blue) signal for TA measurements at non-resonant excitation (top panel), (near)-resonant excitation (middle panel), and for PL collected at non-resonant excitation (bottom panel). (b) For “normal” Auger in defect-free QDs, or QDs with  $\text{Cu}^{2+}$  defects, CIS exhibits “normal” volume scaling for multicarrier lifetimes due to the delocalized wavefunctions of the band-edge states. (c,d) If we compare the magnitude of the early (A) and late (B) time signal, the relationship between carrier density and the “on-set” of Auger can be compared for all three measurements. (d) The onset for Auger interactions is the same regardless of the measurement method, which indicates that while we have

a broad range in lifetimes based on the measurement method, they are all related to multicarrier interactions and Auger dynamics.

**Figure 4.1.2.5:** (a,b) Measurement of the excited-state absorption spectrum for CIS/ZnS QDs at non-resonant (a) and (near)-resonant (b) excitation. (c) Summary of the data in (a,b) at the 1 ps delay time shows that the magnitude of the bleach is relatively weak in comparison to the linear absorption. However, it is much stronger for (near)-resonant excitation measurements due to the dominance of hole localization in TA dynamics, which indicates that the majority of the ensemble has  $\text{Cu}^{1+}$  defects.

**Figure 5.1.2.1** Transmission electron microscopy (TEM) images of  $\text{CuInSe}_x\text{S}_{2-x}$  QDs and their optical spectra. (a) TEM images of  $\text{CuInSe}_{1.6}\text{S}_{0.4}$  QDs with a mean height of 5.5 nm and a standard deviation of 1.8 nm. (b) Optical absorption (blue solid lines), photoluminescence (PL; red solid lines), and early-time TA (green circles, 1-ps pump-probe delay; Gaussian fits are shown by black dashed lines) spectra of  $\text{CuInSe}_x\text{S}_{2-x}$  QDs with a varied Se fraction; all samples have approximately the same height of 5.0 - 5.7 nm. (c) Schematic representation of optical transitions responsible for the VB-to-CB absorption (blue arrow) and intragap PL (red wavy arrow); the latter transition involves a native Cu-related defect ( $\text{Cu}^*$ ).

**Figure 5.1.2.2** Electrochemical studies of  $\text{CuInSe}_x\text{S}_{2-x}$  QDs and energies of optically and electrically active states as a function of a varied Se content ( $f_{\text{Se}}$ ). (a) Cyclic voltammograms (CVs) of  $\text{CuInSe}_{1.6}\text{S}_{0.4}$  QD colloidal solutions; mean QD height is 5.5 nm. The potential is scanned from 0 to 2 V (forward scan), then to -2 V (reverse scan) and finally back to 0 V. An intra-gap wave with onset at -5.14 V (obtained from the intersection

of the red dashed lines) observed during the forward scan is ascribed to oxidation of  $\text{Cu}^{1+}$  to  $\text{Cu}^{2+}$ . The second oxidation wave with onset at  $-5.58$  eV is due to hole injection into the QD VB. The position of the CB level is obtained as a sum of the VB energy and the optical band gap. (b) Energies of the CB (blue solid circles) and VB (green solid squares) levels for  $\text{CuInSe}_x\text{S}_{2-x}$  QDs with different  $f_{\text{Se}}$  based on CV and optical measurements. The purple open diamonds ( $\text{Cu}^*_{\text{EC}}$ ) show the redox potential of the intragap feature ascribed to the  $\text{Cu}^*$  defect, and the red open squares ( $\text{Cu}^*_{\text{PL}}$ ) correspond to the energy of the intragap state obtained based on the apparent Stokes shift from the optical measurements (Figure 5.1.2.1b). The energies of native donor and acceptor defect states obtained from transport measurements are shown by orange open up-point triangles and yellow open down-point triangles, respectively.

**Figure 5.1.2.3** Charge transport measurements of  $\text{CuInSe}_{1.6}\text{S}_{0.4}$  QD films incorporated into FETs. (a) A schematic representation of a bottom-gate, bottom-contact QD-FET. (b) Output characteristics ( $I_{\text{DS}}$  vs.  $V_{\text{DS}}$ ) of a gold-contact FET made of as-synthesized  $\text{CuInSe}_{1.6}\text{S}_{0.4}$  QDs with long native ligands (the mean QD height  $h = 5.5$  nm), which shows a  $p$ -channel behavior. (c) Output characteristics for a gold-contact FETs based on QDs treated with EDT ligands. (d) A top-view SEM image of an In-contact  $\text{CuInSe}_{1.6}\text{S}_{0.4}$  QD-FET along with the plot of the  $\text{In}/(\text{Cu}+\text{In})$  ratio as a function of location along the channel before (red symbols) and after (blue symbols) heat treatment at  $250$  °C, as determined by EDS. (e) Output characteristics of the In-contact  $\text{CuInSe}_{1.6}\text{S}_{0.4}$  QD-FET after thermal annealing, which show a nondegenerate  $n$ -channel behavior. (f) Transfer characteristics ( $I_{\text{DS}}$  vs.  $V_{\text{GS}}$ ) of the device shown in 'e' measured at  $V_{\text{DS}} = 20$  V, which corresponds to the saturation regime. Solid and dotted lines are the forward and the reverse scan,

respectively. The linear extrapolation of the  $(I_{DS})^{0.5}$  transfer curves measured for large positive voltages are used to determine a threshold voltage,  $V_{th}$  (blue lines); values  $V_{th,F}$  and  $V_{th,B}$  are obtained from the forward and reverse (backward) scans, respectively.

**Figure 5.1.2.4** The two-state conductance model for explaining the dependence of carrier mobilities in  $\text{CuInSe}_x\text{S}_{2-x}$  QD films on the  $\text{Se}/(\text{Se}+\text{S})$  ratio and temperature. (a) Electron (blue) and hole (red) mobilities obtained from FET measurements of, respectively,  $n$  (indium contacts; EDT-treated, annealed QD films) and  $p$  (gold contacts; EDT treated QD films) type devices (symbols) in comparison to fit lines produced by a two-state conductance model (lines). Based on the fits,  $\gamma_{C,D} = 1.76$ ,  $\mu_D = 7.2 \times 10^{-6} \text{ cm}^2 \text{ V}^{-1} \text{ s}^{-1}$ ,  $\mu_{CB} = 9 \times 10^{-3} \text{ cm}^2 \text{ V}^{-1} \text{ s}^{-1}$ ,  $\Delta E_{e,S} = 416 \text{ meV}$ ,  $\Delta E_{e,Se} = 17 \text{ meV}$  ( $n$ -type films) and  $\gamma_{V,A} = 0.5$ ,  $\mu_A = 4.6 \times 10^{-6} \text{ cm}^2 \text{ V}^{-1} \text{ s}^{-1}$ ,  $\mu_{VB} = 6.4 \times 10^{-3} \text{ cm}^2 \text{ V}^{-1} \text{ s}^{-1}$ ,  $\Delta E_{h,S} = 330 \text{ meV}$ ,  $\Delta E_{h,Se} = 10 \text{ meV}$  ( $p$ -type films). The energy gap between the band-edge and the defect states as a function of  $f_{Se}$  is displayed in the inset by solid blue ( $n$ -type films) and open red ( $p$ -type films) symbols. The absolute energies of defect states derived from charge transport studies are shown in Figure 5.1.2.2b by orange open up-point triangles (donors) and yellow open down-point triangles (acceptors). (b) A schematic depiction of the two-state conductance model for the  $\text{CuInSe}_x\text{S}_{2-x}$  QD films. In this model, carriers are transported *via* two thermally coupled states. A higher-mobility state is ascribed to the intrinsic CB ( $n$ -type) or VB ( $p$ -type) levels (blue), and the lower mobility state to the native donor ( $n$ -type) or acceptor ( $p$ -type) defects (red). In thermal equilibrium, the relative occupancies of these states and the resulting apparent mobility are defined by the  $f_{Se}$ -dependent inter-state energy gap ( $\Delta E_e$  or  $\Delta E_h$ ) and temperature according to eq 3. (c) Temperature-dependent electron mobility measured in the linear regime for the  $n$ -type  $\text{CuInSe}_{1.6}\text{S}_{0.4}$  QD film ( $h =$

5.5 nm) (symbols) along with a fit (line) using the two-state conductance mode. The  $\Delta E_e$  energy produced by this fit (16.9 meV) is virtually identical to that obtained from the room-temperature  $f_{Se}$ -dependent measurements (17 meV; the inset of panel 'a').

**Figure 5.1.2.5** Effect of ALD treatment on characteristics of the *n*-type  $\text{CuInSe}_{1.6}\text{S}_{0.4}$  QD FET. (a) Output characteristics of the ALD-treated indium-contact  $\text{CuInSe}_{1.6}\text{S}_{0.4}$  QD-FET ( $h = 5.5$  nm). (b) Transfer characteristics of the same device. Charge transport parameters are significantly improved upon ALD treatment as discussed in the text.

## ACKNOWLEDGMENTS

First, I would like to thank my three amazing advisors at UCLA/LANL for guiding me on this long journey: Victor Klimov, Philippe Sautet, and Anastassia Alexandrova. This first sentence of my acknowledgments section is probably among the weirdest for UCLA dissertations. Who requires three advisors? Not many students get the opportunity to spend 4 years of their PhD at another institution (Los Alamos National Laboratory) conducting both theory and experimental work. While my thesis will focus on a relatively small class of materials, the techniques and approaches I wanted to learn spread into so many areas I required more guidance than the typical student. For Victor, I remember meeting you in 2015 at San Francisco during the spring MRS conference. Thank you for writing to the AAPP committee and helping me obtain the fellowship that gave me the funded opportunity to work at LANL. Your guidance through the experimental aspects of these projects helped me grow both as a scientist and as a person, and was an invaluable experience. To Anastassia and Philippe, thank you for aiding me through the process of switching research areas in the middle of my PhD. Your continued guidance on the theory aspects of these projects helped me expand from the world of experiments into computational chemistry. An expansion so great, that my first post-PhD position will be entirely theory. Thank you also to Dante Simonetti, for being so easy to talk to, and for being an understanding catalysis researcher sitting through my long computational chemistry/experimental optics talks. Last, but *very* far from least, I would like to thank my three mentors at CSULB that started me on this path: Xianhui Bu, Sergio Mendez, and Roger Lo. When I started at CSULB, I had no idea I was going to pursue a PhD, or a research career. I wish I could say that my path was one of careful planning, but in reality

I just “winged it” and tried a bunch of random things until I ended up working in Dr. Bu’s crystallography group and on a microfluidics project advised by Dr. Lo and Dr. Mendez. Your guidance, both in the lab and out of the lab are the reason I decided that I wanted to go down the PhD and research road. I can’t thank you enough for all the advice, all the letters of recommendation, and more importantly than both of those, the inspiration. I know I have truly found my passion, and I would not have if it were not for the exposure you gave me.

In addition to my wonderful advisors, I would like to thank all of my other mentors, co-workers, and lab mates at UCLA/LANL. Firstly, I would like to thank Istvan Robel and Jeff Pietryga for their scientific and career guidance. Our many illuminating conversations not only helped me understand the complex, often confusing sets of data I encountered with CIS QDs, but also helped me decide on my ultimate career path. I would also like to thank Nikolay Makarov and Rohan Singh for not only taking so much time to help train me in ultra-fast spectroscopy, but also in being great friends that helped make Los Alamos feel like home. Once upon a time I used to synthesize materials, but since the research shift in the middle my PhD I have not done much in regards to sample preparation. For all of the studies presented here, I was lucky to have amazing synthetic chemists that prepared perfect samples for all of my crazy characterization/calculation ideas including: Hyeong Jin Yun, David So, Hongbo Li, and Jun Du. Jin, thank you also for the amazing laughs during lab breaks, and single-handedly doing all of the FET measurements presented in my final chapter. I would like to also thank Scott Crooker for guiding me through magneto-optical spectroscopy measurements, and your enlightening conversations on optics and condensed matter physics broadly. A special thanks goes to

Ches Simpson for helping me get my start at LANL under the AAPP Fellowship, and Tommy Rockward for taking over the fellowship after Ches' departure. Your faith in my ability to excel at LANL will never be forgotten. Last, but certainly not least at LANL, I would like to thank all the members of our Thursday lunch brigade: Rohan, Nikolay, Istvan, David, Jeff, Zachary Robinson, Kıvanç Güngör, Andrew Fidler, Tom Baker, and Oleksandr (Sasha) Isaienko. Regardless of how the week was going, I always had Thursday New Mexico green chiles (in either burrito or burger form) to look forward to. Kıvanç, I would like to officially name you as the MVP of this team for always preparing coffee and saving us from imminent food comas.

At UCLA, I would like to thank Elisa Jimenez-Izal and Geng Sun for all the DFT training you provided me. Both of you were incredibly patient teachers. I would like to also thank Elisa, and Mai-Anh Ha for all of those great coffee (and other beverage) breaks where we could talk about life. Our conversations were among the brightest, most fun I had at UCLA, and helped me remember that there was more to my time at UCLA than just research. For outside of UCLA/LANL, I would like to give thanks to all of the guys at UbiQD: Nikolay, Hunter McDaniel, Karthik Ramasamy, Matt Bergren, and Aaron Jackson. To Nikolay, I am glad we were able to continue collaborating and maintain our friendship after you left LANL; your pictures from our hikes to the tops of 14,000 ft. mountains, cross-country skiing, rafting, and other adventures will always be the highlight of my time here at LANL. To Hunter and Matt, thank you for securing the NMSBA funding and providing me with the opportunity to collaborate with your start-up company. I have always wanted direct industry experience, and without your hard work I would have never had the opportunity. Thank you also for inviting me to the ugly sweater parties, and letting me

interact with and get to know both you, and the others at the company better. I am sure that as you continue your hard work CIS QDs will truly become ubiquitous. To Karthik, thank you for preparing the Rambo QDs. Much like Sylester Stallone's character, they were rock stable and could not be killed by the laser, which made the entire single dot spectroscopy study possible. Thank you also for the great conversations and fun times cross-country skiing with Nikolay and I.

Now, to one of the hardest parts, to all those who inspired me before, and during my stay at UCLA/LANL. To my father, Paul Fuhr, thank you for always inspiring me to try my best. I learned how to work hard, show up even on the tough days, to be resourceful, to never give up, and to understand that no job was beneath me after all those years of growing up, and watching you. To my best friend, my brother, Michael Kim, thank you for inspiring and supporting me. There were so many dark moments the last few years, moments that I don't even know how to write about, moments that I do not know how I would have gotten through without your friendship. I lost count of the many times I was running on empty, but after every conversation we had I was back to full, and ready for more. I cannot put into words how thankful I am for our friendship, and it will always be one of the greatest highlights of my life. To my girlfriend, Tiana Vo, thank you for being there with me through all the hard moments: before, during, and the many more that will happen after my PhD. I love you. To Steven Chau, only a few months before beginning my journey Chris Ung passed away, and we became closer than ever as we tried to deal with all of our pain. I don't know how I would have been able to re-center, and get ready for my journey without all of those late night talks, which further expanded after I started at LANL and we were both away from home. If it weren't for those talks, I would have felt

so alone. Lawrece Men, every return trip home talking to you was one of my greatest highlights. You're the reason I even got into engineering. I remember staring at your calculus HW and thinking of how much more fun it looked than what I was doing during our CSULB library study hours. Whether it was nerding out, or making dumb jokes, I could always count on you to make me smile. Chris, you are gone but not forgotten, I wish you were here to celebrate with Steven, Mike, Lawrece, and I. Your larger than life personality, can never be replaced, and will never be forgotten by either myself, them, anyone else from cabinet, or for that matter any one else that has ever gotten to know you. On that note, my trips home where I got to spend time with our dear-old cabinet were always my best: Seth Bin, Sam Maeda, Sovanna Chou, Chhou Ou-Ratunil, Polina Sok, and Christine Kieng. Chris would have been happy to see us all stay so close. Thank you for all the laughs and discussions, and a special thanks to Sam and your unbelievably awesome husband Kevin for taking care of Zsa Zsa! She's a handful of a cat, and my last trip at home was made possible only by your generosity.

There are so many others to name I don't know where to begin: but I'll start with Zach Libow (and your awesome family), Garry Taing, Chhaya Tan, and Yuth In. Besides being amazing friends, and providing me with awesome memories, you gave me places to stay during conferences. Some of those conferences ended up being pivotal for my long-term career advancement, and it's hard for me to not look back and think: "If it weren't for them, I wouldn't be here." Thank you! Konrad Braun, for being one of the few Californians brave enough to visit me in New Mexico, and have long cross-country ski journeys, crack out the Dave Chappelle jokes, talk about science, and politics. Every time we hung out, you brightened my day. Draw one line! Shafi Mith, keeping up with you both

in the CSULB and UCLA days helped keep my optimism going through all the tough research hurdles, and I'm very thankful for your friendship. Elaine Lu, Soohye Lee, and Stephanie Cho, thank you for always providing an ear to listen and being so supportive. Every time we talked my day got brighter. Kosal Taing, you were an awesome roommate, and I powered through my first year of exams at UCLA fueled in part by our Korean BBQ hang outs with Henry Chan that made those statistical thermodynamics tests so much more tolerable. Thank you! To Denny Khoun, David Voeur, Leslie Lim, Monica Chea, Santho Toun, Moony Thach, Jules Micheli, Fornia Chann, Daniel Oum, Mama Kim Chu, Yan Katz, and so many others, every time I got to see you, see home, or see Denver, I got to laugh, smile, and was able to stay excited for the day my PhD would be complete, and I could step into the "real world." I guess that day is today, thank you.

Several chapters and sections of chapters in this dissertation are a collection of the previous publications listed below:

**Chapter 2 Section 2.1** is adapted with permission from publication "Light Emission Mechanisms in  $\text{CuInS}_2$  Quantum Dots Evaluated by Spectral Electrochemistry" **Fuhr, A.**; Yun, H. J.; Makarov, N. S.; Li, H.; McDaniel, H.; Klimov, V. I.; *ACS Photonics*, 2017, 4, 2425-2435. Copyright (2017) American Chemical Society. This work was supported by the Center for Advanced Solar Photophysics (CASP), an Energy Frontier Research Center funded by the U.S. Department of Energy, Office of Science, Basic Energy Sciences. And, the Chemical Sciences, Biosciences and Geosciences Division of Basic Energy Sciences, Office of Science, U.S. Department of Energy, and the African American Partnership Program.

**Chapter 3 Section 3.2** is adapted with permission from publication “Heterogeneity in Local Chemical Bonding Explains Spectral Broadening in Quantum Dots with Cu Impurities” **Fuhr, A.**; Alexandrova, A. N.; Sautet, P.; *J. Phys. Chem. C*, 2019, 123, 5705–5713. Copyright (2017) American Chemical Society. This work was supported by the NSF CAREER Award (CHE-1351968) and the African American Partnership Program at Los Alamos National Laboratory.

**Chapter 5** is adapted with permission from publication “Charge Transport Mechanisms in  $\text{CuInSe}_x\text{S}_{2-x}$  Quantum Dot Films” Yun, H.; H. J.; Lim, J.; **Fuhr, A.**; Keene, S.; Law, M.; Pietryga, J. M.; Klimov, V. I.; *ACS Nano*, 2018, 12, 12587-12596. Copyright (2017) American Chemical Society. This work was supported by the Center for Advanced Solar Photophysics (CASP), an Energy Frontier Research Center funded by the U.S. Department of Energy, Office of Science, Basic Energy Sciences. And, the Solar Photochemistry Program of the Chemical Sciences, Biosciences and Geosciences Division of Basic Energy Sciences, Office of Science, U.S. Department of Energy. Additional support was provided by and the African American Partnership Program at Los Alamos National Laboratory, and the UC Laboratory Fees Research Program Collaborative Research and Training Award LFR-17-477148.

## VITA

---

### Education

**Bachelor of Science in Chemical Engineering**, 2013 – California State University, Long Beach, CA

**Bachelor of Arts in Chemistry**, 2013 – California State University, Long Beach, CA

---

### Experience

**Undergraduate Student Researcher**, 2011-2013 – California State University, Long Beach, *Department of Chemistry and Biochemistry, Department of Chemical Engineering*

**Graduate Student Researcher**, 2013-2019 – University of California, Los Angeles, *Department of Chemical and Biomolecular Engineering*

**Teaching Assistant**, 2013-2015 – University of California, Los Angeles, *Department of Chemical and Biomolecular Engineering*

**Graduate Student Researcher**, 2015-2019 – Los Alamos National Laboratory, *Center for Physical Chemistry & Applied Spectroscopy*

---

### Awards

**RISE Fellowship**, 2012-2013 – NIH

**Green Energy Undergraduate Student Poster Award**, 2013 – IEEE

**AAPP Fellowship**, 2015-2019 – Los Alamos National Laboratory

**Ben Lujan Small Business Excellence Award**, 2017 – NMSBA

**Leveraged Project Success Story**, 2017 – NMSBA

---

## PUBLICATIONS & PATENTS

---

### Patents

Cai, M.; Lu, Y.; Yand, L.; Fang, D.; Shen, J.; **Fuhr, A.**; Shen, L.; (2018). "Electrolyte Structure for Metal Batteries", US Patent number 20160254567A1

---

### Publications

Zheng, S.; Wu, T.; Chou, C-T; **Fuhr, A.**; Feng, P.; Bu, X. "Development of Composite Inorganic Building Blocks for Metal-Organic Frameworks", *J. Am. Chem. Soc.*, 2012, 134, 4517-4520.

Zheng, S-T; Zhao, X.; Lau, S.; **Fuhr, A.**; Feng, P.; Bu, X. "Entrapment of Metal Clusters in MOF Channels by Extended Hooks Anchored at Open Metal Sites", *J. Am. Chem. Soc.*, 2013, 135, 10270-10273.

Cao, Y.; Li, X.; Bian, Z.; **Fuhr, A.**; Zhang, D.; Zhu, J.; "Highly Photocatalytic Activity of Brookite/Rutile TiO<sub>2</sub> Nanocrystals with Semi-Embedded Structure", *Appl. Cat. B.*, 2016, 180, 551-553.

**Fuhr, A.**; Yun, H. J.; Makarov, N. S.; Li, H.; McDaniel, H.; Klimov, V. I.; "Light Emission Mechanisms in CuInS<sub>2</sub> Quantum Dots Evaluated by Spectral Electrochemistry", *ACS Photonics*, 2017, 4, 2425-2435.

Yun, H.; H. J.; Lim, J.; **Fuhr, A.**; Keene, S.; Law, M.; Pietryga, J. M.; Klimov, V. I.; "Charge Transport Mechanisms in CuInSe<sub>x</sub>S<sub>2-x</sub> Quantum Dot Films", *ACS Nano*, 2018, 12, 12587-12596

**Fuhr, A.**; Alexandrova, A. N.; Sautet, P.; "Heterogeneity in Chemical Bonding Explains Spectral Broadening in Quantum Dots with Cu Impurities", *J. Phys. Chem. C*, 2019, 123, 5705–5713

---

## CHAPTER 1

### Motivation & Interest in Quantum Dots with Copper Impurities

## **1.1. Introduction: Climate Change & Quantum Dots**

Early signs of ecological deterioration such as widespread coral bleaching of the Great Barrier Reef offer prescient examples of the perils of climate change.<sup>1</sup> *Hallegatte et al.* recently categorized the most pertinent concerns to include: (1) unique and threatened systems (e.g. rainforests and their dependent societies); (2) extreme weather events (e.g. coastal flooding and drought); (3) the uneven distribution of impacts (e.g. effects on poor and rural communities); (4) global aggregate impacts (e.g. loss of biodiversity and economic contraction); and (5) large-scale singular events (e.g. glacier calving in Greenland).<sup>2</sup> Each of these categories were designated to be of “High” or “Very high” concern if global mean temperatures climb to 3 °C above that of the year 1870 (~2.2 °C from 2016). The origins of our precarious climate trajectory are closely associated with rapid industrialization and burgeoning green-house gas emissions (e.g. carbon-dioxide, methane, nitrous oxide, hydro-fluorocarbons, per-fluorinated compounds, and sulfur hexafluoride). Carbon-dioxide (CO<sub>2</sub>), in particular, is closely associated with both global warming and fossil fuel usage, and the cumulative increase in anthropogenic CO<sub>2</sub> since the industrial revolution is nearing 2000 PgC — correlating to a ~0.8 °C rise in the global mean temperature. As described by the Intergovernmental Panel on Climate Change (IPCC), halting the steady rise in anthropogenic CO<sub>2</sub> is pivotal to the sustainability of global society.

The 21<sup>st</sup> conference of the UNFCCC (United Nations Framework Convention on Climate Change) in Paris released a policy roadmap for limiting warming to 2 °C (pursuing efforts to 1.5 °C) above pre-industrial levels by 2100.<sup>3</sup> However, achieving these emission

targets will be difficult. Atmospheric carbon has an exceptionally long lifetime that strictly limits the emissions budget. Further, expanding affordable electricity access in rural communities with low human development indices (HDI) is typically difficult without using fossil fuels, which tend to have higher efficiency and/or lower cost than alternative energy sources. The juxtaposition of expanding inexpensive energy access, while maintaining strict emission standards remains a significant scientific and technological challenge.

There are essentially three areas in which electricity access can inexpensively expand: grid, decentralized, and end-use technology.<sup>4</sup> Photonic devices have the potential to impact each of these realms. Over the last several decades the efficiency of solar cells has steadily improved with the average cost dropping sharply.<sup>4</sup> Thus, leading to a massive expansion of both grid and decentralized (defined as individual housing/building unit) usage. The increasing success of solar cells has spurred interest in new scientific thrusts for unconventional methods of solar energy harvesting (*e.g.* photovoltaic windows and wearable devices).<sup>5</sup> Advances in grid and decentralized solar energy harvesting when coupled with the expansion of energy-efficient end-use technology (*e.g.* replacing incandescent light bulbs and energy inefficient displays with high-performance light-emitting diodes, or LEDs) can vastly improve the feasibility of expanding energy-access while lowering our carbon footprint.<sup>4</sup>

Quantum dots (QDs) have emerged as a viable technological alternative to bulk and organic semiconductors for producing low-cost and high-efficiency solar and LED technology.<sup>5</sup> Yet, several barriers have limited their commercial impact. For example, most early chalcogenide-based QDs use heavy metals (*e.g.* Cd for visible emission, or Pb for near-IR emission), which are highly toxic. This has spurred interest in ternary

quantum dots with copper cations such as Cu-doped ZnSe,  $\text{Cu}_x\text{In}_{2-x}\text{S}_2$  (CIS),  $\text{Cu}_x\text{In}_{2-x}\text{Se}_2$  (CISe), and  $\text{Cu}_x\text{In}_{2-x}\text{Se}_{2-x}\text{S}_x$  (CISeS).<sup>6</sup> However, several studies have shown that the (electro)-optical properties of these materials are distinct from typical II-VI or IV-VI QDs (e.g. large Stokes shifts, long radiative lifetimes, broad linewidths, and tunable polarity for charge transport). Notably, these unique properties have different implications for several (electro)-optical device schemes. For example, reabsorption losses in photovoltaic windows can be mitigated by the large Stokes shift, which improves the external quantum efficiency in larger-scale devices. On the other hand, the broad linewidths decrease color purity for QD-LEDs.<sup>5</sup> Therefore, the future development of synthetic/device architecture routes for achieving high-performance photonic devices hinges on understanding these (electro)-optical processes, and controlling them.

To address these concerns, this thesis will elucidate the unique light absorption, emission, and charge transport mechanisms for QDs with Cu cations. Specifically, theory and experiment will be combined to understand the origin of the large Stokes shift, broad optical spectra, carrier trapping, Auger processes, and transport characteristics of QDs with copper cations broadly, and with particular emphasis on CIE (where E = S,Se) QDs. Structure-property relationships will be explored experimentally *via* electrochemistry, *in situ* spectroelectrochemistry (SEC), single-dot spectroscopy, magneto-optical spectroscopy, and ultra-fast spectroscopy studies. Theory will emphasize density functional theory (DFT) approaches informed by experimental observations, and results for both theory and experiment will be compared to device studies. Special attention will be devoted to connecting theoretical and experimental results to achieve the technological goals outlined above. These are best summarized as ultra-high quantum

yields, fast carrier transport, and exploring the possibility of Stokes-shift and linewidth engineering for photovoltaic windows and QD-LEDs.

## **1.2. Nanocrystal Quantum Dots: Materials Chemistry & Device Physics**

### **1.2.1. Unique Properties Arising from Quantum Confinement**

**Electronic States & Size-Dependent Optical Properties.** Development of high-performance semiconductor (electro)-optical devices requires a thorough understanding of the electronic structure for the active material(s). The periodic potential felt by a particle in the repeating environment of a semiconductor crystal is best represented as Bloch waves (eqn. 1):

$$\psi_{nk}(\vec{r}) = u_{nk}(\vec{r}) \exp (ik \cdot \vec{r}) \quad (1)$$

where the wave functions are represented by band index  $n$  and wave vector  $k$ , and  $u_{nk}$  is a function with the periodicity of the crystal lattice.<sup>5</sup> Band structure for semiconductors is generally depicted by plotting the energy of the particle as a function of its position in wave-vector  $k$ . This is done according to the *effective mass approximation*, which argues that the movement of particles over distances larger than the lattice spacings differs from that of vacuum. As such, they can be approximated as free particles with an effective mass ( $m_{eff}^{c,v}$ ). This simplifies the complex periodic potential felt by the particle in the lattice and allows us to graphically determine the band gap by the curvature of the valence and conduction bands at  $k=0$ . This is shown with eqn. 2 and eqn. 3:

$$E_k^c = \frac{\hbar^2 k^2}{2m_{eff}^c} + E_g \quad (2)$$

$$E_k^c = -\frac{\hbar^2 k^2}{2m_{eff}^v} \quad (3)$$

where  $E_g$  represents the band gap,  $c$  the conduction band, and  $v$  the valence band.

When a photon of a high enough energy is absorbed by the semiconductor, a valence band electron will be excited to the conduction band forming an exciton (electron-hole pair). The natural length scale of the electron, hole, and exciton (bound hydrogenic-like state formed as a result of the Coulombic attraction between the electron and hole) are referred to as the Bohr radii. The Bohr radii is material-dependent and can be approximated by eqn. 4:

$$a_B = \varepsilon \frac{m}{m^*} a_0 \quad (4)$$

where  $\frac{m}{m^*}$  refers to the mass of an electron at rest divided by the mass of the particle,  $\varepsilon$  the dielectric constant, and  $a_0$  the Bohr radius of the Hydrogen atom.<sup>7</sup> However, if the dimensions of the nanocrystal are smaller than the exciton Bohr radius, the electron-hole pair is confined by the dimensions of the material. This is referred to as *quantum confinement*, and results in the relevant band energy minima/maxima becoming increasingly separated. As the spatial separation of the nanocrystal energy levels becomes more pronounced, their interactions weaken until they form a series of quantized energy levels (**Figure 1.2.1.1**). Referred to as the *single-band approximation*, this allows for the band structure to be represented by discrete wave vectors  $k$  approximated from the curvature of the continuous  $\Gamma$ -centered bulk semiconductor Brillouin zone.<sup>5</sup>

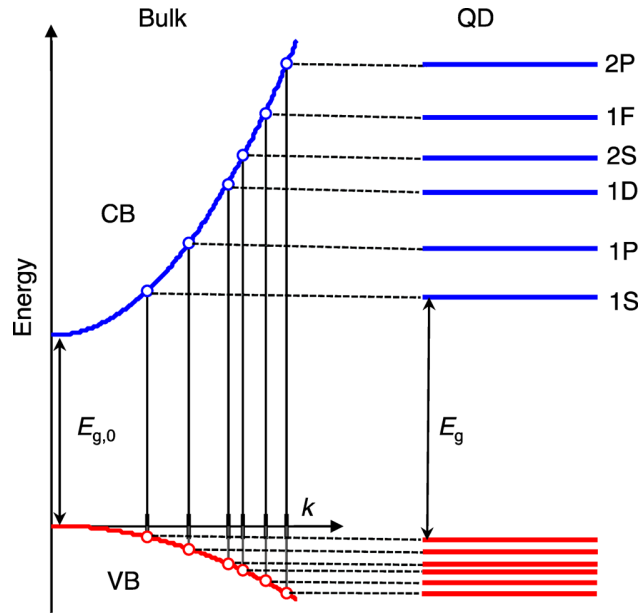


**Figure 1.2.1.1.** Idealized comparison of the energy bands for a bulk semiconductor (left) and spherical QD (right) made of the same material. Bulk semiconductors show a parabolic dispersion of the carrier kinetic energies, which then transform to discrete atomic-like energy levels in QDs. VB and CB refer to the valence and conduction bands, respectively. The band gap is represented by  $E_g$ .

*Quantum dots* (QDs) refer to materials in which confinement occurs in all three spatial dimensions.<sup>5,7</sup> Considering that confinement results from the crystal size shrinking below the exciton Bohr radius, confinement effects become stronger as the nanocrystal radius decreases further. Hence, the band gap of QDs can be altered not only by changing material composition, but also by decreasing crystal size. These unique properties allow for quantum dots to have size-tunable absorption and emission spectra as well as exhibit several other unique phenomena described in subsequent sections.

**Multicarrier Interactions.** Quantum confinement also leads to enhanced multicarrier interactions, and more pronounced Auger processes.<sup>5</sup> Auger recombination emerges when the excitation energy for an e-h pair is transferred to other carriers instead

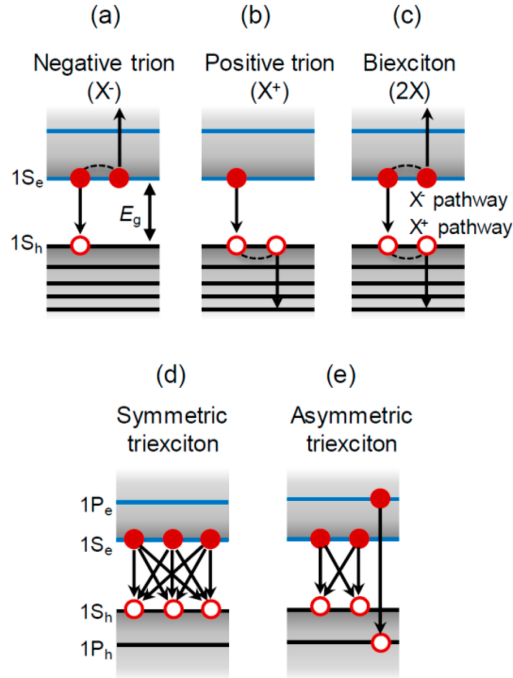


**Figure 1.2.1.2.** Auger recombination pathways normally observed in QDs: (a) negative trion ( $X^-$ ), (b) a positive trion ( $X^+$ ), (c) a biexciton ( $2X$ ), and (d,e) a triexciton ( $3X$ ) where  $X$  refers to the number of e-h pairs. Trions represent the case where the energy released during recombination is transferred to a CB electron ( $X^-$ ) or VB hole ( $X^+$ ). Biexcitons describe two excitons and triexcitons three excitons where Auger recombination can occur via  $X^+$  or  $X^-$  pathways. For triexcitons, there are symmetric (d) and asymmetric (e) pathways where symmetric refers to the case where all charge carriers are in the 1S (CB or VB) states and asymmetric when there are 2-fold degenerate 1S levels resulting in a third carrier in the 1P state.

of undergoing a radiative transition (**Figure 1.2.1.2**).<sup>5, 8</sup> In bulk semiconductors, the Auger decay rate can be described by eqn. 5:

$$r_A \propto \exp\left(-\frac{\gamma_A E_g}{k_B T}\right) \quad (5)$$

where  $\gamma_A$  is an electronic structure-dependent constant specific to the material. The expression predicts Auger recombination to decrease at lower temperatures due to the decreasing kinetic energies of the carriers. Recognizing that translational momentum and energy must be conserved, at absolute zero the carriers have no kinetic energy and Auger recombination cannot occur. However, for QDs the Coulombic e-h energy can be smaller than confinement energy (e.g. exciton binding energy for PbSe is  $\sim 0.6$  meV vs.  $\sim 1$  meV

for confinement).<sup>5</sup> Hence, electron and hole motions are not correlated and the discrete energy levels of QDs are classified by angular momenta.<sup>9-11</sup> Additionally, confinement in a smaller spatial regime results in enhanced Coulomb coupling. This is further augmented by reduced dielectric screening due to the lower dielectric constant of the solvent/medium than the QD itself.<sup>5</sup> As a result, Auger recombination can occur in the 0 K limit for QDs due to the less stringent requirements for conservation of angular momentum, stronger Coulomb coupling, and reduced dielectric screening.

Auger recombination occurs through three basic pathways: negative trions (**Figure 1.2.1.2a**), positive trions (**Figure 1.2.1.2b**), and neutral (**Figure 1.2.1.2c-e**) multiexcitonic states.<sup>12</sup> In this depiction, negative (positive) trion pathways emerge when there is an extra electron (hole) in the conduction (valence) band and neutral multiexcitons occur when 2 (biexciton in **Figure 1.2.1.2c**) or more (triexciton in **Figure 1.2.1.2d,e**) e-h pairs form. The decay rate and the technological relevance of these recombination pathways can best be understood through statistical scaling laws.<sup>12</sup> As the number  $N_x$  of carriers increases, the possible conduction-band to valence-band transitions ( $N_e N_h$ ) and energy transfer pathways ( $N_e + N_h - 2$ ) scales according to eqn. 6:

$$\tau_{N_e, N_h A} = 8\tau_{2A} [N_e N_h (N_e + N_h - 2)]^{-1} \quad (6)$$

where  $\tau_{2A}$  represents the biexciton decay rate. Considering that the Auger decay rate is faster than the charged exciton emission, Auger recombination typically dominates higher excitonic states and decreases quantum yields (QY). Further, as shown in eqn. 7:

$$QY_{N_e, N_h} = \left(8 \frac{\tau_{2A}}{\tau_{1R}}\right) (N_e + N_h - 2)^{-1} \quad (7)$$

radiative recombination rates scale more slowly with increasing carrier density than do Auger rates. Thus, limiting Auger recombination becomes increasingly important as higher carrier densities are achieved. Strictly speaking, the scaling laws described above only perfectly hold for carriers of identical symmetry and where other forms of quenching (*e.g.* surface carrier trapping) are negligible. However, several studies have shown that the statistical argument is a good approximation for understanding radiative and nonradiative multicarrier dynamics (*e.g.* emission pump-power dependence).<sup>13-15</sup>

### **1.2.2. Quantum Dot Photonic Devices: Prospects & Challenges for Lowering Carbon Emissions**

**Photovoltaic Windows.** Luminescent solar concentrators (LSCs) are devices developed to concentrate solar radiation to produce electricity as photovoltaic (PV) windows.<sup>16-17</sup> Recently, QDs have emerged as a viable organic dye alternative to enable the use of LSCs as semitransparent PV windows.<sup>6, 18-19</sup> The conversion of energy-passive to energy-generation units in buildings, when combined with existing solar cell technologies, can aid in achieving zero-emission buildings and greatly lower our dependence on fossil fuels. In a typical design, an optical waveguide (*e.g.* flat plastic or glass slab) is doped or coated with QDs, which absorb both direct and diffuse sunlight and re-emit at a longer wavelength. Internal reflection then allows for the re-emitted light to propagate to the waveguide edges where it can be converted to electricity. For PV windows, the edges are the window frame, which are PV (*e.g.* Si) solar cells.

The ability to use solution-processable materials, the non-angular dependence of absorption, and the low requirement for absorber concentration make PV windows more

cost-effective on a per unit area basis than conventional PV cells.<sup>5-6, 16, 18-19</sup> Additionally, there is an increase in power output associated with conversion of incident photons to spectrally narrow light. This is because LSCs, when matched to a PV device allow for down-conversion of incident photons to the spectral peak of the device external quantum efficiency (EQE), which increases the photon-to-charge-carrier conversion. Thus, they offer a cost-effective route for increasing the solar radiation collection area in “off-grid” technology that enable decentralization of solar energy harvesting.

The efficiency of an LSC is determined by the ability to control the loss pathways (**Figure 1.2.2.1a and 1.2.2.1b**).<sup>5, 19</sup> These can be summarized as: geometric, scattering, and reabsorption losses. In regards to geometric losses, the contrast between the refractive indices of the waveguide material and its surroundings (*e.g.* air) determine the reflectivity and optical transmittance of the top surface of the waveguides. The QDs absorb a fraction of the transmitted light within the waveguide. The fraction of solar radiation absorbed, as determined by their absorption cross-section, concentration, and device thickness is then re-emitted isotropically at lower energy. Electrons and holes generated in the re-emitted light can only be trapped inside the matrix and used in the window’s PV-edges if it approaches the waveguide/air interface with a certain incidence angle ( $\theta \geq \theta_c$ ). Geometric losses refer to the rest of the re-emitted light, which is lost within the “Escape cone” corresponding to the top or bottom surface of the waveguide. Scattering losses refer to the light that is emitted outside of the escape cone, which is then subject to scattering due to surface or bulk defects and is then redirected into the escape cone. Finally, the remaining light can then either be extracted by the PV cells or lost by reabsorption. The reabsorption losses can either be due to emission back into the

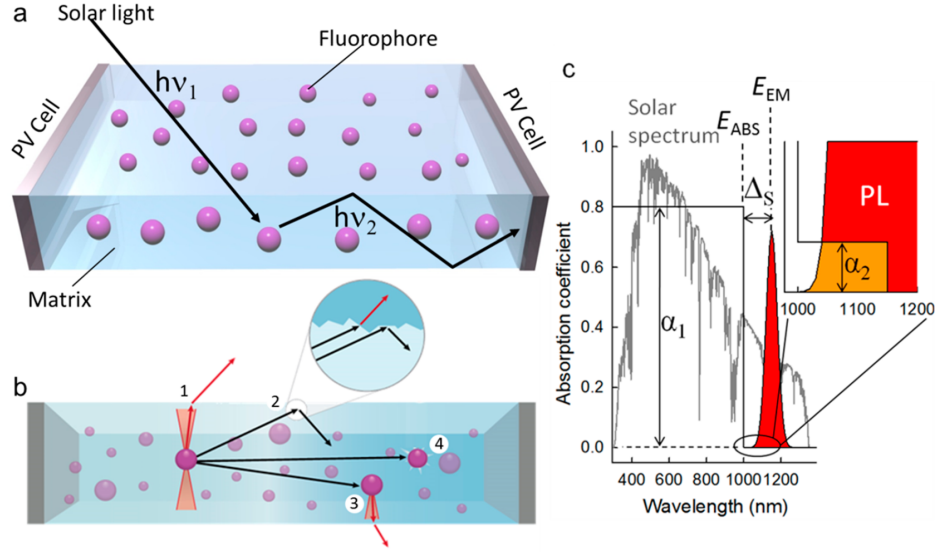


**Figure 1.2.2.1.** Schemes for QD-LSC fabrication are shown in (a) and (b). QDs are represented by purple spheres, blue represents the glass or polymer matrix, and the window edges which form the PV cells are shown in silver. A more detailed description of losses are shown in (b): geometric (1), scattering (2), reabsorption followed by emission into the “Escape cone” (3), and reabsorption followed by nonradiative recombination (4). An ideal LSC material is shown in (c) where step-like absorption ( $\alpha_1$ ), which overlaps with most of the solar spectrum (grey lines) is shown by a black line. To limit reabsorption losses, this material would ideally reemit at a much lower energy ( $\alpha_2$ ).

escape cone, or nonradiative recombination in the QDs.

Performance metrics for LSCs are generally quantified as shown by eqn. 8-10.<sup>5, 19</sup>

For eqn. 8:

$$\eta_{LSC}(\lambda) = [1 - R(\lambda)](1 - e^{-\alpha(\lambda)d})\eta_{TR}(\lambda_{em})\eta_{PL}(\lambda_{em}) \times [1 - \eta_{RA}(\lambda_{em})][1 - \eta_S(\lambda_{em})] \quad (8)$$

$\eta_{LSC}$  represents the single-wavelength external optical efficiency,  $R$  the reflectivity of the waveguide material,  $\eta_{PL}$  re-emitted light (function of quantum yield),  $\eta_{TR}$  geometric losses into the escape cone,  $\eta_S$  scattering losses,  $\eta_{RA}$  reabsorption losses,  $d$  device thickness, and  $\alpha(\lambda)$  absorption cross-section. In this scenario  $\eta_{LSC}(\lambda) = \Phi_{OUT}(\lambda_{em})/\Phi_{IN}(\lambda)$  where  $\Phi_{OUT}(\lambda_{em})$  is the output photon flux at the QD emission wavelength and  $\Phi_{IN}(\lambda)$  is the incident photon flux from the light source. The external quantum efficiency ( $\eta_{LSC, QE}$ ) and power conversion efficiency ( $\eta_{LSC, PE}$ ) are then determined by eqn. 9 and 10:

$$\eta_{LSC,QE} = [\int \eta_{LSC}(\lambda) S(\lambda) d\lambda] [\int S(\lambda) d\lambda]^{-1} \quad (9)$$

$$\eta_{LSC,PE} = [\lambda_{em}]^{-1} [\int \eta_{LSC}(\lambda) S(\lambda) d\lambda] [\int S(\lambda) d\lambda]^{-1} \quad (10)$$

where the spectral density of solar photon flux is  $S(\lambda)$ .

There are several ways to boost LSC performance based on the relations derived from equations 8-10. A clearly important parameter is the development of materials with a large absorption coefficient so as to maximize the fraction of solar radiation that can be converted into electricity.<sup>5, 19</sup> Naturally, this must be coupled with high quantum yields and scattering-free optical waveguides, which allow for the generated charges to be utilized efficiently by the PV cells. Further, an ideal fluorophore would have little to no spectral overlap to limit reabsorption losses ( $\alpha_1 \gg \alpha_2$  in **Figure 1.2.2.1c**). Of these optimization parameters, limiting reabsorption losses and increasing coverage of the solar spectrum are where QDs offer serious advantages over organic fluorophores. Organic fluorophores generally exhibit large band gaps, which are difficult to tune to the near-IR window.<sup>20-21</sup> Extending the conjugated system to decrease the effective band gap is difficult due to the progressive weakening of the dipole moment. This dipole weakening, in addition to intersystem crossing and strong electron-phonon coupling associated with the C-H bonds leads to a reduction in absorption/emission efficiencies.<sup>22-23</sup> The size-dependent band gap of QDs allow for facile tuning to near-IR absorption/emission with high efficiencies. Reabsorption losses, on the other hand, are a direct function of the Stokes shift. The limited tunability of the Stokes shift for organic fluorophores typically results in either small or large Stokes shifts with an absorption profile that has strictly limited coverage of the solar spectrum.<sup>22-25</sup> QDs, on the other hand, have a plethora of methods to tune the band

gap and Stokes shift such as heterostructuring, intra-gap doping, and formation of “native defects” (covered in subsequent sections).<sup>5-6, 16, 18-19</sup>

**Light-Emitting Diodes.** Electroluminescent (EL) devices are generally constructed by sandwiching a luminescent material between two contact electrodes with interceding charge injection layers. Once an electric current is applied, electrons/holes are injected into the semiconductor conduction/valence bands from the contact electrodes, which then radiatively recombine and emit a photon equivalent in energy to the band or HOMO-LUMO gap (**Figure 1.2.2.2a**).<sup>5</sup> Dissimilar to broadband blackbody radiation (incandescent light bulbs), or multiline atomic emission spectra (gas-discharge lamps), EL devices produce specific and spectrally narrow optical transitions. Considering that QDs are synthesized *via* “Wet chemistry” and devices are constructed using similar methodology to organic LEDs (OLEDs), many of the beneficial features of OLEDs (*e.g.* compatibility with both rigid and flexible substrates ranging from glass to fabric, potential for ultra-thin profile, and large area devices) are not lost.

QD-LEDs, while possessing similar benefits to OLEDs, have several significant advantages.<sup>25-28</sup> Most of these advantages stem from the narrow linewidths shown in **Figure 1.2.2.2b** where QD-LEDs are represented by solid lines and OLEDs by dotted lines. Strong electron-phonon coupling in OLEDs result in multiple emission peaks, which average to the broad full-width at half-maximum (fwhm) typically ~40-60 nm.<sup>22-24</sup> Single-dot emission spectra (**Figure 1.2.2.2**) clearly show that this effect is not present in QDs, and the spectral width of the QD ensemble is controlled, conversely, by size, composition, and shape distributions. This suggests that with fastidious control of synthetic and post-synthetic processing conditions, QD ensembles can reach fwhm as narrow as 20 nm.

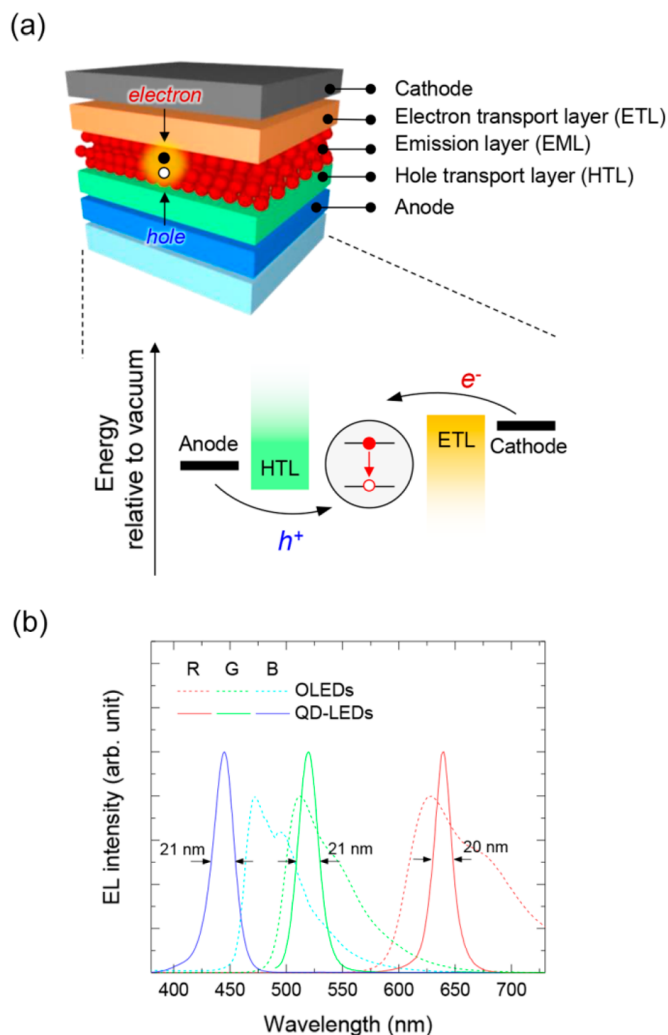


**Figure 1.2.2.2.** Typical device architecture for a QD-LED and the corresponding band diagrams are shown in (a). Electrons and holes are injected into the CB and VB bands after biasing the electrodes. The sharp emission shown in (b), results from recombination of these charge carriers. For (b), spectra for QDs are shown by solid lines and organic emitters in dotted lines. Clearly, the emission linewidth is much narrower for QDs, which leads to higher color purity.

Additionally, the internal quantum efficiency (IQE) of OLEDs, defined as the ratio of emitted photons to e-h pairs electrically generated, is limited to 25% due to spin selection rules. Organic molecules can form an exciton with a total spin state of either 0 (singlet) or 1 (triplet). Considering singlet formation has a 25% probability, and organic emitters strictly obey spin selection rules, the vast majority (75%) of e-h pairs generated are not

utilized.<sup>22-24</sup> QDs, however, typically have small dark-bright exciton splitting (1-15 meV) as dictated by eqn. 13:<sup>5, 29-31</sup>

$$\tau = \frac{\tau_b \tau_d}{\tau_b(1+\exp(-\Delta_{db}/k_B T)) + \tau_d(1+\exp(\Delta_{db}/k_B T))} \quad (13)$$

where  $\tau_i$  refers to the inverse decay rate of the dark (d) and bright (b) exciton, and  $\Delta_{db}$  refers to the splitting energy in their fine structure. This is significantly smaller than thermal energy at room temperature (~26 meV), and allows for efficient thermal excitation of dark to bright excitons at low temperature. The exceptional color purity across the visible light spectrum and ability to circumvent the statistical IQE limitations of OLEDs suggests QDs can be a viable replacement for displays and energy-saving white-light LEDs.

The QD-LED performance is generally evaluated in terms of brightness, energy efficiency, and lifetime. Limitations in device performance are generally dictated by several “loss” mechanisms including: surface trapping, Förster energy transfer, and Auger recombination.<sup>5</sup> Surface trapping originates from structural defects associated with the QD surface during synthesis. Generally, trap lifetimes are shorter than band-edge recombination resulting in an emission quench that becomes increasingly strong at high trap densities. The most common way of increasing the quantum yield of QDs is heterostructuring with a second semiconductor, which fully covers the QD surface (shell-growth). Förster energy transfer, on the other hand, originates from exciton diffusion. After excitation, an e-h pair is generated, which can then either recombine or be transferred to a second QD. Hence, making it susceptible to surface traps in both QDs. As a result, even in an ensemble where most QDs are trap free, the QY decreases significantly as a single exciton samples multiple QDs. This is particularly a problem with QDs, which

generally have small Stokes shifts (with exceptions outlined in subsequent sections), and significant spectral overlap between absorption and emission spectra. The efficiency of Förster energy transfer, the nonradiative analogue to exciton diffusion, increases as the dot-to-dot distance decreases, which makes it a particularly large problem for QD films/solid-state devices.

Auger recombination, as outlined in Section 1.2.1., decreases quantum yields due to the faster rate constant compared to the radiative transition. In LEDs, this is particularly a problem due to excitation stemming from electron/hole injection directly into the QD bands. Dissimilar to optical pumping, the electron and hole generation rates are independent of each other allowing for a higher probability of trion formation. Notably, as biasing increases, the charge imbalance also increases resulting in a higher likelihood of Auger recombination at large current densities. Thus, it appears that the advancement of QD LEDs depends not only on increasing the PL quantum yield of the single exciton states, but suppressing Auger losses as well.

### **1.3. I-III-VI<sub>2</sub> Quantum Dots**

**Basic Description & Competing Theories.** Quantum dots have major advantages over conventional bulk and organic semiconductors for use in solar energy harvesting and energy-saving lighting applications. However, additional to the challenges already outlined, most high-performance devices developed thus far have been based on heavy metal (*e.g.* Pb or Cd) chalcogenides. The high toxicity of which, poses a serious challenge for future commercialization. Recently, non-toxic Cu-containing QDs such as doped II-VI, or ternary I-III-VI<sub>2</sub> QDs including CuInS<sub>2</sub> (CIS), CuInSe<sub>2</sub> (CISE), and CuInSe<sub>2</sub>.

$xS_x$  (CISeS) have emerged as a possible replacement.<sup>6, 32</sup>

Despite the growing interest in using CIE (where E=S,Se), or similar Cu-containing QDs in (electro)-optical devices, a thorough understanding of their unique photophysics remains to be developed. The most notable examples include their abnormally large Stokes shifts and broad spectral linewidths. QDs generally have relatively small energy splitting in their fine structure, and correspondingly exhibit small Stokes shifts (e.g. 0.08 eV for CdSe) and narrow linewidths (~100 meV) in (near)-homogenous ensembles. The photoluminescence (PL) off-set from the absorption edge in CIS, on the other hand, can range from 250-750 meV with linewidths as broad as 350 meV.<sup>6, 33-36</sup> In addition, the radiative lifetime (200-500 ns) is abnormally long compared with CdSe despite having similar oscillator strengths.<sup>6, 33-36</sup> To date, there have been several proposed mechanisms to explain these processes including: symmetry breaking in the exciton band-edge states,<sup>36</sup> strong electron-phonon coupling,<sup>35</sup> and intra-gap defects (**Figure 1.3.1**).<sup>33-34</sup>

The concept of symmetry breaking in the band-edge states was developed by *Shabaev and Efros* (**Figure 1.3.1a**).<sup>36</sup> Most QDs, to date, have cubic lattices that appear spherical at decreasing sizes. CIS, on the other hand, crystallizes in the Chalcopyrite phase and appears to form pyramidal QDs due to the elongated z axis and tetragonal symmetry. *Shabaev and Efros*, therefore proposed that the unusual crystalline phase results in tetragonal splitting of the Hamiltonian in the fine structure. This “symmetry breaking” results in a *p*-type symmetry for the band-edge *odd* hole state, *s* type symmetry for the band-edge *even* hole state, and *s*-type symmetry for the band-edge electron state. Typically, band-edge emission involves an *s*-*s* transition from the even states. For CIS, they argued that the *p*-*s* transition is only weakly allowed due to the low symmetry of the

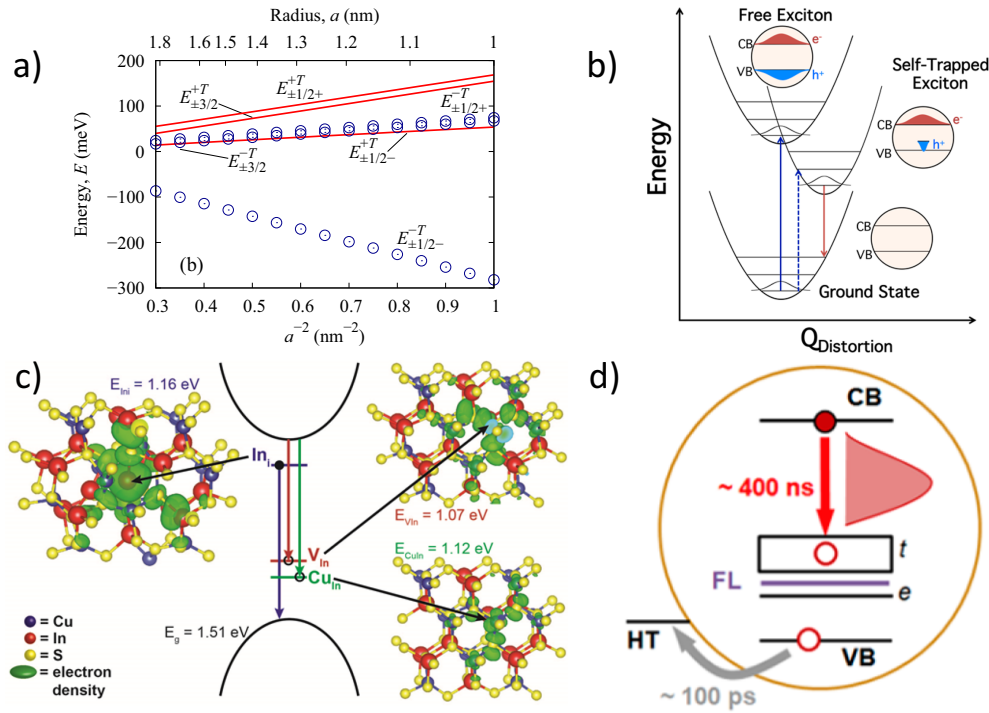


**Figure 1.3.1.** The multiple mechanisms purported to explain CIS emission: (a) Splitting of the band-edge states due to symmetry breaking (b) electron-phonon coupling, (c) an electron localized at an In defect, and (d) a hole localized at a Cu defect.

crystal structure and the energy splitting between the *even* (*s*) and odd (*p*) energy levels increases with decreasing QD diameter. CIS therefore has a large Stokes shift and long radiative lifetime relative to other QDs. Notably, this effect would become more pronounced as QDs become smaller.

The second major argument, advocated by *Knowles and Gamelin*,<sup>35</sup> is strong electron-phonon coupling due to Jahn-Teller distortions in the excited-state of lattice copper (**Figure 1.3.1b**). The proposed “self-trapped exciton” model argues that the electron-phonon coupling energies for the photogenerated hole are significantly larger than the carrier delocalization (resonance) energies. In this scenario, nuclear fluctuations modulate the hole potential resulting in “positive feedback” where hole contraction leads to nuclear distortions in which a new equilibrium geometry is achieved. Considering that

the  $\text{Cu}^{1+/2+}$  transition has a large nuclear reorganization energy due to Jahn-Teller distortions typical for  $d^9$  cations, excitation of the QDs results in localization of the photogenerated hole at the  $\text{Cu}^{1+}$  lattice site and alters the equilibrium geometry to be “ $\text{Cu}^{2+}$ -like” where the contracted hole is localized and stabilized around lattice copper ions. The reorganization energy is expected to be  $\sim 0.25\text{-}0.4$  eV and can therefore explain the large Stokes shift and broad PL.

There is also the possibility of “native defects” forming during QD synthesis (**Figure 1.3.1c,d**).<sup>33-34</sup> Bulk CIS can exhibit, Schottky, anti-site, and Frenkel defects, which result in intra-gap states. While absorption is still dominated by the band-edges, emission occurs from the intra-gap states resulting in a large Stokes shift. However, distinct from CIS QDs, this emission is typically narrow ( $\sim 30$  meV). Hence, it has been proposed that individual CIS QDs have narrow emission due to sharp transitions from either the valence band-edge to a localized donor level (e.g.  $\text{V}_S^{2+}$ ,  $\text{In}_{\text{Cu}}^{2+}$ ,  $\text{In}_i^{3+}$ ), or conduction band-edge to a localized acceptor (e.g.  $\text{Cu}_{\text{In}}^{2-}$ ,  $\text{V}_{\text{Cu}}^-$ ,  $\text{V}_{\text{In}}^{3-}$ ) level. However, variations in the position of the defect in the QD leads to different emission energies, and broadening of the ensemble spectra is due to heterogeneity. For CIS QDs, both In-based donor level (**Figure 1.3.1c**) and Cu-based acceptor level (**Figure 1.3.1d**) defect states have been proposed.

#### **1.4. Thesis Objectives**

The objective of this thesis will be to elucidate the origin of the unique (electro)-optical properties of Cu-containing QDs broadly, and CIE QDs specifically. In particular, I will focus on determining how chemical processing methods affect the possible pathways for single exciton absorption/emission, carrier trapping, Auger recombination, charge

transport, determine the prospects of Stokes shift and linewidth engineering, and evaluate whether other unique physical properties (e.g. magnetic interactions from Cu<sup>2+</sup> defects) can be understood and controlled for different technological applications.

### **1.5. References**

1. Clark, P. U., et al., Consequences of Twenty-First-Century Policy for Multi-Millennial Climate and Sea-Level Change. *Nature Climate Change* 2016, 6, 360-369.
2. Hallegatte, S., et al., Mapping the Climate Change Challenge. *Nature Climate Change* 2016, 6, 663-668.
3. Schleussner, C.-F.; Rogelj, J.; Schaeffer, M.; Lissner, T.; Licker, R.; Fischer, E. M.; Knutti, R.; Levermann, A.; Frieler, K.; Hare, W., Science and Policy Characteristics of the Paris Agreement Temperature Goal. *Nature Climate Change* 2016, 6, 827-835.
4. Alstone, P.; Gershenson, D.; Kammen, D. M., Decentralized Energy Systems for Clean Electricity Access. *Nature Climate Change* 2015, 5, 305-314.
5. Pietryga, J. M.; Park, Y. S.; Lim, J.; Fidler, A. F.; Bae, W. K.; Brovelli, S.; Klimov, V. I., Spectroscopic and Device Aspects of Nanocrystal Quantum Dots. *Chem Rev* 2016, 116, 10513-622.
6. Meinardi, F.; McDaniel, H.; Carulli, F.; Colombo, A.; Velizhanin, K. A.; Makarov, N. S.; Simonutti, R.; Klimov, V. I.; Brovelli, S., Highly Efficient Large-Area Colourless Luminescent Solar Concentrators Using Heavy-Metal-Free Colloidal Quantum Dots. *Nat Nano* 2015, 10, 878-885.
7. Klimov, V. I., *Nanocrystal Quantum Dots*, 2 ed.; CRC Press, 2010.

8. Victor I. Klimov, A. A. M., D. W. McBranch, C. A. Leatherdale, M. G. Bawendi, Quantization of Multiparticle Auger Rates in Semiconductor Quantum Dots. *Science* 2000, 287, 1011-1013.
9. Chepic, D. I. E., A. L.; Ekimov, A. I.; Vanov, M. G.; Kharchenko, V. A.; Kudriavtsev, I. A.; Yazeva, T. V., Auger Ionization of Semiconductor Quantum Drops in a Glass Matrix. *J. Lumin.* 1990, 47, 113-117.
10. Pietryga, J. M. Z., K.K.; Whitehead, M.; Klimov, V. I.; Schaller, R. D. Evidence for Barrierless Auger Recombination in PbSe Nanocrystals: A Pressure-Dependent Study of Transient Optical Absorption. *Phys. Rev. Lett.* 2008, 101, 217401.
11. Wang, L.-W. C., M.; Zunger, A.; Franceschetti, A., Pseudopotential Theory of Auger Processes in CdSe Quantum Dots. *Phys. Rev. Lett.* 2003, 91, 056404.
12. Klimov, V. I., Multicarrier Interactions in Semiconductor Nanocrystals in Relation to the Phenomena of Auger Recombination and Carrier Multiplication. *Annual Review of Condensed Matter Physics* 2014, 5, 285-316.
13. Klimov, V. I. M., J. A.; Schaller, R. D.; Rupasov, V. I. , Scaling of Multiexciton Lifetimes in Semiconductor Nanocrystals. *Phys. Rev. B: Condens. Matter Mater. Phys.* 2008, 77, 195324.
14. Koh, W.-K. K., A. Y.; Stewart, J. T.; Pal, B. N.; Robel, I.; Pietryga, J. M.; Klimov, V. I. , Heavily Doped N-Type PbSe and PbS Nanocrystals Using Ground-State Charge Transfer from Cobaltocene. *Sci. Rep.* 2013, 3.

15. Park, Y.-S. B., W. K.; Pietryga, J. M.; Klimov, V. I. , Auger Recombination of Biexcitons and Negative and Positive Trions in Individual Quantum Dots. *ACS Nano* 2014, 8, 7288-7296.
16. Debije, M. G. V., P. P. C., Solar Concentrators: Thirty Years of Luminescent Solar Concentrator Research: Solar Energy for the Built Environment. *Adv. Eng. Mater.* 2012, 2, 12-35.
17. Currie, M. J. M., J. K.; Heidel, T. D.; Goffri, S.; Baldo, M. A., High-Efficiency Organic Solar Concentrators for Photovoltaics. *Science* 2008, 321, 226-228.
18. Chatten, A. J. B., K. W. J.; Buxton, B. F.; Ekins-Daukes, N. J.; Malik, M. A., Quantum Dot Solar Concentrators. *Semiconductors* 2004, 38, 909-917.
19. Klimov, V. I.; Baker, T. A.; Lim, J.; Velizhanin, K. A.; McDaniel, H., Quality Factor of Luminescent Solar Concentrators and Practical Concentration Limits Attainable with Semiconductor Quantum Dots. *ACS Photonics* 2016, 3, 1138-1148.
20. Krumer, Z. P., S. J.; Van Dijk-Moes, R. J. A.; Zhao, Y.; De Brouwer, A. F. P.; Groeneveld, E.; Van Sark, W. G. J. H. M.; Schropp, R. E. I.; Donega, C. D. M., Tackling Self-Absorption in Luminescent Solar Concentrators with Type-II Colloidal Quantum Dots. *Sol. Energy Mater. Sol. Cells* 2013, 111, 57-65.
21. Giebink, N. C. W., G. P.; Wasielewski, M. R., Resonance-Shifting to Circumvent Reabsorption Loss in Luminescent Solar Concentrators. *Nat. Photonics* 2011, 5, 694-701.

22. Endo, A. S., K.; Yoshimura, K.; Kai, T.; Kawada, A.; Miyazaki, H.; Adachi, C., Efficient up-Conversion of Triplet Excitons into a Singlet State and Its Application for Organic Light Emitting Diodes. *Appl. Phys. Lett.* 2011, 98, 083302.
23. Goushi, K. Y., K.; Sato, K.; Adachi, C., Organic Light- Emitting Diodes Employing Efficient Reverse Intersystem Crossing for Triplet-to-Singlet State Conversion. *Nat. Photonics* 2012, 6, 253-258.
24. Zhang, Q. L., B.; Huang, S.; Nomura, H.; Tanaka, H.; Adachi, C., Efficient Blue Organic Light-Emitting Diodes Employing Thermally Activated Delayed Fluorescence. *Nat. Photonics* 2014, 8, 326-332.
25. Colvin, V. L. S., M. C.; Alivisatos, A. P., Light-Emitting Diodes Made from Cadmium Selenide Nanocrystals and a Semi- Conducting Polymer. *Nature* 1994, 354-457.
26. Yakunin, S. P., L.; Krieg, F.; Bodnarchuk, M. I.; Nedelcu, G.; Humer, M.; De Luca, G.; Fiebig, M.; Heiss, W.; Kovalenko, M. V., Low-Threshold Amplified Spontaneous Emission and Lasing from Colloidal Nanocrystals of Caesium Lead Halide Perovskites. *Nat. Commun.* 2015, 6, 8056.
27. Zhong, X. F., Y.; Knoll, W.; Han, M., Alloyed  $Zn_xCd_{1-x}S$  Nanocrystals with Highly Narrow Luminescence Spectral Width. *J. Am. Chem. Soc.* 2003, 125, 13559-13563.
28. Chen, O. Z., J.; Chauhan, V. P.; Cui, J.; Wong, C.; Harris, D. K.; Wei, H.; Han, H.-S.; Fukumura, D.; Jain, R. K.; et al., Compact High- Quality CdSe–CdS Core–Shell Nanocrystals with Narrow Emission Linewidths and Suppressed Blinking. *Nat. Mater.* 2013, 12, 445-451.

29. Crooker, S. A. B., T.; Hollingsworth, J. A.; Klimov, V. I., Multiple Temperature Regimes of Radiative Decay in CdSe Nanocrystal Quantum Dots: Intrinsic Limits to the Dark-Exciton Lifetime. *Appl. Phys. Lett.* 2003, 82, 2793-2795.
30. Efros, A. L. R., M.; Kuno, M.; Nirmal, M.; Norris, D. J.; Bawendi, M., Band-Edge Exciton in Quantum Dots of Semiconductors with a Degenerate Valence Band: Dark and Bright Exciton States. *Phys. Rev. B: Condens. Matter Mater. Phys.* 1996, 54, 4843-4856.
31. Chamarro, M. G., C.; Lavallard, P.; Lublinskaya, O.; Ekimov, A. I., Enhancement of Electron-Hole Exchange Interaction in CdSe Nanocrystals: A Quantum Confinement Effect. *Phys. Rev. B: Condens. Matter Mater. Phys.* 1996, 53, 1336-1342.
32. Zhong, H.; Lo, S. S.; Mirkovic, T.; Li, Y.; Ding, Y.; Li, Y.; Scholes, G. D., Noninjection Gram-Scale Synthesis of Monodisperse Pyramidal CuInS<sub>2</sub> Nanocrystals and Their Size-Dependent Properties. *ACS Nano* 2010, 4, 5253-5262.
33. Leach, A. D. P.; Shen, X.; Faust, A.; Cleveland, M. C.; La Croix, A. D.; Banin, U.; Pantelides, S. T.; Macdonald, J. E., Defect Luminescence from Wurtzite CuInS<sub>2</sub> Nanocrystals: Combined Experimental and Theoretical Analysis. *The Journal of Physical Chemistry C* 2016, 120, 5207-5212.
34. Li, L.; Pandey, A.; Werder, D. J.; Khanal, B. P.; Pietryga, J. M.; Klimov, V. I., Efficient Synthesis of Highly Luminescent Copper Indium Sulfide-Based Core/Shell Nanocrystals with Surprisingly Long-Lived Emission. *Journal of the American Chemical Society* 2011, 133, 1176-1179.

35. Knowles, K. E.; Nelson, H. D.; Kilburn, T. B.; Gamelin, D. R., Singlet-Triplet Splittings in the Luminescent Excited States of Colloidal Cu(+):CdSe, Cu(+):InP, and CuInS<sub>2</sub> Nanocrystals: Charge-Transfer Configurations and Self-Trapped Excitons. *J Am Chem Soc* 2015, 137, 13138-47.
36. Shabaev, A.; Mehl, M. J.; Efros, A. L., Energy Band Structure Of CuInS<sub>2</sub> and Optical Spectra Of CuInS<sub>2</sub> nanocrystals. *Physical Review B* 2015, 92.

## CHAPTER 2

### Photoluminescence & Magnetic Exchange from Native Defects

## ***2.1. Light Emission Mechanisms in CuInS<sub>2</sub> Quantum Dots Evaluated by Spectral Electrochemistry***

### **2.1.1. Introduction**

Semiconductor nanocrystals or quantum dots (QDs) of I-III-VI<sub>2</sub> ternary semiconductors have attracted considerable attention as benign, heavy-metal-free materials for optical and electro-optical applications.<sup>1,2</sup> Furthermore, recent advances in high-throughput and non-injection fabrication techniques using inexpensive precursors have shown viability of commercial-scale production of these materials.<sup>3-4</sup> QDs of CuInS<sub>2</sub> (CIS), CuInSe<sub>2</sub> (CISE), and CuInSe<sub>x</sub>S<sub>2-x</sub> (CISES) alloys are of particular interest for use as photoactive layers in photovoltaic (PV) devices due to their large absorption cross-sections, long exciton lifetimes, size-tunable absorption with the onset at near-infrared energies, and favorable charge-transport characteristics.<sup>5-11</sup> High emission efficiencies and reduced self-absorption losses (owing to a large apparent Stokes shift,  $\Delta_S$ , between an emission band and an onset of strong-absorption) are also beneficial to light emission applications such as down-conversion in solid-state lighting<sup>12-13</sup> and luminescence solar concentrators.<sup>14-16</sup>

Despite the growing number of demonstrations of practical utility of CISES QDs in various devices,<sup>10-13,16-17</sup> a thorough understanding of their unusual photophysical properties remains to be developed. For example, attempts to explain the large Stokes shift, which is consistently observed regardless of specific preparation methods, has yielded various light-emission models including symmetry breaking for the exciton band-edge states,<sup>18</sup> hole self-localization due to strong electron-phonon coupling leading to

exciton “self-trapping,”<sup>19</sup> and finally involvement of “native defects,” which form intra-gap states serving as radiative-recombination centers.<sup>15-16,20-25</sup> The last of these models has been most commonly invoked for explaining spectroscopic observations.<sup>15,20,24-26</sup> Specifically, striking similarities between optical spectra, photoluminescence (PL) dynamics, and magneto-optical data of copper-doped II-VI and undoped CIS QDs pointed towards the involvement of Cu-related native defects in the emission process in the CIS and CISES systems. In fact, previous studies of bulk and QD forms of Cu-doped II-VI materials indicated that a substitutional  $\text{Cu}^{2+}$  defect could be considered as a state occupied with a preexisting hole, which could couple to a band-edge conduction-band (CB) electron by a radiative transition resulting in slow-decay (hundreds of nanoseconds time scales) but highly efficient intra-gap PL.<sup>20,27</sup> Interestingly, the  $\text{Cu}^{1+}$  state is also an emissive defect, however, it requires prior activation by capture of a photoexcited valence-band (VB) hole.

While the above model ascribing the observed emission to the Cu-related recombination center seems to be most commonly accepted in the recent literature,<sup>15,19-20,24,26</sup> the initial oxidation state of the Cu-defect and whether localization occurs prior to excitation or as the result of excited-state hole capture still remains unclear. Furthermore, a large abundance of other possible native defects (such as sulfur, copper, and indium vacancies or so-called “anti-site” defects) leaves open alternative possibilities for intra-gap emission, which needs to be thoroughly considered.<sup>22,28-32</sup>

Here, we use a combination of electrochemical (EC) and optical methods to determine the band positions in CIS QDs, resolve the intra-gap states involved in radiative and nonradiative processes, and determine their identity. Our EC measurements reveal

clear reduction/oxidation signatures of a state located  $\sim 350$  meV above the valence band-edge, which accounts well for the large Stokes shift of the PL spectrum. The redox behavior and the energy of the intra-gap feature are in agreement with those expected for the  $\text{Cu}^x$  state ( $x = 1+$  or  $2+$ ). We further employ *in situ* spectroelectrochemistry (SEC) measurements to evaluate the initial oxidation state of the  $\text{Cu}^x$  ion based on the effect of the EC potential ( $V_{EC}$ ) on the PL intensity. We find that both  $\text{Cu}^{1+}$  and  $\text{Cu}^{2+}$  defects states are emissive and the prevalence of one *versus* the other seems to be linked to sample stoichiometry. Specifically, the  $\text{Cu}^{2+}$  emission channel is likely dominant in copper-deficient QDs wherein the formation of  $\text{Cu}^{2+}$  defects is facilitated by the requirement of charge-compensation in the presence of a large number of Cu vacancies ( $V_{\text{Cu}}$ ) expected for these type of samples. On the other hand, stoichiometric QDs seem to favor the  $\text{Cu}^{1+}$  states that might occur together with the charge-compensating  $\text{In}^{3+}$  defects in the form of anti-site defect pairs ( $\text{Cu}_{\text{In}} - \text{In}_{\text{Cu}}$ ). The observed dependence of the PL intensity on  $V_{EC}$  suggests that the trap states responsible for PL quenching concentrate primarily near the CB and VB edges leaving the mid-gap region free of trap sites. We also observe that the abundance of traps near the VB edge is higher in stoichiometric samples compared to that in Cu-deficient QDs, which might explain a higher PL efficiency typically observed for the latter type of samples *versus* the former. Finally, inorganic passivation of the QDs with a wide-gap ZnS shell leads to a nearly complete elimination of intra-gap traps, which manifests in the increased PL quantum yield and a  $V_{EC}$ -independent PL signal.

### 2.1.2. Results and Discussion

**Optical Spectra of CIS QDs.** Stoichiometric CIS QDs were synthesized following a previously described route<sup>15</sup> with several modifications as outlined in the Methods

section. Based on measurements using inductively coupled plasma mass spectroscopy (ICP-MS), the Cu to In ratio in the synthesized QDs is 1.01:0.99. The QDs are characterized by a tetrahedral shape and exhibit a chalcopyrite crystal lattice structure (see Figure S6.1.1 of Supporting Information for characterization details); these structural properties are typical of CISeS nanocrystals.<sup>10-11,26,33</sup> In order to investigate the effects of non-stoichiometry (specifically, varied levels of Cu deficiency) on emission, a different procedure based on hot-injection<sup>7</sup> was used to fabricate samples with two different compositions:  $\text{Cu}_{0.56}\text{In}_{1.44}\text{S}_2$ , and  $\text{Cu}_{0.44}\text{In}_{1.56}\text{S}_2$ , as determined by ICP-MS. We also studied stoichiometric core/shell CIS/ZnS samples fabricated by the procedure outlined in the Methods section. All samples were capped with a combination of dodecanethiol and oleylamine ligands. PL quantum yields ( $\Phi$ ) of the Cu-deficient samples were:  $\Phi_{\text{Cu}_{0.56}\text{In}_{1.44}\text{S}_2} = 3\%$  and  $\Phi_{\text{Cu}_{0.44}\text{In}_{1.56}\text{S}_2} = 15\%$ . For the core-only stoichiometric QDs, the PL quantum yield was 1%, and it increased to 55% for the core/shell samples. The observed variation in the PL efficiency between different types of the studied QDs is consistent with the measured PL dynamics that indicate a shorter average PL lifetime for samples with a lower value of  $\Phi$  (see Figure S6.1.2). The large differences in the emission efficiencies suggest varied abundances of electron and/or hole trap sites (composition- and surface-properties-dependent) as discussed later in greater detail.

The optical absorption and emission spectra of core-only stoichiometric CIS QDs of various sizes (increases from A to D) are shown in **Figure 2.1.2.1a**. The peak of the second derivative of the absorption spectrum marks the band-edge transition, which is used here as a measure of the QD band gap ( $E_g$ ). The PL band is red-shifted by  $\sim 0.25$ - $0.40$  eV, similar to previous observations.<sup>5-8,10-11,15-16,19-20,22,24,33</sup> The large apparent PL

Stokes shift ( $\Delta_S$ ; shown by double arrows in **Figure 2.1.2.1a**) can be explained by the involvement of intra-gap states in the emission process (**Figure 2.1.2.1b** top panel). Furthermore, as was discussed earlier, the intra-gap state is likely associated with the  $\text{Cu}^x$  defect,<sup>26</sup> which can be either in the  $\text{Cu}^{1+}$  or the  $\text{Cu}^{2+}$  ground state (**Figure 2.1.2.1b**, the bottom right and left panels, respectively). In the case of the  $\text{Cu}^{2+}$  defect, a pre-existing hole, stemming from a partially filled d shell, can recombine directly with a CB electron. However, in order for emission to proceed through this pathway, the photogenerated hole must be quickly removed from the VB state (*via*, for example, capture by an intra-gap trap such as  $V_{\text{Cu}}$  paired with the  $\text{Cu}^{2+}$  defect; see **Figure 2.1.2.1b**, bottom left) otherwise the emission will occur *via* a much faster band-edge transition (tens of ns time scale versus hundreds of ns for the Cu-mediated recombination) as was previously observed for  $\text{Cu}^{2+}$  doped II-VI QDs.<sup>34</sup> The completion of the recombination cycle in this case requires that the  $\text{Cu}^{1+}$ -like state produced after radiative capture of a CB electron restores its 2+ oxidation state by capturing a hole (process 3 in the diagram in the bottom left panel of **Figure 2.1.2.1b**). Alternatively, emission can continue through the mechanism shown in the bottom right panel of **Figure 2.1.2.1b** as discussed below.

The activation of the  $\text{Cu}^{1+}$  recombination pathway (bottom right panel of **Figure 2.1.2.1b**) requires that the VB hole is first captured at the  $\text{Cu}^{1+}$  defect to form a  $\text{Cu}^{2+}$ -like state, which then recombines with the CB electron to restore the original 1+ configuration. Despite the oxidation-state-dependent emission pathways, the defect offset energy from the VB is expected to be similar for both cases, which would lead to indistinguishable emission spectra. Furthermore, the effects of nonradiative electron trapping are also expected to affect the two emission channels in a similar way, as both of them require

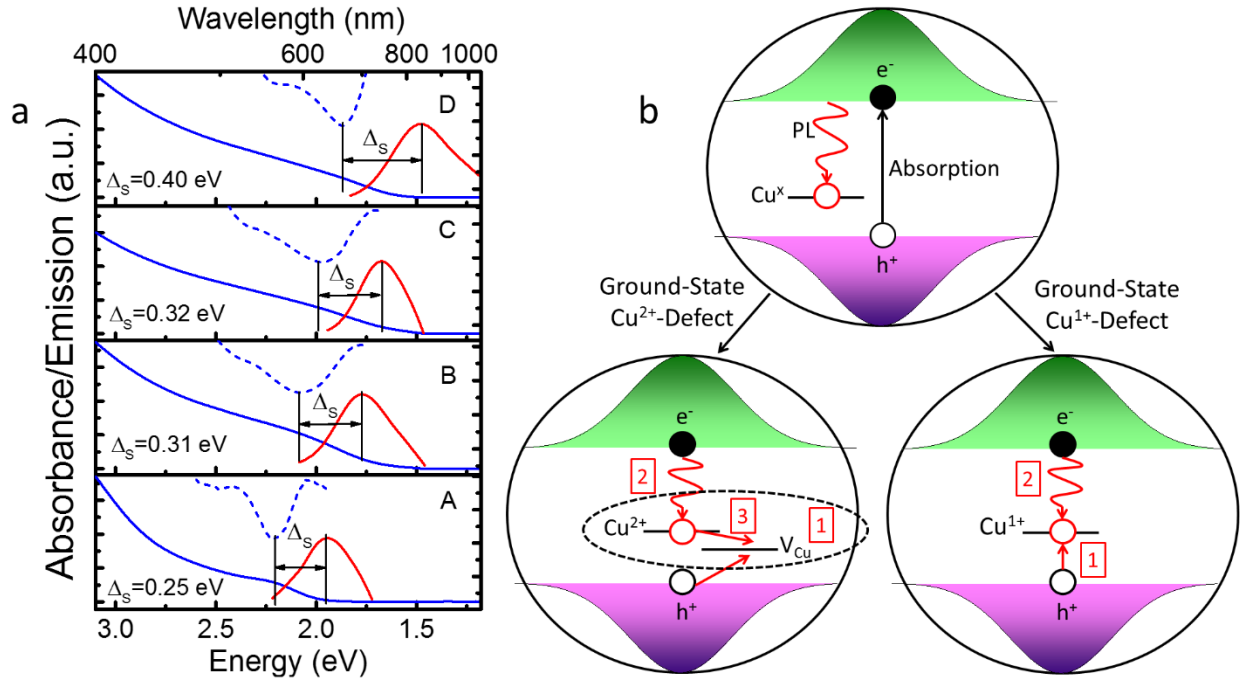


**Figure 2.1.2.1.** (a) Optical measurements for stoichiometric core-only CIS QDs of four different sizes. The blue solid lines represent the absorption spectra, blue dotted lines are the second derivative of the absorption spectra, and the solid red lines are the emission spectra. (b) The Cu-defect related mechanisms for intra-gap emission from CIS QDs. Top: the QD absorption is due primarily to the VB-CB transitions, while the emission is due to radiative recombination of the CB electron with a hole residing in an intra-gap  $\text{Cu}^x$  state ( $x = 1+$  or  $2+$ ). Bottom-left: The  $\text{Cu}^{2+}$  defect contains a pre-existing hole in the ground state, which can directly recombine with the CB electron (process 2). This recombination channel, however, is fairly slow (hundreds of nanoseconds time scales), therefore, in order for it to dominate emission, the photogenerated hole must be quickly removed from the VB state *via* capture by another hole trap (process 1) such as a Cu vacancy (denoted as  $V_{\text{Cu}}$ ) forming a charge-compensated pair with the  $\text{Cu}^{2+}$  defect. The recombination cycle is completed after the electron captured radiatively by the Cu-center recombines with the trapped hole (process 3), which restores the original  $2+$  oxidation state of the Cu defect. Bottom right: To become PL-active, the  $\text{Cu}^{1+}$  state must first capture a VB hole (process 1); this leads to formation of the  $\text{Cu}^{2+}$ -like state, which then radiatively recombines with the CB electron (process 2) to restore the original  $1+$  oxidation state.

that photogenerated electrons remain in the CB state until they undergo radiative recombination. On the other hand, the processes of hole trapping by non-copper-related states have distinct effects on the two emission pathways. Specifically, as discussed earlier, the presence of hole traps is necessary for activating the  $\text{Cu}^{2+}$  emission. The role of such traps can be played by, for example, Cu-vacancies that are expected to accompany the  $\text{Cu}^{2+}$  defects for charge neutrality. On the other hand, the presence of

hole traps is detrimental to the  $\text{Cu}^{1+}$  emission pathway because it requires a photoexcited hole for forming optically active  $\text{Cu}^{2+}$ -like states. These distinctions in the effects of trapping processes on  $\text{Cu}^{1+}$  and  $\text{Cu}^{2+}$  emissions can, in principle, help distinguish between the two PL channels.

**Electrochemical Cyclic Voltammetry Measurements.** Dark-state cyclic voltammetry (CV) measurements are used to further characterize the positions of band edges as well as the properties of intra-gap states involved in both intra-gap emission and nonradiative carrier trapping (**Figure 2.1.2.2**). These experiments were conducted using a three-electrode setup with a 0.1 M tetrabutylammonium perchlorate ( $\text{TBAClO}_4$ )/chloroform solution (1:5 QD: $\text{TBAClO}_4$  molar ratio) as an electrolyte. Distinct from some of the published studies, we do not deposit QDs onto a working electrode but dissolve them directly in the electrolyte, which allows us to probe them in their native solution-based environment. We specifically choose this type of experiment for several reasons. First, strong dot-to-dot electronic interactions or stripping of ligands during film preparation can lead to the formation of intra-gap states, which may not necessarily be present in the solution-phase samples; this makes our work more relevant to published spectroscopic studies that are typically conducted on QD solutions. Furthermore, solution-phase measurements avoid concerns over artificial shifts in the band positions due to variations in film packing, which can affect the ability of electrolyte ions to access the surface of the QDs.<sup>35</sup> Lastly, solution-phase measurements involve diffusion limited EC processes. This therefore mitigates concerns over the irreversibility of the oxidation (reduction) step for hole (electron) injection into the VB (CB), as not all of the QDs will be

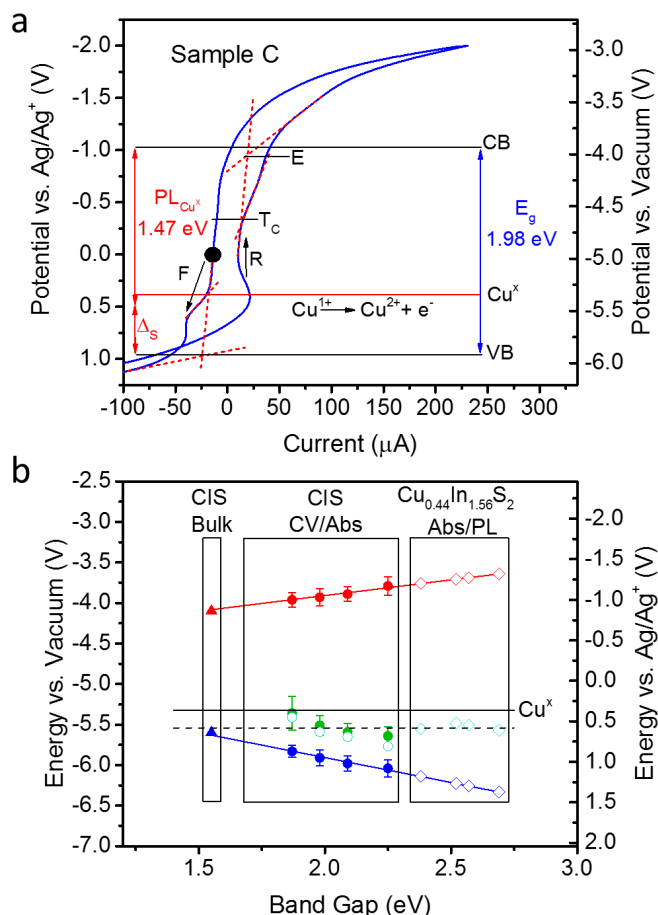


**Figure 2.1.2.2.** (a) CV measurements of CIS QDs conducted with a scan rate of 0.1 V/s (sample C from **Figure 2.1.2.1**). The black circle corresponds to the starting EC potential ( $V_{EC} = 0$  V). “Forward scans” refer to ramping the potential from 0 V to more positive values (labeled “F”) and “reverse scans” refer to scanning to more negative  $V_{EC}$  (labeled “R”). A clear intra-gap oxidation (forward) and reduction (reverse) reactions are observed at potentials of 0.65 V and 0.45 V, respectively. A weak shoulder, which appears at negative  $V_{EC}$  at -0.33 V on the reverse scans, may represent an unoccupied intra-gap trap (denoted T<sub>c</sub>). The VB-edge and Cu<sup>x</sup> positions are derived from the onset potential for CIS QD (or Cu<sup>x</sup>) oxidation on the forward scans using linear fits (dotted red lines), while the T<sub>c</sub> position is determined by the onset potential for the reduction current on the reverse scans. “E” denotes the parasitic electrolyte background current, which makes the CB position difficult to observe in the CV measurements. (b) The CB (red solid circles) and VB (blue solid circles) edge positions for stoichiometric CIS QDs based on combined CV and optical measurements. Green solid circles correspond to the measured redox potentials of the intra-gap feature assigned to the Cu<sup>1+/2+</sup> state, while open turquoise circles correspond to the energy of the intra-gap state obtained based on the apparent Stokes shift from the optical PL and absorption measurements. Open blue and red diamonds correspond, respectively, to the VB and CB edges of Cu-deficient CIS QDs (Cu<sub>0.56</sub>In<sub>1.44</sub>S<sub>2</sub>) obtained from optical measurements (the VB data are placed along the trend line derived from the CV measurements of stoichiometric CIS QDs). The Stokes shifts for these samples are represented by open turquoise diamonds as measured from the PL spectrum. Bulk CIS (closed triangles) band positions are based on refs. 3 and 36. The solid horizontal line shows the standard Cu<sup>1+/2+</sup> redox potential from literature, while the dashed line shows the average Cu<sup>1+/2+</sup> redox potential for CIS QDs as measured here.

oxidized (reduced) during the potential sweep. Film measurements, on the other hand, generally oxidize (reduce) all of the QDs on the forward scan, which can possibly damage the QDs, and make it difficult to determine energy levels on the reverse scan.

The CIS/electrolyte solution is placed in a cuvette with an indium-tin-oxide (ITO) working electrode, a platinum counter electrode, and a silver wire pseudo-reference electrode. ITO is chosen as the working electrode due to its high optical transparency, which allows for the spectroelectrochemical (SEC) measurements to be conducted in the same experimental setup. The starting potential is 0 V versus the silver-wire pseudo-reference electrode and the term “forward scan” refers to increasingly positive  $V_{EC}$  (up to +2 V), while the term “reverse scan” applies to the situation of increasingly negative  $V_{EC}$  (down to -2 V); the scan directions are indicated in **Figure 2.1.2.2a** by the arrows labeled “F” and “R” respectively. These measurements can be interpreted in terms of a deliberate modulation of the Fermi level where positive (negative)  $V_{EC}$  is equivalent to lowering (raising) the Fermi level resulting in an oxidation (reduction) current associated with the state of interest.

**Figure 2.1.2.2a** shows a voltammogram for sample C (zoomed in for clarity) from **Figure 2.1.2.1a**. The voltammogram for the full scan range (see Figure S6.1.3a) reveals two distinct oxidation waves on the forward scan, indicative of two states that, as we discuss below, can be assigned to a defect related intra-gap state and an intrinsic VB edge QD state. For both of these CV features, we determine the formal energy of the state by using the onset potential for the oxidation wave on the forward scan. Based on this definition, the energy of the first state observed at the less positive potential is estimated to be  $+0.45 \text{ V} \pm 0.1 \text{ V}$ . The reverse scan shows a reduction wave corresponding

to the same state peaked at  $\sim +0.45$  eV, indicating that the corresponding redox reaction is reversible (see a more detailed discussion later in this work). After calibration *versus* the normal hydrogen electrode (NHE), we obtain that the detected state is within 0.1 V of the redox potential of the  $\text{Cu}^{1+/2+}$  couple, which is well within the standard error for copper redox reactions in different environments.<sup>37-39</sup> The same intra-gap feature with the redox potential close to that of the  $\text{Cu}^{1+/2+}$  state is observed in the CV measurements of all other samples (Figure S6.1.3b).

While this is the first demonstration of Cu-defects for CIS QDs in their native solution environment, several other studies have also observed a similar intra-gap CV wave in CIS and  $\text{Cu}_{2-x}\text{S}$  QD films.<sup>40-42</sup> In two of these reports it was also assigned to an intra-gap Cu-related defect.<sup>40,42</sup> However, *ref 41* proposed an alternative explanation in terms of thiolate oxidation within the ligand shell. To test this possibility, we have conducted linear sweep voltammetry (LSV) measurements on 1-dodecanethiols ( $\text{CH}_3(\text{CH}_2)_{11}\text{SH}$ , usually abbreviated as DDT) used as ligands in the studied QD samples. These test measurements do not show any significant anodic current at around +0.45 V (Figure S6.1.3c), suggesting that DDT oxidation is unlikely to explain the corresponding intra-gap feature observed for the QD samples, and hence it is not ligand but QD related.

The VB edge is determined from the onset potential for the oxidation current observed at potentials more positive than the  $\text{Cu}^x$  feature in the forward scans (**Figure 2.1.2.2a** and Figure S6.1.3). The oxidation of CIS QDs does not appear to be reversible as indicated by the absence of a corresponding feature during the reverse scan. This differs from the quasi-reversible peaks associated with the intra-gap state assigned to  $\text{Cu}^x$ . While it was not explicitly stated, the signs of irreversible VB oxidation were also

observed in previous studies of QD film samples.<sup>3,40,43</sup> Despite the irreversibility observed in CV measurements, the QDs do not seem to degrade at the onset potential for VB oxidation, as we do not detect any spectral shifts in optical absorption measurements conducted *in situ* while scanning the EC potential (Figure S6.1.4d). These measurements do reveal a spectrally uniform background due to scattering once the Fermi level is pushed just below the VB-edge position. At this point, QDs become positively charged *via* hole injection, which leads to their plating onto the negative Pt counter electrode manifested as a thin deep-red layer covering the electrode surface. A similar spectroscopic effect was previously observed for CdSe QDs where it was attributed to the loss of ligands (due to their oxidation by a VB hole) and subsequent QD aggregation and precipitation.<sup>44-45</sup>

Next, we focus on CV features observed for a reverse scan when the Fermi level is progressively shifted up in energy (**Figure 2.1.2.2a**). As we mentioned earlier, this scan reveals a wave at  $\sim 0.45$  V, which we have attributed to the reversible reduction of the intra-gap  $\text{Cu}^x$  defect. To verify the validity of this assignment, and specifically, to make sure that this feature is not due to any structural changes in the QDs or the passivation layer induced by oxidation, we repeat CV measurements for a potential range ending right before the onset of the VB oxidation current and observe that they are virtually indistinguishable from measurements for a wider variation of the EC potential (Figure S6.1.4a). This provides evidence that the  $\sim 0.45$  V feature is not an artifact from the irreversible oxidation of the QDs but is due to reversible reduction of the intra-gap defect.

As the EC potential is increased further in the negative direction, we observe a new intra-gap reduction feature at *ca.*  $-0.33$  V ( $T_c$ ), which at the first glance might be

indicative of electron injection into the CB state. However, when we conduct LSV measurements, wherein the potential is scanned only in the negative direction starting at 0 V instead of as a reverse scan from +2.0 V, we do not detect this wave (Figure S6.1.4b), indicating that the corresponding state is occupied with electrons, and hence, it must be first oxidized (*i.e.*, depopulated) before it can be reduced. Such sequential oxidation-reduction occurs during our CV measurements, which we start by first lowering the Fermi level and then raising it. Based on these observations, we can assign the -0.33 V feature to an intra-gap state (labeled  $T_C$  in **Figure 2.1.2.2a**) that can serve either as a hole or an electron trap depending on the position of the Fermi level, which controls its occupancy. Similar to our study of the  $Cu^x$  intra-gap feature, we eliminate the possibility of this feature arising from the reduction of surface ligands by making sure that it does not appear in CV measurements of DDT in the electrolyte solution without QDs (Figure S6.1.4c).

As we scan the EC potential to even more negative values in the CV measurements, we observe an onset of a new reduction wave slightly below -1 V (denoted “E” in **Figure 2.1.2.2a**). While this is near the expected position of the CB edge, additional LSV measurements conducted with the same electrolyte but in the absence of the QDs show the same reduction feature (Figure S6.1.4b), indicating that it is not due to the QDs but is instead from the electrolyte itself. The large parasitic background current from electrolyte double-layer charging, and thiolate reduction near the CB edge (inset of **Figure 2.1.2.3c**), both complicate the determination of the CB position from the EC measurements. A similar suppression of the CB peak was observed in previous EC studies of QDs where the Fermi level was pinned either by intra-gap states, the electrode material, or the electrolyte.<sup>46-49</sup> As a result, in order to determine the position of the CB

edge, we add the optical band gap (**Figure 2.1.2.1a**) to the EC-measured energy of the VB edge. The same procedure to determine both band edges (by combining CV and optical measurements) has been previously applied to other QD systems (e.g. PbS).<sup>50</sup>

Next, we convert the VB and CB energies derived from the combined EC and optical measurements to the absolute energy scale versus vacuum and plot them in **Figure 2.1.2.2b** (solid blue and red circles, respectively) as a function of QD band gap, which allows us to eliminate uncertainties associated with size determination. The band-edge energies obtained by us are in good correspondence with literature measurements for similarly sized CIS QDs studied as film samples<sup>3,43</sup> (see comparison in Figure S6.1.3). Using extrapolations based on the trend lines from the CV results, we find that the bulk CIS VB and CB edges are expected to be at -5.63 and -4.08 eV *versus vacuum*. Both of these values are in excellent agreement with literature results for bulk CIS (solid triangles in **Figure 2.1.2.2a**).<sup>3,43</sup>

We also use our EC measurements to address the origin of the Stokes shifts observed in optical measurements. Specifically, we compare the energy of the Cu<sup>x</sup>-related redox feature (solid green circles in **Figure 2.1.2.2b**) to the absolute energy of the PL band (open turquoise circles) obtained by adding the optical Stokes shift  $\Delta_S$  (**Figure 2.1.2.1a**) to the absolute VB-edge energy from the EC measurements. We find very good agreement between the two sets of data suggesting that the intra-gap feature resolved by the EC method is indeed due to the state involved in the emission process. Further, since its energy is close to the documented Cu<sup>x</sup> redox potential (horizontal dashed line in **Figure 2.1.2.2b**) it is likely associated with a copper-related defect.

In the same plot, we also include optical measurements for a series of Cu-deficient ( $\text{Cu}_{0.56}\text{In}_{1.44}\text{S}_2$ ) QDs (open circles). The band gaps are measured from the absorption spectra (Figure S6.1.5) and then they are used to plot the VB and CB energies (open blue and red diamonds respectively in **Figure 2.1.2.2b**) assuming that the QD size-dependent VB edges (open blue diamonds in **Figure 2.1.2.2b**) are aligned along the CV-data-based trend line (blue solid line in **Figure 2.1.2.2b**). The Stokes-shift energies derived from the PL and absorption spectra were used to determine the positions of the PL peak *versus* the VB edge. The PL absolute energies obtained in this way (open turquoise diamonds) are again very close to the Cu-ion redox potential, suggesting that in these copper-deficient samples, the intra-gap PL also involves the  $\text{Cu}^x$  state as in stoichiometric samples. In fact, based on the combined results of optical and EC measurements for the stoichiometric and copper-deficient samples, we estimate that the energy of the Cu-related defect in CIS QDs is approximately  $-5.54 \pm 0.12$  eV versus vacuum. This is slightly lower (by *ca.* 200 meV) than the literature value (compare solid and dashed lines in **Figure 2.1.2.2b**),<sup>37-39</sup> which however, is not surprising and can be attributed to the effects of the environment specific to the CIS crystal lattice.

**Spectroelectrochemical Measurements.** In order to gain deeper insights into the specific oxidation state of  $\text{Cu}^x$  involved in PL, we conduct linear-sweep voltammetry (LSV) measurements of stoichiometric CIS QDs under continuous low-intensity excitation (sub-single-exciton average QD occupancies) at 532 nm and compare currents measured with and without illumination (**Figure 2.1.2.3a**). We observe that the oxidation current from the  $\text{Cu}^{1+}$  to  $\text{Cu}^{2+}$  conversion in the non-illuminated (dark) sample is appreciably higher than

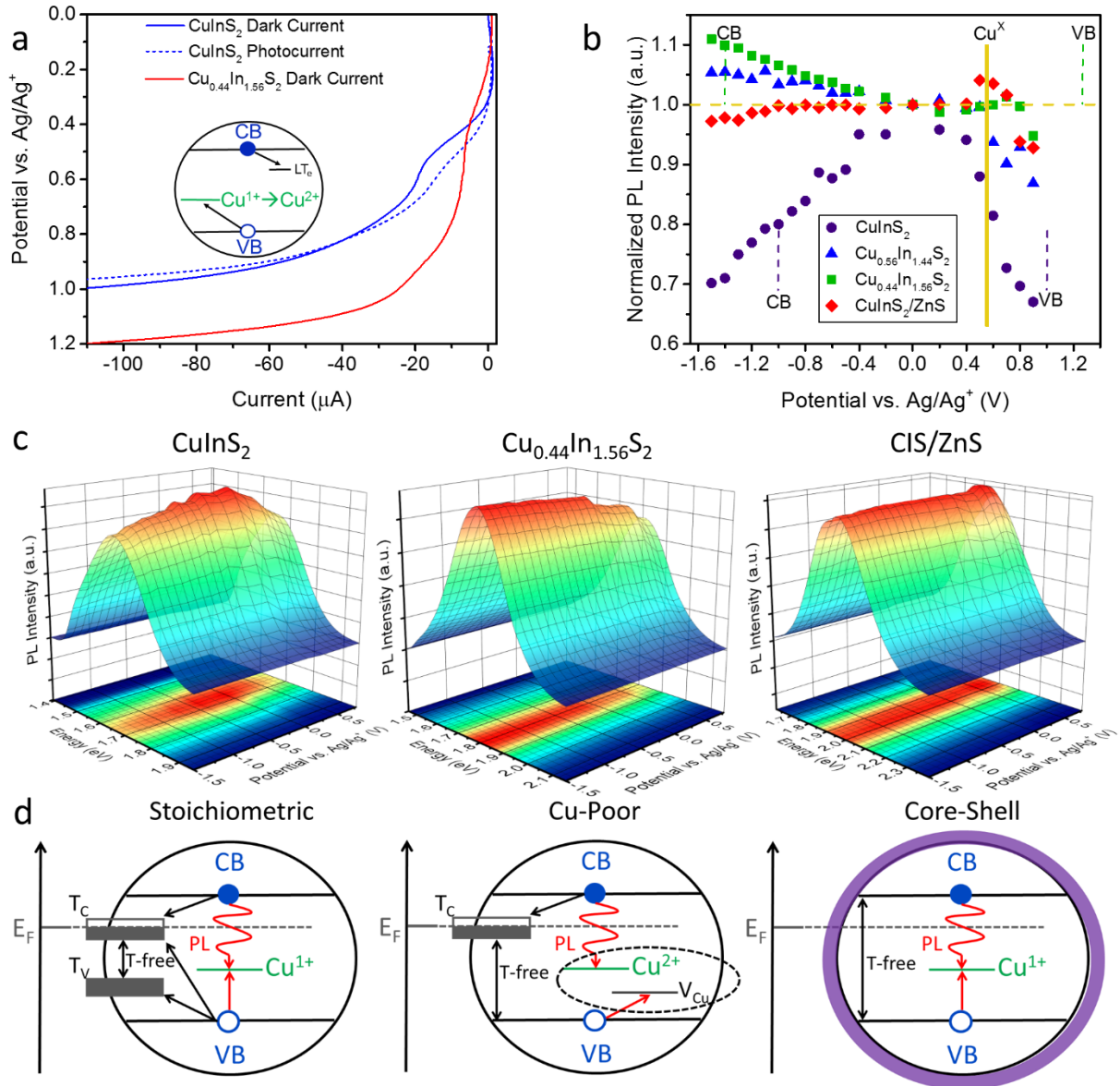


**Figure 2.1.2.3.** (a) LSV measurements of stoichiometric CIS QDs (sample C from **Figure 2.1.2.1a**) without (solid blue line) and with (dotted blue line) continuous wave illumination with low-intensity 532 nm light. The intra-gap Cu<sup>x</sup> oxidation feature becomes significantly less prominent after 30 minutes of continuous illumination, likely due to photoconversion of Cu<sup>1+</sup> to Cu<sup>2+</sup>. Notably, this feature also disappears in the dark current for Cu<sub>0.44</sub>In<sub>1.56</sub>S<sub>2</sub> QDs (solid red line), indicating Cu<sup>2+</sup> defects are more prevalent than Cu<sup>1+</sup> defects. Inset: A possible mechanisms of Cu<sup>1+</sup>-to-Cu<sup>2+</sup> photonconversion (see text for details); LT<sub>e</sub> is a long-lived electron trap. (b) SEC measurements of PL intensity (measured at the peak) as a function of applied bias for core-only stoichiometric CIS QDs (purple solid circles), Cu-deficient CIS QDs (Cu<sub>0.56</sub>In<sub>1.44</sub>S<sub>2</sub> and Cu<sub>0.44</sub>In<sub>1.56</sub>S<sub>2</sub>; green squares and blue triangles, respectively), and stoichiometric CIS with a ZnS shell (red diamonds); the data are normalized to the PL intensity observed with V<sub>EC</sub> = 0. Band-edges for the Cu<sub>0.44</sub>In<sub>1.56</sub>S<sub>2</sub> QDs (roughly equivalent to the band positions for Cu<sub>0.56</sub>In<sub>1.44</sub>S<sub>2</sub>) are shown as vertical dotted green lines, stoichiometric QDs as dotted purple lines, and Cu<sup>x</sup> by the solid yellow line. (c) The full V<sub>EC</sub>-dependent PL spectra for stoichiometric CIS QDs (left panel),

Cu<sub>0.44</sub>In<sub>1.56</sub>S<sub>2</sub> QDs (middle panel), and stoichiometric CIS/ZnS core-shell QDs (right panel). These experiments were done using the same EC setup as the CV/LSV measurements, but holding each potential for 3 minutes before collecting the spectra. Spectra were measured under low-intensity excitation at 500 nm using a Xe lamp. (d) Schematic depictions of relaxation processes in stoichiometric (left) and Cu-deficient (middle) core-only CIS QDs, and stoichiometric CIS/ZnS core/shell samples (right). The results of SEC measurements suggest that the stoichiometric QDs exhibit two trap bands associated with surface defects; one is located near the CB edge ( $T_C$ ) and the other, near the VB edge ( $T_V$ ). The position of the Fermi level ( $E_F$ ), controlled by  $V_{EC}$ , and determines the degree of filling of the trap bands. The occupied states (below  $E_F$ ) serve as hole traps, while unoccupied states (above  $E_F$ ) serve as electron traps. The radiative transition (red wavy arrow) can be quenched by either electron or hole trapping (black arrows). The vertical double-sided arrows show the span of the surface-trap-free region (denoted as the "T-free" region), which manifests in SEC measurements as the range of EC potentials wherein the change in  $V_{EC}$  does not affect the PL intensity.

that under illumination suggesting that at least some of the Cu<sup>1+</sup> defects existing in the ground states are photoconverted to Cu<sup>2+</sup>. This phenomenon is similar to that observed in studies of photoinduced magnetism in Cu-doped II-VI semiconductors (Cu<sup>2+</sup> ions are paramagnetic while Cu<sup>1+</sup> ions are diamagnetic)<sup>51</sup> and also similar to the process of light-induced removal of "kinks" in current-voltage characteristics of related bulk CIGS and CZTS materials well documented in the literature.<sup>52-54</sup> Notably, the Cu<sup>1+</sup> to Cu<sup>2+</sup> conversion is also absent for Cu-poor QDs (**Figure 2.1.2.3a**); as elaborated below, this might indicate that in these samples, Cu<sup>x</sup> is predominantly in the 2+ oxidation state. It should also be noted that these measurements further support our initial assignment of the intra-gap CV wave at around +0.45 V to Cu<sup>x</sup> instead of thiolate oxidation, as the latter should be insensitive to QD stoichiometry or photoexcitation, as the photon energy corresponding to 532-nm light is well below the absorption onset of DDT.

The physics underlying the Cu<sup>1+</sup>-to-Cu<sup>2+</sup> photoconversion can be explained by the existence of long-lived electron traps that have been previously invoked to explain QD photocharging.<sup>51,55-57</sup> Indeed, in the presence of such traps, a photoexcited electron can be quickly removed from the CB state, which would leave behind a long-lived

uncompensated hole. This hole can then be trapped by the  $\text{Cu}^{1+}$  defect and eventually drive its transformation into the  $\text{Cu}^{2+}$  defect accompanied by required structural modifications in the host material including the establishment of appropriate charge compensation. We would like to point out that these structural changes do not occur during a standard photoemission cycle when a hole trapped by a  $\text{Cu}^{1+}$  ion also leads to formation of a  $\text{Cu}^{2+}$ -like state. This state, however, is only short lived (several hundreds of nanoseconds) as the trapped hole quickly recombines with a CB electron to restore the original  $\text{Cu}^{1+}$  configuration.

One important implication of the above measurements is that the thermodynamic equilibrium between the  $\text{Cu}^{1+}$  and  $\text{Cu}^{2+}$  ions existing in the ground states can be distorted in the presence of illumination leading to a considerable amount of  $\text{Cu}^{2+}$  ions even under high Fermi level conditions, which would favor  $\text{Cu}^{1+}$  defects in a standard situation without illumination. A similar effect when the equilibrium between paramagnetic  $\text{Cu}^{2+}$  ions and the nonmagnetic (or less magnetic)  $\text{Cu}^{1+}$  dopants is directly controlled by the intensity of external illumination has been observed and quantitatively analyzed in **ref. 51** in the context of photomagnetization studies.

In **Figure 2.1.2.3b** we display the measurements of the PL intensity (measured at the peak) as a function of EC potential for four different samples: stoichiometric core-only CIS QDs, two core-only Cu-deficient samples ( $\text{Cu}_{0.56}\text{In}_{1.44}\text{S}_2$  and  $\text{Cu}_{0.44}\text{In}_{1.56}\text{S}_2$ ), and a stoichiometric CIS/ZnS core/shell sample; the PL intensity is normalized to the PL signal at  $V_{EC} = 0$  V. **Figure 2.1.2.3c** shows the complete set of PL spectra when the potential is changed in 3 minute intervals for the stoichiometric QDs, core/shell QDs, and QDs with the largest Cu-deficiency ( $\text{Cu}_{0.44}\text{In}_{1.56}\text{S}_2$ ). Some of the previous SEC studies of QDs

explained the observed VEC-dependent modulation of the PL signal by invoking an extended intra-gap "trap band," which can capture electrons into its unoccupied states and holes into the occupied ones.<sup>27</sup> Increasingly negative potentials correspond to raising the Fermi level, which leads to progressive filling of the trap band, translating into suppressed electron trapping and enhanced hole trapping. The lowering of the Fermi level leads to the opposite effects. Here, we apply similar reasoning for explaining our present observations.

For all of the samples, the PL intensity is almost  $V_{EC}$ -independent from -0.4 V to +0.4 V suggesting that in this range of potentials the QD band gap is free of trap states (labeled "T-free" in **Figure 2.1.2.3d**). Outside of this region, we observe sample-dependent behaviors. Core-only stoichiometric CIS QDs show emission quenching under both positive and negative  $V_{EC}$ , which suggests the existence of two trap bands, one near the CB edge and the other near the VB edge ( $T_C$  and  $T_V$  in **Figure 2.1.2.3d** left panel, respectively). The observation of  $T_C$  at *ca.* -0.4 V in SEC measurements is also in agreement with our previous assertion that the CV wave around -0.33 V is an intra-gap state capable of carrier trapping. Interestingly, the magnitude of PL quenching observed for  $V_{EC} > 0.4$  V decreases for the copper-poor  $\text{Cu}_{0.56}\text{In}_{1.44}\text{S}_2$  sample (**Figure 2.1.2.3b** and **Figure 2.1.2.3c** middle panel) compared to the stoichiometric QDs (**Figure 2.1.2.3b** and **Figure 2.1.2.3c** left panel), and then almost completely vanishes in the case of the  $\text{Cu}_{0.44}\text{In}_{1.56}\text{S}_2$  sample. This might indicate the suppression of the trapping associated with the  $T_V$  states due to their increased filling or progressive elimination (schematically represented in the middle panel of **Figure 2.1.2.3d** and discussed below). The PL signal from the stoichiometric core-shell sample is almost  $V_{EC}$ -independent across the entire

range of the studied EC potentials suggesting that overcoating the QD core with the wider gap semiconductor eliminates both the  $T_C$  and  $T_V$  traps. This further suggests that these traps are of surface origin and likely associated with unpassivated dangling bonds, as observed in other types of QD systems and indicated by both transient absorption and pump-dump-probe spectroscopies of CIS QDs.<sup>24-25,27,47,58-59</sup>

The difference in the sign of the PL signal change with raising the Fermi level at  $V_{EC} < -0.4$  eV between stoichiometric and Cu-deficient samples (quenching *versus* enhancement, respectively) might be indicative of the difference in the oxidation state of the Cu-ion involved in the emission process. Under conditions of thermodynamic equilibrium both  $Cu^{1+}$  and  $Cu^{2+}$  defects are expected to coexist in CIS QD ensembles with the relative concentrations linked to the position of the Fermi level, dependent on fabrication procedure, and can further be altered by modifying, for example, the chemical or electrostatic environments, or applying external illumination.

The effect of external stimuli such as the EC potential has likely a greater effect on QD surface states than on the states within the QD. This is suggested, for example, by present (**Figure 2.1.2.3b-d**) and previous observations,<sup>27,34,47,60</sup> which indicate that the beneficial effects of electronic passivation of surface traps due to a varied Fermi energy in EC measurements are similar to those of chemical passivation of a QD with an inorganic shell. On the other hand, one might expect that the modification of the internal intra-gap states (including those associated with  $Cu^x$  defects) due to changes in  $V_{EC}$  does not occur as readily as in the case of surface states because of a large tunneling barrier created by the host semiconductor, which isolates the localized internal defects from the electrode. Given the above considerations, it is reasonable to assume that while we do

observe clear redox signatures of  $\text{Cu}^x$  in the CV measurements, they might be associated with the EC transformation of the Cu surface ions while the interior ions might still maintain their original oxidation state. This assumption helps rationalize the observed  $V_{EC}$ -induced modulation of PL signals in **Figure 2.1.2.3b,c**.

The  $V_{EC}$ -dependent measurements of Cu-deficient samples indicate that the PL intensity is affected primarily by electron trapping (see our earlier discussion). This is exactly what is expected for the emission mechanism associated with the  $\text{Cu}^{2+}$  ion, which does not require hole capture prior to emission and is therefore not susceptible to hole trapping. In this case, the progressive filling of the electron traps by raising the Fermi level (**Figure 2.1.2.3c**, middle) should translate into the increasing emission intensity, as observed in **Figure 2.1.2.3b,c** for Cu-deficient samples. In fact, the formation of  $\text{Cu}^{2+}$  ions is a logical process in Cu-deficient QDs as a large abundance of Cu-vacancies should facilitate the creation of  $\text{Cu}^{2+}$  defects as a means to maintain local charge neutrality. This interpretation is also consistent with the absence of intra-gap oxidation wave for the Cu-deficient QDs in **Figure 2.1.2.3a**. Furthermore, copper vacancies that presumably accompany the  $\text{Cu}^{2+}$  defects are known to be energetically close to the VB and are capable of acting as subpicosecond hole traps;<sup>25</sup> therefore, their pairing with the  $\text{Cu}^{2+}$  ions automatically ensures a quick removal of photogenerated holes from the VB states that would otherwise compete for the CB electron with a Cu-related emission channel (**Figure 2.1.2.1b**, bottom left).<sup>27,34</sup> We would like to point out again that this explanation is based on the assumption that a considerable fraction of Cu defects remains in the 2+ oxidation state even when the Fermi level of the environment is above the  $\text{Cu}^x$  redox potential. In addition to the inhibiting role of the tunneling barrier, which complicates reduction of

internally located  $\text{Cu}^{2+}$  defects, such imbalance between the 1+ and 2+ ions in favor of the latter ones might be facilitated by the process of  $\text{Cu}^{1+}$ -to- $\text{Cu}^{2+}$  photoconversion evident from the measurements in **Figure 2.1.2.3a**.

A distinct (opposite) PL response to changes in  $V_{EC}$  for large negative potentials observed for the stoichiometric sample (**Figure 2.1.2.3b**, purple circles) might be indicative of the different (*i.e.*, 1+) oxidation state of the Cu-defect involved in the emission process compared to the Cu-deficient samples (blue triangles and green squares in **Figure 2.1.2.3b**). In fact, it is logical to expect that in QDs with a balanced stoichiometry, the prevailing defect is a pair of  $\text{Cu}^{1+}$  and  $\text{In}^{3+}$  ions that have swapped their lattice sites. These defects, known as "anti-site" pairs, are automatically charge compensated and are common in bulk CISES materials.<sup>61-63</sup> The  $\text{Cu}^{1+}$  defect is "PL-passive" in the ground state but can be activated by capturing a photogenerated hole as illustrated in **Figure 2.1.2.1b** (bottom right diagram). For this emission mechanism, in addition to electron trapping, the PL efficiency is also affected by hole trapping at the non-Cu-related intra-gap sites. Therefore, raising the Fermi level, which is accompanied by filling of intra-gap states, results in two competing trends: one is the reduction of electron trapping, and the other is the increased hole trapping (**Figure 2.1.2.3c**, left panel). The observed drop of the PL signal in the range of high negative potentials ( $V_{EC} < -0.4$  V) suggests that the effects of increased hole trapping outweighs the benefits due to suppressed electron losses. The roles of electron and hole traps, however, likely reverse in the range of positive potential ( $V_{EC} > 0.4$ ) wherein changes in  $V_{EC}$  presumably modify the occupancy of the  $T_V$  trap band. In this case, the processes of electron trapping likely dominates the observed the  $V_{EC}$ -

dependent modulation of the PL signal leading to the drop of the PL intensity with lowering the Fermi level.

### 2.1.3. Conclusions

To summarize, the conducted EC measurements reveal the presence of a well-defined intra-gap state whose redox potential is consistent with that of a  $\text{Cu}^x$  ion. Further, its energetic offset *versus* the VB edge is close to the Stokes shift inferred from optical measurements confirming the validity of models wherein the PL from CISES QDs is ascribed to an optical transition involving a CB electron and a hole-like state associated with the  $\text{Cu}^x$  defect.

While both types of Cu defects are emissive, the  $\text{Cu}^{1+}$  emission mechanism is susceptible to both hole and electron trapping, while the mechanism involving the  $\text{Cu}^{2+}$  defect is only affected by electron trapping. Interestingly, in the case of stoichiometric samples, application of increasingly negative potentials (raising the Fermi level) leads to a drop of the PL signal, indicating the importance of hole trapping that becomes progressively enhanced due to an increasing number of filled intra-gap sites. This behavior is expected for the  $\text{Cu}^{1+}$  related emission channel, which relies on photogenerated holes for its activation. Conversely, the emission intensity for Cu-deficient QDs shows the opposite trend, *i.e.*, the PL intensity increases as the Fermi level is raised. This is indicative of the  $\text{Cu}^{2+}$  emission channel, which benefits from the progressive filling of intra-gap states resulting in deactivation of electron traps but is not affected by the increasing number of hole traps.

The above results suggest that while both  $\text{Cu}^{1+}$  and  $\text{Cu}^{2+}$  defects are expected to co-exist in the QDs, their relative fractions might be linked to sample stoichiometry. In fact, the SEC and EC measurements suggest that  $\text{Cu}^{1+}$  species seem to prevail in stoichiometric samples where they can occur in the form of anti-site  $\text{Cu}_{\text{In}}\text{-In}_{\text{Cu}}$  defect pairs, while  $\text{Cu}^{2+}$  states are likely more abundant in Cu-deficient samples where they are created as charge compensating species for Cu-vacancies. Our SEC studies also indicate that the balance between  $\text{Cu}^{1+}$  and  $\text{Cu}^{2+}$  defects can be distorted in the presence of illumination, which leads to photoconversion of copper 1+ ions into 2+ species. This process might result in a disproportionately large fraction of  $\text{Cu}^{2+}$  states for high negative EC potentials that otherwise would favor  $\text{Cu}^{1+}$  states.

The conducted studies indicate that in Cu-deficient samples, the trap sites are located primarily near the CB-edge while for the stoichiometric samples, we observe the signatures of an additional trapping band near the VB edge. Our overall assessment is that the stoichiometric samples are more strongly influenced by nonradiative processes involving intra-gap states compared to Cu-deficient samples. This might explain a commonly observed trend that moderate levels of Cu-deficiency lead to the improved PL efficiency.<sup>64-67</sup> The high sensitivity of both  $\text{Cu}^{1+}$  and  $\text{Cu}^{2+}$  emission channels to electron trapping is also consistent with previous transient absorption and pump-dump-probe spectroscopy studies.<sup>24-25</sup>

The measurements of CIS/ZnS QD samples with stoichiometric cores indicate that in addition to dramatically boosting the PL efficiency, the use of the core/shell approach also leads to a nearly complete elimination of the dependence of the PL signal on the applied EC potential. This observation suggests that the use of the passivating ZnS layer

removes both trap bands observed in the stoichiometric core-only samples, and further indicates that these trap sites are located primarily at the QD surfaces.

#### 2.1.4. Methods

**Chemicals and Materials:** The following chemicals were purchased and used as received. Anhydrous copper (I) iodide ( $\text{CuI}$ , 99.995 %), 1-dodecanethiol ( $\text{CH}_3(\text{CH}_2)_{11}\text{SH}$ , DDT,  $\geq 98$  %), anhydrous chloroform ( $\text{CH}_2\text{Cl}_2$ ,  $\geq 99$  %), zinc acetate ( $\text{Zn}(\text{Ac})_2$ , 99.99 %), copper(I) acetate ( $\text{CuAc}$ , 99.99 %), sulfur powder ( $\text{S}$ , 99.99 %), octadecene (ODE, 90 %), oleic acid (OA, 90 %) and anhydrous methanol ( $\text{CH}_3\text{OH}$ ,  $\geq 99$  %) were obtained from Sigma-Aldrich. Anhydrous indium (III) acetate ( $\text{In}(\text{CH}_3\text{COO})_3$ ,  $\text{In}(\text{Ac})_3$ , 99.99 %), and oleylamine ( $\text{CH}_3(\text{CH}_2)_7\text{CH}=\text{CH}(\text{CH}_2)_7\text{CH}_2\text{NH}_2$ , OLAm, 80~90 %) were purchased from Acros Organics. Indium stearate ( $\text{In}(\text{St})_3$ ) was prepared following a previously reported method.<sup>7</sup>

**Synthesis of Stoichiometric Core-Only CIS QDs:** In a typical reaction, 1 mmol of  $\text{CuI}$  and 1 mmol of  $\text{In}(\text{Ac})_3$  was dissolved in 5 mL of DDT (20 mmol) with 1 mL of OLAm in a 50 mL round-bottom flask, the mixture was then degassed under vacuum at 100 °C for 30 min. The temperature was raised to 140 °C until all solid precursors are fully dissolved, which usually takes less than 10 minutes. After that, the temperature was set to 230 °C for 20 minutes. To quench the reaction, the heating element was removed and the QDs were allowed to cool. The resulting CIS QDs were purified by iterative dissolution in chloroform and precipitation with methanol and then stored in chloroform under an inert atmosphere.

**Shell Growth on Stoichiometric CIS Cores:** Separately a solution of 0.5 M Zn-oleate was made by mixing 10 mmol zinc acetate powder with 16 ml of ODE and 4 ml of OA, and heating to 150 °C for 1 hr. To form the thin ZnS shell around stoichiometric CIS cores, 5 mL of the Zn-oleate solution was added to the CIS QD reaction solution for 30 min at 200 °C.

**Synthesis of Cu-Deficient CIS QDs:** Synthesis of the CIS core-only QDs was performed by following previous works with modifications.<sup>7</sup> In a typical reaction, we employed hot injection where  $\text{In}(\text{St})_3$  (386 mg, 0.4 mmol), CuAc (25 mg, 0.2 mmol), DDT (120  $\mu\text{L}$ , 0.5 mmol), OA (126  $\mu\text{L}$ , 0.4 mmol) and 10 mL ODE were loaded into a three-neck flask. The above mixture was heated to 80 °C and degassed under vacuum for 30 min. The mixture was then heated and stabilized at 180 °C under a nitrogen flow. Next, 0.8 mL of S/ODE ([S]=0.5 mol/L) was quickly injected into the above mixture. After the completion of CIS growth (5 min), the reaction was quenched by cooling the solution to room temperature.

**EC and Optical Studies:** An Indium-tin-oxide (ITO) glass slide was used for the working electrode, platinum wire as a counter electrode, and a silver wire as a pseudoreference electrode. CIS QDs were diluted to 5 mg/ml in air-free chloroform in a Nitrogen glove box. 0.1 M tetrabutylammonium perchlorate ( $\text{TBAClO}_4$ ) was weighed in the glove box before adding to the QD solution. The CIS: $\text{TBAClO}_4$  molar ratio was roughly 1:5 so that the electrolyte salt can effectively passivate the NC surface. Dark state CV measurements were conducted after placing the electrodes in a quartz cuvette with the NC/electrolyte solution and connecting to the potentiostat (CH Instruments). The cuvette was covered in black tape to eliminate ambient light. The scan rate was set to 0.1 V/s and data collection at 0.001 V for the scan range of 2 V to -2 V. All measurements were done using static

solution samples without stirring. Voltage sweeps were continuous (0.1 V/s rate), and the current was collected without any additional wait times. The steady-state current for the electrolyte was measured at 0 V for 5 minutes and the average was subtracted from the CV scans as a background correction. Visible PL spectra were recorded using a Horiba Scientific Fluoromax-4 spectrometer. Absorption spectra were taken with an Agilent 8543 UV-Vis spectrophotometer. SEC measurements were conducted by holding the potential for each step for 3 minutes. This insured that a considerable fraction of the QDs was charged/discharged before each optical measurement.

#### **2.1.5. References**

1. Pons, T.; Pic, E.; Lequeux, N.; Cassette, E.; Bezdetnaya, L.; Guillemin, F.; Marchal, F.; Dubertret, B. Cadmium-Free CuInS<sub>2</sub>/ZnS Quantum Dots for Sentinel Lymph Node Imaging with Reduced Toxicity. *ACS Nano* 2010, 4, 2531-2538.
2. Aldakov, D.; Lefrancois, A.; Reiss, P. Ternary and Quaternary Metal Chalcogenide Nanocrystals: Synthesis, Properties and Applications. *J. Mater. Chem. C* 2013, 1, 3756-3776.
3. Zhong, H.; Lo, S. S.; Mirkovic, T.; Li, Y.; Ding, Y.; Li, Y.; Scholes, G. D. Noninjection Gram-Scale Synthesis of Monodisperse Pyramidal CuInS<sub>2</sub> Nanocrystals and Their Size-Dependent Properties. *ACS Nano* 2010, 4, 5253-5262.
4. Nam, D-E.; Song, W-S.; Yang, H. Facile, Air-Insensitive Solvothermal Synthesis of Emission-Tunable CuInS<sub>2</sub>/ZnS Quantum Dots with High Quantum Yields. *J. Mater. Chem.* 2011, 21, 18220-18226.

5. Castro, S. L.; Bailey, S. G.; Raffaele, R. P.; Banger, K. K.; Hepp, A. F. Synthesis and Characterization of Colloidal CuInS<sub>2</sub> Nanoparticles from a Molecular Single-Source Precursor. *J. Phys. Chem. B* 2004, 108, 12429-12435.
6. Allen, P. M.; Bawendi, M. G. Ternary I-III-VI Quantum Dots Luminescent in the Red to Near-Infrared. *J. Am. Chem. Soc.* 2008, 130, 9240-9241.
7. Xie, R.; Rutherford, M.; Peng, X. Formation of High-Quality I-III-VI Semiconductor Nanocrystals by Tuning Relative Reactivity of Cationic Precursors. *J. Am. Chem. Soc.* 2009, 131, 5691-5697.
8. Bose, R.; Jana, S.; Manna, G.; Chakraborty, S.; Pradhan, N. Rate of Cation Exchange and Change in Optical Properties during Transformation of Ternary to Doped Binary Nanocrystals. *J. Phys. Chem. C* 2013, 117, 15835-15841.
9. Draguta, S.; McDaniel, H.; Klimov, V. I. Tuning Carrier Mobilities and Polarity of Charge Transport in Films of CuInSe<sub>x</sub>S<sub>2-x</sub> Quantum Dots. *Adv. Mater.* 2015, 27, 1701-1705.
10. McDaniel, H.; Fuke, N.; Makarov, N. S.; Pietryga, J. M.; Klimov, V. I. An Integrated Approach to Realizing High-Performance Liquid-Junction Quantum Dot Sensitized Solar Cells. *Nat. Commun.* 2013, 4
11. McDaniel, H.; Fuke, N.; Pietryga, J. M.; Klimov, V. I. Engineered CuInSe<sub>x</sub>S<sub>2-x</sub> Quantum Dots for Sensitized Solar Cells. *J. Phys. Chem. Lett.* 2013, 4, 355-361.

12. Chuang, P-H.; Lin, C. C.; Liu, R-S. Emission-Tunable CuInS<sub>2</sub>/ZnS Quantum Dots: Structure, Optical Properties, and Application in White Light-Emitting Diodes with High Color Rendering Index. *ACS Appl. Mater. Interfaces* 2014, 6, 15379-15387.
13. Kim, N.; Na, W.; Yin, W.; Jin, H.; Ahn, T. K.; Cho, S. M.; Chae, H. CuInS<sub>2</sub>/ZnS Quantum Dot-Embedded Polymer Nanofibers for Color Conversion Films. *J. Mater. Chem. C* 2016, 4, 2457-2462.
14. Kolny-Olesiak, J.; Weller, H. Synthesis and Application of Colloidal CuInS<sub>2</sub> Semiconductor Nanocrystals. *ACS Appl. Mater. Interfaces* 2013, 5, 12221-12237.
15. Li, L.; Pandey, A.; Werder, D. J.; Khanal, B. P.; Pietryga, J. M.; Klimov, V. I. Efficient Synthesis of Highly Luminescent Copper Indium Sulfide-Based Core/Shell Nanocrystals with Surprisingly Long-Lived Emission. *J. Am. Chem. Soc.* 2011, 13, 1176-1179.
16. Meinardi, F.; McDaniel, H.; Carulli, F.; Colombo, A.; Velizhanin, K. A.; Makarov, N. S.; Simonutti, R.; Klimov, V. I.; Brovelli, S. Highly Efficient Large-Area Colourless Luminescent Solar Concentrators using Heavy-Metal-Free Colloidal Quantum Dots. *Nat. Nano.* 2015, 10, 878-885.
17. Du, J.; Du, Z.; Hu, J-S.; Pan, Z.; Shen, Q.; Sun, J.; Long, D.; Dong, H.; Sun, L.; Zhong, X.; Wan, L-J. Zn–Cu–In–Se Quantum Dot Solar Cells with a Certified Power Conversion Efficiency of 11.6%. *J. Am. Chem. Soc.* 2016, 138, 4201-4209.
18. Shabaev, A.; Mehl, M. J.; Efros, A. L. Energy Band Structure of CuInS<sub>2</sub> and Optical Spectra of CuInS<sub>2</sub> Nanocrystals. *Phys. Rev. B* 2015, 92, 035431.

19. Knowles, K. E.; Nelson, H. D.; Kilburn, T. B.; Gamelin, D. R. Singlet–Triplet Splittings in the Luminescent Excited States of Colloidal Cu<sup>+</sup>:CdSe, Cu<sup>+</sup>:InP, and CuInS<sub>2</sub> Nanocrystals: Charge-Transfer Configurations and Self-Trapped Excitons. *J. Am. Chem. Soc.* 2015, 137, 13138-13147.
20. Rice, W. D.; McDaniel, H.; Klimov, V. I.; Crooker, S. A. Magneto-Optical Properties of CuInS<sub>2</sub> Nanocrystals. *J. Phys. Chem. Lett.* 2014, 5, 4105-4109.
21. Santra, P. K.; Nair, P. V.; George Thomas, K.; Kamat, P. V., CuInS<sub>2</sub>-Sensitized Quantum Dot Solar Cell. Electrophoretic Deposition, Excited-State Dynamics, and Photovoltaic Performance. *J. Phys. Chem. Lett.* 2013, 4, 722-729.
22. Leach, A. D. P.; Shen, X.; Faust, A.; Cleveland, M. C.; La Croix, A. D.; Banin, U.; Pantelides, S. T.; Macdonald, J. E. Defect Luminescence from Wurtzite CuInS<sub>2</sub> Nanocrystals: Combined Experimental and Theoretical Analysis. *J. Phys. Chem. C.* 2016, 120, 5207-5212.
23. Debnath, T.; Maiti, S.; Maity, P.; Ghosh, H. N. Subpicosecond Exciton Dynamics and Biexcitonic Feature in Colloidal CuInS<sub>2</sub> Nanocrystals: Role of In–Cu Antisite Defects. *J. Phys. Chem. Lett.* 2015, 6, 3458-3465.
24. Berends, A. C.; Rabouw, F. T.; Spoor, F. C. M.; Bladt, E.; Grozema, F. C.; Houtepen, A. J.; Siebbeles, L. D. A.; de Mello Donegá, C. Radiative and Nonradiative Recombination in CuInS<sub>2</sub> Nanocrystals and CuInS<sub>2</sub>-Based Core/Shell Nanocrystals. *J. Phys. Chem. Lett.* 2016, 7, 3503-3509.

25. Kraatz, I. T.; Booth, M.; Whitaker, B. J.; Nix, M. G. D.; Critchley, K. Sub-Bandgap Emission and Intraband Defect-Related Excited-State Dynamics in Colloidal CuInS<sub>2</sub>/ZnS Quantum Dots Revealed by Femtosecond Pump–Dump–Probe Spectroscopy. *J. Phys. Chem. C* 2014, 118, 24102-24109.
26. Zang, H.; Li, H.; Makarov, N. S.; Velizhanin, K. A.; Wu, K.; Park, Y-S.; Klimov, V. I. Thick-Shell CuInS<sub>2</sub>/ZnS Quantum Dots with Suppressed “Blinking” and Narrow Single-Particle Emission Line Widths. *Nano Lett.* 2017, 17, 1787-1795.
27. Brovelli, S.; Galland, C.; Viswanatha, R.; Klimov, V. I. Tuning Radiative Recombination in Cu-Doped Nanocrystals via Electrochemical Control of Surface Trapping. *Nano Lett.* 2012, 12, 4372-4379.
28. Binsma, J. J. M.; Giling, L. J.; Bloem, J. Luminescence of CuInS<sub>2</sub>. *J. Lumin.* 1982, 27, 35-53
29. Wakita, K.; Fujita, F.; Yamamoto, N. Photoluminescence Excitation Spectra of CuInS<sub>2</sub> Crystals. *J. Appl. Phys.* 2001, 90, 1292-1296.
30. Tell, B.; Shay, J. L.; Kasper, H. M. Electrical Properties, Optical Properties, and Band Structure of CuGaS<sub>2</sub> and CuInS<sub>2</sub>. *Phys. Rev. B* 1971, 4, 2463-2471.
31. Yoshino, K.; Ikari, T.; Shirakata, S.; Miyake, H.; Hiramatsu, K. Sharp Band Edge Photoluminescence of High-Purity CuInS<sub>2</sub> Single Crystals. *Appl. Phys. Lett.* 2001, 78, 742-744.
32. Hofhuis, J.; Schoonman, J.; Goossens, A. Elucidation of the Excited-State Dynamics in CuInS<sub>2</sub> Thin Films. *J. Phys. Chem. C* 2008, 112, 15052-15059.

33. Makarov, N. S.; McDaniel, H.; Fuke, N.; Robel, I.; Klimov, V. I. Photocharging Artifacts in Measurements of Electron Transfer in Quantum-Dot-Sensitized Mesoporous Titania Films. *J. Phys. Chem. Lett.* 2014, 5, 111-118.
34. Viswanatha, R.; Brovelli, S.; Pandey, A.; Crooker, S. A.; Klimov, V. I. Copper-Doped Inverted Core/Shell Nanocrystals with “Permanent” Optically Active Holes. *Nano Lett.* 2011, 11, 4753-4758.
35. Boehme, S. C.; Wang, H.; Siebbeles, L. D. A.; Vanmaekelbergh, D.; Houtepen, A. J. Electrochemical Charging of CdSe Quantum Dot Films: Dependence on Void Size and Counterion Proximity. *ACS Nano* 2013, 7, 2500-2508.
36. Johnson, B.; Korte, L.; Lußky, T.; Klaer, J.; Lauermann, I. CuInS<sub>2</sub>-CdS Heterojunction Valence Band Offset Measured with Near-UV Constant Final State Yield Spectroscopy. *J. Appl. Phys.* 2009, 106, 073712.
37. Bard, A., Faulkner, L. *Electrochemical Methods: Fundamentals and Applications*. 2 ed.; John Wiley & Sons: 2000.
38. Sanz, L.; Palma, J.; García-Quismondo, E.; Anderson, M. The Effect of Chloride Ion Complexation on Reversibility and Redox Potential of the Cu(II)/Cu(I) Couple for use in Redox Flow Batteries. *J. Power Sources* 2013, 224, 278-284.
39. Hoffeditz, W. L.; Katz, M. J.; Deria, P.; Cutsail Iii, G. E.; Pellin, M. J.; Farha, O. K.; Hupp, J. T. One Electron Changes Everything. A Multispecies Copper Redox Shuttle for Dye-Sensitized Solar Cells. *J. Phys. Chem. C* 2016, 120, 3731-3740.

40. Akkerman, Q. A.; Genovese, A.; George, C.; Prato, M.; Moreels, I.; Casu, A.; Marras, S.; Curcio, A.; Scarpellini, A.; Pellegrino, T.; Manna, L.; Lesnyak, V. From Binary  $\text{Cu}_2\text{S}$  to Ternary  $\text{Cu-In-S}$  and Quaternary  $\text{Cu-In-Zn-S}$  Nanocrystals with Tunable Composition via Partial Cation Exchange. *ACS Nano* 2015, 9, 521-531.
41. Lefrançois, A.; Pouget, S.; Vaure, L.; Lopez-Haro, M.; Reiss, P. Direct Synthesis of Highly Conductive tert-Butylthiol-Capped  $\text{CuInS}_2$  Nanocrystals. *ChemPhysChem* 2016, 17, 654-659.
42. Vinokurov, K.; Elimelech, O.; Millo, O.; Banin, U. Copper Sulfide Nanocrystal Level Structure and Electrochemical Functionality towards Sensing Applications. *ChemPhysChem* 2016, 17, 675-680.
43. Sandroni, M.; Wegner, K. D.; Aldakov, D.; Reiss, P. Prospects of Chalcopyrite-Type Nanocrystals for Energy Applications. *ACS Energy Lett.* 2017, 1076-1088.
44. Aldana, J.; Wang, Y. A.; Peng, X. Photochemical Instability of CdSe Nanocrystals Coated by Hydrophilic Thiols. *J. Am. Chem. Soc.* 2001, 123, 8844-8850.
45. Knauf, R. R.; Lennox, J. C.; Dempsey, J. L. Quantifying Ligand Exchange Reactions at CdSe Nanocrystal Surfaces. *Chem. Mater.* 2016, 28, 4762-4770.
46. Boehme, S. C.; Vanmaekelbergh, D.; Evers, W. H.; Siebbeles, L. D. A.; Houtepen, A. J. In Situ Spectroelectrochemical Determination of Energy Levels and Energy Level Offsets in Quantum-Dot Heterojunctions. *J. Phys. Chem. C* 2016, 120, 5164-5173.

47. Boehme, S. C.; Azpiroz, J. M.; Aulin, Y. V.; Grozema, F. C.; Vanmaekelbergh, D.; Siebbeles, L. D. A.; Infante, I.; Houtepen, A. J. Density of Trap States and Auger-Mediated Electron Trapping in CdTe Quantum-Dot Solids. *Nano Lett.* 2015, 15, 3056-3066.
48. Bard, A. J.; Bocarsly, A. B.; Fan, F. R. F.; Walton, E. G.; Wrighton, M. S. The Concept of Fermi Level Pinning at Semiconductor/Liquid Junctions. Consequences for Energy Conversion Efficiency and Selection of Useful Solution Redox Couples in Solar Devices. *J. Am. Chem. Soc.* 1980, 102, 3671-3677.
49. Bloom, B. P.; Mendis, M. N.; Wierzbinski, E.; Waldeck, D. H. Eliminating Fermi-Level Pinning in PbS Quantum Dots using an Alumina Interfacial Layer. *J. Mater. Chem. C* 2016, 4, 704-712.
50. Hyun, B-R.; Zhong, Y-W.; Bartnik, A. C.; Sun, L.; Abruña, H. D.; Wise, F. W.; Goodreau, J. D.; Matthews, J. R.; Leslie, T. M.; Borrelli, N. F. Electron Injection from Colloidal PbS Quantum Dots into Titanium Dioxide Nanoparticles. *ACS Nano* 2008, 2, 2206-2212.
51. Pandey, A.; Brovelli, S.; Viswanatha, R.; Li, L.; Pietryga, J. M.; Klimov, V. I.; Crooker, S. A. Long-Lived Photoinduced Magnetization in Copper-Doped ZnSe-CdSe Core-Shell Nanocrystals. *Nat. Nano.* 2012, 7, 792-797.
52. Guillemoles, J-F.; Kronik, L.; Cahen, D.; Rau, U.; Jasenek, A.; Schock, H-W. Stability Issues of Cu(In,Ga)Se<sub>2</sub>-Based Solar Cells. *J. Phys. Chem. B* 2000, 104, 4849-4862.

53. Yu, H.-J.; Lee, W.-J.; Wi, J.-H.; Cho, D.-H.; Han, W. S.; Chung, Y.-D.; Kim, T.-S.; Song, J.-H. Light-Soaking Effects and Capacitance Profiling in Cu(In,Ga)Se<sub>2</sub> Thin-Film Solar Cells with Chemical-Bath-Deposited ZnS Buffer Layers. *Phys. Chem. Chem. Phys.* 2016, 18, 33211-33217.
54. Neuschitzer, M.; Sanchez, Y.; López-Marino, S.; Xie, H.; Fairbrother, A.; Placidi, M.; Haass, S.; Izquierdo-Roca, V.; Perez-Rodriguez, A.; Saucedo, E. Optimization of CdS buffer Layer for High-Performance Cu<sub>2</sub>ZnSnSe<sub>4</sub> Solar Cells and the Effects of Light Soaking: Elimination of Crossover and Red Kink. *Prog. Photovolt: Res. Appl.* 2015, 23, 1660-1667.
55. Padilha, L. A.; Robel, I.; Lee, D. C.; Nagpal, P.; Pietryga, J. M.; Klimov, V. I. Spectral Dependence of Nanocrystal Photoionization Probability: The Role of Hot-Carrier Transfer. *ACS Nano* 2011, 5, 5045-5055.
56. Peterson, J. J.; Krauss, T. D. Photobrightening and Photodarkening in PbS Quantum Dots. *Phys. Chem. Chem. Phys.* 2006, 8, 3851-3856.
57. McGuire, J. A.; Sykora, M.; Robel, I.; Padilha, L. A.; Joo, J.; Pietryga, J. M.; Klimov, V. I. Spectroscopic Signatures of Photocharging due to Hot-Carrier Transfer in Solutions of Semiconductor Nanocrystals under Low-Intensity Ultraviolet Excitation. *ACS Nano* 2010, 4, 6087-6097.
58. Li, H.; Wu, Z.; Lusk, M. T. Dangling Bond Defects: The Critical Roadblock to Efficient Photoconversion in Hybrid Quantum Dot Solar Cells. *J. Phys. Chem. C* 2014, 118, 46-53.

59. Wang, R.; Shang, Y.; Kanjanaboos, P.; Zhou, W.; Ning, Z.; Sargent, E. H. Colloidal Quantum Dot Ligand Engineering for High Performance Solar Cells. *Energy Environ. Sci.* 2016, 9, 1130-1143.
60. Galland, C.; Ghosh, Y.; Steinbruck, A.; Sykora, M.; Hollingsworth, J. A.; Klimov, V. I.; Htoon, H. Two Types of Luminescence Blinking Revealed by Spectroelectrochemistry of Single Quantum Dots. *Nature* 2011, 479, 203-207.
61. Ueng, H. Y.; Hwang, H. L., The Defect Structure of  $\text{CuInS}_2$ . Part I: Intrinsic Defects. *J. Phys. Chem. Solids* 1989, 50, 1297-1305.
62. Zhang, S. B.; Wei, S-H.; Zunger, A.; Katayama-Yoshida, H. Defect Physics of the  $\text{CuInSe}_2$  Chalcopyrite Semiconductor. *Phys. Rev. B* 1998, 57, 9642-9656.
63. Oikkonen, L. E.; Ganchenkova, M. G.; Seitsonen, A. P.; Nieminen, R. M. Mass Transport in  $\text{CuInSe}_2$  from First Principles. *J. Appl. Phys.* 2013, 113, 133510.
64. Jara, D. H.; Stampelcoskie, K. G.; Kamat, P. V. Two Distinct Transitions in  $\text{Cu}_x\text{InS}_2$  Quantum Dots. Bandgap versus Sub-Bandgap Excitations in Copper-Deficient Structures. *Phys. Chem. Lett.* 2016, 7, 1452-1459.
65. Kim, Y-K.; Ahn, S-H.; Chung, K.; Cho, Y-S.; Choi, C-J. The Photoluminescence of  $\text{CuInS}_2$  Nanocrystals: Effect of Non-Stoichiometry and Surface Modification. *J. Mater. Chem.* 2012, 22, 1516-1520.
66. Hua, J.; Cheng, H.; Yuan, X.; Zhang, Y.; Liu, M.; Meng, X.; Li, H.; Zhao, J. Photoluminescence Quenching and Electron Transfer in  $\text{CuInS}_2/\text{ZnS}$  Core/Shell Quantum Dot and FePt Nanoparticle Blend Films. *RSC Adv.* 2015, 5, 30981-30988.

67. Chen, B.; Zhong, H.; Zhang, W.; Tan, Z.; Li, Y.; Yu, C.; Zhai, T.; Bando, Y.; Yang, S.; Zou, B. Highly Emissive and Color-Tunable CuInS<sub>2</sub>-Based Colloidal Semiconductor Nanocrystals: Off-Stoichiometry Effects and Improved Electroluminescence Performance. *Adv. Func. Mater.* 2012, 22, 2081-2088.

## 2.2. Defect-Controllable Magneto-Optical Properties in $\text{Cu}_x\text{In}_{2-x}\text{S}_y$ Quantum Dots

### 2.2.1. Introduction & Low-Temperature Spectra

Considerable attention has been given to implementing low-cost, solution processable electronic and electro-optical devices using II-VI quantum dots (QDs).<sup>1-5</sup> However, devices utilizing these QD structures as active layers have limited commercial viability due to their toxic, heavy metal cations (e.g. Cd). Ternary I-III-VI QDs such as  $\text{Cu}_x\text{In}_{2-x}\text{E}_y$  (where E=S or Se), which replace heavy metal 2+ (II) cations with lighter 1+ (I) and 3+ (III) cations have been proposed as environmentally friendly alternatives to CdE QDs.<sup>6-15</sup> However, their (electro)-optical properties vastly differ from typical II-VI materials. For example, the Stokes shift ( $\Delta_S$ ) is far larger (~300-750 meV), spectral linewidths significantly broader (~300-400 meV), and they have considerably longer radiative lifetimes (~200-400 ns) than CdSe QDs.<sup>16-26</sup> This is generally attributed to the radiative relaxation of a delocalized conduction band (CB) electron and a hole localized at  $\text{Cu}^x$  (where  $x=1+$  or  $2+$ ) defects (**Figure 2.2.1.1a**, top panel).<sup>7-9,20-27</sup> Nonetheless, there is still significant debate as to whether this process is due to strong electron-phonon coupling of lattice  $\text{Cu}^{1+}$  cations,<sup>26</sup> or “native defects” based on  $\text{Cu}^{1+}$  or  $\text{Cu}^{2+}$  cations.<sup>20,23</sup> In the latter case, it has been proposed that photoluminescence (PL) in (near)-stoichiometric QDs is dominated by  $\text{Cu}^{1+}$  defects ( $[\text{Ar}]3d^{10}$ ), and require capture of a VB hole or direct excitation to form  $\text{Cu}^{2+}$ -like states prior to emission (**Figure 2.2.1.1a**, bottom left panel).  $\text{Cu}^{2+}$  defects ( $[\text{Ar}]3d^9$ ), on the other hand, prevail in far-off stoichiometry, Cu-deficient QDs and are “emission ready.” Specifically, they have a pre-existing hole in the  $\text{Cu}^x$  defect state that can directly recombine with a CB electron (**Figure 2.2.1.1a**, bottom right panel).<sup>20</sup>

An interesting prediction that arises from the defect hypothesis would be multifunctional, stoichiometry-controllable optical and magneto-optical properties in *single*-component QDs, which typically can only be achieved in nanocomposite, or extrinsically doped QDs. Specifically, the net spin for  $\text{Cu}^{2+}$  defects, which primarily form in Cu-deficient CIS QDs should be equivalent to the paramagnetic lower  $\Gamma_7$  doublet of  $\text{Cu}^{2+}$  dopants in II-VI QDs.<sup>28</sup> This would lead to dual dilute magnetic semiconductor (DMS) and emissive behavior in a single, un-doped QD, which can be further enhanced by decreasing the Cu:In ratio. In addition, considering that these defects are unoccupied they should also be non-absorptive, and therefore CIS QDs with  $\text{Cu}^{2+}$  defects should exhibit sharper absorption spectra than (near)-stoichiometric QDs where occupied  $\text{Cu}^{1+}$  defects lead to a pronounced low energy “tail” in the absorption spectra and “smear” the band-edge transition. Here, we verify these predictions with low-temperature linear spectroscopy and magnetic circular dichroism (MCD) measurements of CIS QDs with different Cu:In ratios. We clearly observe stronger spin-exchange interactions, and reduced intra-gap absorption in Cu-deficient QDs, which are expected to manifest from the replacement of  $\text{Cu}^{1+}$  defects with  $\text{Cu}^{2+}$  defects as QDs are made increasingly Cu-deficient. Further, we use density functional theory (DFT) calculations to explain the chemical origin of these mechanisms. For (near)-stoichiometric QDs,  $\text{Cu}^{1+}$  and  $\text{In}^{3+}$  atoms switch lattice positions ( $\text{Cu}_{\text{In}}'' + \text{In}_{\text{Cu}}''$ ) and lead to “ $\text{Cu}^{1+}$  defects.” Cu-deficient QDs, on the other hand, have a large concentration of copper vacancies ( $V_{\text{Cu}}'$ ), which are charge-compensated by the oxidation of a second Cu atom ( $\text{Cu}^{1+} \rightarrow \text{Cu}^{2+} + e^-$ ) leading to  $V_{\text{Cu}}' + \text{Cu}_{\text{Cu}}\cdot$  defect pairs.

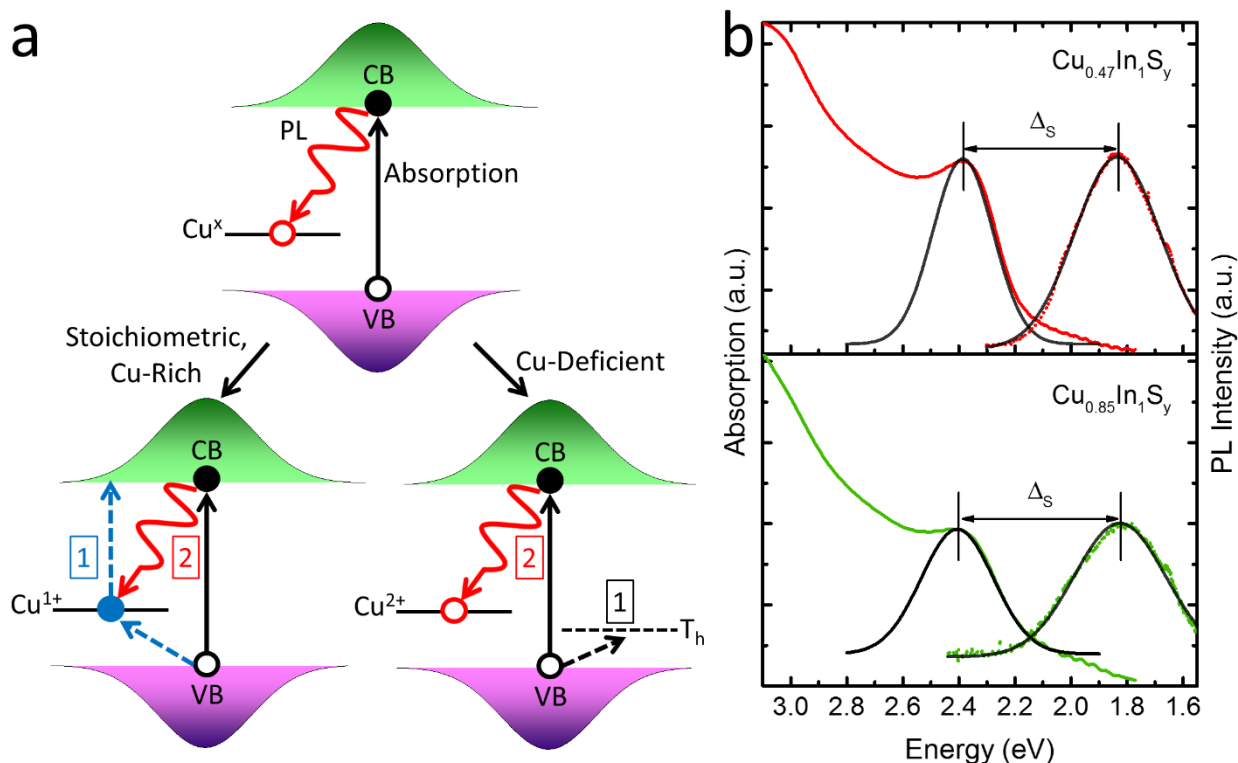


**Figure 2.2.1.1.** (a) Absorption/emission mechanism for CIS QDs (top panel). For Cu-rich, stoichiometric, or near-stoichiometric QDs (bottom left panel) there is an additional absorption band from  $\text{Cu}^{1+}$  defects (dashed blue line), which require “photoactivation” prior to  $\text{Cu}^x$  emission. For far-off stoichiometry, Cu-deficient QDs (right bottom panel) Cu defects are predominantly in the 2+ oxidation state and are therefore “emission ready.” Hence, the band-edge hole is trapped (dashed black lines) at a separate state labeled  $T_h$ . (b) Low-temperature (15 K) absorption (solid colored lines) and emission (dotted colored lines) spectra for CIS QDs with two different Cu:In ratios. Solid black lines represent Gaussian fits.

Pyramidal ( $\sim 2.25$  nm by height as shown in Figure S6.2.1) CIS QDs with varied Cu-to-In ratios (0.85:1 and 0.47:1) were synthesized and spin-coated onto glass substrates. We compare their low-temperature (15 K) absorption and PL emission spectra in **Figure 2.2.1.1b**. The Stokes shift ( $\Delta_S$ ) between the band-edge absorption and PL emission peaks is large for both samples (554 meV for  $\text{Cu}_{0.47}\text{In}_1\text{S}_y$  and 578 meV for  $\text{Cu}_{0.85}\text{In}_1\text{S}_y$ , respectively). Both absorption and PL emission spectra are fitted with a Gaussian function (solid black lines). Despite similar PL linewidths (371 meV for  $\text{Cu}_{0.47}\text{In}_1\text{S}_y$  and 379 meV for  $\text{Cu}_{0.85}\text{In}_1\text{S}_y$ , respectively), the absorption spectrum is

significantly narrower for  $\text{Cu}_{0.47}\text{In}_1\text{S}_y$  (253 meV) than  $\text{Cu}_{0.85}\text{In}_1\text{S}_y$  (304 meV). This is expected based on our earlier stated prediction that both  $\text{Cu}^{1+}$  and  $\text{Cu}^{2+}$  defects are emissive. Yet, only  $\text{Cu}^{1+}$  can directly absorb a photon due to its filled electron configuration ( $[\text{Ar}]3d^{10}$  vs.  $[\text{Ar}]3d^9$ ). Hence, the PL linewidths are not expected to be strongly affected by the relative concentration of  $\text{Cu}^{1+}/\text{Cu}^{2+}$  defects, while the absorption spectrum should be much narrower if there is a larger concentration of  $\text{Cu}^{2+}$  defects.

### 2.2.2. Magneto-Optical Spectroscopy & Density Functional Theory

**Magneto-Optical Spectroscopy.** Considering that the unpaired electron expected from the  $d^9$  electron configuration should have a net spin, we therefore use MCD spectroscopy (**Figure 2.2.1.2a** for  $\text{Cu}_{0.47}\text{In}_1\text{S}_y$ , and **Figure S6.2.2**  $\text{Cu}_{0.85}\text{In}_1\text{S}_y$ )<sup>22,28-29</sup> to measure the field-induced (top panel) and temperature-dependent (bottom panel) Zeeman splitting energies ( $\Delta E_Z$ ) for band-edge carriers. For both samples, ( $\Delta E_Z$ ) increases nonlinearly with magnetic field (0 to 6 T) at constant (3 K) temperature (**Figure 2.2.1.2b**), and markedly decreases as the temperature is raised (3 K to 20 K) at a constant (6 T) magnetic field (**Figure 2.2.1.2c**). These characteristics are hallmarks for dilute magnetic semiconductors (DMS) where the average spin alignment of magnetic defects improves at high magnetic fields and low temperatures.

Unlike other QDs with DMS characteristics, magnetism in CIS arises from “native” defects instead of extrinsic dopants.<sup>22, 26, 28-29</sup> However, we expect the nature of spin-exchange to be similar, and fit the data in **Figure 2.2.1.2b** using  $J=1/2$  for  $\text{Cu}^{2+}$  defects in equation 1:

$$\Delta E_Z = g_{ex}\mu_B H + \Delta E_{spd}\langle S_Z \rangle \quad (1)$$

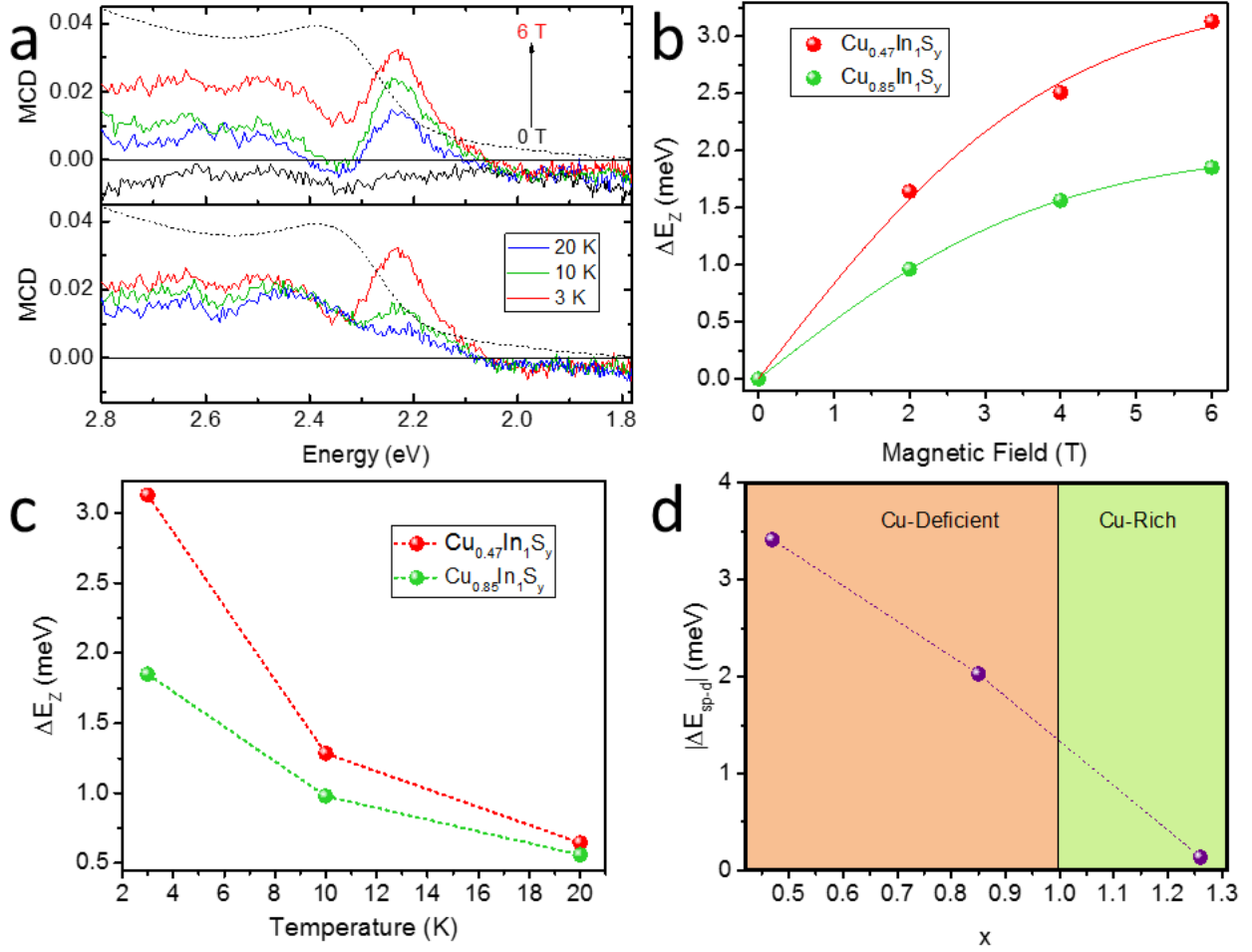


**Figure 2.2.1.2.** (a) Magnetic field- ( $T = 3\text{ K}$ , top panel) and temperature-dependent ( $H = 6\text{ T}$ , bottom panel) MCD measurements for  $\text{Cu}_{0.47}\text{In}_1\text{S}_y$ . The linear absorption spectra ( $3\text{ K}$ , dashed black lines) is also shown. (b,c) The H- (b) and T-dependent (c) Zeeman splitting energies ( $\Delta E_Z$ ). Red circles represent  $\text{Cu}_{0.47}\text{In}_1\text{S}_y$  and green circles indicate  $\text{Cu}_{0.85}\text{In}_1\text{S}_y$ . The solid lines in (b) represent fits to the experimental data using equation 1, while the dashed lines in (c) are simply a visual guide for the data. (d) The stoichiometry-dependent  $\Delta E_{spd}$  where “x” refers to the Cu/In ratio.

where  $g_{ex}\mu_B B$  is the term describing linear Zeeman splitting due to the intrinsic diamagnetism of the CIS exciton, while the second term describes additional Zeeman splitting of the band-edges arising from spin-exchange with  $\text{Cu}^{2+}$  defects. We define  $g_{ex}$  as the exciton g-factor,  $\mu_B$  represents the Bohr magneton, and  $H$  the applied magnetic field.<sup>22,28-29</sup> For the second term,  $\Delta E_{spd}$  describes the strength of spin-exchange interactions between the d electrons of the magnetic impurity and the p or s orbitals of the

host semiconductor along the average spin projection  $\langle S_Z \rangle$  of the magnetic field. This usage is not strictly correct for CIS QDs in which the band-edge density of states (DOS) have a large d component due to lattice Cu atoms. However, the standard Brillouin function ( $\langle S_Z \rangle = B_J(g_{Cu}\mu_B JH/k_B T)$ ) for describing paramagnetic ions with spin J at magnetic field H and temperature T still yields remarkably good fits (**Figure 2.2.1.2b** solid lines) to the experimental data using  $g_{ex} = 0.2$  (typical for CIS QDs),<sup>22</sup>  $g_{Cu} = 1.14$  for  $Cu_{0.85}In_1Sy$ , and  $g_{Cu} = 1.11$  for  $Cu_{0.47}In_1Sy$ . Notably,  $g_{Cu}$  in CIS is nearly identical to  $Cu^{2+}$  doped ZnSe ( $g_{Cu} = 1.10$ ), and relatively small as expected for  $d^9$  cations where Jahn-Teller effects suppress magnetic exchange interactions.<sup>28,30-35</sup> Indeed, this offers further support that the paramagnetic impurities are  $Cu^{2+}$  defects.

The only fit parameter that significantly changes is the maximum energy for spin-exchange ( $\Delta E_{spd}$ ). We compare  $\Delta E_{spd}$  values for both of our Cu-deficient QDs with Cu-rich QDs (Cu:In  $\sim 1.26$ ) measured previously (**Figure 2.2.1.2d**).<sup>22</sup> The spin-exchange energy increases as QDs become more Cu-deficient, and  $\Delta E_{spd}$  for Cu-deficient QDs is more than an order of magnitude higher than Cu-rich QDs ( $\Delta E_{spd,Cu_{0.47}In_1Sy} = 3.42 \text{ meV}$ ,  $\Delta E_{spd,Cu_{0.85}In_{1.08}Sy} = 2.02 \text{ meV}$ , and  $\Delta E_{spd,Cu_{1.26}In_1Sy} = 135 \text{ } \mu\text{eV}$ , respectively). These trends are generally quantified using equation 2:

$$\Delta E_{spd} = J[Cu^{2+}]N_0(\alpha - \beta) \quad (2)$$

where J is the spin of the  $Cu^{2+}$  defect,  $[Cu^{2+}]$  is the concentration of  $Cu^{2+}$  defects, and  $N_0(\alpha - \beta)$  is the combined exchange constant for s-d and p-d interactions. However, separating each contribution to  $\Delta E_{spd}$  for CIS is nontrivial due to the large concentration of non-magnetic lattice copper atoms and corresponding d character of the band-edges.

Specifically, while X-ray photoelectron spectroscopy (XPS) can determine the concentration of  $\text{Cu}^{2+}$  by satellite peaks in copper oxides, density functional theory (DFT) and X-Ray absorption spectroscopy (XAS) studies have shown that Cu chalcogens do not precisely obey the  $d^9$  and  $d^{10}$  formalism due to covalent bonding.<sup>36-37,38,39</sup> These limitations aside,  $\Delta E_{spd}$  should still be directly proportional to  $[\text{Cu}^{2+}]$ , and we can infer from these measurements that the increase in  $\Delta E_{spd}$  in more Cu-deficient QDs is due to a larger concentration of  $\text{Cu}^{2+}$  defects.

**Density Functional Theory Calculations.** We next perform DFT calculations to determine the structural origin of the stoichiometry-controllable paramagnetic behavior in CIS QDs. Defect formation energies were determined using various charge balanced defect pairs in a  $2 \times 2 \times 2$  (128 atom) supercell to negate the influence of surfaces (**Figure 2.2.1.3**). This is justified by experimental studies, which showed that passivating the surfaces of CIS QDs with a ZnS shell improves quantum yields without significantly altering the emission energy or linewidth.<sup>20-21</sup> This suggests that optical defects are not due to dangling bond surface states. The charge-balanced, stoichiometric defect pairs we considered include anti-site defects in which the Cu and In atoms swap lattice positions ( $\text{Cu}_{\text{In}}'' + \text{In}_{\text{Cu}}''$ ), Frenkel pairs where a copper or indium vacancy is created in conjunction with its corresponding interstitial ( $\text{V}_{\text{Cu}}' + \text{Cu}_i'$  and  $\text{V}_{\text{In}}''' + \text{In}_i'''$ ). To predict the properties of Cu-deficient QDs, we calculated the formation energy of a single copper vacancy ( $\text{V}_{\text{Cu}}'$ ). This introduces an electronic hole in the later described QD calculations, which localizes on a Cu atom, and forms a  $\text{Cu}^{2+}$  ( $\text{Cu}_{\text{Cu}}'$ ) center for charge-compensation ( $\text{V}_{\text{Cu}}' + \text{Cu}_{\text{Cu}}'$ ). ( $\text{Cu}_{\text{In}}'' + \text{In}_{\text{Cu}}''$ ) and ( $\text{V}_{\text{Cu}}' + \text{Cu}_{\text{Cu}}'$ ) have the lowest formation energies of the series. However, the formation energy of these defect pairs are still significantly higher than  $k_B T$

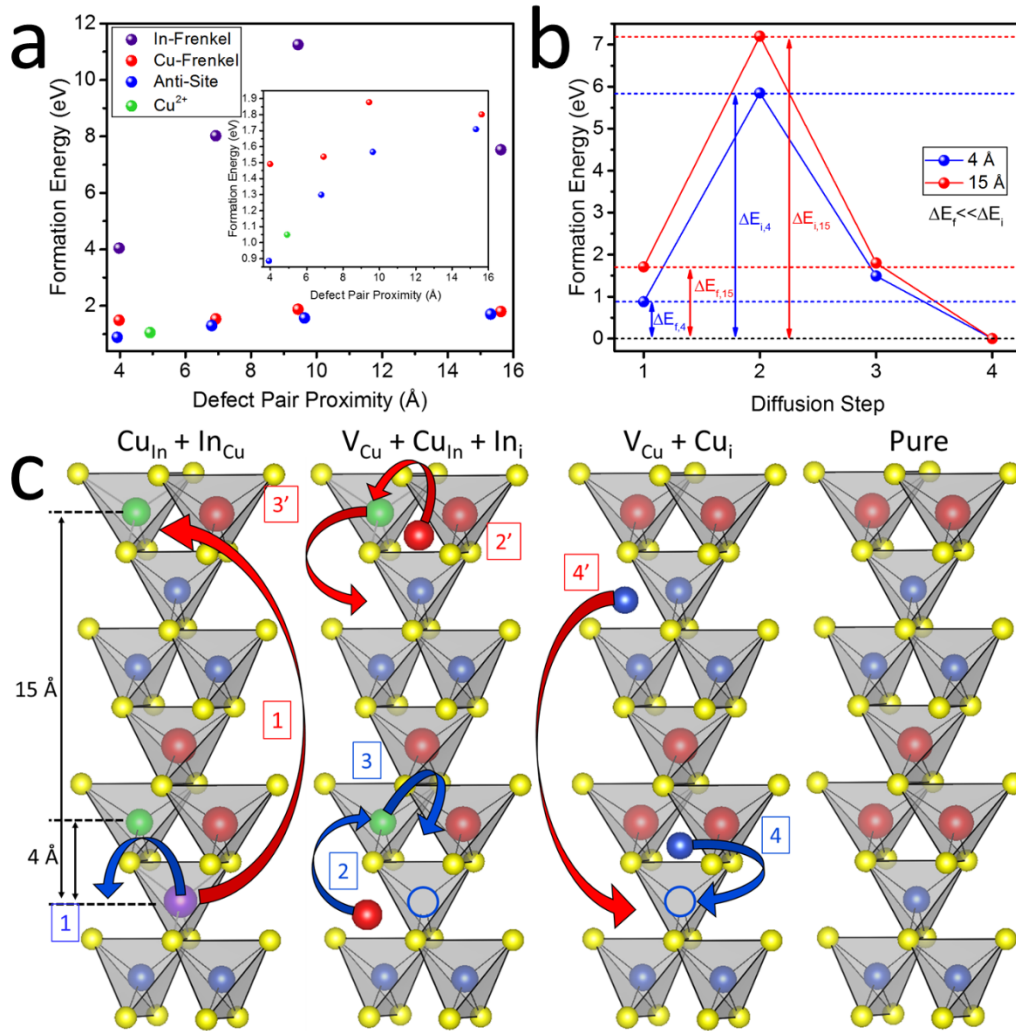


**Figure 2.2.1.3.** (a) Defect formation energy as a function of spatial separation between defects. (b,c) The formation energies of anti-site defects are lower than intermediate defects required for “self-purification.” Hence, defects in CIS are kinetically trapped during synthesis.

(~26 meV). To test their stability, we calculate the formation energy of several intermediate defect structures required for “back-diffusion” into the original lattice sites (**Figure 2.2.1.3b** for energies, and **Figure 2.2.1.3c** for corresponding structures). Considering that the intermediate states have higher formation energy than either ( $\text{V}_{\text{Cu}}' + \text{Cu}_{\text{Cu}}'$ ) or ( $\text{Cu}_{\text{In}}'' + \text{In}_{\text{Cu}}''$ ), we conclude that defects are kinetically trapped during synthesis, and “self-purification” does not occur.

Considering that ( $\text{Cu}_{\text{In}}'' + \text{In}_{\text{Cu}}''$ ) and ( $\text{V}_{\text{Cu}}' + \text{Cu}_{\text{Cu}}'$ ) have the lowest formation energies, we calculate their density of states (DOS) in  $\sim 1.7$  nm pyramidal QDs constructed by exposing the (112) surface facets (**Figure 2.2.1.4**). The DOS for anti-site defects separated by 7 Å and 11 Å are shown in **Figure 2.2.1.4a**. In order to determine the identity of each energy state, we plot iso-energetic contours (purple and green for occupied and unoccupied energy levels, respectively) of the associated charge density (square modulus of the one electron wavefunction) as exemplified by anti-site defects separated by 11 Å in **Figure 2.2.1.4c**. We define the VB (CB) as the highest occupied (lowest unoccupied) delocalized state, and surface intra-gap states ( $S_{\text{St}}$ ) as delocalized across surface atoms. Optically-active defect states ( $\text{Cu}_{\text{In}}''$  or  $\text{Cu}_{\text{Cu}}'$ ), on the other hand, are localized to the intentionally created defect coordination sphere. However, we note here that surface state contributions to the electronic structure are overestimated due to our inability to include passivation layers of native ligands (*e.g.* dodecanethiol), which would significantly increase computational expense. The  $\text{Cu}_{\text{In}}''$  state is occupied (below, or at the Fermi level, or  $E_{\text{F}}$ ), and is therefore not paramagnetic. However, the state is showed as “half-filled” in the DOS due to the artificial 0.05 eV electron smearing used in the Fermi-Dirac portion of the DFT calculations. The  $\text{Cu}_{\text{In}}''$  state is  $\sim 480$  meV ( $\sim 590$  meV) above the VB when the defects are separated by 7 Å (11 Å). We define these values as the “theoretical Stokes shifts” (labeled as  $\Delta_{\text{S}}$  in **Figure 2.2.1.4a**), which are remarkably close to the optical Stokes shift ( $\sim 580$  meV) measured experimentally. In addition, the position of the defect affects its energy vs. the band-edges, which indicates that  $\Delta_{\text{S}}$  is impacted by the local defect bonding environment as expected by single-particle spectroscopy studies on CIS QDs, and DFT studies on related Cu-doped ZnSe QDs.<sup>23,36</sup>

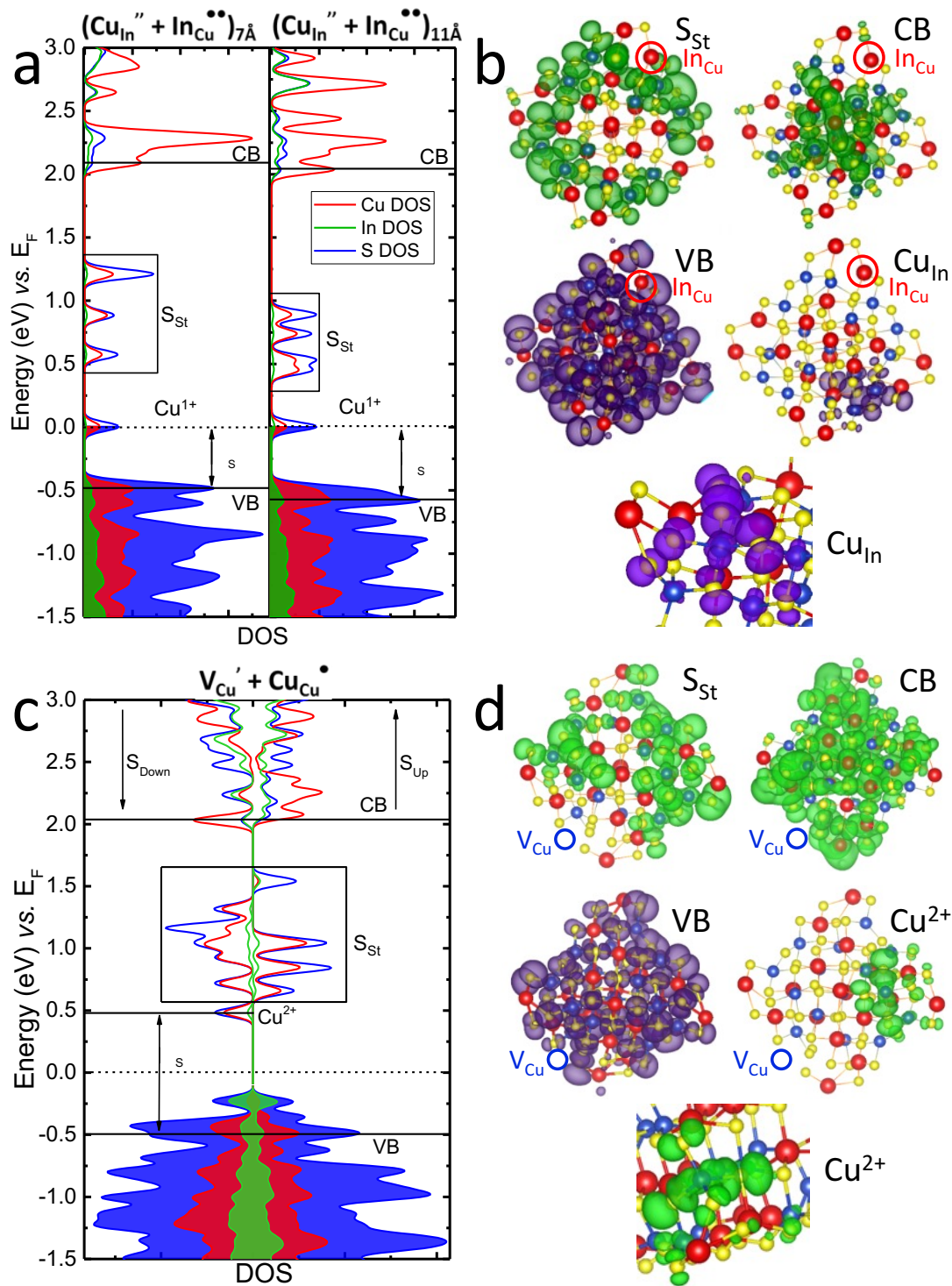


**Figure 2.2.1.4.** (a) DOS for anti-site defects on a model QD with two different defect pair separation distances (7 Å and 11 Å for the left and right panel, respectively). Solid black lines mark the band-edges, dashed black lines the Fermi level, and black squares trap-like surface states (labeled  $S_{\text{St}}$ ). The charge density for each labeled state is depicted in (b) for  $(\text{Cu}_{\text{In}} + \text{In}_{\text{Cu}})_{11\text{\AA}}$  using purple (occupied) and green (unoccupied) iso-surfaces. (c,d) The same analysis is used for

QDs with a single copper vacancy. For (c), calculations were spin-polarized due to the paramagnetism of  $\text{Cu}^{2+}$ ; and the two columns represent different electron spins. In both (b) and (d), the bottom center panel shows a second, zoomed-in image of the  $\text{Cu}^x$  defect for clarity.

Next, we repeat these calculations on QDs with a single  $V_{\text{Cu}}$ ' (**Figure 2.2.1.4c,d**).

The resulting DOS (**Figure 2.2.1.4c**) has a spin-polarized and unoccupied state above  $E_F$ , which is also close to the experimental Stokes shift ( $\sim 740$  meV). Representing its charge density in real-space (**Figure 2.2.1.4d**) further shows that the state is highly localized around a Cu coordination sphere. This corresponds with a  $\text{Cu}^{2+}$  ( $\text{Cu}_{\text{Cu}}$ ' ) defect in which the removal of an electron and conversion to the  $3d^9$  electron configuration is accompanied by a spin-polarized paramagnetic state. Indeed, 79.5% of the magnetization density is localized to  $\text{Cu}_{\text{Cu}}$ ' ; the additional 21.5% is delocalized across other unoccupied states in the DOS and is also most likely an artifact resulting from our 0.05 eV smearing. These results indicate that copper vacancies can be charge-compensated by the oxidation of a second Cu atom. Hence, enhancement of  $\Delta E_{spd}$  in Cu-deficient QDs can be explained by a larger concentration of subensembles with  $V_{\text{Cu}}$ '. Interestingly, we also note that the charge density of the DFT predicted  $\text{Cu}^{2+}$  defect has a large contribution from p electrons in neighboring S atoms ( $\sim 55\%$ ), and is not completely localized on Cu. This matches expectations from DFT and complementary XAS studies on CuS, which showed that  $\text{Cu}^{2+}$  states in copper chalcogens do not exist in strictly  $d^9$  configurations due to charge sharing with neighboring S atoms.<sup>36-39</sup> Therefore, it is likely that the same chemical bonding effects, which complicate the experimental determination of  $\text{Cu}^{2+}$  in CuS using X-Ray and EPR methods, are also present in CIS QDs.

### 2.2.3. Conclusions

In summary, CIS QDs exhibit stoichiometry-controllable, multifunctional DMS behavior and optical pathways. From our MCD studies, we show that magnetic exchange interactions can be enhanced by over an order of magnitude by making QDs Cu-deficient. This finding is counter-intuitive given that a reduction in Cu concentration results in an increase in magnetic Cu states. DFT calculations explain this peculiarity as a consequence of creating a larger concentration of subensembles with  $V_{Cu}$ , which are charge-compensated by the oxidation of a second Cu atom ( $Cu^{1+} \rightarrow Cu^{2+}$ ). Altogether, this marks the first report of stoichiometry-controllable magnetic behavior *via* “native” defects in QDs, which normally require extrinsic dopants. Moreover, these findings confirm previous hypotheses that predicted stoichiometry-controllable optical pathways in CIS QDs.

#### 2.2.4. Methods

**Chemicals and Materials:** The following chemicals were purchased and used as received. Anhydrous copper (I) iodide ( $CuI$ , 99.995 %), 1-dodecanethiol ( $CH_3(CH_2)_{11}SH$ , DDT,  $\geq 98$  %), anhydrous chloroform ( $CH_2Cl_2$ ,  $\geq 99$  %), and anhydrous methanol ( $CH_3OH$ ,  $\geq 99$  %) were obtained from Sigma-Aldrich. Anhydrous indium (III) acetate ( $In(CH_3COO)_3$ ,  $In(Ac)_3$ , 99.99 %), and oleylamine ( $CH_3(CH_2)_7CH=CH(CH_2)_7CH_2NH_2$ , OLAm, 80~90 %) were purchased from Acros Organics.

**Synthesis of CIS QDs:** Typically, x mmol of  $CuI$  ( $x=1, 0.5,$  and  $0.25$ ) and 1 mmol of  $In(Ac)_3$  were dissolved in 5 mL of DDT and 1 mL of OLAm in a 50 mL round-bottom flask, and the mixture was degassed under vacuum at 100 °C for 30 min. The temperature of the reactant mixture was raised to 140 °C until all solid precursors were fully dissolved,

which usually took less than 10 min. For nucleation and growth, the temperature was set to 230 °C for 20 minutes. The heating element was then removed and the QDs were allowed to cool. The resulting QDs were purified by iterative dissolution in chloroform and precipitation with methanol and then stored in chloroform under an N<sub>2</sub> atmosphere.

**Film Preparation for Temperature-Dependent PL and MCD Measurements:** A QD solution (4 mL in chloroform) was added to a 5 ml solution of 2 % w/w PVP in chloroform. After vigorous stirring, the mixture is transferred to a centrifuge tube, and then the QDs are precipitated by adding hexane. After centrifuging with 5000 rpm for 5 minutes, the supernatant is discarded. The precipitated pellet is dissolved in 600 μL of 1 % w/w butanol/chloroform solution for preparing a QD/polymer solution. The film is made by dropping the QDs/polymer solution on a 5 mm X 5 mm slide glass followed by successive spin coating with 500 rpm for 2 minutes and 2000 rpm for 1 minute.

**Magneto-Optical Measurements:** QD films were mounted in a variable-temperature insert (1.5-300 K) of a 7 T superconducting magnet with direct optical access. Right- and left circularly polarized light was passed through the sample in the Faraday geometry, and the normalized difference in transmission was collected using an avalanche photodiode. A white light probe was derived from a Xe lamp through a spectrometer and mechanically chopped at 137 Hz, and modulated between left- and right polarizations at 50 kHz using a photoelastic modulator.

**DFT Calculations:** All geometries and electronic structures were calculated using plane-wave PAW DFT in VASP.<sup>40-42</sup> PBE<sup>43</sup> was used for all geometry optimizations and HSE06<sup>44</sup> for all electronic structure calculations. An energy cut-off of 280 eV was used in

all calculations, and all structures were relaxed, until forces were smaller than 0.05 eV/Å per atom. A screening parameter of  $\omega=0.13$  was used for HSE06 calculations as described in previous reports.<sup>45,46</sup> For reproducing the properties of bulk CuInS<sub>2</sub>, the Brillouin zone was sampled with a (6X6X3) Monkhorst-Pack k-point grid on a single unit-cell. The formation energy of different defect pairs were calculated using the following equation:

$$E_{form} = E_{tot}(def) - E_{tot}(no\ def) + \sum_{\alpha} n_{\alpha} \mu_{\alpha}$$

where  $E_{tot}(def)$  represents the total energy of the defective supercell,  $E_{tot}(no\ def)$  represents the total energy of the non-defective supercell,  $\mu_{\alpha}$  is the chemical potential of atom  $\alpha$  added or subtracted to the system, and  $n_{\alpha}$  represents the number of atoms added (-1) or subtracted (+1) into the system. Here, the final term is 0 for all cases other than for the single copper vacancy, which is the only defect system studied here that altered the stoichiometry. For these calculations, a 2X2X2 supercell was used and the size of the Monkhorst-Pack grid was decreased to (2X2X1). QDs were constructed based on (112) surface facets as described in the main article. A vacuum spacing of  $\sim 15$  Å was set between QDs to avoid spurious interactions between each nanocrystal, and the Brillouin zone was sampled at the Gamma point only.

### 2.2.5. References

1. Pietryga, J. M.; Park, Y.-S.; Lim, J.; Fidler, A. F.; Bae, W. K.; Brovelli, S.; Klimov, V. I., Spectroscopic and Device Aspects of Nanocrystal Quantum Dots. Chemical Reviews 2016, 116 (18), 10513-10622.

2. Mashford, B. S.; Stevenson, M.; Popovic, Z.; Hamilton, C.; Zhou, Z.; Breen, C.; Steckel, J.; Bulovic, V.; Bawendi, M.; Coe-Sullivan, S.; Kazlas, P. T., High-efficiency quantum-dot light-emitting devices with enhanced charge injection. *Nature Photonics* 2013, 7, 407.
3. Klimov, V. I.; Mikhailovsky, A. A.; Xu, S.; Malko, A.; Hollingsworth, J. A.; Leatherdale, C. A.; Eisler, H.-J.; Bawendi, M. G., Optical Gain and Stimulated Emission in Nanocrystal Quantum Dots. *Science* 2000, 290 (5490), 314-317.
4. Sargent, E. H., Colloidal quantum dot solar cells. *Nature Photonics* 2012, 6, 133.
5. Hetsch, F.; Zhao, N.; Kershaw, S. V.; Rogach, A. L., Quantum dot field effect transistors. *Materials Today* 2013, 16 (9), 312-325.
6. Draguta, S.; McDaniel, H.; Klimov, V. I., Tuning Carrier Mobilities and Polarity of Charge Transport in Films of  $\text{CuInSe}_x\text{S}_{2-x}$  Quantum Dots. *Advanced Materials* 2015, 27 (10), 1701-1705.
7. Meinardi, F.; McDaniel, H.; Carulli, F.; Colombo, A.; Velizhanin, K. A.; Makarov, N. S.; Simonutti, R.; Klimov, V. I.; Brovelli, S., Highly efficient large-area colourless luminescent solar concentrators using heavy-metal-free colloidal quantum dots. *Nat Nano* 2015, 10 (10), 878-885.
8. Yun, H. J.; Lim, J.; Fuhr, A. S.; Makarov, N. S.; Keene, S.; Law, M.; Pietryga, J. M.; Klimov, V. I., Charge-Transport Mechanisms in  $\text{CuInSe}_x\text{S}_{2-x}$  Quantum-Dot Films. *ACS Nano* 2018.

9. Jara, D. H.; Yoon, S. J.; Stampelcoskie, K. G.; Kamat, P. V., Size-Dependent Photovoltaic Performance of CuInS<sub>2</sub> Quantum Dot-Sensitized Solar Cells. *Chemistry of Materials* 2014, 26 (24), 7221-7228.
10. Bergren, M. R.; Makarov, N. S.; Ramasamy, K.; Jackson, A.; Guglielmetti, R.; McDaniel, H., High-Performance CuInS<sub>2</sub> Quantum Dot Laminated Glass Luminescent Solar Concentrators for Windows. *ACS Energy Letters* 2018, 3 (3), 520-525.
11. McDaniel, H.; Fuke, N.; Makarov, N. S.; Pietryga, J. M.; Klimov, V. I., An integrated approach to realizing high-performance liquid-junction quantum dot sensitized solar cells. *Nat Commun* 2013, 4.
12. McDaniel, H.; Fuke, N.; Pietryga, J. M.; Klimov, V. I., Engineered CuInSe<sub>x</sub>S<sub>2-x</sub> Quantum Dots for Sensitized Solar Cells. *The Journal of Physical Chemistry Letters* 2013, 4 (3), 355-361.
13. Kim, J.-Y.; Yang, J.; Yu, J. H.; Baek, W.; Lee, C.-H.; Son, H. J.; Hyeon, T.; Ko, M. J., Highly Efficient Copper–Indium–Selenide Quantum Dot Solar Cells: Suppression of Carrier Recombination by Controlled ZnS Overlayers. *ACS Nano* 2015, 9 (11), 11286-11295.
14. Du, J.; Du, Z.; Hu, J.-S.; Pan, Z.; Shen, Q.; Sun, J.; Long, D.; Dong, H.; Sun, L.; Zhong, X.; Wan, L.-J., Zn–Cu–In–Se Quantum Dot Solar Cells with a Certified Power Conversion Efficiency of 11.6%. *Journal of the American Chemical Society* 2016, 138 (12), 4201-4209.

15. Chuang, P.-H.; Lin, C. C.; Liu, R.-S., Emission-Tunable CuInS<sub>2</sub>/ZnS Quantum Dots: Structure, Optical Properties, and Application in White Light-Emitting Diodes with High Color Rendering Index. *ACS Appl. Mater. Interfaces* 2014, 6 (17), 15379-15387.
16. Castro, S. L.; Bailey, S. G.; Raffaele, R. P.; Banger, K. K.; Hepp, A. F., Synthesis and Characterization of Colloidal CuInS<sub>2</sub> Nanoparticles from a Molecular Single-Source Precursor. *The Journal of Physical Chemistry B* 2004, 108 (33), 12429-12435.
17. Allen, P. M.; Bawendi, M. G., Ternary I-III-VI Quantum Dots Luminescent in the Red to Near-Infrared. *Journal of the American Chemical Society* 2008, 130 (29), 9240-9241.
18. Xie, R.; Rutherford, M.; Peng, X., Formation of High-Quality I-III-VI Semiconductor Nanocrystals by Tuning Relative Reactivity of Cationic Precursors. *Journal of the American Chemical Society* 2009, 131 (15), 5691-5697.
19. Bose, R.; Jana, S.; Manna, G.; Chakraborty, S.; Pradhan, N., Rate of Cation Exchange and Change in Optical Properties during Transformation of Ternary to Doped Binary Nanocrystals. *The Journal of Physical Chemistry C* 2013, 117 (30), 15835-15841.
20. Fuhr, A.; Yun, H. J.; Makarov, N. S.; Li, H.; McDaniel, H.; Klimov, V. I., Light-Emission Mechanism in CuInS<sub>2</sub> Quantum Dots Evaluated by Spectral Electrochemistry. *ACS Photonics* 2017.
21. Li, L.; Pandey, A.; Werder, D. J.; Khanal, B. P.; Pietryga, J. M.; Klimov, V. I., Efficient Synthesis of Highly Luminescent Copper Indium Sulfide-Based Core/Shell

Nanocrystals with Surprisingly Long-Lived Emission. *Journal of the American Chemical Society* 2011, 133 (5), 1176-1179.

22. Rice, W. D.; McDaniel, H.; Klimov, V. I.; Crooker, S. A., Magneto-Optical Properties of  $\text{CuInS}_2$  Nanocrystals. *The Journal of Physical Chemistry Letters* 2014, 5 (23), 4105-4109.

23. Zang, H.; Li, H.; Makarov, N. S.; Velizhanin, K. A.; Wu, K.; Park, Y.-S.; Klimov, V. I., Thick-Shell  $\text{CuInS}_2/\text{ZnS}$  Quantum Dots with Suppressed “Blinking” and Narrow Single-Particle Emission Line Widths. *Nano Letters* 2017.

24. Jara, D. H.; Stampelcoskie, K. G.; Kamat, P. V., Two Distinct Transitions in  $\text{Cu}_x\text{InS}_2$  Quantum Dots. Bandgap versus Sub-Bandgap Excitations in Copper-Deficient Structures. *The Journal of Physical Chemistry Letters* 2016, 7 (8), 1452-1459.

25. Berends, A. C.; Rabouw, F. T.; Spoor, F. C. M.; Bladt, E.; Grozema, F. C.; Houtepen, A. J.; Siebbeles, L. D. A.; de Mello Donegá, C., Radiative and Nonradiative Recombination in  $\text{CuInS}_2$  Nanocrystals and  $\text{CuInS}_2$ -Based Core/Shell Nanocrystals. *The Journal of Physical Chemistry Letters* 2016, 7 (17), 3503-3509.

26. Knowles, K. E.; Nelson, H. D.; Kilburn, T. B.; Gamelin, D. R., Singlet–Triplet Splittings in the Luminescent Excited States of Colloidal  $\text{Cu}^+:\text{CdSe}$ ,  $\text{Cu}^+:\text{InP}$ , and  $\text{CuInS}_2$  Nanocrystals: Charge-Transfer Configurations and Self-Trapped Excitons. *Journal of the American Chemical Society* 2015, 137 (40), 13138-13147.

27. Nagamine, G.; Nunciaroni, H. B.; McDaniel, H.; Efros, A. L.; de Brito Cruz, C. H.; Padilha, L. A., Evidence of Band-Edge Hole Levels Inversion in Spherical CuInS<sub>2</sub> Quantum Dots. *Nano Letters* 2018, 18 (10), 6353-6359.
28. Pandey, A; Brovelli, S; Viswanatha, R; Li, L; Pietryga, J. M.; Klimov, V. I.; Crooker, S. A., Long-lived photoinduced magnetization in copper-doped ZnSe-CdSe core-shell nanocrystals. *Nat Nano* 2012, 7 (12), 792-797.
29. Bussian, D. A.; Crooker, S. A.; Yin, M.; Brynda, M.; Efros, A. L.; Klimov, V. I., Tunable magnetic exchange interactions in manganese-doped inverted core-shell ZnSe-CdSe nanocrystals. *Nature Materials* 2008, 8, 35.
30. Kacman, P., Spin interactions in diluted magnetic semiconductors and magnetic semiconductor structures. *Semiconductor Science and Technology* 2001, 16 (4), R25.
31. Schulz, H. J., Optical properties of 3d transition metals in II-VI compounds. *Journal of Crystal Growth* 1982, 59 (1), 65-80.
32. Blinowski, J.; Kacman, P., Kinetic exchange in diluted magnetic semiconductors. *Physical Review B* 1992, 46 (19), 12298-12304.
33. de wit, M., Zeeman Effect in the Absorption Spectrum of Copper-Doped Zinc Sulfide. 1969; Vol. 177, p 441-447.
34. Telahun, T.; Scherz, U.; Thurian, P.; Heitz, R.; Hoffmann, A.; Broser, I., Nonlinear Zeeman behavior of Cu<sup>2+</sup> centers in ZnS and CdS explained by a Jahn-Teller effect. 1996; Vol. 53, p 1274-1286.

35. Abragam, A.; Jacquinot, J. F.; Chapellier, M.; Goldman, M., Spin-lattice relaxation of Kramers doublets with hyperfine structure in cubic symmetry. *Journal of Physics C: Solid State Physics* 1972, 5 (18), 2629.
36. Fuhr, A. S.; Sautet, P.; Alexandrova, A. N., Heterogeneity in Local Chemical Bonding Explains Spectral Broadening in Quantum Dots with Cu Impurities. *The Journal of Physical Chemistry C* 2019, 123 (9), 5705-5713.
37. Grioni, M.; Goedkoop, J. B.; Schoorl, R.; de Groot, F. M. F.; Fuggle, J. C.; Schäfers, F.; Koch, E. E.; Rossi, G.; Esteva, J. M.; Karnatak, R. C., Studies of copper valence states with Cu L<sub>3</sub> x-ray-absorption spectroscopy. *Physical Review B* 1989, 39 (3), 1541-1545.
38. Mazin, I. I., Structural and electronic properties of the two-dimensional superconductor CuS with  $1\frac{1}{3}$  valent copper. *Physical Review B* 2012, 85 (11), 115133.
39. Kumar, P.; Nagarajan, R.; Sarangi, R., Quantitative X-ray absorption and emission spectroscopies: electronic structure elucidation of Cu<sub>2</sub>S and CuS. *Journal of Materials Chemistry C* 2013, 1 (13), 2448-2454.
40. Kresse, G.; Furthmüller, J., Efficiency of ab-initio total energy calculations for metals and semiconductors using a plane-wave basis set. *Computational Materials Science* **1996**, 6 (1), 15-50.
41. Kresse, G.; Furthmüller, J., Efficient iterative schemes for ab initio total-energy calculations using a plane-wave basis set. *Physical Review B* **1996**, 54 (16), 11169-11186.

42. Kresse, G.; Hafner, J., *Ab initio* molecular-dynamics simulation of the liquid-metal-amorphous-semiconductor transition in germanium. *Physical Review B* **1994**, *49* (20), 14251-14269
43. Perdew, J. P.; Burke, K.; Ernzerhof, M., Generalized Gradient Approximation Made Simple. *Physical Review Letters* **1996**, *77* (18), 3865-3868.
44. Heyd, J.; Scuseria, G. E.; Ernzerhof, M., Hybrid functionals based on a screened Coulomb potential. *The Journal of Chemical Physics* **2003**, *118* (18), 8207-8215.
45. (a) Pohl, J.; Albe, K., Thermodynamics and kinetics of the copper vacancy in  $\text{CuInSe}_2$ ,  $\text{CuGaSe}_2$ ,  $\text{CuInS}_2$ , and  $\text{CuGaS}_2$  from screened-exchange hybrid density functional theory. *Journal of Applied Physics* **2010**, *108* (2), 023509;
46. Chen, H.; Wang, C.-Y.; Wang, J.-T.; Hu, X.-P.; Zhou, S.-X., First-principles study of point defects in solar cell semiconductor  $\text{CuInS}_2$ . *Journal of Applied Physics* **2012**, *112* (8), 084513.

## CHAPTER 3

Compositional Heterogeneity & Types of Stokes Shifts: Low Photon Flux

Spectral Broadening Mechanisms

### **3.1. Effect of Stoichiometry on Reabsorption in $\text{Cu}_x\text{In}_{2-x}\text{S}_y$ Quantum Dots: Determining the “Real” vs. “Apparent” Stokes Shift**

#### **3.1.1. Introduction**

Ternary  $\text{Cu}_x\text{In}_{2-x}\text{E}_y$  (where E=S or Se) quantum dots (QDs) have emission tunable across the visible and near-infrared (near-IR) spectral ranges, which make them prospective environmentally benign alternatives to highly toxic Cd- (visible) and Pb-based (near-IR) emitting QDs for optical and electro-optical devices.<sup>1-10</sup> However, despite their similar emission energies, many of the (electro)-optical properties of CIS QDs such as large Stokes shifts between the onset of strong absorption and emission ( $\Delta_S \approx 300\text{-}750$  meV), long radiative lifetimes ( $\sim 200\text{-}400$  ns), broad spectral linewidths ( $\sim 300\text{-}400$  meV for emission), and tunable charge transport pathways vastly differ from typical II-VI and IV-VI materials.<sup>1, 3, 11-21</sup> These unusual properties can be advantageous for many technological applications, but several challenges persist for their use in commercial devices. For example, the large  $\Delta_S$  reduces spectral overlap between absorption and emission, and correspondingly suppresses reabsorption losses in luminescent solar concentrators (LSCs).<sup>2, 22</sup> Yet, because of the broad absorption and emission linewidths, spectral overlap is not entirely removed, and consequently LSCs utilizing CIS QDs as the optically active layer still suffer from reabsorption losses. Designing large-scale “reabsorption-free” LSCs would therefore call for near-IR emitting CIS QDs with sharper absorption and emission spectra, and/or even larger Stokes shifts. The broad emission spectrum is also a barrier for CIS QDs that emit in the visible spectral range where the high color purities required for their use in solid-state lighting applications (e.g. light-emitting diodes, or LEDs) cannot be achieved without narrow emission spectra.<sup>23</sup>

Despite the necessity for reducing spectral overlap for LSCs and achieving sharper emission spectra for LEDs, the (electro)-optical absorption and emission mechanisms for CIS QDs is still largely debated, and consequently the roadmap to achieving these goals is unclear. While emission is generally attributed to radiative recombination between holes localized on copper cations and delocalized conduction band (CB) electrons, it is still debated whether the origin of this effect is optically-active  $\text{Cu}^x$  defects (where  $x = 1+$  or  $2+$ ), or self-trapped excitons from lattice  $\text{Cu}^{1+}$  cations.<sup>15-16, 18-21, 24</sup> Specifically, for *each* of these proposed mechanisms, considering that  $\text{Cu}^{1+}$  states have a filled d shell ( $[\text{Ar}]3d^{10}$ ), it is generally agreed that emission from  $\text{Cu}^{1+}$  requires photo-activation *via* capture of a valence band (VB) hole to form  $\text{Cu}^{2+}$ -like states ( $[\text{Ar}]3d^9$ ) prior to radiative recombination with a CB electron. However, for the self-trapped exciton model, the  $\text{Cu}^{1+}$  states arise from lattice  $\text{Cu}^{1+}$  atoms, and the large  $\Delta_S$  and broad emission linewidths are due to strong electron-phonon coupling, which leads to a significant nuclear reorganization of the  $\text{Cu}^{1+}$  coordination sphere in the excited state.<sup>21</sup> For the defect mechanism, on the other hand,  $\text{Cu}^{1+}$  states arise from  $\text{Cu}^{1+}$  lattice impurities (*e.g.* vacancies, interstitials, or so-called anti-site defects where  $\text{Cu}^{1+}$  and  $\text{In}^{3+}$  atoms swap lattice positions). In this case, CIS QDs have intra-gap  $\text{Cu}^{1+}$  energy-levels, which results in a 3-level system where the large  $\Delta_S$  is due to the energy difference between the intra-gap  $\text{Cu}^{1+}$  defect state and the VB, and spectral linewidths for individual QDs are expected to be *intrinsically narrow*. Considering that defects are indicative of cation disorder in QDs, these  $\text{Cu}^{1+}$  defects can be located in different positions for each individual QD in the ensemble (*e.g.* surface vs. subsurface), which then form subensembles where either the *ground-state* energy off-set of the  $\text{Cu}^{1+}$  defects from the VB is varied, or the *excited-state*

wavefunction overlap between the CB electron and the hole localized at the  $\text{Cu}^{1+}$  state is altered based on the location of the defect.<sup>18, 25</sup> For both cases, broadening of the CIS QD ensemble emission is predominantly due to heterogeneity in the position of  $\text{Cu}^{1+}$  defects, which leads to subensembles with large variations in emission energy and  $\Delta_S$ . Narrow single particle emission, variations in emission energy due to the positional disorder of defects, and corresponding inhomogeneous broadening of ensemble emission would also occur with *emissive*  $\text{Cu}^{2+}$  defects. Hence, for QDs with either  $\text{Cu}^{1+}$  or  $\text{Cu}^{2+}$  defects, or ensembles with both defects heterogeneity in the spatial distribution of  $\text{Cu}^x$  is expected to have the same impact on ensemble emission linewidths. However, considering that  $\text{Cu}^{2+}$  defects have a partially occupied electron configuration ( $[\text{Ar}]3d^9$ ), or a pre-existing hole in their ground state electronic structure, radiative recombination occurs without prior localization of a VB hole, which is instead trapped in another state (e.g. surface or dangling bond).<sup>15-16</sup> This would be expected to lead to similar emission linewidths and radiative lifetimes, but higher quantum yields (QYs) than QDs with  $\text{Cu}^{1+}$  defects since hole trapping would not lead to optical losses, and only electron trapping would reduce optical efficiency. Alternatively, it has also been proposed that the pre-existing hole in the  $\text{Cu}^{2+}$  defect can be a source of positive trion recombination, and the VB hole collides with the pre-existing hole in the  $\text{Cu}^{2+}$  defect structure instead of localizing at a  $\text{Cu}^{1+}$  defect state.<sup>24</sup> Consequently,  $\text{Cu}^{2+}$  defects are expected to be non-emissive, or “dark” in this mechanistic scheme.

Determining the likelihood of each of these proposed optical pathways in QD ensembles is pivotal to screening materials for use in different (electro)-optical devices. For example, the filled d shell for  $\text{Cu}^{1+}$  defects could also lead to absorption transitions

distinct from the band-edge (**Figure 3.1.2.1a, left panel**). This would lead to a “real” Stokes shift ( $\Delta_{S,R}$ ) between absorption from the ground-state  $\text{Cu}^{1+}$  defect and emission from the excited-state hole localized  $\text{Cu}^{2+}$  defect, which would occur *via* a vibronically-coupled Franck-Condon shift in the  $\text{Cu}^x$  defect energy during the  $\text{Cu}^{1+} \rightarrow \text{Cu}^{2+}$  photoconversion process. The final emissive  $\text{Cu}^{2+}$  state would then also exhibit an “apparent” Stokes shift ( $\Delta_{S,A}$ ), which would represent the energy difference between the band-edge absorption ( $\text{VB} \rightarrow \text{CB}$ ) and the  $\text{Cu}^{2+}$  emission ( $\text{CB} \rightarrow \text{Cu}^{2+}$ ). Considering that  $\text{Cu}^{2+}$  defects do not localize holes (**Figure 3.1.2.1a, right panel**), or have separate absorption transitions, subensembles with  $\text{Cu}^{1+}$  defects would exhibit both  $\Delta_{S,R}$  and  $\Delta_{S,A}$  whereas subensembles with  $\text{Cu}^{2+}$  defects would *only* exhibit  $\Delta_{S,A}$ . Hence, absorption from subensembles with  $\text{Cu}^{1+}$  defects would broaden the ensemble absorption spectrum, and lead to smaller Stokes shifts. On the other hand, synthesizing ensembles with a greater concentration of  $\text{Cu}^{2+}$  defects could reduce intragap absorption, lead to sharper absorption spectra, and reduce spectral overlap with emission. Moreover, for *both* LSCs and LEDs high quantum yields (QYs) are required for use in commercial devices. And, as mentioned earlier, there is still debate as to whether  $\text{Cu}^{2+}$  defects emit. In the case of *emissive*  $\text{Cu}^{2+}$  defects, as mentioned earlier, hole trapping does not reduce QY, and a larger relative population of subensembles with  $\text{Cu}^{2+}$  defects should lead to higher QY.<sup>15</sup> On the other hand, if  $\text{Cu}^{2+}$  defects lead to Auger losses from positive trion recombination even at low excitation densities then lower QYs are expected for ensembles with a higher concentration of QDs with  $\text{Cu}^{2+}$  defects.<sup>24</sup> Here, we explore these possibilities by changing the ratio of  $\text{Cu}^{1+}$  and  $\text{Cu}^{2+}$  defects in QD ensembles *via* altering the Cu-to-In ratio in CIS QDs. We find that  $\text{Cu}^{1+}$  defects have a higher concentration in (near)-

stoichiometric and Cu-rich QDs, which correspondingly have broader absorption linewidths and larger spectral overlap with emission than far-off, highly Cu-deficient QDs, which have a larger concentration of  $\text{Cu}^{2+}$  defects. Moreover, by combining several spectroscopic methods we are able to distinguish  $\text{Cu}^{1+}$  defect absorption from band-edge absorption, and can quantitatively distinguish the “real” vs. “apparent” Stokes shifts in these materials. Finally, we use density functional theory (DFT) calculations to show that the so-called absorptive “ $\text{Cu}^{1+}$ ” states are anti-site  $\text{Cu}_{\text{In}}$  defects, which form when  $\text{Cu}^{1+}$  and  $\text{In}^{3+}$  ions switch lattice positions to form charge balanced defect pairs ( $\text{Cu}_{\text{In}} + \text{In}_{\text{Cu}}$ ). These form in larger concentrations for (near)-stoichiometric QDs than far-off stoichiometry QDs due to the (near)-equal concentration of both cations. On the other hand, Cu-deficient QDs have non-absorptive  $\text{Cu}^{2+}$  defects due to their large concentration of copper vacancies ( $V_{\text{Cu}}$ ), which require charge compensation by the oxidation of a second Cu atom ( $\text{Cu}^{1+} \rightarrow \text{Cu}^{2+} + e^-$ ) to also form charge-balanced defect pairs ( $V_{\text{Cu}} + \text{Cu}_{\text{Cu}}$ ).

### 3.1.2. Results and Discussion

**Stoichiometry-Dependent Optical Properties.** CIS QDs with different Cu-to-In ratios (1.12:1, 0.85:1, and 0.47:1 as determined by inductively coupled plasma atomic emission spectrometry) were synthesized following the procedure outlined in the Methods section. 1-Dodecanethiol and oleylamine act as the capping ligands for all samples. Transmission electron microscope (TEM) measurements indicate that QDs have a tetrahedral shape and d-spacing of 3.2 Å, which corresponds to the (112) lattice plane of  $\text{Cu}_x\text{In}_{2-x}\text{S}_2$  with a chalcopyrite structure (Figure S6.3.1). The average QD size as determined by the tetrahedral height, as well as the standard deviation, are roughly

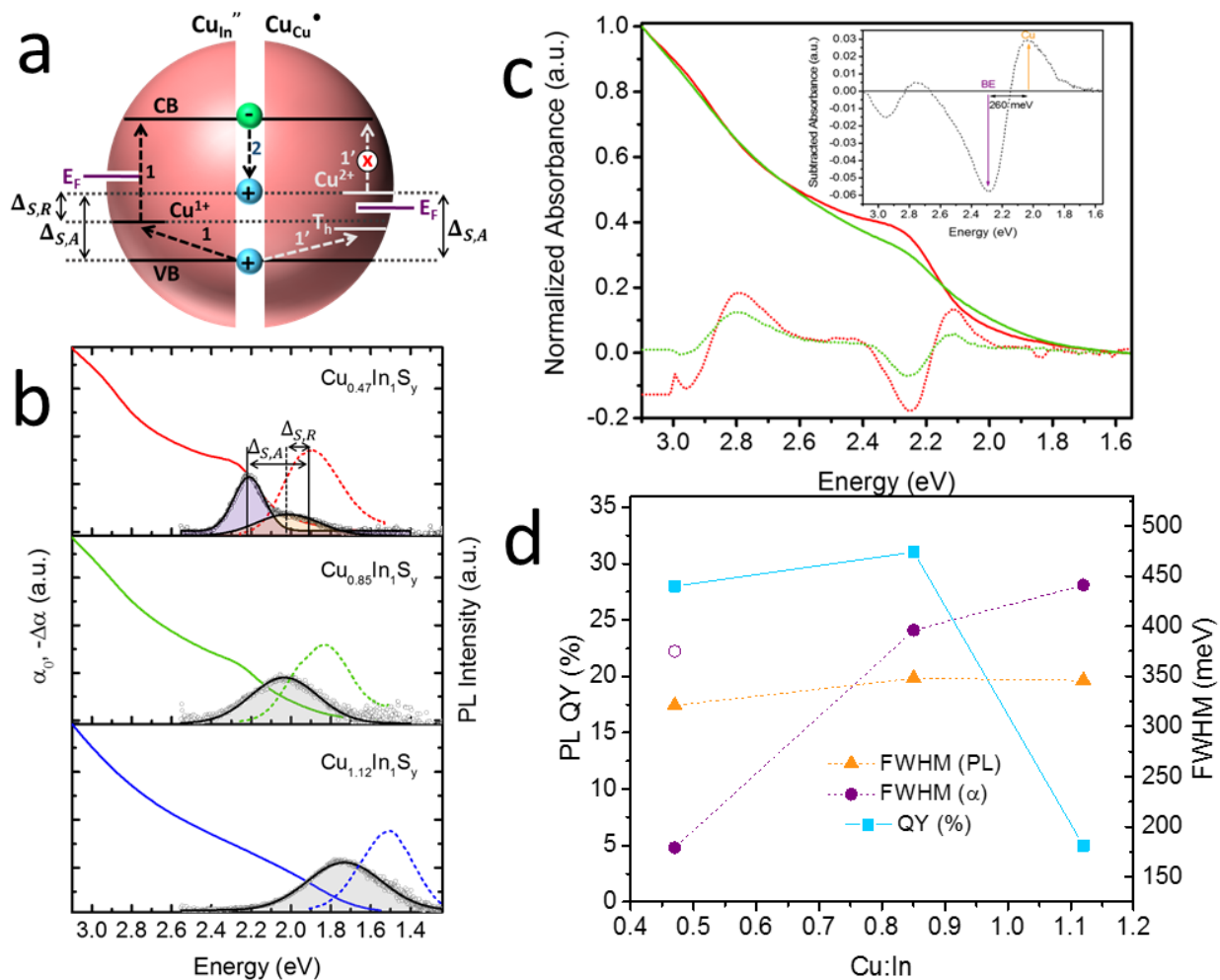


**Figure 3.1.2.1.** (a) Scheme distinguishing between the two Stokes shifts in CIS QDs. Cu-rich, stoichiometric, and near-stoichiometric QDs have a larger concentration of subensembles with Cu<sup>1+</sup>, or anti-site defects, which have a filled *d* shell that requires “photoactivation” *via* either intra-gap absorption or hole localization from the VB (left panel). Cu-deficient QDs (right panel), on the other hand, have larger subensembles of Cu<sup>2+</sup> defects, which are “emission ready” due to a pre-existing hole in its *d* shell and do not undergo this photoconversion process. Correspondingly, *both* subensembles have an apparent Stokes shift (Δ<sub>S,A</sub>, both panels) represented by the energy difference between Cu<sup>2+</sup> defect (ground-state or photogenerated) emission and band-edge absorption. However, only subensembles with Cu<sup>1+</sup> defects have a “real Stokes shift,” which represents the energy difference between Cu<sup>1+</sup> defect absorption, and photogenerated Cu<sup>2+</sup> defect emission. This energy separation is due to the vibronically coupled Franck-Condon shift in Cu<sup>x</sup> defect energy during the photoconversion process. (b) The linear absorption spectra (solid colored lines) are compared to the transient absorption spectra (grey scatter plots) fitted to Gaussian peaks (solid black lines for all samples with grey infilling for Cu-rich and slightly Cu-deficient QDs, purple infilling for excitonic absorption and orange infilling for weak Cu<sup>1+</sup> defect absorption in highly Cu-deficient QDs), and the PL spectra (dashed colored lines). (c) The second derivatives of the two Cu-deficient QDs show near-identical band gaps, but highly Cu-deficient QDs have significantly narrower absorption spectra due to the removal of Cu<sup>1+</sup> defects. The figure inset shows the “subtraction spectrum” where the linear absorption spectrum of Cu<sub>0.85</sub>In<sub>1</sub>S<sub>y</sub> is

subtracted from  $\text{Cu}_{0.47}\text{In}_1\text{S}_y$ . The negative peak represents a decrease in the relative intensity of the band-edge transition whereas the positive peak represents an increase in the intensity of Cu-defect absorption as QDs become closer to stoichiometric, or Cu-rich. (d) Comparison of the PL and TA FWHM (right axis for both cases) as determined from the high energy peak of the Bi-Gaussian fit for the TA bleach of  $\text{Cu}_{0.47}\text{In}_1\text{S}_y$ , and the only peak of the single Gaussian fit for the TA bleach of all other samples (purple closed circles). For PL, a single Gaussian fit was used for all samples (orange closed triangles). Since highly Cu-deficient QDs have two bands in the TA spectrum, an additional point is shown for the  $\text{Cu}^{1+}$  defect absorption shoulder (purple open circle). Both data sets are compared to the QY for the same samples (turquoise closed squares and left axis).

equivalent for both Cu-deficient QDs ( $2.22 \pm 0.26$  nm and  $2.28 \pm 0.33$  nm for  $\text{Cu}_{0.47}\text{In}_1\text{S}_y$  and  $\text{Cu}_{0.85}\text{In}_1\text{S}_y$ , respectively), while the Cu-rich QDs are slightly larger ( $2.47 \pm 0.59$  nm).

In **Figure 3.1.2.1b**, we compare the absorption (solid colored lines) and PL emission (dashed colored lines) spectra with the transient absorption (TA, grey scatter plot) bleach at low excitation fluence ( $\langle N \rangle < 0.1$ ). The TA bleach for the Cu-rich ( $\text{Cu}_{1.12}\text{In}_1\text{S}_y$ ) and slightly Cu-deficient ( $\text{Cu}_{0.85}\text{In}_1\text{S}_y$ ) QDs is significantly red-shifted from the onset of strong linear absorption, and can be fitted by a single Gaussian function (solid black line with grey infilling). However, the TA bleach for the extremely Cu-deficient QDs ( $\text{Cu}_{0.47}\text{In}_1\text{S}_y$ ) requires a Bi-Gaussian fit. We indicate the Gaussian fit for the high-energy TA bleach (peak at 2.22 eV) using a solid black line with purple infilling. This peak is similar in energy to the second derivative of the linear absorption spectrum (2.25 eV as shown by the dashed red lines in **Figure 3.1.2.1b**). On the other hand, the peak of the Gaussian fit for the lower-energy “shoulder” of the TA spectrum (solid black line with orange infilling) is red-shifted by 190 meV, and centered at 2.03 eV.

The low-energy “shoulder” in the TA spectrum shows two peaks and is near-identical to the “tail” of the linear absorption spectrum for  $\text{Cu}_{0.47}\text{In}_1\text{S}_y$ ; therefore, the Gaussian fits to these two peaks are expected to represent distinct absorptive states. Considering that the high-energy (2.22 eV) TA bleach is near identical to the peak of the

second-derivative of the linear absorption spectrum (2.25 eV), it most likely marks the band-edge (BE) excitonic transition ( $VB \rightarrow CB$ ). Hence, the low-energy shoulder characterizes intra-gap absorption from occupied defects ( $Cu^{1+}$ , or  $Cu_{In}'' \rightarrow CB$ , as shown schematically in **Figure 3.1.2.1a** with black dashed arrow). Absorption from  $Cu_{In}''$ , or  $Cu^{1+}$  defects are considerably closer in energy to the PL peak (dashed colored lines) than the BE excitonic transition. This, as mentioned earlier, is indicative of the difference between the real Stokes shift ( $\Delta_{S,R}$  in **Figures 3.1.2.1a,b**), which results from the vibronically coupled Franck-Condon shift in  $Cu^x$  defect energy during the photoactivation process, and the apparent Stokes shift ( $\Delta_{S,A}$  in **Figures 3.1.2.1a,b**) resulting from the energy difference between excitonic absorption and  $Cu^x$  emission. As expected by their near-identical size and size dispersion, the peak of the second derivative of the linear absorption spectrum for  $Cu_{0.85}In_1S_y$  and  $Cu_{0.47}In_1S_y$  (**Figure 3.1.2.1c**), which is used here as an indicator of the QD band gaps ( $E_g$ ) are near-equal (2.24 eV vs. 2.25 eV). However, the TA bleach for  $Cu_{0.85}In_1S_y$  is unexpectedly red-shifted (180 meV) from the  $E_g$  determined by the second derivative of the linear absorption spectrum, and is closer in energy to the shoulder of the TA spectrum for  $Cu_{0.47}In_1S_y$  (2.06 eV vs. 2.03 eV, respectively). While direct comparison with the Cu-rich ( $Cu_{1.12}In_1S_y$ ) QDs is difficult due to differences in their average size and size dispersion from the Cu-deficient QDs, its corresponding bleach is also significantly red-shifted from the onset of strong absorption. These findings indicate that the TA bleach for CIS QDs represents a convolution of BE and  $Cu^{1+}$ , or  $Cu_{In}''$  defect absorption with the latter gradually dominating the spectra as QDs are made increasingly Cu-rich.

To better understand the implications of these findings on the Stokes shifts and spectral broadening, we compare the linear absorption spectra for the two Cu-deficient QDs (**Figure 3.1.2.1c**) due to their similar size ( $\sim 2.25$  nm) and size dispersion ( $\sim \pm 0.3$  nm). Interestingly, while the shape of the PL spectra in **Figure 3.1.2.1b**, and its Stokes shift from the band-edge transition ( $E_g$ ) determined *via* the second derivative (**Figure 3.1.2.1c**) appears to be relatively unaffected by stoichiometry when size/size dispersion is controlled, the absorption spectra clearly becomes broader as QDs are made progressively more Cu-rich. The broadening of the absorption spectra as QDs are made more Cu-rich suggests an increase in the heterogeneity of states capable of optical absorption, and most likely is not a consequence of size dispersion alone given that  $\text{Cu}_{0.47}\text{In}_1\text{S}_y$  and  $\text{Cu}_{0.85}\text{In}_1\text{S}_y$  have near-identical size dispersions. A more likely explanation for the broadening of the absorption spectra as QDs become more Cu-rich is a larger concentration of occupied  $\text{Cu}^{1+}$ , or anti-site  $\text{Cu}_{\text{In}}$  defect states from which an electron can be directly excited into the CB (left panel of **Figure 3.1.2.1a**). Indeed, this explanation is consistent with our interpretation of the stoichiometry-dependent shifts observed in the TA bleach where the TA signal becomes increasingly dominated by intra-gap absorption as QDs become progressively more Cu-rich. If we subtract the linear absorption spectrum for  $\text{Cu}_{0.85}\text{In}_1\text{S}_y$  from  $\text{Cu}_{0.47}\text{In}_1\text{S}_y$  (inset of **Figure 3.1.2.1c**), we observe a decrease in the intensity of excitonic absorption (negative peak  $\sim 2.29$  eV) and increase intra-gap absorption (positive peak  $\sim 2.03$  eV). This is near identical to the proposed energy difference between the excitonic absorption peak and  $\text{Cu}^{1+}$  ( $\text{Cu}_{\text{In}}$ ) defect absorption shoulder in the TA spectrum for  $\text{Cu}_{0.47}\text{In}_1\text{S}_y$ , and indicates that the peak of the single Gaussian fit to the TA bleach for  $\text{Cu}_{0.85}\text{In}_1\text{S}_y$  is from  $\text{Cu}_{\text{In}}$  defect absorption.

Consequently, if we determine the Stokes shift for (near)-stoichiometric CIS QDs using the TA bleach we get a significantly smaller value (in this case, ~200 meV smaller) than if we use the second derivative of the linear absorption spectra, which is not the case for highly off-stoichiometric, Cu-deficient QDs where the high energy bleach is nearly identical to the second derivative. Hence, the Stokes shift for (near)-stoichiometric/Cu-rich CIS QDs can vary significantly based on the measurement method due to the absorption of  $\text{Cu}^{1+}$ , or anti-site  $\text{Cu}_{\text{In}}$  defects, which also lead to broadening of their respective linear absorption spectra.

In previous spectral electrochemistry (SEC) studies it was hypothesized that Cu-deficient QDs have a larger concentration of  $\text{Cu}^{2+}$  defects whereas (near)-stoichiometric QDs have a larger concentration of  $\text{Cu}^{1+}$  defects, which lead to higher QY for Cu-deficient QDs.<sup>24</sup> This is because, as mentioned earlier,  $\text{Cu}^{2+}$  defects are “emission ready,” and do not require photoactivation *via* a band-edge hole (right panel of **Figure 3.1.2.1a**). Hence, photon emission involving  $\text{Cu}^{2+}$  defects is affected *only* by electron traps whereas emission *via*  $\text{Cu}^{1+}$  defects is also affected by hole trapping. Indeed, if this interpretation is correct then Cu-deficient QDs should have narrower absorption spectra, *and* higher QYs than (near)-stoichiometric QDs. If we further consider that in *both* proposed mechanisms the final emitting state is  $\text{Cu}^{2+}$ , the PL linewidths should not be significantly affected by the  $\text{Cu}^{1+}/\text{Cu}^{2+}$  defect ratio, and are instead only affected by positional disorder of the  $\text{Cu}^x$  defects as described earlier.

To confirm this interpretation, we compare the spectral linewidths at the full-width at half maximum (FWHM) for each stoichiometry (**Figure 3.1.2.1d**) with their corresponding QYs ( $\Phi$ ). The linewidth for the TA peak as determined by the single

Gaussian fit for (near)-stoichiometric QDs, and the high energy peak for the double Gaussian fit of the highly Cu-deficient QDs narrows substantially as the QDs become more Cu-deficient (closed purple circles, right y axis). Specifically, the BE bleach for  $\text{Cu}_{0.47}\text{In}_1\text{S}_y$  is  $\sim 262$  meV, or 60% narrower than the bleach for  $\text{Cu}_{1.12}\text{In}_1\text{S}_y$ , and  $\sim 217$  meV, or 55% narrower than the bleach for  $\text{Cu}_{0.85}\text{In}_1\text{S}_y$ . Interestingly though, the FWHM for the intra-gap shoulder (open purple circle) of the double Gaussian fit for  $\text{Cu}_{0.47}\text{In}_1\text{S}_y$  — heretofore referred to as “ $\text{Cu}^{1+}$  defect absorption” — does not appreciably differ from the bleach of the other structures (e.g.  $\sim 21$  meV, or  $\sim 5\%$  narrower than the single Gaussian fit for  $\text{Cu}_{0.85}\text{In}_1\text{S}_y$ ). QY also increases as QDs are made more Cu-deficient ( $\Phi_{\text{Cu}_{1.12}\text{In}_1\text{S}_y} = 5\%$ ,  $\Phi_{\text{Cu}_{0.85}\text{In}_1\text{S}_y} = 30\%$ ,  $\Phi_{\text{Cu}_{0.47}\text{In}_1\text{S}_y} = 28\%$ , as represented by the left y axis and turquoise squares in **Figure 3.1.2.1d**). In addition, the PL linewidth (orange closed triangles, right y axis) does not narrow significantly as the Cu-to-In ratio is changed ( $\sim 27$  meV, or 7%). All samples exhibit long PL lifetimes ( $\sim 230$  ns as measured by time-correlated single photon counting experiments) typically observed for  $\text{Cu}^x$  emission (Figure S6.3.2), but the relative amplitude for the radiative component as determined by multi-exponential fits of the PL dynamics increases as QDs are made more Cu-deficient, and roughly matches the expected increase in QY. This confirms our earlier argument that the TA signal in (near)-stoichiometric and Cu-rich QDs is dominated by  $\text{Cu}^{1+}$  defect absorption, which convolutes our determination of the BE feature by TA, leads to two different Stokes shifts, broadens the linear absorption spectra, and leads to lower QY due to their susceptibility to hole trapping. Cu-deficient QDs, conversely, show both the narrow BE feature and a very weak broad  $\text{Cu}^{1+}$  defect absorption shoulder due to the higher concentration of  $\text{Cu}^{2+}$  defects,

which have a  $d$  shell only partially filled and is therefore incapable of promoting an electron to the CB *via* direct, intra-band gap excitation.

The observed increase in PL efficiency in Cu-deficient QDs due to the larger concentration of  $\text{Cu}^{2+}$  defects further asserts that while positive trion hole recombination may be possible with  $\text{Cu}^{2+}$  defects as previously hypothesized,<sup>24</sup>  $\text{Cu}^{2+}$  defects are not “dark.” Indeed, the changes in bleach linewidth are nearly an order of magnitude larger than the changes in emission linewidth ( $\sim 200$  meV *vs.*  $\sim 20$  meV), and spectral narrowing of the TA signal is accompanied by an increase in QY. Hence, after hole localization *both*  $\text{Cu}^{1+}$  and  $\text{Cu}^{2+}$  defects are emissive whereas *only*  $\text{Cu}^{1+}$  defects are absorptive. We caution here, however, that while these distinctions are useful for explaining the increase in PL efficiency generally observed for Cu-deficient QDs in comparison with stoichiometric or Cu-rich QDs, it should be noted that electron trapping due to surface states is the predominant quenching mechanism for CIS QDs,<sup>15, 20</sup> and increases in QY are contingent on the surface chemistry of the QDs being relatively unaltered.<sup>15, 20</sup> Minor changes in surface passivation (*e.g.* ligand coverage) may therefore explain the slightly lower ( $\sim 2\%$ ) QY for  $\text{Cu}_{0.47}\text{In}_1\text{S}_y$  in comparison with  $\text{Cu}_{0.85}\text{In}_1\text{S}_y$ .

Three-dimensional photoluminescence excitation (3D-PLE) spectra, collected by varying both the monitoring PL wavelength and the excitation energy (**Figure 3.1.2.2** for summarized data and Figure S6.3.3 for full contour plots) are used to characterize the energy distribution of  $\text{Cu}^{1+}$  defect absorption transitions in CIS QDs, and quantitatively determine the variation in Stokes shift energies. All measurements used dilute concentrations of CIS QDs in chloroform (OD  $\sim 0.01$  at the band-edge transition in a 1 mm cuvette) to limit issues associated with aggregation, solution-phase energy transfer, or

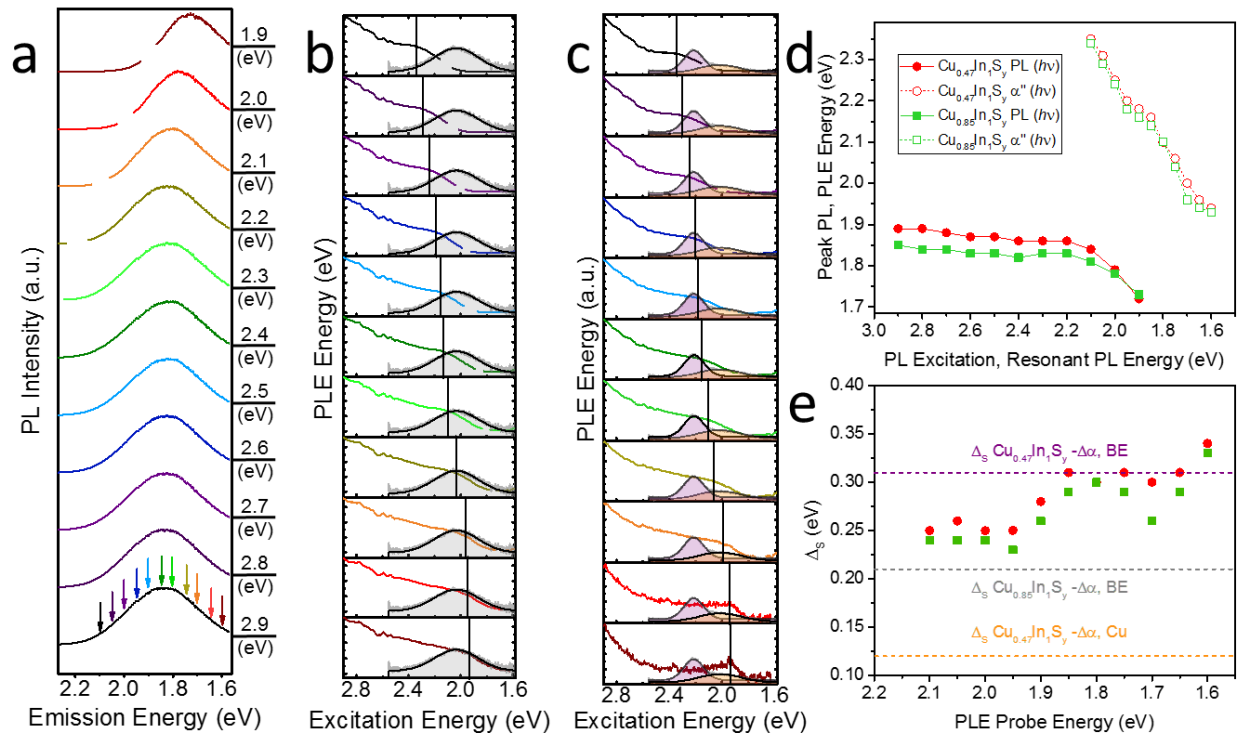


**Figure 3.1.2.2.** 3D-PL measurements for CIS QDs. (a) Excitation energy-dependent PL for  $\text{Cu}_{0.85}\text{In}_1\text{S}_y$ . We observe little change in the spectral shape for above band gap (2.9 to 2.3 eV), resonant (2.3 eV), or shallow intra-gap excitation (2.3 eV to 2.1 eV). This is expected since the proposed energy of the absorptive intra-gap  $\text{Cu}^{1+}$  defects is  $\sim 2.05$  eV. However, for deep intra-gap excitation (2.1 eV, or lower in energy) the PL peak red-shifts due to QD size selection for both samples (for sample  $\text{Cu}_{0.85}\text{In}_1\text{S}_y$  see Figure S6.3.3). (b) PL excitation energy (PLE) measurements resonant with the PL energies marked by colored arrows with corresponding colors in (a) for  $\text{Cu}_{0.85}\text{In}_1\text{S}_y$ . (c) The same measurements shown in (b) are repeated for  $\text{Cu}_{0.47}\text{In}_1\text{S}_y$ . The black lines for both (b) and (c) mark the peak of the PLE second derivative, and is used as an indicator of the absorptive transition responsible for PL emission at the marked probe energies. The TA measurements shown in Figure 3.1.2.1 are superimposed with these measurements for comparison. (d) The data from (a,b,c) is summarized and compared with  $\text{Cu}_{0.85}\text{In}_1\text{S}_y$  being represented by green squares and  $\text{Cu}_{0.47}\text{In}_1\text{S}_y$  represented by red circles. In each case, the PL peak energy is marked by solid symbols and the second derivative of the resonant PLE is marked with open symbols. (e) The PLE probe energy-dependent Stokes shift is measured by calculating energy difference between the peak of the PLE second derivative and the probe energy at which it was collected. The dashed lines indicate the Stokes shift as predicted by the absorptive transition energies from the TA and PL measurements. The large variations in Stokes shift cannot be explained by size dispersion, and is in agreement with our proposed emission mechanism where the absorptive transitions responsible for PL arise from two distinct absorptive states: band-edges and  $\text{Cu}^{1+}$  defects.

reabsorption due to polydispersity in QD size.<sup>26</sup> **Figure 3.1.2.2a** shows the PL spectra as a function of photoexcitation energy for  $\text{Cu}_{0.85}\text{In}_1\text{S}_y$  (for  $\text{Cu}_{0.47}\text{In}_1\text{S}_y$ , see Figure S6.3.3) falling within the 2.9 eV to 1.9 eV range, selected from the 3D-PL spectra in 0.1 eV

increments (labelled on the right y axis). We do not observe any significant shifts in the PL energy ( $\sim 30$  meV) when the excitation energy is varied from far above the band gap (2.9 eV) to the resonant limit of the BE transition (2.3 eV), indicating that hot carriers do not play a significant role in determining the Stokes shifts of CIS QDs.

Interestingly, the PL energy also does not significantly shift in the intra-gap 2.3 to 2.1 eV excitation regime ( $\sim 20$  meV). This is particularly noteworthy given that 2.1 eV is  $\sim 200$  meV *lower* in energy than the BE transition (roughly equivalent to the difference in predicted Stokes shifts based on the second derivative of the linear absorption spectra and the TA bleach in **Figure 3.1.2.1**), and further indicates that the heterogeneity of absorptive states is *not* predominantly due to polydispersity in QD size, which would manifest in large shifts in the PL energy with intra-gap excitation. In fact, this directly shows that the PL typically associated with Cu defects *do not* require capture of a VB hole for a radiative transition, but can instead be directly excited by a lower energy photon *independently* from the BE transition. Thus, it leads to convolution of the TA bleach by different absorptive transitions, which correspondingly would result in different Stokes shifts, and broadening of the absorption spectra for QD ensembles with a larger concentration of  $\text{Cu}^{1+}$  defects. We further note that the lowest excitation energy in this measurement (2.1 eV) is nearly resonant with the absorption energy of the  $\text{Cu}^{1+} \rightarrow \text{CB}$  defect transition predicted from TA measurements ( $\sim 2.06$  eV), and the subtraction spectra in the inset of **Figure 3.1.2.1** ( $\sim 2.03$  eV). As the excitation energy further decreases below 2.1 eV, we start to observe a more significant red-shift in the PL spectra ( $\sim 110$  meV). These shifts are most likely the combined consequence of both polydispersity in QD size and variation in emission energies due to an inhomogeneous

distribution of defects within the crystal lattice, the latter of which can lead to variations in the energy off-set between the band-edges and the absorptive defect states as described in more detail elsewhere,<sup>25</sup> and cannot be quantitatively distinguished from shifts due to size dispersion here.

**Figure 3.1.2.2b** shows the PLE spectra using solid lines with colors corresponding with the probe energies marked by arrows of the same color in **Figure 3.1.2.2a**. The peak of the second derivative for each PLE spectra is marked by a solid black line, and the corresponding TA spectrum at 3.61 eV excitation is shown as a grey scatter plot with the Gaussian fit represented by black lines and grey infilling for  $\text{Cu}_{0.85}\text{In}_1\text{S}_y$ . **Figure 3.1.2.2c** depicts the same measurements with  $\text{Cu}_{0.47}\text{In}_1\text{S}_y$ . In this case, as mentioned earlier, a double-Gaussian fit to the TA spectrum is required and marked with purple infilling for the BE feature and with orange infilling for  $\text{Cu}^{1+}$  defect absorption. The second derivative of the PLE probed at the PL peak for both samples exhibits a large red-shift from the expected  $E_g$  determined by the second derivative of the linear absorption spectrum. However, the shift is significantly larger for  $\text{Cu}_{0.85}\text{In}_1\text{S}_y$  (~150 meV, or 2.09 eV vs. 2.24 eV) than  $\text{Cu}_{0.47}\text{In}_1\text{S}_y$  (~100 meV, or 2.15 eV vs. 2.25 eV). In fact, the peak of the second derivative of the  $\text{Cu}_{0.85}\text{In}_1\text{S}_y$  PLE probed at the PL peak has a similar energy to the peak of its corresponding TA bleach (2.06 eV), and the  $\text{Cu}^{1+}$  defect absorption predicted by the subtraction spectrum (2.03 eV, inset of **Figure 3.1.2.1c**). For the more Cu-deficient QDs ( $\text{Cu}_{0.47}\text{In}_1\text{S}_y$ ), the second derivative of the PLE probed at the PL peak (~2.15 eV) is intermediate between the BE and  $\text{Cu}^{1+}$  defect absorption determined by the double-Gaussian fit of the TA bleach (~2.25 eV and 2.03 eV, respectively). Hence, we can conclude that the Stokes shift of CIS QDs is due to  $\text{Cu}^x$  emission, and a combination of

BE (“Apparent” Stokes shift, or  $\Delta_{S,A}$ ) and  $\text{Cu}^{1+}$  defect absorption (“Real” Stokes shift, or  $\Delta_{S,R}$ ). Changes in stoichiometry therefore not only affect the absorption linewidth by altering the relative contribution of each absorptive transition, but also reflect two distinct Stokes shifts that directly impact reabsorption losses in LSCs.

The PLE spectra corresponding with the blue side of the emission peak for  $\text{Cu}_{0.47}\text{In}_1\text{S}_y$  (2.1 to 1.9 eV) shows a large shift in second derivative energy ( $\sim 270$  meV, or 2.37 eV to 2.1 eV). As the probe energy is moved to the red side of the spectra (1.9 eV to 1.6 eV) slightly smaller shifts are observed ( $\sim 160$  meV, or 2.1 to 1.94 eV). Similar trends were observed for the  $\text{Cu}_{0.85}\text{In}_1\text{S}_y$  QDs (Figure S6.3.3), and the energy shifts for both samples are plotted in **Figure 3.1.2.2d** (open red circles for  $\text{Cu}_{0.47}\text{In}_1\text{S}_y$  and open green squares for  $\text{Cu}_{0.85}\text{In}_1\text{S}_y$ ). While it is difficult to entirely eliminate polydispersity in QD size as a contributing factor to the large distribution of PLE second derivative energies, the change in PL energy resonant with the PLE excitation (shown in **Figure 3.1.2.2d** as closed red circles for  $\text{Cu}_{0.47}\text{In}_1\text{S}_y$  and closed green squares for  $\text{Cu}_{0.85}\text{In}_1\text{S}_y$ ) is almost 4 fold smaller than the change in PLE energy ( $\sim 110$  meV variation in PL energy compared with  $\sim 420$  meV variation in PLE energy for both stoichiometries). Considering, as mentioned earlier, that size polydispersity should have a roughly equal effect on *both* the PL and PLE energies, it appears to be unlikely that size polydispersity alone can account for the large shifts in PLE energy, and they are instead occurring *via* absorption from  $\text{Cu}^{1+}$  defects, which becomes weaker as QDs are made more Cu-deficient. Lastly, we determined the probe/excitation energy dependent Stokes shift for both samples (**Figure 3.1.2.2e**) as the energy difference between the PLE probe energy and the peak of its second derivative, and compare to the Stokes shifts determined by TA/PL measurements

for  $\text{Cu}_{0.85}\text{In}_1\text{S}_y$  (grey dashed line), and  $\text{Cu}_{0.47}\text{In}_1\text{S}_y$  (purple dashed line based on BE absorption, and orange dashed line for  $\text{Cu}^{1+}$  defect absorption). Notably, the PLE measured Stokes shift is always considerably larger than predicted by  $\text{Cu}^{1+}$  defect absorption, and is intermediate between that of the BE absorption of  $\text{Cu}_{0.47}\text{In}_1\text{S}_y$  and the convoluted absorption of  $\text{Cu}_{0.85}\text{In}_1\text{S}_y$ , which further confirms that there are two different Stokes shifts for CIS QDs.

**Two-Band Absorption Dynamics.** To monitor the dynamic behavior of the band-edge and  $\text{Cu}^{1+}$  defect absorption bands we use spectrally resolved femtosecond transient absorption spectroscopy. **Figure 3.1.2.3a** displays the time-evolution of the pump-induced changes in absorption ( $-\Delta\alpha$ ) for CIS QDs with three different Cu-to-In ratios. In each case, blue lines represent the bleach at a 1 ps delay, while green represents 10 ps, and red 100 ps. As mentioned earlier, the most Cu-rich QDs ( $\text{Cu}_{1.12}\text{In}_1\text{S}_y$ ) and slightly Cu-deficient ( $\text{Cu}_{0.85}\text{In}_1\text{S}_y$ ) show a bleach that is a convolution of both the band-edge and  $\text{Cu}^{1+}$  defect absorption, and we expect that the dynamics are dominated by  $\text{Cu}^{1+}$  defect absorption. Notably, the intensity of the bleach significantly changes at different delay times for  $\text{Cu}_{1.12}\text{In}_1\text{S}_y$ , but the shape is relatively unaffected. For slightly Cu-deficient QDs, we notice a slight red shift and broadening at longer delay times. The most Cu-deficient QDs ( $\text{Cu}_{0.47}\text{In}_1\text{S}_y$ ), on the other hand, show two definitive absorption bands as described earlier. Interestingly, the band-edge absorption feature is strongest in the first 1 ps before rapidly decreasing after 10 ps. Considering that the low energy shoulder has a small increase in the first 10 ps, but otherwise does not significantly change, the shape of the bleach is altered from a clear high energy peak with a weak shoulder to a near-single, broad Gaussian shape similar to the spectra for the two (near)-stoichiometric QDs. We

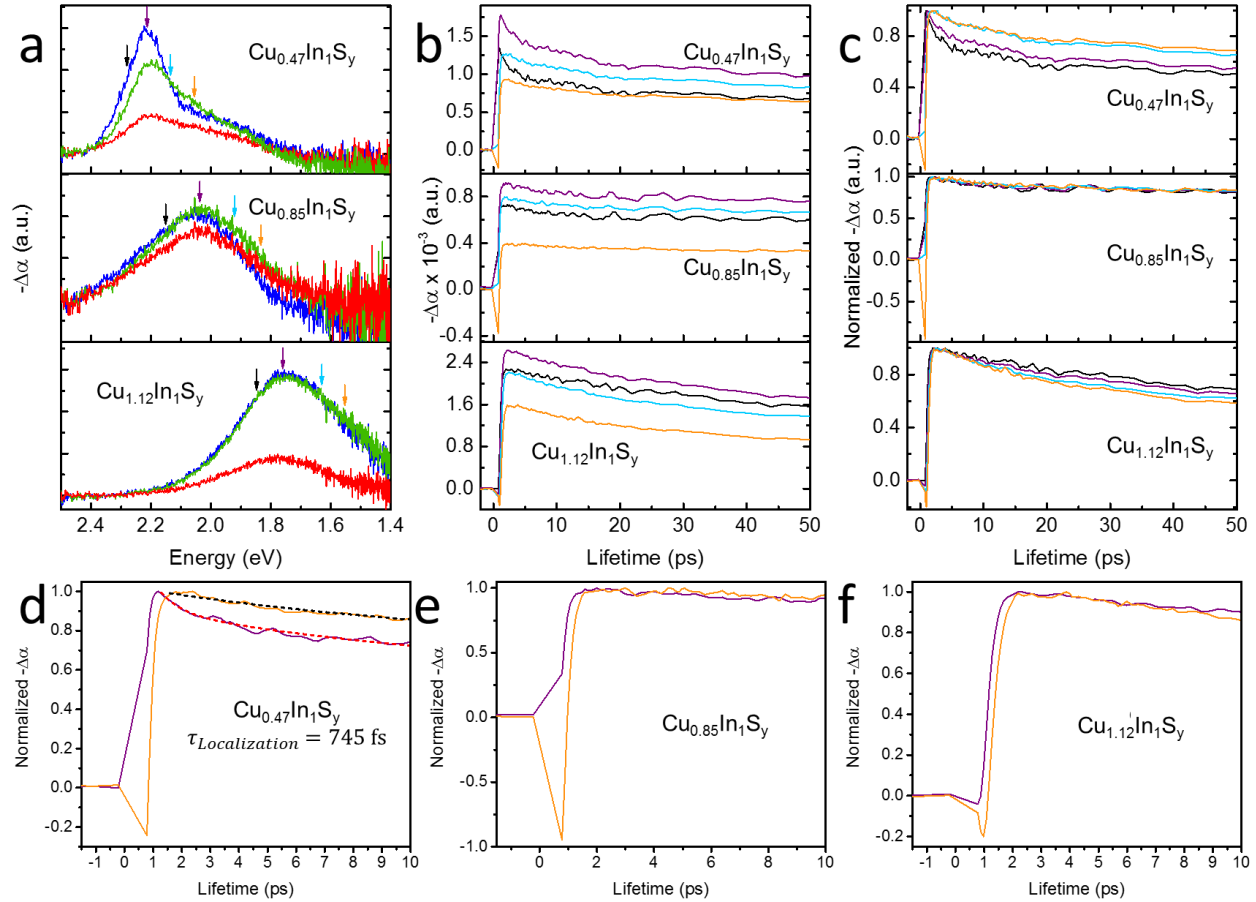


**Figure 3.1.2.3.** (a) Femtosecond spectrally resolved transient absorption measurements: blue represents the spectra in the first 1 ps, green at 10 ps, and red at 100 ps. (b,c) The decay curves for the probe energies marked with the same colors in (a) where (b) is the raw data and (c) is the measurement normalized to the peak TA intensity. For each case, the panels are in the same order as in (a) where the Cu-rich QDs are in the bottom panel, and the most Cu-deficient in the top panel. (d-f) The decay curve at the TA peak (purple) is compared to the decay curve at the reddest probe energy (orange). For the (near)-stoichiometric QDs (e,f) there is no significant difference between the decay rates at different probe energies (with a small difference in the relative amplitude of the decays in Cu-rich QDs due to excessive electron trapping). For highly Cu-deficient QDs, the decay curve at the TA peak has to be fitted with a tri-exponential function (dashed red lines) whereas only a bi-exponential (dashed black lines) is needed for the decay on the red side. The additional component in the TA fit most likely represents hole localization, and its time constant is  $\sim 745$  fs.

interpret these results to reflect a competition between band-edge absorption and  $\text{Cu}^{1+}$  defect absorption where the bleach for near-stoichiometric QDs is dominated by  $\text{Cu}^{1+}$  defects, but is instead governed by the band-edge (for 1 ps), and eventually combination of the two transitions at longer delay times for the highly Cu-deficient QDs. This is

expected as highly Cu-deficient QDs have a larger concentration of  $\text{Cu}^{2+}$  defects, which as mentioned earlier do not absorb a photon in this spectral range, and will not show in the TA bleach or linear absorption spectra.

Considering that most of the shape change in the TA bleach happens after 1 ps, this suggests that the hole capture rate from the VB to the  $\text{Cu}^{1+}$  defect state is less than, or equal to 1 ps. We next plot the dynamics as a function of probe energy (**Figure 3.1.2.3b** for the original data, and **Figure 3.1.2.3c** for the measurements normalized to the peak intensity). For each case, the colors of the TA decays represent the different probe energies marked in **Figure 3.1.2.3a** by arrows with the same colors. Notably,  $\text{Cu}_{1.12}\text{In}_1\text{S}_y$  has a significantly lower quantum yield than the other two samples ( $\sim 5\%$  vs.  $\sim 30\%$ ) and the different decay rates most likely are the result of electron trapping, which are expected to be more significant for these QDs due to their lower emission efficiency. The two Cu-deficient QDs, on the other hand, have near identical size, size-dispersion, and quantum yields and show distinct behaviors. As QDs become more Cu-deficient, they lose their near uniform decay rates as a function of probe energy, and we instead observe large differences (**Figure 3.1.2.3c**) in their probe energy-dependent decays. We compare the difference between the TA peak and the TA probe energy for each sample in **Figures 3.1.2.3d-3f**. The TA decays probed at the bleach peak are fitted using dashed red lines, while the red side is fitted with dashed black lines. For  $\text{Cu}_{0.85}\text{In}_1\text{S}_y$  and  $\text{Cu}_{1.12}\text{In}_1\text{S}_y$  there is no significant difference (other than slight changes in the relative amplitudes for  $\text{Cu}_{1.12}\text{In}_1\text{S}_y$  due to electron trapping) in the fit parameters. However, for  $\text{Cu}_{0.45}\text{In}_1\text{S}_y$  we need an additional component to fit the TA peak (tri-exponential), which is  $\sim 745$  fs. Considering that most of the BE bleach is lost after 1 ps in **Figure 3.1.2.1a**, we believe

this decay rate represents the localization of carriers from the BE to  $\text{Cu}^{1+}$  defects. Hence, even at very low concentrations of  $\text{Cu}^{1+}$  defects hole localization occurs  $\sim 745$  fs, and is expected to be even faster in QD ensembles with higher concentrations of  $\text{Cu}^{1+}$  defects (e.g. in (near)-stoichiometric QDs), which would make BE and  $\text{Cu}^{1+}$  defect absorption indistinguishable in TA measurements where the localization rate may be faster than the IRF. This is in agreement with previous hypotheses that hole localization occurs at the sub-picosecond time-scale.<sup>20</sup>

**Density Functional Theory Calculations & Chemical Origin of the Stokes Shift.** DFT calculations were then performed to determine the structural origin of intra-gap absorption in CIS QDs. For each calculation, we use a conventional exchange-correlation DFT functional (Perdew-Burke-Ernzerhof, or PBE) for determining the local geometric minimum and the Heyd-Scuseria-Ernzerhof (HSE06) hybrid range separated exchange-correlation functional for electronic structure calculations (details in Methods section). HSE06 was chosen for electronic structure calculations due to its ability to accurately reproduce the electronic properties of bulk semiconductors,<sup>27</sup> while PBE was chosen for geometry optimizations due to its lower computational expense. This procedure was validated by calculating the lattice constants of a bulk CIS chalcopyrite unit-cell using PBE and the band gap using HSE06. In both cases, we find excellent agreement with experimental studies. We propose that “ $\text{Cu}^{1+}$ ” defects are caused by anti-site “swapping” of  $\text{Cu}^{1+}$  and  $\text{In}^{3+}$  lattice positions ( $\text{Cu}_{\text{In}} + \text{In}_{\text{Cu}}$ ), while “ $\text{Cu}^{2+}$ ” defects arise from a required charge-compensation of negatively charged copper vacancies ( $\text{V}_{\text{Cu}} + \text{Cu}_{\text{Cu}}$ ). We next calculate the density of states (DOS) for a  $2 \times 2 \times 2$  (128 atom) supercell with anti-site defects to mimic stoichiometric or Cu-rich QDs (**Figure 3.1.2.4a**), and

copper vacancies to predict the properties of Cu-deficient QDs (**Figure 3.1.2.4b**). We use a supercell instead of a QD due to the prevalence of unpassivated surface states that would result in several additional absorption bands in our calculations of the absorption spectrum that are not present in experiment. We mark the band-edges of the DOS for both systems with solid black lines where VB represents the HOMO and CB represents the LUMO of the supercell. The theoretical band gap (1.47 eV) is near-identical for both systems and close to experiment for bulk CIS (1.52 eV).<sup>28</sup> The DOS for anti-site defects shows an occupied (below the Fermi level, or  $E_F$ )  $\text{Cu}^x$  state, which is consistent with our expectations of “ $\text{Cu}^{1+}$ ” defects. On the other hand, the DOS for copper vacancies show a spin-polarized state above the  $E_F$  (unoccupied), which indicates that  $\text{Cu}^{2+}$  ( $\text{Cu}_{\text{Cu}}^{\bullet}$ ) forms to charge-compensate copper vacancies ( $\text{V}_{\text{Cu}}$ ). In both cases, the theoretical Stokes shift (energy difference between VB and  $\text{Cu}^x$ ) is close to experiment, which allows us to conclude that “absorptive  $\text{Cu}^{1+}$  defects” arise from anti-site swapping of  $\text{Cu}^{1+}$  and  $\text{In}^{3+}$  atoms ( $\text{Cu}_{\text{In}} + \text{In}_{\text{Cu}}^{\bullet}$ ) and “non-absorptive  $\text{Cu}^{2+}$  defects” occur to charge compensate copper vacancies ( $\text{V}_{\text{Cu}} + \text{Cu}_{\text{Cu}}^{\bullet}$ ).

To directly relate these DOS to the experimental absorption spectra, we compute their theoretical absorption spectra using linear response theory (**Figure 3.1.2.4b**). This is done using equations 1 and 2:

$$\kappa(\omega) = \sqrt{\frac{\varepsilon_1(\omega)^2 + \varepsilon_2(\omega)^2 - \varepsilon_1(\omega)}{2}} \quad (1)$$

$$\alpha(\omega) = \frac{4\pi}{\lambda} \kappa(\omega) \quad (2)$$

where the linear absorption coefficient ( $\alpha$ ) is determined *via* calculating the real  $\varepsilon_1(\omega)$  and

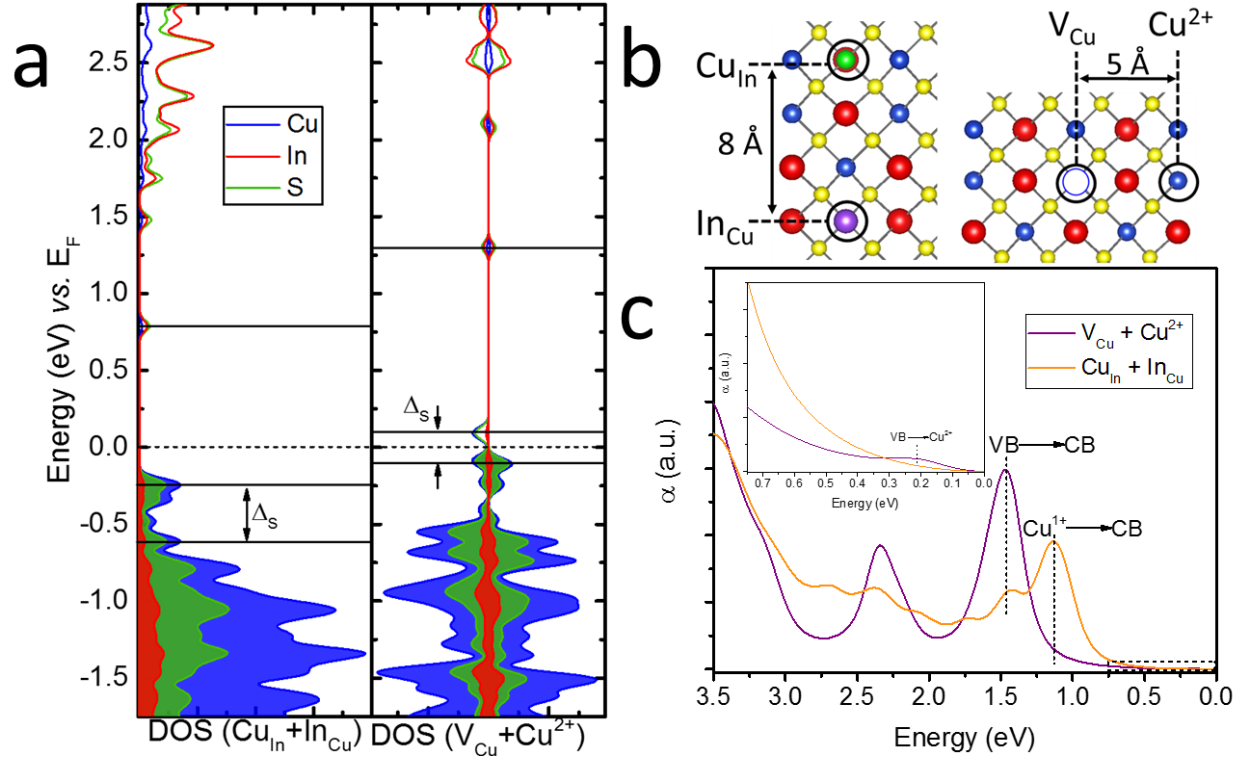


**Figure 3.1.2.4.** (a) DOS for CIS supercells with two different defect pairs. The left panel represents anti-site “Cu<sup>1+</sup> defects” whereas the right panel represents copper vacancies. For the right panel, copper vacancies result in an unoccupied state above the Fermi level, which is spin-polarized due to the removal of an electron from Cu<sup>x</sup>. Hence, the DOS for both spins are represented, and the intra-gap state is referred to as a “Cu<sup>2+</sup> defect” due to its partially filled d shell. (b) Scheme representing the two defect pairs calculated in (a). Cu<sup>1+</sup> defects form after anti-site swapping with In<sup>3+</sup> to make charge-balanced defect pairs. For copper vacancies, the negative charge associated with the removal of a copper atom is charge-compensated by the oxidation of a second copper atom. As a result, we expect Cu<sup>2+</sup> defects to occur in higher concentrations in QD ensembles that are highly Cu-deficient due to the increased prevalence of copper vacancies. (c) The computed linear absorption based on the DOS shown in (a), which indicates that the absorption of a photon promotes an electron from Cu<sup>1+</sup>, or anti-site Cu<sub>In</sub> defects to the CB, which leads to a low energy transition that broadens the absorption spectrum. Cu<sup>2+</sup> defects, on the other hand, do not show this transition due to their partially occupied d shell, which leads to sharper spectra and a more distinct VB → CB absorption peak.

$\epsilon_2(\omega)$  terms of the frequency-dependent dielectric constant. For both cases, we observe a transition near the predicted band-edge transition energy (1.5 eV) as expected by the identical band gaps. However, if CIS has anti-site defects there is a second lower energy transition near the VB → CB transition energy due to the excitation of an electron from a Cu<sup>1+</sup> defect to the CB. If CIS has copper vacancies, on the other hand, there is an IR

transition for a VB electron to the unoccupied  $\text{Cu}^{2+}$  defect (inset of **Figure 3.1.2.4b**), which is outside of the detection range of our TA measurements. This transition is not expected to significantly affect spectral broadening of the excitonic absorption due to its large energy separation from the VB (in QDs this should be between 200 to 750 meV, or roughly equal to the Stokes shift) whereas the  $\text{Cu}^{1+}$  defect absorption, which arises from anti-site  $\text{Cu}_{\text{In}}$  will “smear” excitonic absorption in (near)-stoichiometric QDs with a high concentration of anti-site defects.

As mentioned earlier, anti-site “ $\text{Cu}^{1+}$  defects” must absorb a photon to be photoconverted to  $\text{Cu}^{2+}$  prior to emission whereas  $\text{Cu}^{2+}$  defects are “emission ready.” This photoconversion process results in a vibronically-coupled Franck-Condon shift to a different defect energy in the excited state (**Figure 3.1.2.1a**). We call this process the “real” Stokes shift, or  $\Delta_{S,R}$  in which there is an energy off-set between the intra-gap  $\text{Cu}^{1+}$  defect ( $\sim 200$  meV) from the VB, and an additional shift after photoconversion to excited state  $\text{Cu}^{2+}$  (results in an additional  $\sim 200$  meV shift in energy). Hence, the energy separation between the VB and the excited-state  $\text{Cu}^{2+}$  defect ( $\sim 400$  meV), which we call the “apparent” Stokes shift, or  $\Delta_{S,A}$  is larger than the energy separation between the ground state  $\text{Cu}^{1+}$  defect and the excited-state  $\text{Cu}^{2+}$  defect ( $\sim 200$  meV), or the “real Stokes shift.” For (near)-stoichiometric QDs with a large concentration of anti-site defects the additional absorption transitions broaden the linear absorption spectra, and lead to smaller predicted Stokes shifts if the TA bleach is compared to the PL. Conversely, for highly Cu-deficient QDs there is a larger concentration of  $\text{Cu}^{2+}$  defects required for charge compensation of Cu vacancies. These defects are “emission ready” and only exhibit an “apparent Stokes shift” since there is no excited-state hole localization, or corresponding

vibronically-coupled Franck-Condon shift. Hence, comparison of the TA bleach to emission leads to a larger predicted Stokes shift, and the linear absorption spectra are narrower due to excitonic transitions dominating the spectra.

### 3.1.3. Conclusions

CIS QDs with different Cu-to-In ratios (1.12:1, 0.85:1, and 0.47:1) were synthesized, and their linear spectra compared. We conclude that CIS QDs exhibit two absorptive transitions. Absorption for these QDs is a combination of excitonic (VB  $\rightarrow$  CB) and defect ( $\text{Cu}^{1+} \rightarrow \text{CB}$ ) transitions. DFT calculations show that “ $\text{Cu}^{1+}$  defects” arise from anti-site swapping of  $\text{Cu}^{1+}$  and  $\text{In}^{3+}$  atoms into charge-compensated  $\text{Cu}_{\text{In}} + \text{In}_{\text{Cu}}$  pairs. Considering that the oxidation state of  $\text{Cu}_{\text{In}}$  is still 1+, it has a filled d shell that is capable of direct excitation by an incident photon. These transitions are stronger in (near)-stoichiometric QDs where there is an almost equal concentration of Cu and In atoms, or in Cu-rich QDs where excess Cu also leads to  $\text{Cu}_{\text{In}}$  defects. Highly Cu-deficient QDs, on the other hand, have a large concentration of copper vacancies, and DFT calculations show that these defects are charge-compensated by the oxidation of a second Cu atom ( $\text{Cu}^{1+} \rightarrow \text{Cu}^{2+} + e^-$ ). The electron configuration for  $\text{Cu}^{2+}$  defects shows that the d shell in this case is only partially occupied, and therefore will not undergo direct excitation. Resultantly, the linear absorption spectra for (near)-stoichiometric and Cu-rich QDs is broader than highly Cu-deficient QDs where *both* excitonic and  $\text{Cu}^{1+}$  defect absorption are occurring in the case of the former, and *only* excitonic absorption is occurring in the latter.

After hole localization, which can occur either in the ground state (oxidation of Cu to charge compensate copper vacancies in highly Cu-deficient QDs) or in the excited (direct excitation of anti-site defects) emission occurs *via* recombination of a delocalized CB electron and a  $\text{Cu}^{2+}$  defect. The energy off-set between the VB and the  $\text{Cu}^{2+}$  defect is the “Apparent Stokes shift.” For highly Cu-deficient QDs that are “emission ready” due to their pre-existing hole in the ground state electronic configuration, this is easily measured by comparing the TA bleach with the PL spectra. However, for (near)-stoichiometric QDs there is a second Stokes shift, which we call the “Real Stokes shift.” This is because anti-site defects have their own energy off-set from the VB, and after absorption of an incident photon undergo a vibronically-coupled excited state photoconversion to  $\text{Cu}^{2+}$ . Here, the energy separation between ground-state  $\text{Cu}^{1+}$  defects and excited state  $\text{Cu}^{2+}$  defects is the “Real Stokes shift” whereas the final energy separation between the VB and the excited state  $\text{Cu}^{2+}$  defects is the “Apparent Stokes shift.” In this case, comparison of the TA bleach with PL usually indicates the real Stokes shift considering that excitation of an electron from  $\text{Cu}^{1+}$  to the CB dominates the TA bleach. This hole localization process is extremely fast even in QDs with a lower concentration of  $\text{Cu}^{1+}$  defects ( $\sim 745$  fs), which explains the near-indistinguishable excitonic and Cu absorption in (near)-stoichiometric QDs. A key conclusion based on these findings is that since highly Cu-deficient QDs have a larger concentration of  $\text{Cu}^{2+}$  defects the Apparent Stokes shift dominates the linear and transient spectra and leads to reduced spectral overlap between absorption and emission. Further considering that these defects are not susceptible to hole trapping, and lead to higher QY (assuming no other significant surface chemistry changes), synthesizing QD ensembles with a larger concentration of  $\text{Cu}^{2+}$  defects is a viable route

to reducing reabsorption and increasing QY for CIS QD LSCs. Furthermore, the  $\text{Cu}^{1+}/\text{Cu}^{2+}$  defect ratio can at least partially be controlled by altering the QD stoichiometry with highly Cu-deficient QDs having a higher QY and reduced reabsorption due to the larger concentration of QDs with  $\text{Cu}^{2+}$  defects.

### 3.1.4. Methods

**Synthesis of QDs, Linear Spectroscopy, & DFT Calculations:** The QDs were synthesized following the procedure outlined in Section 2.2.4. DFT calculations were conducted also using the procedure outlined in Section 2.2.4, but on CIS supercells instead of clusters (details in main text). The DOS, and linear absorption spectrum were computed with  $\Gamma$ -centered 2X2X2 K-Points. Linear spectroscopy measurements were conducted using the apparatus described in Section 2.1.4.

**Transient Absorption Spectroscopy Measurements:** TA spectra were collected using a LabView-controlled home built setup with a standard pump-probe configuration. The excitation source was the frequency tripled output of a Pharos amplified Yb:KGW laser (<190 fs pulse duration), and a broad-band, white light supercontinuum probe. For each sample, a pump-fluence-dependent measurement was conducted to determine the absorption cross-section, and all of the spectra shown in the main text reflect the dynamics collected at carrier densities of  $\sim 0.1$  exciton per QD to avoid Auger interactions.

### 3.1.5. References

1. Draguta, S.; McDaniel, H.; Klimov, V. I., Tuning Carrier Mobilities and Polarity of Charge Transport in Films of  $\text{CuInSe}_x\text{S}_{2-x}$  Quantum Dots. *Advanced Materials* 2015, 27 (10), 1701-1705.

2. Meinardi, F.; McDaniel, H.; Carulli, F.; Colombo, A.; Velizhanin, K. A.; Makarov, N. S.; Simonutti, R.; Klimov, V. I.; Brovelli, S., Highly efficient large-area colourless luminescent solar concentrators using heavy-metal-free colloidal quantum dots. *Nat Nano* 2015, 10 (10), 878-885.
3. Yun, H. J.; Lim, J.; Fuhr, A. S.; Makarov, N. S.; Keene, S.; Law, M.; Pietryga, J. M.; Klimov, V. I., Charge-Transport Mechanisms in  $\text{CuInSe}_x\text{S}_{2-x}$  Quantum-Dot Films. *ACS Nano* 2018.
4. Jara, D. H.; Yoon, S. J.; Stampelcoskie, K. G.; Kamat, P. V., Size-Dependent Photovoltaic Performance of  $\text{CuInS}_2$  Quantum Dot-Sensitized Solar Cells. *Chemistry of Materials* 2014, 26 (24), 7221-7228.
5. Bergren, M. R.; Makarov, N. S.; Ramasamy, K.; Jackson, A.; Guglielmetti, R.; McDaniel, H., High-Performance  $\text{CuInS}_2$  Quantum Dot Laminated Glass Luminescent Solar Concentrators for Windows. *ACS Energy Letters* 2018, 3 (3), 520-525.
6. McDaniel, H.; Fuke, N.; Makarov, N. S.; Pietryga, J. M.; Klimov, V. I., An integrated approach to realizing high-performance liquid-junction quantum dot sensitized solar cells. *Nat Commun* 2013, 4.
7. McDaniel, H.; Fuke, N.; Pietryga, J. M.; Klimov, V. I., Engineered  $\text{CuInSe}_x\text{S}_{2-x}$  Quantum Dots for Sensitized Solar Cells. *The Journal of Physical Chemistry Letters* 2013, 4 (3), 355-361.
8. Kim, J.-Y.; Yang, J.; Yu, J. H.; Baek, W.; Lee, C.-H.; Son, H. J.; Hyeon, T.; Ko, M. J., Highly Efficient Copper–Indium–Selenide Quantum Dot Solar Cells: Suppression of

Carrier Recombination by Controlled ZnS Overlayers. ACS Nano 2015, 9 (11), 11286-11295.

9. Du, J.; Du, Z.; Hu, J.-S.; Pan, Z.; Shen, Q.; Sun, J.; Long, D.; Dong, H.; Sun, L.; Zhong, X.; Wan, L.-J., Zn–Cu–In–Se Quantum Dot Solar Cells with a Certified Power Conversion Efficiency of 11.6%. Journal of the American Chemical Society 2016, 138 (12), 4201-4209.

10. Chuang, P.-H.; Lin, C. C.; Liu, R.-S., Emission-Tunable CuInS<sub>2</sub>/ZnS Quantum Dots: Structure, Optical Properties, and Application in White Light-Emitting Diodes with High Color Rendering Index. ACS Appl. Mater. Interfaces 2014, 6 (17), 15379-15387.

11. Castro, S. L.; Bailey, S. G.; Raffaele, R. P.; Banger, K. K.; Hepp, A. F., Synthesis and Characterization of Colloidal CuInS<sub>2</sub> Nanoparticles from a Molecular Single-Source Precursor. The Journal of Physical Chemistry B 2004, 108 (33), 12429-12435.

12. Allen, P. M.; Bawendi, M. G., Ternary I–III–VI Quantum Dots Luminescent in the Red to Near-Infrared. Journal of the American Chemical Society 2008, 130 (29), 9240-9241.

13. Xie, R.; Rutherford, M.; Peng, X., Formation of High-Quality I–III–VI Semiconductor Nanocrystals by Tuning Relative Reactivity of Cationic Precursors. Journal of the American Chemical Society 2009, 131 (15), 5691-5697.

14. Bose, R.; Jana, S.; Manna, G.; Chakraborty, S.; Pradhan, N., Rate of Cation Exchange and Change in Optical Properties during Transformation of Ternary to Doped Binary Nanocrystals. The Journal of Physical Chemistry C 2013, 117 (30), 15835-15841.

15. Fuhr, A.; Yun, H. J.; Makarov, N. S.; Li, H.; McDaniel, H.; Klimov, V. I., Light-Emission Mechanism in  $\text{CuInS}_2$  Quantum Dots Evaluated by Spectral Electrochemistry. *ACS Photonics* 2017.
16. Li, L.; Pandey, A.; Werder, D. J.; Khanal, B. P.; Pietryga, J. M.; Klimov, V. I., Efficient Synthesis of Highly Luminescent Copper Indium Sulfide-Based Core/Shell Nanocrystals with Surprisingly Long-Lived Emission. *Journal of the American Chemical Society* 2011, 133 (5), 1176-1179.
17. Rice, W. D.; McDaniel, H.; Klimov, V. I.; Crooker, S. A., Magneto-Optical Properties of  $\text{CuInS}_2$  Nanocrystals. *The Journal of Physical Chemistry Letters* 2014, 5 (23), 4105-4109.
18. Zang, H.; Li, H.; Makarov, N. S.; Velizhanin, K. A.; Wu, K.; Park, Y.-S.; Klimov, V. I., Thick-Shell  $\text{CuInS}_2/\text{ZnS}$  Quantum Dots with Suppressed “Blinking” and Narrow Single-Particle Emission Line Widths. *Nano Letters* 2017.
19. Jara, D. H.; Stampelcoskie, K. G.; Kamat, P. V., Two Distinct Transitions in  $\text{Cu}_x\text{InS}_2$  Quantum Dots. Bandgap versus Sub-Bandgap Excitations in Copper-Deficient Structures. *The Journal of Physical Chemistry Letters* 2016, 7 (8), 1452-1459.
20. Berends, A. C.; Rabouw, F. T.; Spoor, F. C. M.; Bladt, E.; Grozema, F. C.; Houtepen, A. J.; Siebbeles, L. D. A.; de Mello Donegá, C., Radiative and Nonradiative Recombination in  $\text{CuInS}_2$  Nanocrystals and  $\text{CuInS}_2$ -Based Core/Shell Nanocrystals. *The Journal of Physical Chemistry Letters* 2016, 7 (17), 3503-3509.

21. Knowles, K. E.; Nelson, H. D.; Kilburn, T. B.; Gamelin, D. R., Singlet–Triplet Splittings in the Luminescent Excited States of Colloidal Cu<sup>+</sup>:CdSe, Cu<sup>+</sup>:InP, and CuInS<sub>2</sub> Nanocrystals: Charge-Transfer Configurations and Self-Trapped Excitons. *Journal of the American Chemical Society* 2015, 137 (40), 13138-13147.
22. Klimov, V. I.; Baker, T. A.; Lim, J.; Velizhanin, K. A.; McDaniel, H., Quality Factor of Luminescent Solar Concentrators and Practical Concentration Limits Attainable with Semiconductor Quantum Dots. *ACS Photonics* 2016, 3 (6), 1138-1148.
23. Pietryga, J. M.; Park, Y.-S.; Lim, J.; Fidler, A. F.; Bae, W. K.; Brovelli, S.; Klimov, V. I., Spectroscopic and Device Aspects of Nanocrystal Quantum Dots. *Chemical Reviews* 2016, 116 (18), 10513-10622.
24. van der Stam, W.; de Graaf, M.; Gudjonsdottir, S.; Geuchies, J. J.; Dijkema, J. J.; Kirkwood, N.; Evers, W. H.; Longo, A.; Houtepen, A. J., Tuning and Probing the Distribution of Cu<sup>+</sup> and Cu<sup>2+</sup> Trap States Responsible for Broad-Band Photoluminescence in CuInS<sub>2</sub> Nanocrystals. *ACS Nano* 2018, 12 (11), 11244-11253.
25. Fuhr, A. S.; Sautet, P.; Alexandrova, A. N., Heterogeneity in Local Chemical Bonding Explains Spectral Broadening in Quantum Dots with Cu Impurities. *The Journal of Physical Chemistry C* 2019, 123 (9), 5705-5713.
26. Voznyy, O.; Levina, L.; Fan, F.; Walters, G.; Fan, J. Z.; Kiani, A.; Ip, A. H.; Thon, S. M.; Proppe, A. H.; Liu, M.; Sargent, E. H., Origins of Stokes Shift in PbS Nanocrystals. *Nano Letters* 2017, 17 (12), 7191-7195.

27. Le Bahers, T.; Rérat, M.; Sautet, P., Semiconductors Used in Photovoltaic and Photocatalytic Devices: Assessing Fundamental Properties from DFT. *The Journal of Physical Chemistry C* 2014, 118 (12), 5997-6008.
28. Yamamoto, Y.; Yamaguchi, T.; Tanaka, T.; Tanahashi, N.; Yoshida, A., Characterization of CuInS<sub>2</sub> thin films prepared by sputtering from binary compounds. *Solar Energy Materials and Solar Cells* 1997, 49 (1), 399-405.
29. Sandberg, R. L.; Padilha, L. A.; Qazilbash, M. M.; Bae, W. K.; Schaller, R. D.; Pietryga, J. M.; Stevens, M. J.; Baek, B.; Nam, S. W.; Klimov, V. I., Multiexciton Dynamics in Infrared-Emitting Colloidal Nanostructures Probed by a Superconducting Nanowire Single-Photon Detector. *ACS Nano* 2012, 6 (11), 9532-9540.
30. Kresse, G.; Furthmüller, J., Efficiency of ab-initio total energy calculations for metals and semiconductors using a plane-wave basis set. *Computational Materials Science* 1996, 6 (1), 15-50.
31. Kresse, G.; Furthmüller, J., Efficient iterative schemes for ab initio total-energy calculations using a plane-wave basis set. *Physical Review B* 1996, 54 (16), 11169-11186.
32. Kresse, G.; Hafner, J., *Ab initio* molecular-dynamics simulation of the liquid-metal-amorphous-semiconductor transition in germanium. *Physical Review B* 1994, 49 (20), 14251-14269.
33. Kresse, G.; Hafner, J., Ab initio molecular dynamics for liquid metals. *Physical Review B* 1993, 47 (1), 558-561.

34. Perdew, J. P.; Burke, K.; Ernzerhof, M., Generalized Gradient Approximation Made Simple. *Physical Review Letters* 1996, 77 (18), 3865-3868.
35. Heyd, J.; Scuseria, G. E.; Ernzerhof, M., Hybrid functionals based on a screened Coulomb potential. *The Journal of Chemical Physics* 2003, 118 (18), 8207-8215.
36. Pohl, J.; Albe, K., Thermodynamics and kinetics of the copper vacancy in  $\text{CuInSe}_2$ ,  $\text{CuGaSe}_2$ ,  $\text{CuInS}_2$ , and  $\text{CuGaS}_2$  from screened-exchange hybrid density functional theory. *Journal of Applied Physics* 2010, 108 (2), 023509.
37. Chen, H.; Wang, C.-Y.; Wang, J.-T.; Hu, X.-P.; Zhou, S.-X., First-principles study of point defects in solar cell semiconductor  $\text{CuInS}_2$ . *Journal of Applied Physics* 2012, 112 (8), 084513.

## **3.2. Heterogeneity in Local Chemical Bonding Explains Spectral Broadening in Quantum Dots with Cu Impurities**

### **3.2.1. Introduction**

The size-tunable band gap, solution processability, and multiexcitonic effects of II-VI and IV-VI quantum dots (QDs) make these materials attractive for a broad range of electro-optical applications.<sup>1</sup> Unfortunately, the use of toxic heavy metals (e.g. Cd or Pb) have limited their commercial viability.<sup>2-3</sup> While environmental concerns have spurred research interest in heavy-metal-free multinary and transition metal doped structures, their optical transitions are not well understood, and significantly differ from Cd and Pb chalcogenides.<sup>4-13</sup> For example, QDs with Cu, or Mn cations have large Stokes shifts ( $\Delta_S$ , defined as the energy difference between absorption and emission energies), broad ensemble spectral linewidths, long radiative lifetimes, and tunable magnetic exchange interactions.<sup>6, 14</sup> One possible reason for these peculiar properties is the smaller ionic radii of 3d transition metals, which have greater polarizing power than Cd or Pb, and should form more covalent bonds with early chalcogens. This, in addition to their complex multinary structure make it easier for *extrinsic* (dopant), or *intrinsic* (native defect) impurities to localize photo- or electro-excited carriers to small regions of the crystal lattice where local structural distortions will more strongly affect carrier interactions than delocalized band-edge states.

Of these transition metal based structures, QDs with Cu impurities are particularly interesting. Radiative recombination occurs through a hole localized at a Cu impurity and a delocalized conduction band electron.<sup>4, 7-12, 15</sup> This is distinct from Mn doped QDs where

Mn transitions localize *both* carriers.<sup>16-18</sup> Consequently, Mn emission can only shift within a small range of the visible spectral window due to changes in local strain environment altering the crystal field splitting energy.<sup>18</sup> Cu impurities, on the other hand, have emission energies that are far more tunable, and extend across the visible and infrared regime making them appealing for a broader range of applications.<sup>4, 7-12, 15, 19</sup> However, for each of these applications, improvements in device performance will require a better understanding on how modified environment can affect the optical transitions. We propose here that chemical bonding plays a key role. Specifically,  $\Delta_S$  can vary by > 500 meV for Cu impurities in QDs with the same basic structure (*e.g.* CIS QDs),<sup>9, 20</sup> and even more (>1 eV) when comparing different structures (*e.g.* Cu doped CdS and CdTe QDs).<sup>12</sup> Further, single particle spectroscopy studies have shown that the intrinsic photoluminescence (PL) linewidth for CIS QDs is over 80% narrower (60 vs. 352 meV) than the ensemble; and, there are large dot-to-dot variations in PL linewidth (~150 meV), emission energy (~300 meV), and radiative lifetimes (~250 ns) within the *same* ensemble.<sup>10</sup> Controlling these properties will be essential to achieving narrow emission for high color purity LEDs, reduce spectral overlap for reabsorption-free solar windows, and tune emission energy for infrared photodetectors.<sup>3, 10, 21-25</sup>

In this work, we use density functional theory (DFT) calculations to systematically investigate the effects of the local environment and chemical bonding on the Cu impurity energy levels in Cu-doped ZnSe QDs. We predict the effects of structural heterogeneity on electronic states by altering the bonding environment of Cu impurities, and compare the electronic structure, charge distribution, and absorption spectra for several kinetically trapped local minima. The Stokes shift and spectral linewidth for QDs with Cu impurities

is highly sensitive to the impurity position (e.g. surface vs. subsurface), coordination environment (e.g. tetrahedral vs. distorted trigonal planar), and concentration (**Figure 3.2.2.1**). We further note that while there are significant variations in the experimental properties of Cu impurities in QDs, large Stokes shifts, broad linewidths, and long radiative lifetimes are consistently observed across all structures, and suggest that our predictions should be applicable to similar materials such as Cu-doped InP or CIS QDs.<sup>8</sup>

19

### 3.2.2. Results and Discussion

**Properties of Cu Impurities in ZnSe QDs.** We systematically explored the effect of Cu impurity position, coordination environment, and concentration on the optical properties of ZnSe QDs (**Figure 3.2.2.1**). Chalcogen-rich (Zn:Se ratio ~1:1.25), spherical ZnSe QDs based on the zinc blende crystal phase were constructed exposing (111) and (200) surface facets, and terminated by pseudo-hydrogens to maintain charge balance. This eliminates most of the dangling bond surface states by using  $x\text{H}$  where  $x$  is the fractional charge used to achieve local charge neutrality (here,  $x = 0.25$ ),<sup>35-38</sup> and mimics the surface passivation of long-chain organic ligands typically used in experiment to disperse QDs in organic solvents.<sup>4, 7-8, 11</sup> This approach is effective at reducing the surface state contribution to the density of states (DOS) and predicting optical absorption and emission energies. However, considering the extreme sensitivity of the absolute QD band positions to ligand selection,<sup>39-40</sup> this approach would not be accurate for determining QD band positions vs. vacuum. We determined the local minima structures using the Perdew-Burke-Ernzerhof (PBE) functional because of its ability to provide good geometries and low computational expense.<sup>30</sup> However, the Heyd-Scuseria-Ernzerhof (HSE06) functional

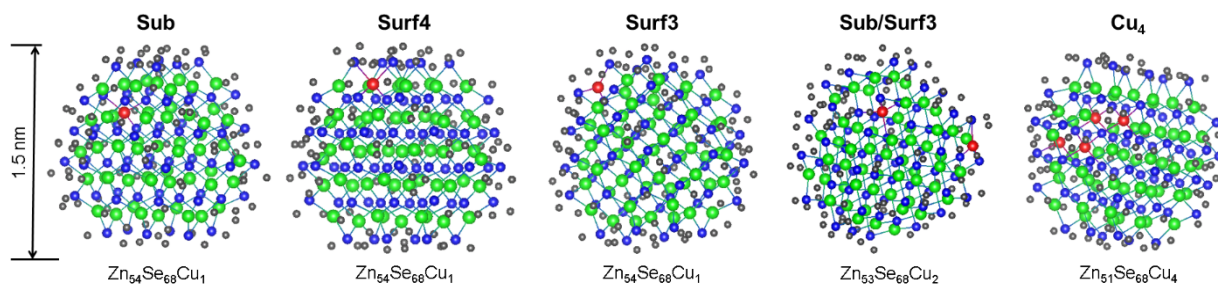


**Figure 3.2.2.1.** Calculated local minima for 1.5 nm ZnSe QDs doped with  $\text{Cu}^{1+}$  atoms. “Sub” refers to subsurface impurities, “Surf4” and “Surf3” refer to surface impurities with a coordination number of 4 or 3, “Sub/Surf3” refers to QDs with 2 Cu impurities in the “Sub” and “Surf3” positions, and “Cu<sub>4</sub>” refers to QDs with 4 Cu atoms doped as a cluster. For Sub and Surf3, additional calculations with  $\text{Cu}^{2+}$  dopants are also described. Zn atoms are depicted in green, Se in blue, Cu in red, and pseudo-hydrogens in grey.

was used for all other calculations due to its ability to accurately predict semiconductor band gaps.<sup>41</sup> We tested this procedure on bulk ZnSe (Figure S6.4.1), and found excellent agreement with experiment.<sup>42</sup>

For direct comparison with QDs, we calculated the electronic structure of bulk ZnSe doped with either  $\text{Cu}^{1+}$  or  $\text{Cu}^{2+}$  impurities (Figure S6.4.2). Considering that the expected oxidation state of Zn in ZnSe is 2+, Cu impurities that replace Zn as anti-site  $\text{Cu}_{\text{Zn}}$  defects are expected to be  $\text{Cu}^{2+}$ . Indeed, the spin-polarized density of states (DOS) show a Cu state with an unpaired electron above the Fermi level (unoccupied), which is the expected behavior of a paramagnetic  $d^9$  impurity. The properties of  $\text{Cu}^{1+}$  impurities, on the other hand, are calculated as an anti-site defect with an additional electron ( $\text{Cu}_{\text{Zn}}^-$ ). In this case, the Cu state is below the Fermi level (occupied) as expected of a  $d^{10}$  cation. While we will eventually show that traditional description of Cu oxidation states is complicated due to covalent bonding, this result suggests that describing their photophysics in the context of  $d^{10}$  (occupied) or  $d^9$  (unoccupied) cations is still informative. **Figure 3.2.2.2a** shows the calculated DOS for a QD doped with  $\text{Cu}^{1+}$  at a subsurface lattice site, which exemplifies the basic optical properties (e.g. large Stokes shift)

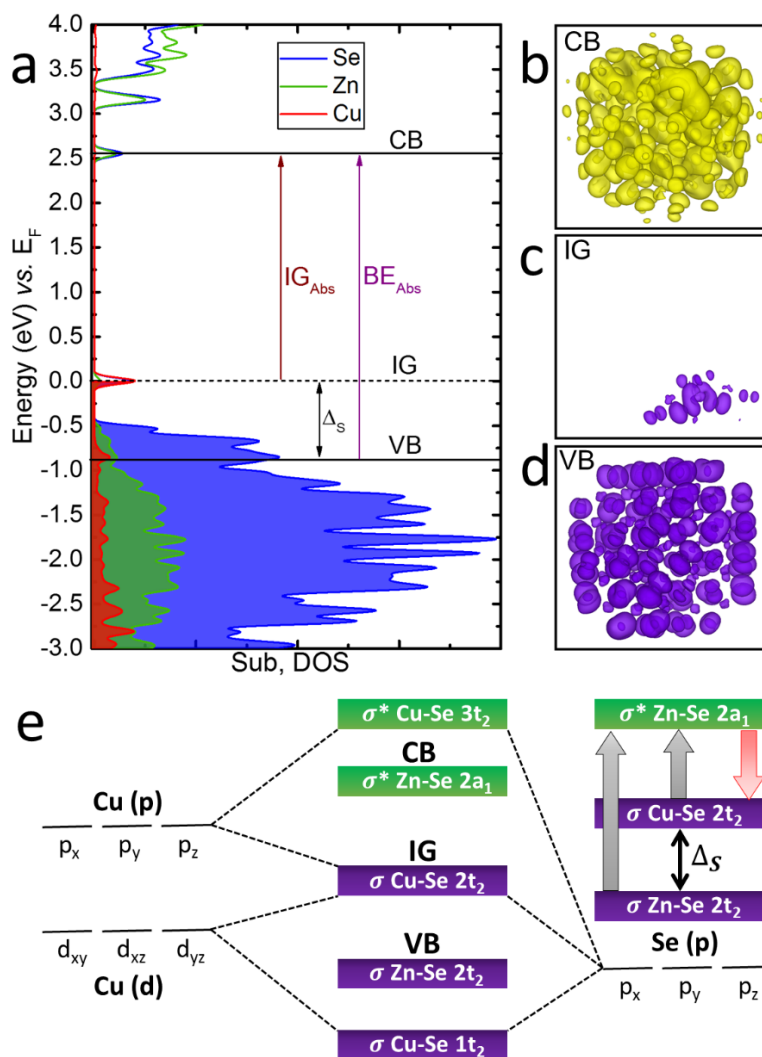


**Figure 3.2.2.2.** (a) DOS for subsurface  $\text{Cu}^{1+}$  doped ZnSe QDs. Band-edges (BE) are marked by solid black lines and the intragap “IG”  $\text{Cu}^{1+}$  impurity state is marked by a dashed line (here, at the Fermi level). Possible optical absorption transitions are marked by colored arrows and the theoretical Stokes shift, or  $\Delta_S$  (energy off-set between IG and VB) is also labeled. The CB was determined to be the lowest unoccupied delocalized state (b), IG to be the Cu-Se occupied localized state (c), and VB to be the highest occupied delocalized state (d) based on the charge density distributions, which are shown in purple for occupied, and yellow for unoccupied energy levels. All unlabeled states between VB and IG are surface “trap-like” states. (e) The molecular orbital (MO) diagram for the QD, which includes the local tetrahedral coordination environment predicting the orbital hybridization for Cu-Se  $\sigma$  bonds. The BE states for Zn are also shown, and their full description is presented in Figure S6.4.3 using bulk ZnSe. The panel on the right of (e) depicts possible optical absorption (grey arrows) and emission (red arrow) transitions corresponding with the MO diagram.

predicted for all of the Cu doped QD systems studied here. The band-edge (BE) states are marked by solid black lines and labeled as “VB” for valence band or “CB” for the

conduction band. BE and impurity states were determined by analyzing the charge density distribution for each DOS (**Figure 3.2.2.2b-d**). CB (**Figure 3.2.2.2b**) refers to the lowest unoccupied delocalized state, and VB (**Figure 3.2.2.2d**) is the highest occupied delocalized state. The electronic wave function squared for the Cu impurity (labeled “IG” for intragap state) is localized to the Cu-Se tetrahedra (**Figure 3.2.2.2c**), and marked by a dashed line in the DOS. We note here that our description of “delocalized” states, while reflecting a significant symmetry-allowed mixing of molecular orbitals (MOs), does not necessarily indicate a highly shared charge distribution over the entire QD. Considering that QDs are smaller than the exciton Bohr radius (distance between the electron-hole pair), excitons formed *via* BE states are localized by the confinement potential. Hence, BE excitons will be delocalized across the entire QD regardless of whether the chemical bonds forming the VB and CB states are truly delocalized.

The VB has almost 90% Se (p) orbital character, while the CB has a nearly equal contribution of Se (~60%) and Zn (~40%) (s) electrons. Further comparison with bulk ZnSe shows similar trends, but with less Se character for both bands (~81% in the VB and ~45% in the CB). This small deviation is expected due to the higher concentration of Se atoms in the QD. Indeed, the orbital DOS for the QD CB in Figure S6.4.4 shows that the (s) electron ratio for Se and Zn is roughly the same as the bulk calculation (Zn:Se $\approx$ 1.10:1 for the QD, and 1.17:1 for bulk), but there is a larger Se (p) contribution in the CB that is roughly equivalent to the excess Se (~22.9%). Nonetheless, the orbital contribution of ZnSe in both the QD and bulk calculations can be explained using simple crystal field theory considerations (summarized in **Figure 3.2.2.2e** and shown in more detail in Figure S6.4.3). Three of the metal (d) orbitals (specifically,  $d_{xy}$ ,  $d_{xz}$ ,  $d_{yz}$ ) exhibit

the same  $t_2$  symmetry as the metal (p) orbitals in tetrahedrally coordinated transition metal complexes. These MOs overlap to form  $\sigma$  bonds with the (p) orbitals of the ligand (here, Se), which also exhibit  $t_2$  symmetry. For  $Zn^{2+}$ , which has an  $[Ar]3d^{10}$  electron configuration, the  $\sigma$  bonding orbitals would form occupied  $1t_2$  and  $2t_2$  states. The latter of which would act as the QD HOMO. The anti-bonding  $3t_2$  states, however, would be higher in energy than the anti-bonding  $\sigma^*$  states formed between the metal and ligand (s) orbitals, which have the  $a_1$  symmetry and act as the LUMO (**Figure 3.2.2.2e** and Figure S6.4.3). This description of the band structure using crystal field theory will be important in our later description of Cu bonding and shifts in ground state energy levels. However, we note here that the other two (d) orbitals in Cu and Zn ( $d_z^2$ ,  $d_{x^2-y^2}$ ) would have the e symmetry and should form an additional nonbonding energy level (Figure S6.4.3). In both cases, the e state would be below  $2t_2$ . This is insignificant for predicting optical trends for Zn as the  $2t_2$  state would still be the highest occupied delocalized state (VB). On the other hand, for Cu, this may lead to additional absorptive/emissive sub-band gap infrared transitions not discussed here (e.g.  $2t_2 \rightarrow 2e$ ) if the Cu  $2e$  state is higher in energy than the VB.<sup>43</sup>

The QDs studied here are far smaller than the exciton Bohr radius for ZnSe (1.5 nm vs 4.5 nm).<sup>44</sup> Consequently, they are in the strong confinement regime and have a significantly larger band gap than in the bulk calculation. The confinement energy (defined as the energy difference between the bulk band gap and the gap of the quantum confined structure) is  $\sim 0.9$  eV, which is close to what is predicted by the effective mass model.<sup>45</sup> IG, in the case of  $Cu^{1+}$  is at the Fermi level, and is therefore occupied. Hence, a maroon arrow marking a possible optical absorption transition (labeled  $IG_{abs}$ ) is shown in addition

to the expected BE absorption transition ( $BE_{abs}$ ) in the DOS (**Figure 3.2.2.2a**), and a scheme is included in **Figure 3.2.2.2e** next to the MO diagram for the expected absorption/emission transitions. Additional unlabeled states between the VB ( $\sim -1$  eV) and Cu ( $\sim 0$  eV) are of surface origin (Figure S6.4.5) and typically form traps. The projected density of states (PDOS) indicate that IG has a large ( $\sim 42\%$ ) contribution from Se (p) atomic orbitals, and the projected charge density is localized across the entire Cu-Se tetrahedra. Similar to our ZnSe bulk calculations, we plot the PDOS (Figure S6.4.4) for each MO of the QD, and also find that the Cu IG level is predominantly composed of the  $d_{xy}$ ,  $d_{xz}$ ,  $d_{yz}$  orbitals with a small contribution from the Cu (p) orbitals. This suggests that, much like in ZnSe, the  $t_2$  symmetry allows Cu to form  $\sigma$  bonds with the (p) orbitals of Se, and IG is the Cu-Se  $2t_2$  state.

**Chemical Bonding Effects on Cu Impurity Energy Levels.** **Figure 3.2.2.3a** shows the DOS for  $Cu^{1+}$  impurities in 3 different configurations: subsurface (Sub), surface with tetrahedral geometry (Surf4), and surface with distorted trigonal planar geometry (Surf3). These configurations represent three of the four possible impurity environments for ZnSe. The fourth, Surf2, is unlikely to form due to the high diffusivity of Cu in QDs.<sup>7, 11</sup> We calculated the formation energies for the different impurity configurations using eq 1.

$$\Delta E_{Cu-conf.} = E_{Cu:QD} - E_{QD} + \sum_{\alpha} n_{\alpha} (E_{\alpha}^{solid} + \mu_{\alpha}) \quad (1)$$

where  $E_{Cu:QD} - E_{QD}$  represents the energy difference between the “pure” QD and QD with Cu impurities,  $E_{\alpha}^{solid}$  is the energy per atom of elemental solid  $\alpha$  (Cu or Zn),  $n_{\alpha}$  is the number of atoms added ( $n_{\alpha} = -1$ ) or removed ( $n_{\alpha} = +1$ ), and  $\mu_{\alpha}$  is the chemical potential of  $\alpha$ , which can range from  $\Delta H_{f \alpha X_n}^{bulk} \leq \mu_{\alpha} \leq \mu_{\alpha}^{bulk}$ . The lower bound corresponds with the

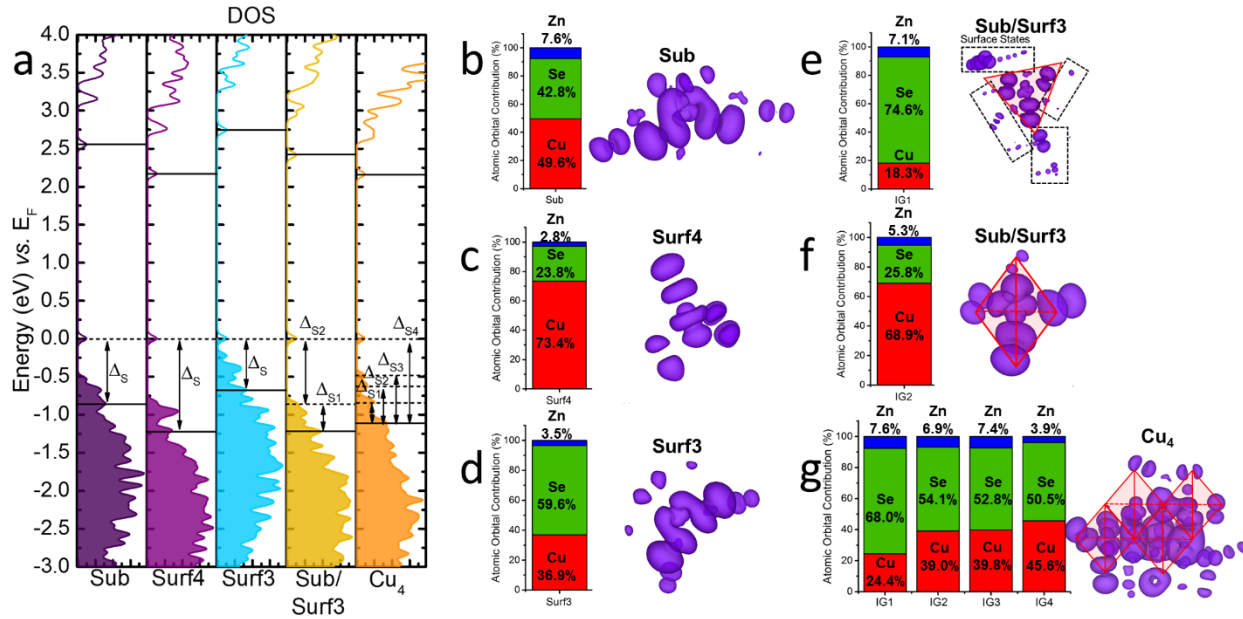


**Figure 3.2.2.3.** (a) Effect of impurity position, coordination environment, and concentration on the DOS. The charge density distribution for each labeled IG state (marked by dashed lines) is depicted in (b-g) along with its orbital contribution to the corresponding DOS. A higher concentration of Cu (1.85%, 3.77%, and 7.84%, respectively) leads to additional absorptive/emissive states. For moderately doped QDs (e-f) the charge density of each labeled state is separately localized on its respective impurity ( $\Delta_{S1}$  on the 3-coordinated surface Cu, and  $\Delta_{S2}$  on the subsurface Cu). At higher impurity concentrations (g) the charge density is localized on all 4 Cu dopants regardless of the IG state energy.

$\alpha$  poor condition and the upper bound corresponds with the  $\alpha$  rich condition.<sup>46-47</sup> For simplicity, we assumed  $\Delta\mu_\alpha = 0$  for both Cu and Zn, which corresponds with Cu-rich and Zn-rich synthesis conditions. The formation energy for each structure is negative ( $\Delta E_{Sub} = -0.382 eV$ ,  $\Delta E_{Surf4} = -1.758 eV$ , and  $\Delta E_{Surf3} = -0.214$ ), thus suggesting that Se has a higher affinity towards Cu than Zn, and that Cu-Se chemical bonds should correspondingly be stronger than Zn-Se. However, we note here that our calculated Cu impurity formation energies are not precise, as the reaction conditions for synthesizing Cu-doped ZnSe QDs are generally Cu-poor and Zn-rich.<sup>4,7</sup> This would lead to a negative  $\Delta\mu_{Cu}$ , result in positive formation energies, and prevent the formation of a competing  $Cu_{2-x}Se_x$  phase.<sup>46</sup> In addition, while Surf4 has the lowest formation energy of the series, binding

with surface ligands and leaching of Cu into the solution are commonly observed in experiment.<sup>7, 11</sup> A full understanding of the most stable impurity environments would require studies comparing the impurity formation energy at different surface facets to their binding energy with organic ligands. Issues with determining the absolute formation energy of Cu impurities aside, the *comparative* formation energies between the different bonding environments should not be significantly affected by  $\Delta\mu_{Cu}$ . Surf4 is the thermodynamically most stable impurity ( $\sim -1.376$  eV vs.  $\Delta E_{Sub}$ ), and Surf3 is the least stable ( $\sim +0.168$  eV vs.  $\Delta E_{Sub}$ ). The large difference in formation energies indicate that the different configurations are not thermodynamically competitive, and we postulate that they are kinetically trapped during crystal growth as described with Mn impurities.<sup>48-49</sup>

In each of these cases, the impurity concentration is the same ( $\sim 1.85\%$  based on the Cu/Zn ratio). Hence, two additional calculations (also shown in **Figure 3.2.2.3a**) were performed in which the concentration was increased to  $3.77\%$  (Sub/Surf3) and  $7.84\%$  (Cu<sub>4</sub>). For the case where the impurity concentration is  $3.77\%$ , one Cu atom is in the Sub configuration and the other is in the Surf3 configuration. The QD with the highest concentration of Cu impurities ( $7.84\%$ ) is labeled Cu<sub>4</sub> to indicate that it includes 4 Cu impurities, similar to what is expected for Cu doped QDs synthesized by the cluster-seeded method.<sup>48</sup> Three of the Cu impurities are in the subsurface while one is on the surface, and all are tetrahedrally coordinated. For all impurity bonding environments and concentrations,  $\Delta_S$  is defined as the energy difference between the VB and the Cu state in accordance with the optical absorption and emission mechanisms described in **Figure 3.2.2.2e**. Clearly, there is considerable variation in the ground state energy and orbital hybridization for Cu impurities as their position, bonding environment, and concentration

change. For example, the DOS for the Sub IG state has a considerably larger orbital contribution from Cu than the IG state in Surf3, but a smaller Cu contribution than the IG state in Surf4. Correspondingly, its theoretical  $\Delta_S$  is intermediate between the two. If the impurity concentration increases to 3.77% (as in Sub/Surf3), we observe two distinct IG states related to the two different Cu impurities. The distorted trigonal planar Cu impurity on the surface (same environment as Surf3) has a smaller Stokes shift ( $\Delta_{S1}$ ), and a larger Se contribution than the impurity located in the subsurface ( $\Delta_{S2}$ ). Interestingly, the DOS for the Cu<sub>4</sub> composition similarly shows multiple Cu states, but the charge density distribution appears to be delocalized over all four Cu tetrahedra. This complicates a further discussion of the individual Cu impurities in Cu<sub>4</sub> (**Figure 3.2.2.3g**). In Figure S6.4.6 we project the DOS states on each Cu tetrahedra, and show that they all contribute significantly to all IG states, although dominant ones are still present in each state. Moreover, Surf4 is still the Cu impurity with the largest Stokes shift ( $\Delta_{S4}$ ), and has the largest Cu contribution.

We summarize these results in **Figure 3.2.2.4**, and come back to our earlier strategy of describing Cu energy levels with crystal field theory. As shown in **Figure 3.2.2.4a-c**, tetrahedral Cu impurities clearly have a larger  $\Delta_S$ , and orbital contribution from Cu, than in the distorted trigonal planar geometry. This suggests that the smaller  $\Delta_S$  for Surf3 is due to breaking of tetrahedral symmetry, which increases the orbital overlap between Cu (d) and Se (p) in the distorted trigonal planar geometry, and results in higher Se character in the DOS. This relationship between coordination number and Se contribution can be explained by VESPR. As the coordination number reduces from 4 to 3 the average bond angle increases from 108.5° to 119.2° (ideal 109.5° for tetrahedral

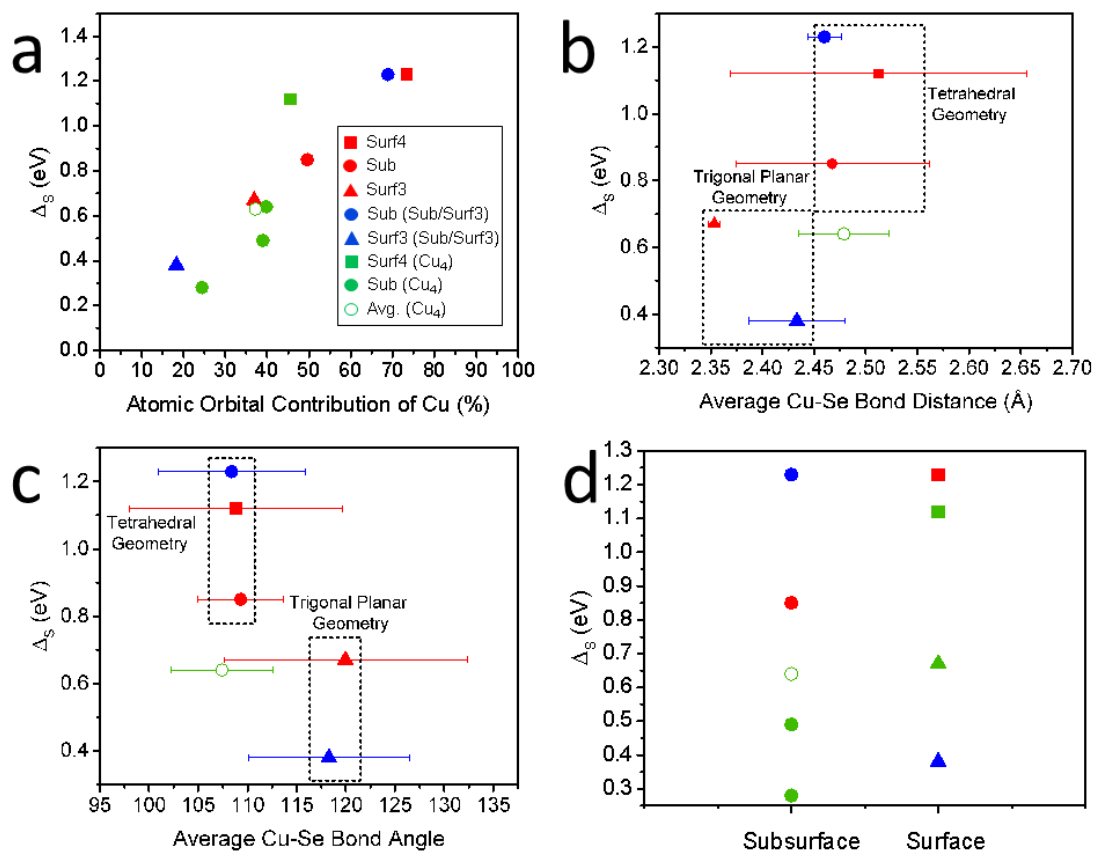


**Figure 3.2.2.4.** Summary of the effects of chemical bonding on the theoretical Stokes shift. The clearest trends emerge in (a-c), which show that the ground state energy of Cu impurities is predominantly determined by coordination geometry and orbital contribution from Cu. IG states with less Cu character and in the distorted trigonal planar geometry tend to have smaller Stokes shifts. All bond distances and angles are presented as the average between each Cu-Se bond in the coordination sphere, and error bars represent the standard deviation from the average bond angle or distance. (d) There does not appear to be a trend in changes of the ground state energy for surface vs. subsurface Cu impurities.

and 120° for trigonal planar, respectively) in order to reduce repulsion between Se (p) electrons. The reduced Se-Se repulsion allows for the average Cu-Se bond length contraction from ~2.48 to 2.39 Å. The bonds become stronger and more covalent. The covalency is additionally afforded by the AO-hybridization on Cu, which becomes more pronounced in the context of the reduced symmetry of Cu coordination (Figure S6.4.7). As a result of stronger and more covalent bonding, the IG state is lower in energy.

Considering that the distorted trigonal planar geometry is unlikely to occur for

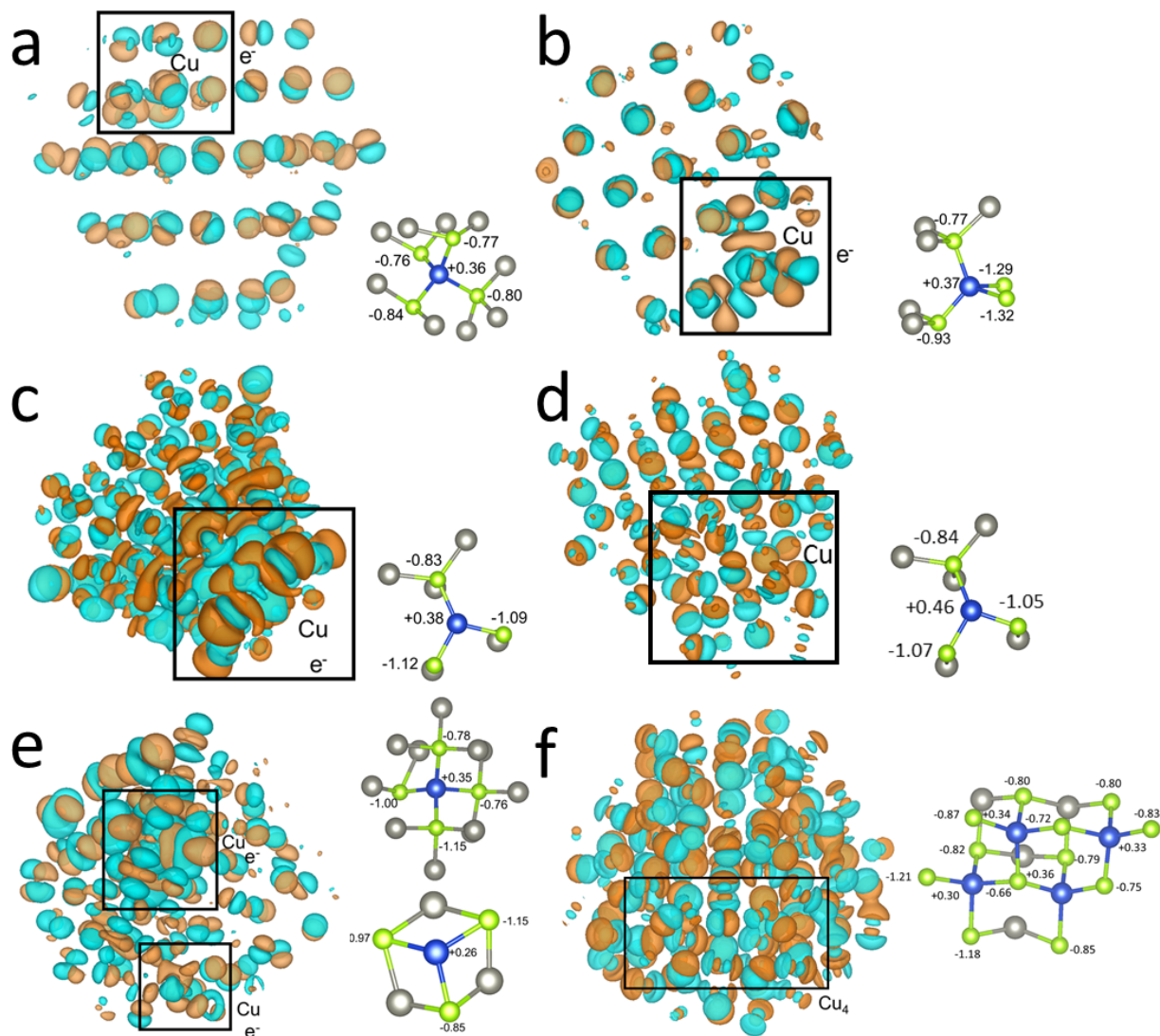


**Figure 3.2.2.5.** Charge density difference plots and Bader charges for each of the Cu impurity centers. QDs with a single Cu<sup>1+</sup> impurity are shown in (a-c), which represent the Sub, Surf4, and Surf3 systems, respectively. Calculations for Surf3 (d) and Surf4 (Figure S6.4.8) were repeated using single Cu<sup>2+</sup> impurities. QDs with multiple Cu<sup>1+</sup> impurities are shown in (e-f) where (e) represents the Sub/Surf3 system and (f) represents the Cu<sub>4</sub> system.

subsurface impurities, this implies that  $\Delta_S$  should be consistently smaller for surface Cu.

However, if we plot  $\Delta_S$  for surface vs. subsurface Cu in **Figure 3.2.2.4d**, we clearly observe that there is no correlation between  $\Delta_S$  and proximity to the surface. Surface impurities with tetrahedral coordination (Surf4) have a *larger*  $\Delta_S$  than at the subsurface location. We explore reasons for this observation in **Figure 3.2.2.5** by analyzing the

charge density difference plots and Bader charges (Table S6.4.1). The charge distribution confirms that the surface and subsurface Zn-Se bonds are more ionic, whereas the Cu-Se bonds are more covalent. However, both become more polar at the surface: the average charge of the Se surface atoms (-1.18 e) is significantly more negative than Se in the subsurface (-0.83 e), whereas the average Bader charge on Cu and Zn is relatively unchanged (at  $q(\text{Cu}) \approx +0.37$  e and  $q(\text{Zn}) \approx +0.80$  e). This effect might be impacted by the model nature of the passivation with pseudo-hydrogen atoms. Specifically, the “mimicking” of ligand passivation with pseudo-hydrogens should be similar to experiments utilizing chalcogen-rich QDs and/or thiol surface passivation,<sup>7</sup> but may not be applicable to experiments using metal-rich QDs and/or different ligands (e.g. oleic acid).<sup>4</sup> On the other hand, the basic optical properties of Cu impurities (e.g.  $\Delta_S$  and linewidth) are not significantly affected by ligand exchange, which generally only has a notable impact on quantum yield due to a shift in the Fermi level that alters the carrier trapping mechanism.<sup>7</sup>

<sup>9</sup> We therefore expect that differences between charge-distribution at the surface vs. the subsurface should also occur for other surface treatments as well, but the exact effects on chemical bonding may somewhat vary based on the specific surface and/or passivating ligand. The higher bond polarity is destabilizing for covalent Cu-Se bonds, and leads to increased repulsion between Se atoms, and stretches the Cu-Se bonds (average around  $\sim 0.05$  Å, or an increase from  $\sim 2.47$  to  $\sim 2.52$  Å). The overlap between Cu (d) and Se (p) orbitals reduces, increasing the energy of the Cu-Se states relative to the VB. However, the destabilizing effects of increased bond polarity at the surface are mostly overcome by the switch from  $T_d$  to  $D_{3h}$  symmetry, which allows for a bond contraction as described earlier. Accordingly, this indicates that the energy of  $\Delta_S$  is a

consequence of covalent overlap, which is affected by geometry and reflects itself in the charge distribution.

As expected,  $\text{Cu}^{2+}$  is less covalent than  $\text{Cu}^{1+}$  both in Sub, and Surf3. However, it is still more covalent than Zn-Se, which can be explained by Fajan's rules for polarizing power.  $\text{Cu}^{2+}$  should have a greater polarizing power than  $\text{Zn}^{2+}$  due to its unfilled (d) shell, which reduces shielding and makes charge transfer from Se (p) more favorable. The changes in charge and bond length after an electron is added are largely asymmetric, and suggestive of Jahn-Teller effects. Indeed, these Jahn-Teller effects are expected, as indicated in computational chemistry studies on homogeneous broadening mechanisms (electron-phonon coupling) in Cu-doped QDs.<sup>51</sup>

In order to determine if our observations were an artifact of the jellium positive background induced to compensate the electron injected in the QD to create  $\text{Cu}^{1+}$ , we repeated our calculations for Sub and Surf3 without the addition of an electron. In this case, calculations were spin-polarized due to the magnetic exchange interactions observed experimentally in QDs with  $\text{Cu}^{2+}$  ( $d^9$ ) impurities.<sup>6, 8</sup> **Figure 3.2.2.5c,d** shows a comparison of Surf3 with ( $\text{Cu}^{1+}$ ) and without ( $\text{Cu}^{2+}$ ) an extra electron, while Figure S6.4.8 shows the same comparison for the Sub QD. In both cases, Bader charges are far from what is expected by the typical description of Cu oxidation states in QDs. In the  $\text{Cu}_{\text{Zn}}$ , or " $\text{Cu}^{2+}$ " scenario, the Bader charge on Cu is only +0.46 e for both Surf3 (**Figure 3.2.2.5d**) and Sub (Figure S6.4.8). After an electron is added, the charge on Cu in Surf3 and Sub changes by -0.08 e and -0.1 e, respectively. The more negative charge on Cu is accompanied by a small bond contraction (average  $\sim 0.01$  Å for Sub, and  $\sim 0.03$  Å for Surf3). However, the overall qualitative picture holds true without the background charge.

**Effects of Variations in Chemical Bonding on Optical Spectra.** We calculate the absorption spectrum for ZnSe QDs as a function of Cu<sup>1+</sup> impurity concentration using linear response theory (independent orbital approximation/single particle level, see **Figure 3.2.2.6**). The absorption coefficient ( $\alpha$ ) of the materials was calculated from the frequency-dependent dielectric constant with eq. 2 and eq. 3.

$$\kappa(\omega) = \sqrt{\frac{\varepsilon_1(\omega)^2 + \varepsilon_2(\omega)^2 - \varepsilon_1(\omega)}{2}} \quad (2)$$

$$\alpha(\omega) = \frac{4\pi}{\lambda} \kappa(\omega) \quad (3)$$

where  $\kappa(\omega)$  is the extinction coefficient, and  $\varepsilon_1(\omega)$  and  $\varepsilon_2(\omega)$  are the real and imaginary terms of the dielectric constant, respectively. The transitions near 2.7 eV in the absorption spectra represent the direct excitation of an electron from the Cu<sup>1+</sup> impurity to the CB, transitions ~3.4 eV represent VB→CB or BE absorption, and higher energy transitions reflect absorption from either the VB or Cu<sup>1+</sup> to higher energy unoccupied states. As expected, the BE transition is relatively constant (~3.4 eV) regardless of the Cu impurity concentration, and reflects the confinement energy expected from the DOS. IG and higher energy transitions, on the other hand, are strongly dependent on the concentration of Cu<sup>1+</sup>. The BE peak becomes less clear as it is “smeared” by the additional low energy “tail,” and high energy transitions from Cu<sup>1+</sup> to the CB and higher energy states. These results indicate that broadening of experimental absorption spectra is predominantly a reflection of the concentration of Cu<sup>1+</sup> impurities. This also suggests that, if hole localization from the VB is fast enough, at high concentrations of Cu<sup>1+</sup> impurities the bleach in transient absorption spectroscopy measurements could become dominated by low energy impurity transitions instead of BE absorption as proposed in a recent study on

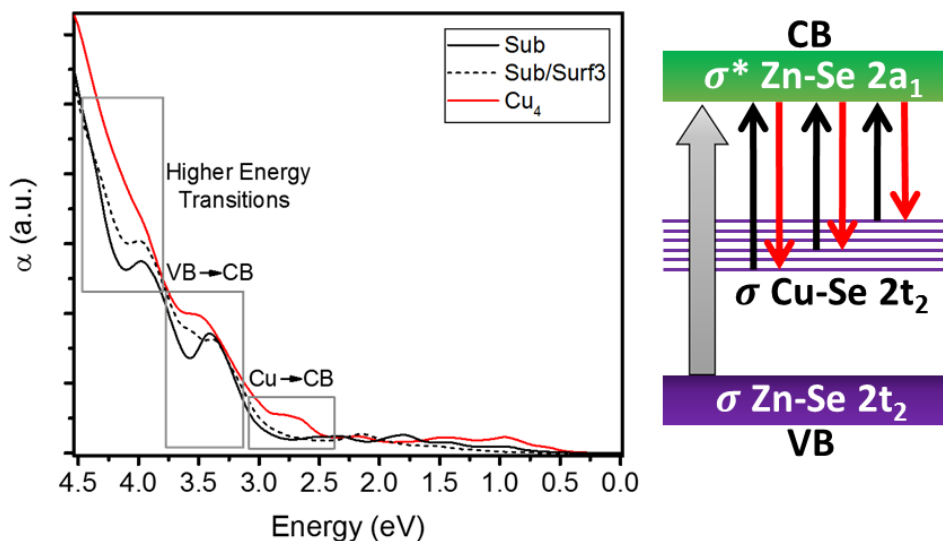


**Figure 3.2.2.6.** Computed absorption spectra for Cu doped ZnSe QDs with different impurity concentrations (left panel). A high Cu content leads to additional absorptive states, and inhomogeneous broadening. Considering that these impurities are also emissive, the same effects should also lead to broadening of emission spectra (right panel). For the scheme, BE absorption is marked by the grey arrow, Cu absorption by black arrows, and Cu emission by red arrows.

related CIS QDs.<sup>52</sup>

In addition to the absorption transitions, the scheme in **Figure 3.2.2.6** also shows expected emission transitions. While these are not directly calculated, extensive experimental work has shown that emission in QDs with Cu impurities arise from a CB electron recombining with a hole localized at Cu.<sup>4, 7-8, 11, 19</sup> Therefore, variations in the ground state energy of Cu<sup>1+</sup> due to heterogeneity should also be reflected in the emission spectra. We note, however, that broadening of the absorption spectra by Cu impurities can *only* occur due to variations in the *ground* state energy of Cu<sup>1+</sup>. PL broadening, on the other hand, will also reflect changes in the ground state energy of Cu<sup>2+</sup> impurities, Franck-Condon shifts, electron-phonon coupling, and other *excited* state interactions.<sup>10,</sup>  
<sup>49</sup> These limitations aside, recent single particle spectroscopy measurements on CIS QDs, which also emit *via* Cu impurities has shown that variations in emission energy are

far larger than expected based on polydispersity of QD size.<sup>10</sup> In addition, these measurements revealed that the PL linewidth can be as narrow as 60 meV, and vary by ~150 meV in the same ensemble. This suggests that inhomogeneous broadening (e.g. variations in QD structure) more significantly impacts the ensemble linewidth than electron-phonon coupling, which would be an intrinsic optical process and reflected in all room temperature spectra. It was therefore hypothesized that the emission energy of Cu impurities is highly sensitive to their location in the QD. Our calculations confirm this interpretation. Hence, we predict that Cu impurities in other QD systems such as ZnSe should also show narrow emission spectra if the Cu impurity concentration is low, and photon anti-bunching experiments indicate that emission is from a single-particle. Moreover, our calculations predict that if heterogeneity is better controlled, ensemble spectra can also be narrow and Cu impurities can be utilized in environmentally benign high color purity LEDs.

An additional phenomenon that our calculations may help explain is the mysteriously large variation of radiative lifetimes and spectral linewidths for Cu impurities at the single particle level, which also cannot be accounted for fully in other models. For example, electron-phonon coupling mechanisms expect larger singlet-triplet splitting energies for Cu impurities located closer to the QD core.<sup>49</sup> This would suggest a systemic relation between Stokes shift and linewidth for individual particles. In a separate study, it was hypothesized that excited-state holes localized at Cu impurities near the QD surface would exhibit stronger wave function overlap with the delocalized CB electron than impurities located below the surface.<sup>49</sup> This would result in smaller Stokes shifts and shorter radiative lifetimes for surface Cu impurities. However, while the radiative lifetimes

and spectral linewidths for CIS QDs at the single particle level can vary by as much as 250 ns and 150 meV, there is no systematic relation between the Stokes shift and the PL linewidths or radiative lifetimes. Instead, experimental measurements of PL linewidths and radiative lifetimes have a “random” distribution when plotted vs. single-particle emission energy.<sup>10</sup> Inability to reconcile either of these models with experimental variations in radiative lifetimes and PL linewidths indicates that an *additional* factor must contribute to large variations in the emission energy. According to our DFT calculations, heterogeneity also alters the *ground* state energy of the impurity, which should not have any notable effect on the radiative lifetime. The Stokes shift for individual particles is therefore most likely a convolution of heterogeneity in the *ground* state energy due to chemical bonding effects, additional shifts in the *excited* state due to changes in the wave function overlap between a localized hole and delocalized CB electron,<sup>10</sup> and homogeneous broadening due to electron-phonon coupling.<sup>49</sup> Considering that only excited state interactions should have an impact on the radiative lifetime, and both effects should alter the Stokes shift, the net result would be a random distribution of experimental radiative lifetimes as a function of emission energy. In addition, variations in the concentration of Cu impurities across experimental ensembles would also broaden individual spectra, and it would be difficult to deconvolute the effects of electron-phonon coupling as a function of emission energy in experimental ensembles where the concentration of impurities per QD is not uniform, thereby, also leading to a “random” distribution of PL linewidths as a function of Stokes shift in single-particle experiments. An interesting, but unexplored consequence of the “random” distribution of PL linewidths and radiative lifetimes might be significant variation in the rates of nonradiative decay.

While this is beyond the scope of our study, nonadiabatic molecular dynamics may prove to be a useful tool for resolving this mystery.<sup>53-55</sup>

### 3.2.3. Conclusions

In this study, we used DFT calculations to show the influence of chemical bonding on the properties of Cu impurities in ZnSe QDs. We find that Cu-Se bonds are covalent, and therefore highly sensitive to their proximity to the QD surface, and coordination number. If Cu-Se retains its tetrahedral coordination at the QD surface, the increased polarity from excess electrons on Se will destabilize the coordination sphere due to increased Se-Se repulsion. Correspondingly, the Cu-Se bonds will stretch, the overlap between Cu (d) and Se (p) electrons will be reduced, and the energy of the intragap (IG) state will increase relative to the band-edges (BEs). This would lead to an increased Stokes shift at the single particle level. However, if the tetrahedral coordination is lost and Cu-Se becomes distorted trigonal planar at the surface, Se-Se repulsion will be reduced due to an increase in bond angles, the Cu-Se bonds will contract, and increased overlap between Cu (d) and Se (p) electrons would decrease the Stokes shift. If the concentration of impurities is high, this would lead to multiple IG states, several absorption/emission transitions, and single particle spectra will broaden. Accordingly, broad ensemble spectra can be explained by a combination of electron-phonon coupling and the coexistence of several kinetically trapped local Cu-Se minima where large variations in absorption/emission energy lead to spectral broadening after ensemble averaging.

A clear experimental implication from our study is that spectral broadening for QDs with Cu impurities is predominantly due to inhomogeneity, and can be controlled if the per

QD concentration of impurities, and their spatial distribution across the ensemble are uniform. Moreover, our calculations show that modeling efforts to study doped or defective QDs where impurities are optically active should emphasize structural/spectral variations in the ensemble, which form subensembles with distinct optical properties. Correspondingly, prediction of their optical properties should be based on several local minima instead of a global minimum.

### 3.2.4. Methods

Plane-wave PAW DFT in VASP<sup>26-29</sup> was used for all geometry optimizations and electronic structure calculations. For geometry optimizations, we used the PBE<sup>30</sup> functional. While, HSE06<sup>31</sup> was used for all electronic structure and charge distribution calculations. The energy cut-off (320 eV) was the same for all calculations, and all structures were relaxed until forces were smaller than 0.05 eV/Å per atom. The screening parameter for all HSE06 calculations was  $\omega=0.13$ , as described in previous reports.<sup>32-33</sup> The experimental properties of bulk ZnSe were reproduced by sampling the Brillouin zone of a ZnSe unit cell with a (6x6x6) Monkhorst-Pack k-point grid. Bulk Cu<sup>1+</sup> and Cu<sup>2+</sup>-doped ZnSe calculations utilized a 2x2x2 supercell where the Brillouin zone was sampled using a Gamma-centered (2x2x2) k-point grid. Spherical QDs were constructed based on the (111) and (200) surface facets with a vacuum spacing of ~ 15 Å to isolate each QD, and avoid QD-QD interactions. The geometry for the entire QD (including pseudo-hydrogens) was optimized. For QDs, the Brillouin zone was sampled at the Gamma point only. Cu<sup>2+</sup> impurities in both bulk and QD calculations were modeled by replacing a Zn<sup>2+</sup> atom with Cu, and using the MAGMOM tag to capture magnetic interactions. Cu<sup>1+</sup> calculations used

the same procedure, but without the MAGMOM tag and with an electron added to the cell. Atomic charges were calculated using the Bader charge algorithm with PW-DFT.<sup>34</sup>

### 3.2.5. References

1. Pietryga, J. M.; Park, Y.-S.; Lim, J.; Fidler, A. F.; Bae, W. K.; Brovelli, S.; Klimov, V. I., Spectroscopic and Device Aspects of Nanocrystal Quantum Dots. *Chem. Rev.* 2016, 116, 10513-10622.
2. Pons, T.; Pic, E.; Lequeux, N.; Cassette, E.; Bezdetnaya, L.; Guillemin, F.; Marchal, F.; Dubertret, B., Cadmium-Free CuInS<sub>2</sub>/ZnS Quantum Dots for Sentinel Lymph Node Imaging with Reduced Toxicity. *ACS Nano* 2010, 4, 2531-2538.
3. Aldakov, D.; Lefrancois, A.; Reiss, P., Ternary and quaternary metal chalcogenide nanocrystals: synthesis, properties and applications. *J. Mater. Chem. C* 2013, 1, 3756-3776.
4. Brovelli, S.; Galland, C.; Viswanatha, R.; Klimov, V. I., Tuning Radiative Recombination in Cu-Doped Nanocrystals via Electrochemical Control of Surface Trapping. *Nano Lett.* 2012, 12, 4372-4379.
5. Meinardi, F.; McDaniel, H.; Carulli, F.; Colombo, A.; Velizhanin, K. A.; Makarov, N. S.; Simonutti, R.; Klimov, V. I.; Brovelli, S., Highly efficient large-area colourless luminescent solar concentrators using heavy-metal-free colloidal quantum dots. *Nat. Nano.* 2015, 10, 878-885.

6. Pandey A; Brovelli S; Viswanatha R; Li L; Pietryga, J. M.; Klimov, V. I.; Crooker, S. A., Long-lived photoinduced magnetization in copper-doped ZnSe-CdSe core-shell nanocrystals. *Nat. Nano.* 2012, 7, 792-797.
7. Viswanatha, R.; Brovelli, S.; Pandey, A.; Crooker, S. A.; Klimov, V. I., Copper-Doped Inverted Core/Shell Nanocrystals with “Permanent” Optically Active Holes. *Nano Lett.* 2011, 11, 4753-4758.
8. Knowles, K. E.; Nelson, H. D.; Kilburn, T. B.; Gamelin, D. R., Singlet–Triplet Splittings in the Luminescent Excited States of Colloidal  $\text{Cu}^+:\text{CdSe}$ ,  $\text{Cu}^+:\text{InP}$ , and  $\text{CuInS}_2$  Nanocrystals: Charge-Transfer Configurations and Self-Trapped Excitons. *J. Am. Chem. Soc.* 2015, 137, 13138-13147.
9. Fuhr, A.; Yun, H. J.; Makarov, N. S.; Li, H.; McDaniel, H.; Klimov, V. I., Light-Emission Mechanism in  $\text{CuInS}_2$  Quantum Dots Evaluated by Spectral Electrochemistry. *ACS Photonics* 2017, 4, 2425-2435.
10. Zang, H.; Li, H.; Makarov, N. S.; Velizhanin, K. A.; Wu, K.; Park, Y.-S.; Klimov, V. I., Thick-Shell  $\text{CuInS}_2/\text{ZnS}$  Quantum Dots with Suppressed “Blinking” and Narrow Single-Particle Emission Line Widths. *Nano Lett.* 2017, 17, 1787-1795.
11. Hughes, K. E.; Hartstein, K. H.; Gamelin, D. R., Photodoping and Transient Spectroscopies of Copper-Doped  $\text{CdSe}/\text{CdS}$  Nanocrystals. *ACS Nano* 2018, 12, 718-728.
12. Knowles, K. E.; Hartstein, K. H.; Kilburn, T. B.; Marchioro, A.; Nelson, H. D.; Whitham, P. J.; Gamelin, D. R., Luminescent Colloidal Semiconductor Nanocrystals

Containing Copper: Synthesis, Photophysics, and Applications. *Chem. Rev.* 2016, 116, 10820-10851.

13. Maiti, S.; Dana, J.; Jadhav, Y.; Debnath, T.; Haram, S. K.; Ghosh, H. N., Electrochemical Evaluation of Dopant Energetics and the Modulation of Ultrafast Carrier Dynamics in Cu-Doped CdSe Nanocrystals. *J. Phys. Chem. C* 2017, 121, 27233-27240.

14. Bussian, D. A.; Crooker, S. A.; Yin, M.; Brynda, M.; Efros, A. L.; Klimov, V. I., Tunable magnetic exchange interactions in manganese-doped inverted core-shell ZnSe-CdSe nanocrystals. *Nat. Mater.* 2008, 8, 35.

15. Li, L.; Pandey, A.; Werder, D. J.; Khanal, B. P.; Pietryga, J. M.; Klimov, V. I., Efficient Synthesis of Highly Luminescent Copper Indium Sulfide-Based Core/Shell Nanocrystals with Surprisingly Long-Lived Emission. *J. Am. Chem. Soc.* 2011, 133, 1176-1179.

16. Chen, H.-Y.; Maiti, S.; Son, D. H., Doping Location-Dependent Energy Transfer Dynamics in Mn-Doped CdS/ZnS Nanocrystals. *ACS Nano* 2012, 6, 583-591.

17. Peng, B.; Liang, W.; White, M. A.; Gamelin, D. R.; Li, X., Theoretical Evaluation of Spin-Dependent Auger De-Excitation in Mn<sup>2+</sup>-Doped Semiconductor Nanocrystals. *J. Phys. Chem. C* 2012, 116, 11223-11231.

18. Xu, X.; Wang, W.; Liu, D.; Hu, D.; Wu, T.; Bu, X.; Feng, P., Pushing up the Size Limit of Metal Chalcogenide Supertetrahedral Nanocluster. *J. Am. Chem. Soc.* 2018, 140, 888-891.

19. Rice, W. D.; McDaniel, H.; Klimov, V. I.; Crooker, S. A., Magneto-Optical Properties of CuInS<sub>2</sub> Nanocrystals. *J. Phys. Chem. Lett.* 2014, 5, 4105-4109.
20. Zhong, H.; Zhou, Y.; Ye, M.; He, Y.; Ye, J.; He, C.; Yang, C.; Li, Y., Controlled Synthesis and Optical Properties of Colloidal Ternary Chalcogenide CuInS<sub>2</sub> Nanocrystals. *Chem. Mater.* 2008, 20, 6434-6443.
21. Klimov, V. I.; Baker, T. A.; Lim, J.; Velizhanin, K. A.; McDaniel, H., Quality Factor of Luminescent Solar Concentrators and Practical Concentration Limits Attainable with Semiconductor Quantum Dots. *ACS Photonics* 2016, 3, 1138-1148.
22. Jiang, Y.; Cho, S.-Y.; Shim, M., Light-emitting diodes of colloidal quantum dots and nanorod heterostructures for future emissive displays. *J. Mater. Chem. C* 2018, 6, 2618-2634.
23. Konstantatos, G.; Howard, I.; Fischer, A.; Hoogland, S.; Clifford, J.; Klem, E.; Levina, L.; Sargent, E. H., Ultrasensitive solution-cast quantum dot photodetectors. *Nature* 2006, 442, 180.
24. Bergren, M. R.; Makarov, N. S.; Ramasamy, K.; Jackson, A.; Guglielmetti, R.; McDaniel, H., High-Performance CuInS<sub>2</sub> Quantum Dot Laminated Glass Luminescent Solar Concentrators for Windows. *ACS Energy Lett.* 2018, 520-525.
25. Sandroni, M.; Wegner, K. D.; Aldakov, D.; Reiss, P., Prospects of Chalcopyrite-Type Nanocrystals for Energy Applications. *ACS Energy Lett.* 2017, 1076-1088.

26. Kresse, G.; Furthmüller, J., Efficiency of ab-initio total energy calculations for metals and semiconductors using a plane-wave basis set. *Comput. Mater. Sci.* 1996, 6, 15-50.
27. Kresse, G.; Furthmüller, J., Efficient iterative schemes for ab initio total-energy calculations using a plane-wave basis set. *Phys. Rev. B* 1996, 54, 11169-11186.
28. Kresse, G.; Hafner, J., *Ab Initio* molecular-dynamics simulation of the liquid-metal-amorphous-semiconductor transition in germanium. *Phys. Rev. B* 1994, 49, 14251-14269.
29. Kresse, G.; Hafner, J., Ab initio molecular dynamics for liquid metals. *Phys. Rev. B* 1993, 47, 558-561.
30. Perdew, J. P.; Burke, K.; Ernzerhof, M., Generalized Gradient Approximation Made Simple. *Phys. Rev. Lett.* 1996, 77, 3865-3868.
31. Heyd, J.; Scuseria, G. E.; Ernzerhof, M., Hybrid functionals based on a screened Coulomb potential. *J. Chem. Phys.* 2003, 118, 8207-8215.
32. Pohl, J.; Albe, K., Thermodynamics and kinetics of the copper vacancy in  $\text{CuInSe}_2$ ,  $\text{CuGaSe}_2$ ,  $\text{CuInS}_2$ , and  $\text{CuGaS}_2$  from screened-exchange hybrid density functional theory. *J. Appl. Phys.* 2010, 108, 023509.
33. Chen, H.; Wang, C.-Y.; Wang, J.-T.; Hu, X.-P.; Zhou, S.-X., First-principles study of point defects in solar cell semiconductor  $\text{CuInS}_2$ . *J. Appl. Phys.* 2012, 112, 084513.
34. Tang, W.; Sanville, E.; Henkelman, G., A grid-based Bader analysis algorithm without lattice bias. *J. of Phys.: Condensed Matter* 2009, 21, 084204.

35. Peng, H.; Li, J.; Li, S.-S.; Xia, J.-B., First-Principles Study on Rutile TiO<sub>2</sub> Quantum Dots. *J. Phys. Chem. C* 2008, 112, 13964-13969.
36. Gai, Y.; Peng, H.; Li, J., Electronic Properties of Nonstoichiometric PbSe Quantum Dots from First Principles. *J. Phys. Chem. C* 2009, 113, 21506-21511.
37. Li, J.; Wang, L.-W., Band-structure-corrected local density approximation study of semiconductor quantum dots and wires. *Phys. Rev. B* 2005, 72, 125325.
38. Huang, X.; Lindgren, E.; Chelikowsky, J. R., Surface passivation method for semiconductor nanostructures. *Phys. Rev. B* 2005, 71, 165328.
39. Kroupa, D. M.; Voros, M.; Brawand, N. P.; McNichols, B. W.; Miller, E. M.; Gu, J.; Nozik, A. J.; Sellinger, A.; Galli, G.; Beard, M. C. *Nat. Commun.* 2017, 8, 15257.
40. Brown, P. R.; Kim, D.; Lunt, R. R.; Zhao, N.; Bawendi, M. G.; Grossman, J. C.; Bulovic, V. Energy Level Modification in Lead Sulfide Quantum Dot Thin Films through Ligand Exchange. *ACS Nano* 2014, 8, 5863
41. Le Bahers, T.; Rérat, M.; Sautet, P., Semiconductors Used in Photovoltaic and Photocatalytic Devices: Assessing Fundamental Properties from DFT. *J. Phys. Chem. C* 2014, 118, 5997-6008.
42. Theis, D., Wavelength-modulated reflectivity spectra of ZnSe and ZnS from 2.5 to 8 eV. *Phys. Status Solidi b* 1977, 79, 125-130.
43. Suzuki, A.; Shionoya, S., Mechanism of the Green-Copper Luminescence in ZnS Crystals. I. Direct Evidence for the Pair Emission Mechanism. *J. Phys. Soc. Jpn.* 1971, 31, 1455-1461.

44. Reiss, P., ZnSe based colloidal nanocrystals: synthesis, shape control, core/shell, alloy and doped systems. *New J. Chem.* 2007, 31, 1843-1852.
45. Proshchenko, V.; Dahnovsky, Y., Long-lived emission in Mn doped CdS, ZnS, and ZnSe diluted magnetic semiconductor quantum dots. *Chem. Phys.* 2015, 461, 58-62.
46. Persson, C.; Zhao, Y.-J.; Lany, S.; Zunger, A., n-type doping of CuInSe<sub>2</sub> and CuGaSe<sub>2</sub>. *Phys. Rev. B* 2005, 72, 035211.
47. Chen, S.; Walsh, A.; Gong, X.-G.; Wei, S.-H., Classification of Lattice Defects in the Kesterite Cu<sub>2</sub>ZnSnS<sub>4</sub> and Cu<sub>2</sub>ZnSnSe<sub>4</sub> Earth-Abundant Solar Cell Absorbers. *Adv. Mater.* 2013, 25, 1522-1539.
48. Norris, D. J.; Efros, A. L.; Erwin, S. C., Doped Nanocrystals. *Science* 2008, 319, 1776-1779.
49. Erwin, S. C.; Zu, L.; Haftel, M. I.; Efros, A. L.; Kennedy, T. A.; Norris, D. J., Doping semiconductor nanocrystals. *Nature* 2005, 436, 91.
50. Jawaid, A. M.; Chattopadhyay, S.; Wink, D. J.; Page, L. E.; Snee, P. T., Cluster-Seeded Synthesis of Doped CdSe:Cu<sub>4</sub> Quantum Dots. *ACS Nano* 2013, 7, 3190-3197.
51. Nelson, H. D.; Li, X.; Gamelin, D. R., Computational Studies of the Electronic Structures of Copper-Doped CdSe Nanocrystals: Oxidation States, Jahn–Teller Distortions, Vibronic Bandshapes, and Singlet–Triplet Splittings. *J. Phys. Chem. C* 2016, 120, 5714-5723.

52. Jara, D. H.; Stampelcoskie, K. G.; Kamat, P. V., Two Distinct Transitions in  $\text{Cu}_x\text{InS}_2$  Quantum Dots. Bandgap versus Sub-Bandgap Excitations in Copper-Deficient Structures. *J. Phys. Chem. Lett.* 2016, 7, 1452-1459.
52. Trivedi, D. J.; Wang, L. J.; Prezhdo, O. V. Auger-Mediated Electron Relaxation Is Robust to Deep Hole Traps: Time-Domain Ab Initio Study of CdSe Quantum Dots. *Nano Lett.* 2015, 15, 2086–2091.
53. Long, R.; Prezhdo, O. V. Ab Initio Nonadiabatic Molecular Dynamics of the Ultrafast Electron Injection from a PbSe Quantum Dot into the  $\text{TiO}_2$  Surface. *J. Am. Chem. Soc.* 2011, 133, 19240–19249. 53.
54. Neukirch, A. J.; Hyeon-Deuk, K.; Prezhdo, O. V. Time Domain Ab Initio Modeling of Excitation Dynamics in Quantum Dots. *Coord. Chem. Rev.* 2014, 263, 161–181.

### **3.3. Distinguishing between Homogeneous & Inhomogeneous Spectral Broadening: Single Particle & Temperature-Dependent Ensemble Spectroscopy of $\text{Cu}_x\text{In}_{2-x}\text{S}_y$ Quantum Dots**

#### **3.3.1. Introduction**

$\text{Cu}_x\text{In}_{2-x}\text{S}_y$  (CIS) quantum dots (QDs) are attractive non-toxic alternatives to Cd-containing QDs for solid-state-lighting.<sup>1-10</sup> However, the broad emission linewidths (typically >250 meV) limit their utility in commercial devices.<sup>11-21</sup> Single-particle spectroscopy and temperature-dependent ensemble spectroscopy can help distinguish between *homogeneous* broadening (e.g. electron-phonon coupling) and *inhomogeneous* broadening (e.g. spatial distribution of optically-active defects, or polydispersity of QD sizes) mechanisms. Discerning between these spectral broadening mechanisms can serve two primary functions: (1) provide further evidence confirming that emission is due to Cu impurities (native defects for CIS, or extrinsic Cu dopants for ZnSe) instead of self-trapped excitons (see Chapter 2 and Chapter 3, sections 3.1 and 3.2); and (2) determine whether the broad ensemble photoluminescence (PL) spectra is intrinsic to CIS QDs, or if it results from sample heterogeneity where dot-to-dot variations in the emission wavelength are averaged to a single broad peak in the ensemble PL. For the self-trapped exciton emission model, spectral linewidths are expected to be *intrinsically* broad, which leaves little room to develop synthetic, or device fabrication strategies to sharpen the spectra for various (electro)-optical applications. If the origin of PL broadening is due to heterogeneity, on the other hand, then improvement of synthetic techniques can, in principle reduce heterogeneity and lead to experimental, device-scale ensembles with narrow PL linewidths ideal for high color purity light emitting diodes (LEDs).

Here, we use single particle spectroscopy to show that individual CIS QDs developed by UbiQD can have linewidths as narrow as  $\sim 50$  meV. This is an important and exciting result, which suggests that there are no fundamental obstacles towards using these QDs in solid-state lighting applications, and other technology that require narrow emission linewidths. In this thesis chapter, we present the spectra from 11 individual CIS QDs, and show that the broad linewidths typically observed in the ensemble are not intrinsic, but instead are due to variations in the peak emission energy. This likely results from sample heterogeneities due to the nonuniformity of QD sizes, and the positional disorder of intra-gap defects that serve as radiative recombination centers in these materials (see DFT calculations in Chapter 3, section 3.2). Furthermore, we use temperature-dependent ensemble PL measurements to determine the strength of electron-phonon coupling for QD ensembles, and find that their contribution to spectral broadening is negligible in comparison to heterogeneity. These results clearly show that narrow ensemble linewidths are achievable with CIS QDs with future improvements to synthetic/device fabrication protocols.

### **3.3.2. Results & Discussion**

Single-particle spectra for CIS QDs were measured using a Hanbury Brown Twiss interferometry setup with time-correlated single photon detectors (TCSPC). A dilute QD solution is spin-coated onto a glass slide where each particle has a large spatial separation, and placed on a mechanical stage with a laser excitation source. The emission is separated by a beam splitter, the signal is measured by two TCSPC detectors, and the stage is moved repeatedly to measure the spectra of each QD individually. We

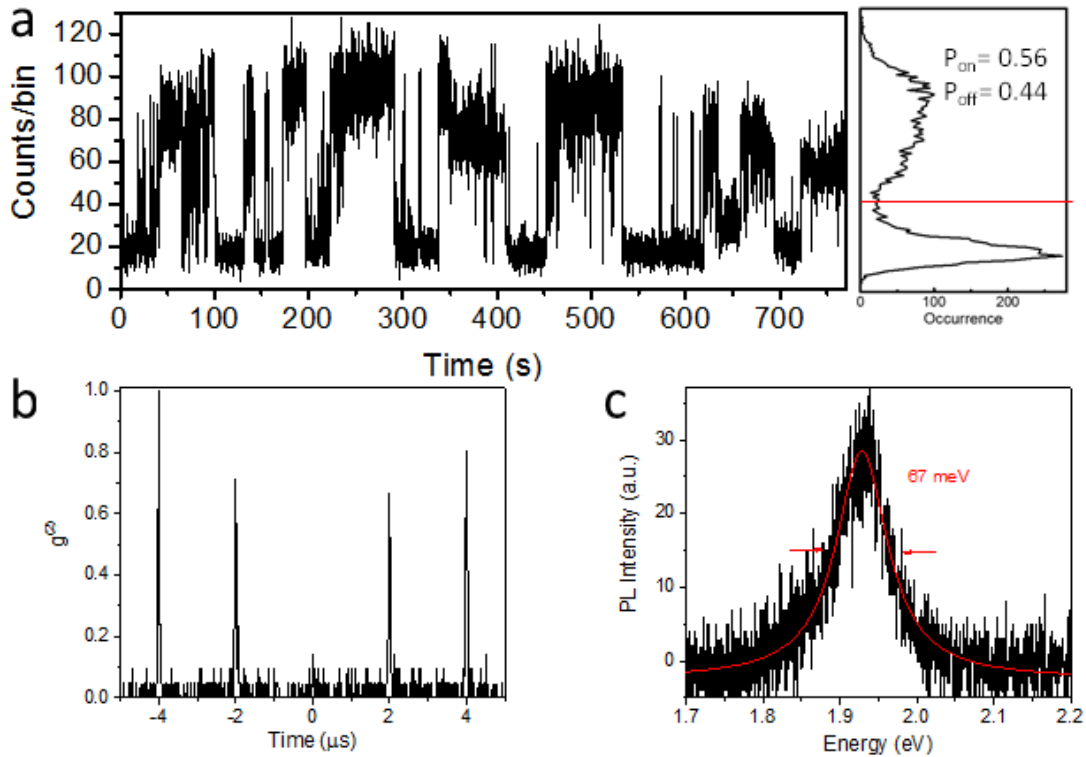


**Figure 3.3.2.1.** Examples of single-QD spectroscopic measurements for the UbiQD samples. (a) The PL intensity trajectory shows random fluctuations between the states of low (OFF) and high (ON) emissivity. This behavior is usually referred to as “blinking,” and is generally ascribed to either trapping at surface defects, and/or QD photoionization followed by nonradiative Auger recombination. Based on this measurement, the average ON-time fraction is ~60%, which allows us to classify these dots as “weakly blinking.” (b) The strong photon antibunching behavior revealed by the second-order PL intensity-correlation function confirms that these measurements are conducted on a single-dot instead of a cluster. (c) A single-dot PL spectrum indicates a linewidth of 67 meV as determined based on the full width at half maximum (FWHM) of a Lorentzian fit (red line) of the experimental spectrum (black line).

observe two hallmarks for single QD emission: spontaneous charging leading to fluorescence intermittency, or “blinking” (**Figure 3.3.2.1a**) and a photon antibunching  $g^{2(0)}$  constant below 0.5 (~0.14 as shown in **Figure 3.3.2.1b**). After isolating individual QDs, the PL spectra is measured under continuous excitation (**Figure 3.3.2.1c**), and the linewidth determined by a Lorentzian fit. As can clearly be observed, the linewidth is significantly narrower than ensemble spectra (~60 meV vs. ~300 meV), which is narrow enough for commercial LEDs.

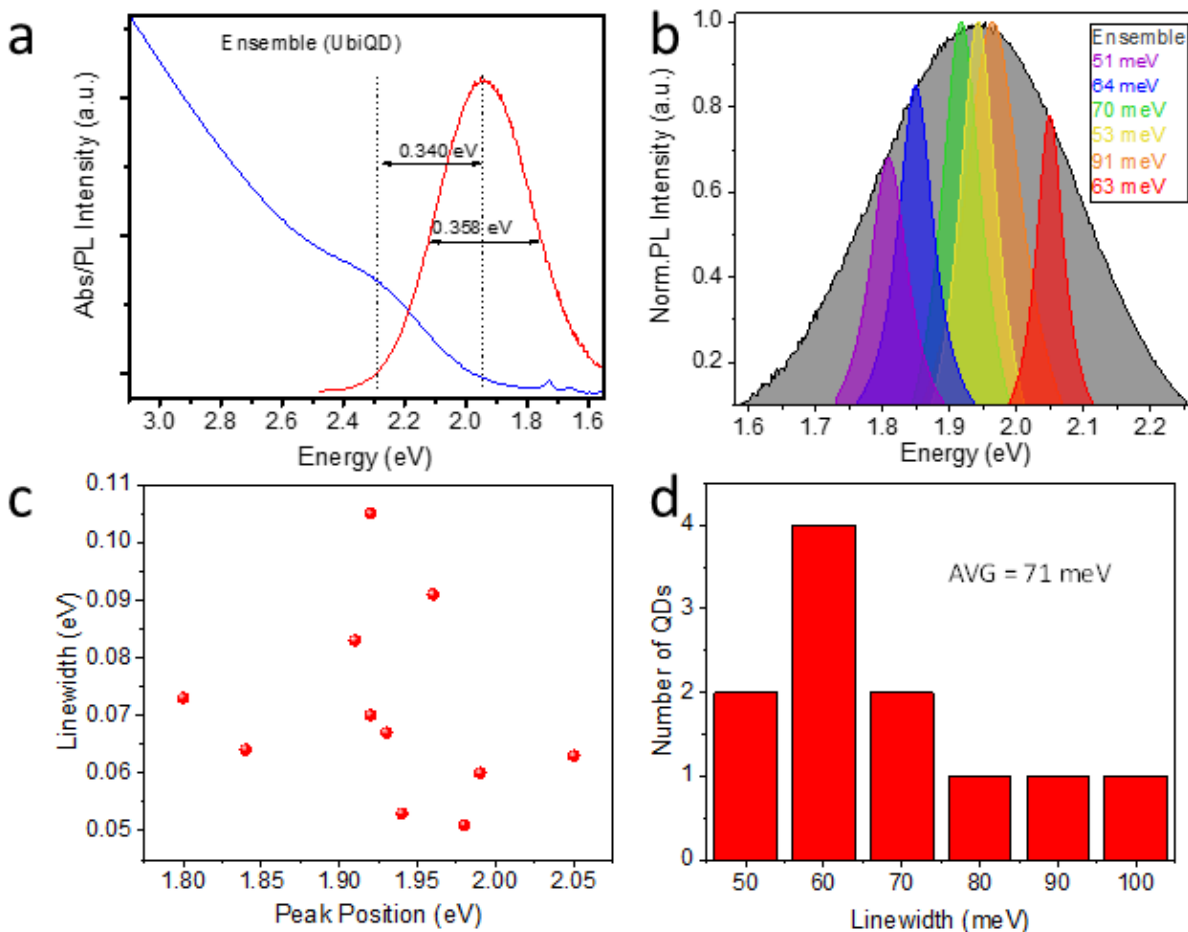


**Figure 3.3.2.2.** Statistical analysis of single-particle data in comparison to ensemble measurements. (a) Ensemble absorption (blue line) and emission (red line) spectra exhibit a large Stokes shift ( $\sim 340$  meV) and a broad linewidth ( $\sim 358$  meV) typical of CIS QDs. (b) The Lorentzian fits for several single-particle PL spectra (colored lines) are projected onto the ensemble PL spectrum. As can be seen, the single-particle spectra are significantly narrower than the ensemble spectrum, but have widely varied peak emission energies. (c) The single-dot linewidth vs. peak position does not show any correlations between the two. (d) The histogram of single-QD linewidths. All of the measured QDs show linewidths less than  $\sim 100$  meV, while the majority of the dots ( $\sim 70\%$ ) have linewidths in the 50-to-70 meV range. The average linewidth is  $71 \pm 16$  meV.

The above described experiment was repeated with 11 QDs from an experimental ensemble synthesized by UbiQD. In **Figure 3.3.2.2a** we show the ensemble absorption (blue solid line) and emission (red solid line), which exhibits the large Stokes shift (340 meV) and broad PL linewidth (358 meV) typical for CIS QDs. The ensemble PL is shown again as a solid black line with grey infilling in **Figure 3.3.2.2b**, and directly compared to

the Lorentzian fits of the single particle spectra (colored lines and infilling) for 6 different individual CIS QDs in the same ensemble. While there is some variation in the single particle linewidths, each appears to be significantly narrower than the ensemble average. Finally, we show in **Figure 3.3.2c,d** statistical analysis for 11 different individual QDs, and find that the average linewidth is  $71 \pm 16$  meV, which is nearly 80% narrower than the ensemble. However, variations in peak energy are large ( $\sim 270$  meV). This confirms that the PL linewidths for CIS QDs are *not* intrinsically broad, and the dominant broadening mechanism for QD ensembles is *inhomogeneous broadening* due to heterogeneity. Indeed, this is in agreement with DFT calculations (see Chapter 3 section 3.2), which predicted that heterogeneity in local chemical bonding explains spectral broadening for QDs with Cu impurities. Specifically, as-synthesized QD ensembles have several distinct subensembles where the position of Cu defects vary (e.g. sub-surface, surface with a tetrahedral geometry, or surface with a trigonal planar geometry), which alters their energy relative to the valence band (VB) and leads to different Stokes shifts across the ensemble.

**Temperature-Dependent Photoluminescence Experiments.** In order to address the role of stoichiometry in phonon-assisted processes for both radiative and non-radiative decay channels, we measure the temperature-dependent steady state PL for the two core-only samples described in Chapter 3 section 3.1. In **Figure 3.3.2.3a** we show the PL spectra for  $\text{Cu}_{0.47}\text{In}_1\text{S}_y$  QDs at temperatures ranging from 15 K to 296 K. The emission intensity for both spectra rapidly increases at lower temperatures. The temperature-controlled spectrally integrated PL intensity for both Cu-deficient QDs are

then plotted in **Figure 3.3.2.3b** (green squares for  $\text{Cu}_{0.85}\text{In}_1\text{S}_y$  and red circles for  $\text{Cu}_{0.47}\text{In}_1\text{S}_y$ ) and fitted using the following Arrhenius formula:

$$I(T) = \frac{1}{1 + C_1 \exp\left(\frac{-E_{A1}}{k_B T}\right) + C_2 \exp\left(\frac{-E_{A2}}{k_B T}\right)} \quad (1)$$

where  $I(T)$  represents the PL intensity normalized to the 15 K measurement,  $C_1$  and  $C_2$  are constants corresponding with the strength of two different phonon-assisted nonradiative recombination processes,  $E_{A1}$  and  $E_{A2}$  are the activation energies corresponding with the same processes, and  $k_B T$  refers to the Boltzmann constant and temperature, respectively. As shown in **Figure 3.3.2.3b**, we obtained excellent fits to the experimental data (solid lines for  $\text{Cu}_{0.85}\text{In}_1\text{S}_y$  and dashed lines for  $\text{Cu}_{0.47}\text{In}_1\text{S}_y$ ) using  $E_{A1}$  and  $E_{A2}$  of 51.0 and 6.1 meV for  $\text{Cu}_{0.47}\text{In}_1\text{S}_y$ , and  $E_{A1}$  and  $E_{A2}$  of 59.2 and 5.2 meV for  $\text{Cu}_{0.85}\text{In}_1\text{S}_y$ , respectively. Our  $E_{A1}$  values (~50 to 59 meV) are close to those obtained using time-resolved measurements on core only stoichiometric CIS QDs (56 meV). These values are also close to those measured for transverse optical (TO) phonons with  $E$ -symmetry (~45 meV) in bulk  $\text{CuInSe}_{2-x}\text{S}_x$ . Further comparison to bulk measurements indicates that our  $E_{A2}$  values (~5 to 6 meV) are similar to the range predicted for acoustic phonons (6-10 meV). These comparisons to bulk measurements can, in principle, help us distinguish the effects of optical and acoustic phonon modes on the PL line shape and intensity.

**Figure 3.3.2.3c** compares the temperature controlled PL spectra for  $\text{Cu}_{0.47}\text{In}_1\text{S}_y$  normalized to the PL peak for each temperature. The energy of the PL peak and its corresponding linewidth do not seem to significantly change with temperature. We quantitatively compare the effect of temperature on Stokes shift and linewidth (as

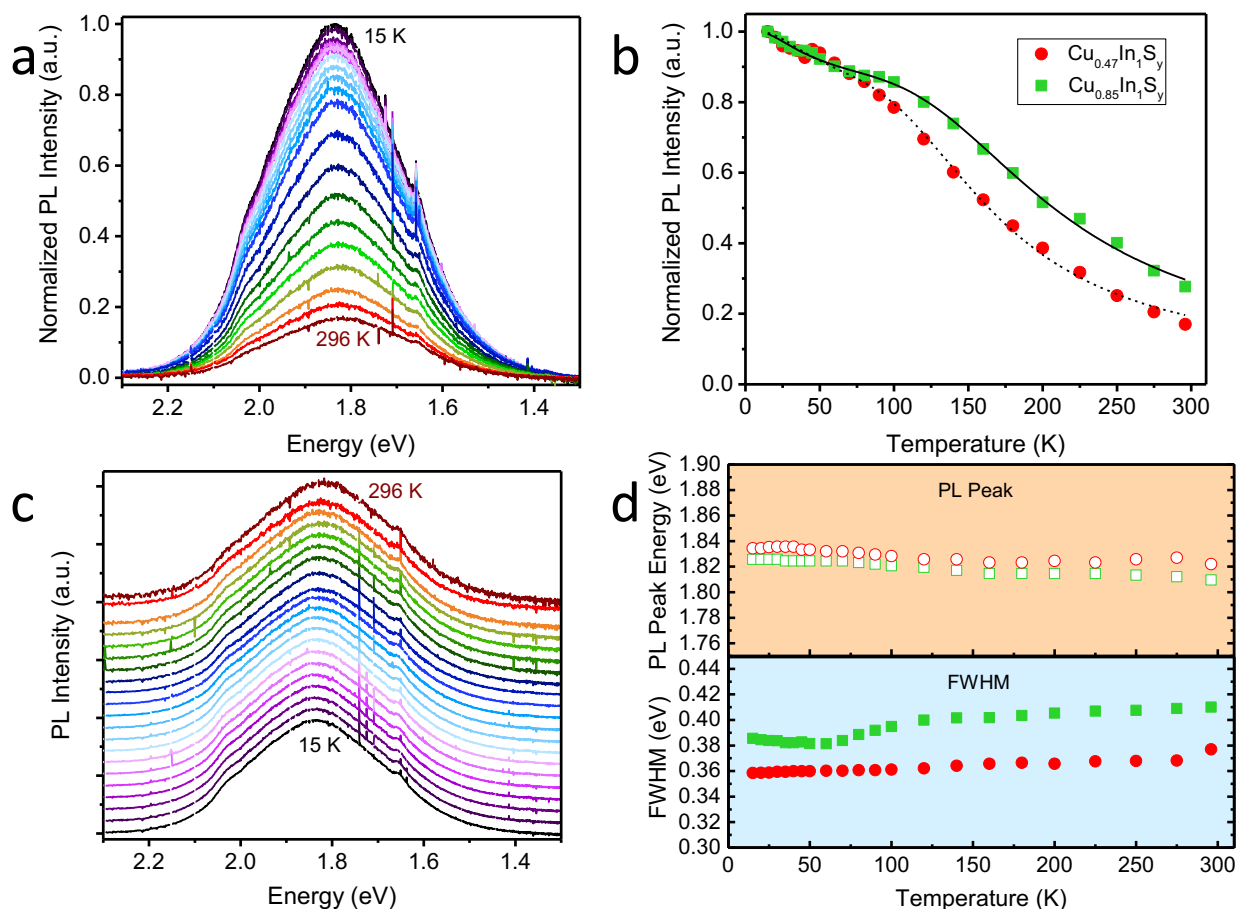


**Figure 3.3.2.3.** Temperature controlled PL spectra for Cu<sub>0.47</sub>In<sub>1</sub>S<sub>y</sub> QDs are shown in (a). The same measurement was repeated with Cu<sub>0.85</sub>In<sub>1</sub>S<sub>y</sub> QDs. The spectrally integrated PL intensity for both measurements are presented as a scatter plot in (b) with Cu<sub>0.47</sub>In<sub>1</sub>S<sub>y</sub> QDs represented by closed red circles, and Cu<sub>0.85</sub>In<sub>1</sub>S<sub>y</sub> QDs represented with closed green squares. In both cases, fits based on equation 1 are shown as black lines (solid for Cu<sub>0.85</sub>In<sub>1</sub>S<sub>y</sub> QDs and dashed for Cu<sub>0.47</sub>In<sub>1</sub>S<sub>y</sub> QDs). In (c), the PL spectra for Cu<sub>0.47</sub>In<sub>1</sub>S<sub>y</sub> QDs is normalized to the peak intensity for each temperature. The same procedure is repeated for Cu<sub>0.85</sub>In<sub>1</sub>S<sub>y</sub> QDs, and changes in peak position (top panel) and FWHM (bottom panel) are both plotted in (d). In both cases, Cu<sub>0.47</sub>In<sub>1</sub>S<sub>y</sub> QDs are shown as red circles (closed for FWHM and open for peak position) and Cu<sub>0.85</sub>In<sub>1</sub>S<sub>y</sub> QDs are represented as green squares (closed for FWHM and open for peak position).

determined by the FWHM) for both samples in **Figure 3.3.2.3d**. The PL peak for both samples shifts by less than 2% (top panel), while the FWHM changes by ~5% (18 meV) for Cu<sub>0.47</sub>In<sub>1</sub>S<sub>y</sub> and ~7% (~28 meV) for Cu<sub>0.85</sub>In<sub>1</sub>S<sub>y</sub>. Based on these results, we can conclude that strong electron-phonon coupling, which spectrally manifests in changes to the homogeneous linewidth cannot explain the broad PL linewidths in ensemble

measurements. Instead, inhomogeneous broadening due to lack of control over the spatial distribution of defects is most likely the dominant effect. Indeed, these conclusions agree with our single-particle spectroscopy results and DFT calculations. We also observe that the majority of homogeneous broadening is due to TO phonons as indicated by most of the line narrowing occurring between 60 and 100 K for both samples, which is close to the temperature required to activate TO phonons ( $\sim 60$  to  $70$  K based on  $E_{A1}$ ).

### 3.3.3. Conclusions

In conclusion, we have demonstrated that the CIS QDs fabricated by UbiQD have narrow single-particle emission linewidths ( $71 \pm 16$  meV on average). This suggests that broad linewidths observed in the ensemble measurements ( $\sim 360$  meV) mostly originate from sample heterogeneity, which results in a wide dot-to-dot variation in peak PL energies, and is further confirmed by the relatively weak electron-phonon coupling measured in temperature-dependent ensemble PL measurements of core-only CIS QDs. These results further indicate that it is feasible to achieve narrow ensemble PL linewidths *via* reducing sample heterogeneities, which can be attained by further refining CIS QD synthesis, and device fabrication procedures. Thus, there are no fundamental obstacles to using CIS QDs specifically, or non-toxic Cu-based QDs broadly in solid-state lighting devices.

### 3.3.4. Methods

**Single-Particle Spectroscopy Measurements.** CIS QDs were provided by UbiQD in powder form. The CIS QDs were then dispersed in a 2 wt. % PMMA/chloroform solution. Ensemble photoluminescence (PL) spectra were collected using a Horiba Scientific

Fluoromax-4 spectrometer and optical absorption was measured using an Agilent 8543 UV-visible spectroscopy system. For single-dot studies, the dilute CIS QD solution was spun-cast onto cover-glass slides to form a submonolayer film protected from photodegradation by the polymer matrix. Single-particle spectra were collected using a pulsed laser (PicoQuant; 405 nm wavelength and 40 ps pulse duration) with a laser repetition rate of 500 kHz. Anti-bunching and blinking measurements were used to distinguish emission from single particles *versus* particle clusters.

**Temperature-Dependent PL Measurements.** Films were prepared by adding a QD solution (4 mL in chloroform) to a 5 ml solution of 2 % w/w PVP in chloroform. After vigorous stirring, the mixture was transferred to a centrifuge tube, and then the QDs are precipitated by adding hexane. After centrifuging with 5000 rpm for 5 minutes, the supernatant was discarded. The precipitated pellet was dissolved in 600  $\mu$ L of 1 % w/w butanol/chloroform solution for preparing a QD/polymer solution. The film was made by dropping the QDs/polymer solution on a 5 mm X 5 mm slide glass followed by successive spin coating with 500 rpm for 2 minutes and 2000 rpm for 1 minute. The temperature-dependent PL was measured using a closed cycle He cryostat with a 405 nm LED excitation source.

### 3.3.5. References

1. Pietryga, J. M.; Park, Y.-S.; Lim, J.; Fidler, A. F.; Bae, W. K.; Brovelli, S.; Klimov, V. I., Spectroscopic and Device Aspects of Nanocrystal Quantum Dots. *Chem. Rev.* 2016, 116, 10513-10622.

2. Pons, T.; Pic, E.; Lequeux, N.; Cassette, E.; Bezdetnaya, L.; Guillemin, F.; Marchal, F.; Dubertret, B., Cadmium-Free CuInS<sub>2</sub>/ZnS Quantum Dots for Sentinel Lymph Node Imaging with Reduced Toxicity. *ACS Nano* 2010, 4, 2531-2538.
3. Aldakov, D.; Lefrancois, A.; Reiss, P., Ternary and quaternary metal chalcogenide nanocrystals: synthesis, properties and applications. *J. Mater. Chem. C* 2013, 1, 3756-3776.
4. Brovelli, S.; Galland, C.; Viswanatha, R.; Klimov, V. I., Tuning Radiative Recombination in Cu-Doped Nanocrystals via Electrochemical Control of Surface Trapping. *Nano Lett.* 2012, 12, 4372-4379.
5. Meinardi, F.; McDaniel, H.; Carulli, F.; Colombo, A.; Velizhanin, K. A.; Makarov, N. S.; Simonutti, R.; Klimov, V. I.; Brovelli, S., Highly efficient large-area colourless luminescent solar concentrators using heavy-metal-free colloidal quantum dots. *Nat. Nano.* 2015, 10, 878-885.
6. Pandey A; Brovelli S; Viswanatha R; Li L; Pietryga, J. M.; Klimov, V. I.; Crooker, S. A., Long-lived photoinduced magnetization in copper-doped ZnSe-CdSe core-shell nanocrystals. *Nat. Nano.* 2012, 7, 792-797.
7. Viswanatha, R.; Brovelli, S.; Pandey, A.; Crooker, S. A.; Klimov, V. I., Copper-Doped Inverted Core/Shell Nanocrystals with “Permanent” Optically Active Holes. *Nano Lett.* 2011, 11, 4753-4758.
8. Knowles, K. E.; Nelson, H. D.; Kilburn, T. B.; Gamelin, D. R., Singlet–Triplet Splittings in the Luminescent Excited States of Colloidal Cu<sup>+</sup>:CdSe, Cu<sup>+</sup>:InP, and CuInS<sub>2</sub>

Nanocrystals: Charge-Transfer Configurations and Self-Trapped Excitons. *J. Am. Chem. Soc.* 2015, 137, 13138-13147.

9. Fuhr, A.; Yun, H. J.; Makarov, N. S.; Li, H.; McDaniel, H.; Klimov, V. I., Light-Emission Mechanism in CuInS<sub>2</sub> Quantum Dots Evaluated by Spectral Electrochemistry. *ACS Photonics* 2017, 4, 2425-2435.

10. Zang, H.; Li, H.; Makarov, N. S.; Velizhanin, K. A.; Wu, K.; Park, Y.-S.; Klimov, V. I., Thick-Shell CuInS<sub>2</sub>/ZnS Quantum Dots with Suppressed “Blinking” and Narrow Single-Particle Emission Line Widths. *Nano Lett.* 2017, 17, 1787-1795.

11. Hughes, K. E.; Hartstein, K. H.; Gamelin, D. R., Photodoping and Transient Spectroscopies of Copper-Doped CdSe/CdS Nanocrystals. *ACS Nano* 2018, 12, 718-728.

12. Knowles, K. E.; Hartstein, K. H.; Kilburn, T. B.; Marchioro, A.; Nelson, H. D.; Whitham, P. J.; Gamelin, D. R., Luminescent Colloidal Semiconductor Nanocrystals Containing Copper: Synthesis, Photophysics, and Applications. *Chem. Rev.* 2016, 116, 10820-10851.

13. Maiti, S.; Dana, J.; Jadhav, Y.; Debnath, T.; Haram, S. K.; Ghosh, H. N., Electrochemical Evaluation of Dopant Energetics and the Modulation of Ultrafast Carrier Dynamics in Cu-Doped CdSe Nanocrystals. *J. Phys. Chem. C* 2017, 121, 27233-27240.

14. Bussian, D. A.; Crooker, S. A.; Yin, M.; Brynda, M.; Efros, A. L.; Klimov, V. I., Tunable magnetic exchange interactions in manganese-doped inverted core-shell ZnSe-CdSe nanocrystals. *Nat. Mater.* 2008, 8, 35.

15. Li, L.; Pandey, A.; Werder, D. J.; Khanal, B. P.; Pietryga, J. M.; Klimov, V. I., Efficient Synthesis of Highly Luminescent Copper Indium Sulfide-Based Core/Shell Nanocrystals with Surprisingly Long-Lived Emission. *J. Am. Chem. Soc.* 2011, 133, 1176-1179.
16. Chen, H.-Y.; Maiti, S.; Son, D. H., Doping Location-Dependent Energy Transfer Dynamics in Mn-Doped CdS/ZnS Nanocrystals. *ACS Nano* 2012, 6, 583-591.
17. Peng, B.; Liang, W.; White, M. A.; Gamelin, D. R.; Li, X., Theoretical Evaluation of Spin-Dependent Auger De-Excitation in  $Mn^{2+}$ -Doped Semiconductor Nanocrystals. *J. Phys. Chem. C* 2012, 116, 11223-11231.
18. Xu, X.; Wang, W.; Liu, D.; Hu, D.; Wu, T.; Bu, X.; Feng, P., Pushing up the Size Limit of Metal Chalcogenide Supertetrahedral Nanocluster. *J. Am. Chem. Soc.* 2018, 140, 888-891.
19. Rice, W. D.; McDaniel, H.; Klimov, V. I.; Crooker, S. A., Magneto-Optical Properties of  $CuInS_2$  Nanocrystals. *J. Phys. Chem. Lett.* 2014, 5, 4105-4109.
20. Zhong, H.; Zhou, Y.; Ye, M.; He, Y.; Ye, J.; He, C.; Yang, C.; Li, Y., Controlled Synthesis and Optical Properties of Colloidal Ternary Chalcogenide  $CuInS_2$  Nanocrystals. *Chem. Mater.* 2008, 20, 6434-6443.
21. Klimov, V. I.; Baker, T. A.; Lim, J.; Velizhanin, K. A.; McDaniel, H., Quality Factor of Luminescent Solar Concentrators and Practical Concentration Limits Attainable with Semiconductor Quantum Dots. *ACS Photonics* 2016, 3, 1138-1148.

## CHAPTER 4

### Multicarrier Interactions for Quantum Dots with Cu Impurities

## **4.1. Localized & Delocalized Auger Interactions in Quantum Dots with Native Defects**

### **4.1.1. Introduction**

$\text{Cu}_x\text{In}_{2-x}\text{E}_y$  (where E=S or Se), or CIE quantum dots (QDs) are attractive materials for a broad range of (electro)-optical applications.<sup>1-10</sup> However, they have unusual optical properties such as their large Stokes shifts ( $\Delta_S \approx 300-750$  meV) and broad spectral linewidths ( $\sim 300-400$  meV for emission) in the single exciton regime.<sup>1, 3, 11-21</sup> In the previous chapters of this thesis, and in several recent reports, we resolved the mechanisms for these unusual properties, and determined that subensembles with different  $\text{Cu}^x$  defects were the primary origin of this effect.<sup>3, 15, 22-23</sup> Interestingly though, the time-scale of emission dynamics at the single exciton level is also significantly different than “typical” II-VI QDs with similar oscillator strengths.<sup>3, 15, 22-23</sup> Yet, the relationship between the different subensembles of  $\text{Cu}^x$  defects, and the emission rate for CIE QDs is not well understood. Moreover, all of our discussion thus far have focused on the *single* exciton regime, and there is little understanding of how the different CIE subensembles alter multicarrier interactions such as trion and biexciton lifetimes. The latter of which, is particularly important for predicting device performance where alterations in QD volume not only shift the emission energy due to quantum confinement, but also simultaneously increase the strength of Coulomb interactions, and resultantly enhance Auger decay as described in Chapter 1.

Here, we resolve the relationship between  $\text{Cu}^x$  defects and emission lifetime at the single exciton level. We conclude that while the oxidation state of  $\text{Cu}^x$  (where  $x=1+$  or  $2+$ )

alters the localization pathway at the single exciton level, and correspondingly effects the Stokes shift and spectral linewidths, the radiative lifetime is unaffected due to “identical” emission states for both subensembles. Specifically, regardless of the mechanism for hole localization, excited state interactions are still between delocalized CB electrons and localized  $\text{Cu}^x$  holes, which leads to weak wavefunction overlap. Therefore, emission occurs on the several hundred nanosecond time-scale, which is an order of magnitude longer than the tens of nanoseconds time-scale for CdSe QDs, which have similar oscillator strengths and are expected to exhibit similar single exciton lifetimes. This observation has led to the hypothesis that CIE QDs do not have the “typical” delocalized VB states due to weak overlap of the  $d$  orbitals for lattice Cu ions.<sup>25</sup> We show evidence to the contrary of this hypothesis using DFT calculations, which indicate that the wavefunction for the VB state *is* delocalized, and only the  $\text{Cu}^x$  state is localized. This is confirmed by time-resolved spectroscopy measurements where tens of nanoseconds lifetime emission is observed for a small subensemble of QDs that are defect-free. At higher carrier densities, we observe that this small subensemble in addition to the subensemble of QDs with  $\text{Cu}^{2+}$  defects where VB holes are not localized to the  $\text{Cu}^x$  state (see Chapters 2-3) exhibit “normal” multicarrier lifetimes. For these two cases, Auger interactions (*e.g.* trions or biexcitons) occur between delocalized states, and correspondingly their lifetimes and volume scaling do not differ significantly from CdSe, or related QDs. On the other hand, for the subensemble of QDs that have  $\text{Cu}^{1+}$  defects hole localization is faster than “normal,” delocalized Auger decay (*e.g.* hole localization for  $\text{Cu}^{1+}$  defects is  $\sim 150$  fs vs. the delocalized biexciton lifetime is  $\sim 10$  ps), and holes are captured at  $\text{Cu}^{1+}$  defect states before delocalized Auger decay can occur. In fact, hole

localization can even be faster than carrier cooling (~350 fs), which makes hole localization difficult to resolve unless measurements are conducted under (near)-resonant excitation conditions where carrier cooling does not affect spectral dynamics. Hence, for this subensemble of QDs Auger interactions occur between delocalized CB electrons and holes localized at  $\text{Cu}^x$ . Similar to single exciton behavior, poor overlap of the localized hole wavefunction and delocalized electron wavefunction lead to an order of magnitude increase in Auger lifetimes (e.g. the “normal” biexciton lifetime for CIE QDs is ~10 ps vs. the localized biexciton lifetime is ~300 ps).

#### 4.1.2. Results and Discussion

**Single Exciton Optical Properties of CIS QDs.** Core-only CISES QDs (with different Se/S ratios), CIS/ZnS core/shell, and CISE/ZnS core/shell QDs were synthesized following the procedures described in the Methods section. For each sample, the stoichiometry was determined using inductively coupled plasma atomic emission spectrometry, and the QD size using transmission electron microscope (TEM) images. While we describe the spectra for a broad range of stoichiometries and QD sizes, all the samples studied here have a tetrahedral shape, and exhibit the Chalcopyrite structure (Figure S6.5.1). Previously, the single exciton absorption and emission mechanisms in CIE QDs (where E=Se, or S) has been described in the context of subensembles with different  $\text{Cu}^x$  defects (where  $x=1+$ , or  $2+$ ), which form intra-gap states, and make CIE QDs a three-level system as shown in **Figure 4.1.2.1a,b**, and Chapters 2-3.<sup>15-18, 22, 24</sup> For excitation energies greater than the band gap ( $h\nu > E_g$ ), high energy ‘hot’ carriers are created and relax lower-lying states *via* phonon emission ( $\tau_{cool}$  in **Figure 4.1.2.1a**).

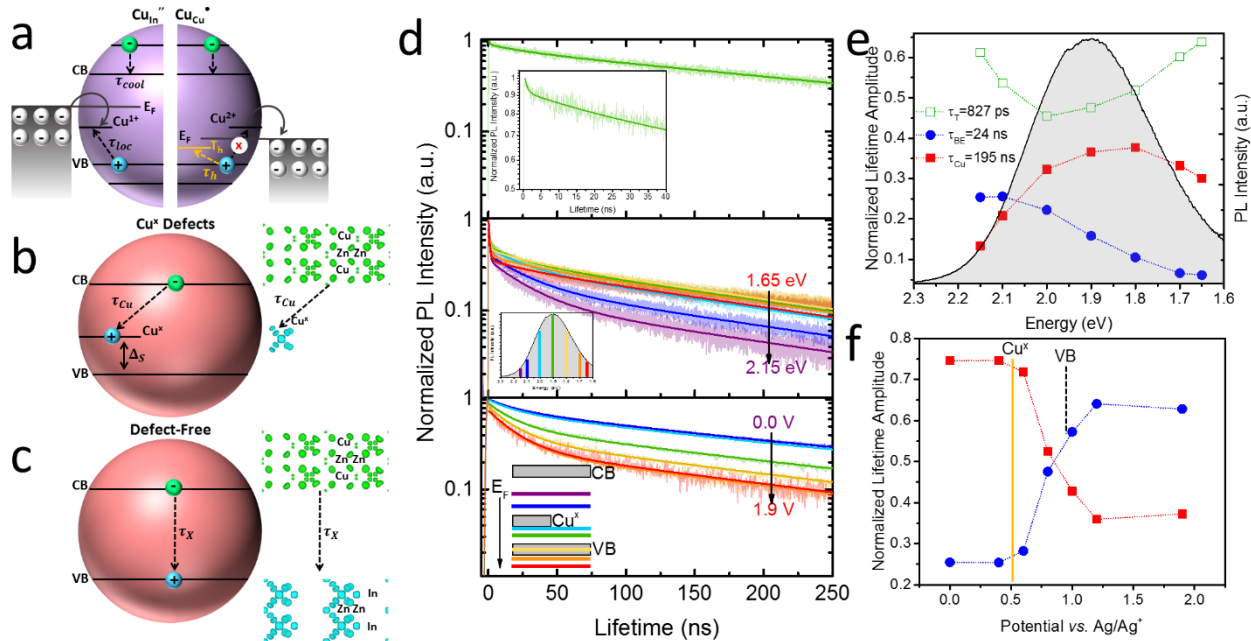


**Figure 4.1.2.1.** (a) Absorption mechanisms for subensembles of CIS QDs with  $\text{Cu}^x$  defects. VB holes are either localized to the  $\text{Cu}^x$  state ( $x=1+$ ) or to a trap state ( $x=2+$ ). For  $\text{Cu}^{2+}$ , holes are already localized to  $\text{Cu}^x$  in the ground-state. (b) After holes are localized (by either  $\text{Cu}^x$  defect mechanism), emission occurs by recombination between a CB electron and a  $\text{Cu}^x$  hole. DFT calculations show that the  $\text{Cu}^x$  hole is localized to the Cu-S defect tetrahedra, and the CB electron is delocalized. (c) If QDs are defect-free, band-edge recombination occurs. Dissimilar to other reports,<sup>25</sup> we show with DFT that both band-edges are delocalized, and therefore recombination for band-edge carriers is faster than for  $\text{Cu}^x$  due to improved wavefunction overlap. (d) The top panel shows SNSPD measurements ( $\langle N \rangle < 0.1$ ) for CIS/ZnS core/shell QDs with 85% QY. Tri-exponential fits yield:  $\tau_t = 760 \text{ ps}$ ,  $\tau_{BE} = 27 \text{ ns}$ , and  $\tau_{Cu} = 297 \text{ ns}$ . If these measurements are repeated at different probe energies for core-only CIS with 28% QY (middle panel) we obtain nearly identical decay rates from a global tri-exponential fit. The bottom panel shows spectral electrochemistry measurements for the same core-only CIS. Since the dynamics are measured with TCSPC in the SEC measurements, the trapping component is too fast to be observed (resolution  $\sim 1.5 \text{ ns}$ ). However, both the BE and  $\text{Cu}^x$  lifetimes can still be found. As the Fermi level is lowered the oxidation state for  $\text{Cu}^x$  defects can be changed ( $\text{Cu}^{1+} \rightarrow \text{Cu}^{2+}$ ). (e) The relative amplitudes of each of the 3 decays for the middle panel of (d) are plotted, and projected against the steady-state PL spectra in the background (black lines, grey shading). The “Gaussian-like” shape of the trapping and  $\text{Cu}^x$  components reflect different QY across the ensemble with trapping being weakest, and  $\text{Cu}^x$  emission being strongest at the PL peak. The BE component becomes weaker on the red side as expected by the smaller Stokes shift. (f) SEC measurements in the bottom panel of (d) are summarized. When the Fermi level is below the  $\text{Cu}^x$  state, there is an increase in the concentration of  $\text{Cu}^{2+}$  defects, which do not localize VB holes. Correspondingly, in subensembles without a separate hole trapping state BE recombination becomes competitive with  $\text{Cu}^x$  recombination, and the relative amplitude of the BE component increases.

Depending on the Fermi-level ( $E_F$ ) of the subensemble, or identity of the defect, valence band (VB) holes are removed either by localization at the  $\text{Cu}^x$  state ( $\tau_{loc}$  in the left panel

of **Figure 4.1.2.1a**), or by trapping in a separate, possibly other defect-, or surface dangling bond-related state ( $\tau_h$  in the right panel of **Figure 4.1.2.1a**). Specifically, if  $\text{Cu}^x$  is below  $E_F$ , or forms due to anti-site swapping of  $\text{Cu}^{1+}$  and  $\text{In}^{3+}$  cations ( $\text{Cu}_{\text{In}}''$ , in the  $\text{Cu}_{\text{In}}'' + \text{In}_{\text{Cu}}''$  defect pair) it is “occupied,” or has a  $d$  shell filled with electrons ( $[\text{Ar}]3d^{10}$  electron configuration). These so-called “ $\text{Cu}^{1+}$ ,” or “anti-site copper defects” require localization of a VB hole prior to emission (left panel of **Figure 4.1.2.1a**). On the other hand, if  $\text{Cu}^x$  is above  $E_F$ , or forms to charge-compensate copper vacancies ( $\text{Cu}_{\text{Cu}}'$ , in the  $V_{\text{Cu}}' + \text{Cu}_{\text{Cu}}'$  defect pair), it is only *partially* occupied, or has a  $d$  shell missing an electron ( $[\text{Ar}]3d^9$  electron configuration). In this case, we refer to  $\text{Cu}^x$  as “ $\text{Cu}^{2+}$  defects,” which have a hole localized in its  $d$  shell prior to photoexcitation. Hence,  $\text{Cu}^{2+}$  defects are “emission ready,” and do not require VB hole localization prior to emission. Instead, VB holes can be trapped at a separate state ( $T_h$  in the right panel of **Figure 4.1.2.1a**).

Regardless of whether the hole is localized in the excited state (high  $E_F$ , or  $\text{Cu}_{\text{In}}''$  defects), or in the ground state (low  $E_F$ , or  $\text{Cu}_{\text{Cu}}'$  defects) emission will then occur *via* radiative recombination between a CB electron and a hole localized in the  $\text{Cu}^x$  state (left panel of **Figure 4.1.2.1b**). This leads to a large Stokes shift ( $\Delta_S$ ) between band-edge absorption and  $\text{Cu}^x$  emission as described in previous reports, and Chapters 2-3.<sup>15-18, 22,</sup>  
<sup>24</sup> However, based on these proposed hole localization and trapping schemes, if *no*  $\text{Cu}^x$  defects are present, or CIE QDs are defect-free emission should then occur *via* band-edge recombination (left panel of **Figure 4.1.2.1c**) as expected in typical two-level QD systems. Previously, it has been hypothesized that the energy level structure of CIE QDs have a delocalized LUMO (conduction band, or CB), but poor overlap of the lattice (non-defect)  $\text{Cu}^{1+}$   $d$  orbitals lead to a series of localized HOMO states instead of a delocalized

valence band (VB).<sup>25</sup> For this mechanistic scheme, radiative relaxation would not involve two delocalized states as typically observed in II-VI QDs, but would instead occur between a delocalized CB electron and a localized VB hole regardless of whether the QDs have Cu<sup>x</sup> defects, or if they are defect free. This would suggest that defects have little impact on the emission energy, or on the radiative lifetimes for CIS QDs. To test this hypothesis, we employ density functional theory (DFT) calculations to determine the spatial distribution of the one electron square wavefunction for the VB, Cu<sup>x</sup>, and CB states in a Zn-alloyed CIS Chalcopyrite supercell using plane wave pseudopotentials, and periodic boundary conditions as implemented in the Vienna Ab initio Software Package (VASP, see Methods sections for details). We use a supercell instead of a ZCIS cluster to avoid issues associated with the inadequate passivation of QD surfaces due to the absence of long-chain organic ligands, which are difficult to include in DFT calculations due to increased computational expense. The absence of these long-chain ligands leads to artificial localization of the square wavefunction to the cluster surface, and makes it difficult to assess the degree of (de)localization of the band-edges. In addition, we specifically choose Zn-alloyed CIS since the majority of our later-described experimental studies will use CIS/ZnS core/shell QDs, which are expected to have an alloyed interface. If we plot the iso-contours of the charge density for the LUMO (green shading in the right panel of **Figure 4.1.2.1b,c**), which is taken here to indicate the square modulus of the one electron wavefunction, we observe a CB electron that is delocalized across the In-S bonds. If we apply this same methodology to the HOMO for a supercell with Cu<sub>In</sub>” defects (turquoise iso-contour in the right panel of **Figure 4.1.2.1b**), the wavefunction is localized to the defect state. This should lead to weak wavefunction overlap in the excited state,

and slow radiative recombination between the delocalized CB electron and hole localized at the  $\text{Cu}^x$  defect state ( $\tau_{Cu}$  in **Figure 4.1.2.1b**). However, energetically below this state there is a second occupied state where the square wavefunction is delocalized across the Cu-S bonds of the Chalcopyrite lattice (turquoise shading in the right panel of **Figure 4.1.2.1c**). Based on these calculations, wavefunction overlap between occupied and unoccupied states should be much stronger for VB/CB, or “band-edge” transitions than  $\text{Cu}^x/\text{CB}$  transitions, and we expect band-edge (BE) excitons in defect-free QDs ( $\tau_x$  in **Figure 4.1.2.1c**) to have a radiative decay rate that is an order of magnitude faster than emission from  $\text{Cu}^x$  defects. Furthermore, Zn orbitals do not significantly contribute to band-edge states, and correspondingly alloying structures with Zn should not impact emission transition rates, and instead should only passivate dangling surface bonds, reduce trapping, or ultra-fast non-radiative losses, and increase quantum yields (QY). Hence, we expect these differences in  $\tau_x$  and  $\tau_{Cu}$  lifetimes to occur in *both* Zn-alloyed and Zn-free CIE QDs.

We test these predictions by conducting a series of time-resolved PL measurements at low carrier densities ( $\langle N \rangle < 0.1$ , **Figure 4.1.2.1d-f**). In the top panel of **Figure 4.1.2.1d**, we use the 3.1 eV second harmonic of a Ti:Sapphire laser (50 fs pulse duration) to excite CIS/ZnS core/shell QDs, and monitor its emission dynamics with a superconducting nanowire single photon detector (SNSPD,  $\Delta t \sim 70$  ps). The band gap for our CIS/ZnS core/shell structure is  $\sim 2.3$  eV as described later by transient absorption spectroscopy measurements, and it has a near unity quantum yield ( $\Phi = 85\%$ ). Hence, we expect our measurements to be only weakly affected by trapping. The PL dynamics can be accurately fitted to a tri-exponential function, which yields three decay rates: 760

ps, 27 ns, and 297 ns. The slowest of these decay rates is most likely PL from  $\text{Cu}^x$  defects ( $\tau_{\text{Cu}} = 297 \text{ ns}$ ), which typically occurs on the several hundred nanosecond time-scale and is observed in almost all QDs with Cu cations.<sup>15-18, 20-21, 23-24, 26-28</sup> The relative amplitude of the 760 ps decay time constant is  $\sim 16\%$  of the total PL dynamics. This is nearly equal to the expected optical losses ( $\sim 15\%$ ) from trapping based on the 85% QY, and we therefore attribute this fast decay to the rate of non-radiative losses due to carrier trapping in our CIS/ZnS core/shell QDs ( $\tau_T = 760 \text{ ps}$ ). The 27 ns decay component is similar to the radiative lifetime for PL in CdSe QDs, which occurs *via* delocalized-to-delocalized CB electron-to-VB hole relaxation.<sup>29</sup> Based on their similar oscillator strength with CIS QDs, we expect band-edge exciton recombination to also occur on the tens of ns time-scale, and we therefore attribute this time constant to the decay of band-edge excitons ( $\tau_{\text{BE}} = 27 \text{ ps}$ ). This confirms our interpretation of the DFT calculated one electron square wavefunction for the VB and CB states, which predicted that wavefunction overlap for VB/CB transitions in CIS QDs would be stronger than for  $\text{Cu}^x/\text{CB}$  transitions, and would therefore result in a significantly faster decay rate than for  $\text{Cu}^x$  PL. This picture is further confirmed by repeating these measurements on core-only CIS QDs (middle panel **Figure 4.1.2.1d**), and CISe/ZnS core/shell structures (Figure S6.5.2). In all three cases, tri-exponential fits yield a long lifetime of several hundred ns ( $\tau_{\text{Cu}}$ ) and a shorter decay component of tens of ns ( $\tau_{\text{BE}}$ ). Typically,  $\tau_{\text{BE}}$  has a relative amplitude of  $\sim 10\text{-}20\%$  of the total decay signal regardless of the relative QY for the QD, which suggests that this decay component is unrelated to nonradiative losses from trapping ( $\tau_T$ ).

As mentioned earlier, the large Stokes shift for CIS QDs is expected to represent the energy difference between BE absorption and  $\text{Cu}^x$  emission. This would imply that

BE emission in subensembles of defect-free QDs should have a much smaller Stokes shift than subensembles with  $\text{Cu}^x$  defects. In addition, hole trapping for QDs with  $\text{Cu}^{2+}$  defects is expected to occur from non-optically active impurities such as surface dangling bonds. The spatial distribution of these defects would therefore be inhomogeneous, and variations in wavefunction overlap with the VB holes should result in a wide range of VB hole removal rates across the subensemble. This is distinct from hole localization with  $\text{Cu}^{1+}$  defects, which occurs predominantly from internal defects and are expected to have faster localization rates than surface hole traps. Hence, for QDs with  $\text{Cu}^{2+}$  defects the band-edge transition could occasionally occur if hole trapping states are absent, or are significantly slower than hole localization for  $\text{Cu}^{1+}$  defects. Based on these arguments, we can expect two general trends for radiative lifetimes for CIS QD ensembles with  $\text{Cu}^{1+}$  defects,  $\text{Cu}^{2+}$  defects, and defect free subensembles. First, if the broad emission spectra for CIS includes a band-edge exciton component its contribution to the average PL should be significantly stronger on the blue side of the spectrum due to the smaller Stokes shift. Further, if the relative population of QD subensembles with  $\text{Cu}^{2+}$  defects is higher, band-edge emission should become more competitive with  $\text{Cu}^x$  emission due to non-uniform VB hole removal rates with surface hole traps — in particular — exhibiting slower VB hole removal rates than internal traps. Subensembles with  $\text{Cu}^{1+}$  defects, on the other hand, should always exhibit efficient removal of VB holes and entirely block the band-edge transition. We test these hypotheses using our earlier described SNSPD setup to measure the probe energy-dependent PL dynamics for core-only CIS QDs using global tri-exponential fits (**Figure 4.1.2.1d**, middle panel), which will allow us to determine the relative contribution of each transition to the red and blue side of the PL spectrum.

Second, we use time-resolved spectro-electrochemistry (TR-SEC) measurements to intentionally modulate the Fermi-level ( $E_F$ ) for the ensemble *via* an externally controlled electrochemical potential (**Figure 4.1.2.1d**, bottom panel), which alters the population distribution of QDs with  $\text{Cu}^{1+}$  ( $E_F$  above  $\text{Cu}^x$ ) and  $\text{Cu}^{2+}$  defects ( $E_F$  below  $\text{Cu}^x$ ). In this case, we use the same 3-electrode SEC setup described in our previous report,<sup>15</sup> but monitor PL dynamics using time-correlated single photon counting (TCSPC) instead of steady-state PL.

We first compare the changes in relative amplitude of each decay component as obtained from the global tri-exponential fits (colored lines in **Figure 4.1.2.1d**) as the probe energy is moved from the red-side to the blue-side of the PL spectrum for core-only QDs with a near-identical band gap to the CIS/ZnS core/shell structures, but with a lower QY (~28%). We specifically use core-only QDs to allow for later comparison to TR-SEC measurements (bottom panel of **Figure 4.1.2.1d**), which are difficult with CIS/ZnS core/shell structures where the alloyed ZnS shell provides a large dielectric tunneling barrier to electron transfer from the ITO electrode.<sup>15</sup> For each decay curve in the middle panel of **Figure 4.1.2.1d**, the colors used for the original SNSPD measurements (semi-transparent lines), and for the tri-exponential global fit (solid lines) correspond with the probe energies marked on the PL spectrum in the figure inset. The decay rates used for the universal fit are nearly identical to the CIS/ZnS core/shell QDs ( $\tau_{Cu} = 195 \text{ ns}$ ,  $\tau_{BE} = 24 \text{ ns}$ ,  $\tau_T = 830 \text{ ps}$ ), but the relative amplitude of the “trap decay” at the PL peak (~1.9 eV, marked with green lines) is much larger than for the CIS/ZnS core/shell QDs (~48% instead of ~16%). This is expected based on the lower QY for core-only QDs in comparison with core/shell structures (~28% vs. 85%). The relative amplitude of  $\tau_T$ ,

however, is still somewhat lower than expected based on the QY for these samples (predicting ~48% trap-related optical losses instead of ~72%). Hence, most likely there is an additional trapping component (~24% of the total decay) beyond the resolution limit of our SNSPD detector ( $\Delta t \sim 70$  ps). If we plot the relative amplitudes of each decay component as a function of probe energy (shown in **Figure 4.1.2.1e** with  $\tau_T$  represented by open green squares,  $\tau_{BE}$  with solid blue circles,  $\tau_{Cu}$  with solid red squares, and dotted lines with colors matching their corresponding symbol used as visual guides for the data), the relative amplitude of the  $Cu^x$  transition is highest at the probe energy marking the emission peak, and decreases on both the blue and red side of the spectrum. Conversely, the amplitude for  $\tau_T$  shows the opposite trend, which indicates that changes in the relative amplitude for  $\tau_{Cu}$  and  $\tau_T$  merely reflect differences in trapping across the ensemble, and QY is highest at the peak emission energy. The relative amplitude for  $\tau_{BE}$ , on the other hand, decreases as the probe energy is shifted from the red side (1.65 eV) of the spectrum to the blue side (2.15 eV). Hence, as predicted earlier, band-edge excitonic transitions dominate the blue side of the spectrum due to the smaller Stokes shift whereas  $Cu^x$  emission dominates the red side of the PL spectrum, and the weak band-edge emission occurring at the PL peak most likely is due to a poor size dispersion across the ensemble. Notably, core/shell QDs show the same general trends, but the relative amplitude for  $Cu^x$  is much higher at all of the marked probe energies due to the higher QY (Figure S6.5.3).

As mentioned earlier, we expect that BE emission is stronger for the subensembles of QDs with  $Cu^{2+}$  defects due to the large variability in hole trapping rates, and the additional possibility of subensembles without a second hole trapping state to remove VB

holes. Considering that the emission rate for BE excitons is faster than  $\text{Cu}^x$  emission we expect that BE transitions become significantly stronger in subensembles with slower, or non-existent hole trapping. This is because, even if  $\text{Cu}^{2+}$  defects are “emission ready” due to the ground-state hole in their  $d$  shell,  $\text{Cu}^x$  emission is too slow to occur efficiently without the removal of VB holes to stop competition from BE transitions ( $\sim 20$  ns vs.  $\sim 200$  ns for  $\tau_{\text{Cu}}$  and  $\tau_{\text{BE}}$ , respectively). As mentioned earlier, we use TR-SEC to test this possibility by monitoring emission dynamics as a function of electrochemical potential, which modulates  $E_F$  and alters the relative population of subensembles with  $\text{Cu}^{1+}$  and  $\text{Cu}^{2+}$  defects (colored lines in the bottom panel of **Figure 4.1.2.1d**). Specifically, if the electrochemical potential is more positive (here, greater than  $\sim +0.5$  V, which marks the  $\text{Cu}^x$  state as determined in a previous study<sup>15</sup>) the Fermi-level is below the  $\text{Cu}^x$  state and there is a larger relative population of subensembles with  $\text{Cu}^{2+}$  defects. On the other hand, if  $E_F$  is less positive (here, less than  $\sim +0.5$  V) than there is a larger concentration of QDs with  $\text{Cu}^{1+}$  defects. In the bottom panel of **Figure 4.1.2.1d**, we show the TCSPC collected PL dynamics at different  $E_F$ . Similar to our earlier measurements using the SNSPD detector, we use semi-transparent shading for the original data and solid colors for the multi-exponential global fits. However, in this case, we use bi-exponential instead of tri-exponential fits due to non-radiative trapping occurring on a faster time-scale than the detection limit of our TCSPC detector ( $\tau_T \sim 800$  ps as measured by SNSPD, while  $\Delta t = 1.5$  ns for the TCSPC detector). As the Fermi level is lowered below the  $\text{Cu}^x$  state, the relative amplitude for  $\tau_{\text{BE}}$  ( $\sim 19$  ns) increases, while the relative amplitude for  $\tau_{\text{Cu}}$  ( $\sim 209$  ns) decreases (bottom panel of **Figure 4.1.2.1d**). Using the same symbols described in **Figure 4.1.2.1e** (omitting  $\tau_T$ , which as mentioned earlier is beyond the detection limit of

our TCSPC detector) we plot the  $E_F$ -dependent amplitudes for BE and  $\text{Cu}^x$  PL in **Figure 4.1.2.1f**. As stated earlier, when  $E_F$  is lowered below the  $\text{Cu}^x$  state  $\text{Cu}^{1+}$  defects are converted to  $\text{Cu}^{2+}$ , and the relative amplitude for  $\tau_{Cu}$  decreases. This confirms that variability in the distribution of hole trap lifetimes across the ensemble leads to band-edge excitonic emission becoming more competitive with the  $\text{Cu}^x$  transition for  $\text{Cu}^{2+}$  defects than for  $\text{Cu}^{1+}$  defects where, in the latter case hole localization always outcompetes the band-edge transition. Notably, as  $E_F$  is lowered even further (below the VB) no other significant changes are observed in the relative amplitudes of the different decay components. This is to be expected as depopulation of electrons from the VB damages QDs and leads to a uniform drop in the PL intensity for both BE and  $\text{Cu}^x$  transitions, which is not captured in our measurement of PL dynamics due to carrier trapping in CIS QDs occurring on the picosecond time-scale, which is beyond the detection limit of our TCSPC detector.

As suggested by SEC experiments, while the BE transition can sometimes be competitive with  $\text{Cu}^x$  emission for subensembles with  $\text{Cu}^{2+}$  defects, VB hole localization for subensembles with  $\text{Cu}^{1+}$  defects is extremely fast, and effectively blocks the BE transition. Previous studies using spectrally-resolved transient absorption (TA) spectroscopy of CIS QDs with different Cu:In ratios have suggested that hole localization for CIS QDs with  $\text{Cu}^{1+}$  defects occurs at the sub-picosecond time-scale (see Chapter 3 section 3.1.2). Interestingly, this is similar to the expected time-scale for carrier cooling of 'hot' carriers in II-VI QDs, and it is unclear how phonon emission, or hole localization can affect Auger dynamics for multiexcitons in CIS QDs. To address these issues, we conduct TA experiments using the frequency doubled (2.41 eV) and frequency tripled (3.61 eV)

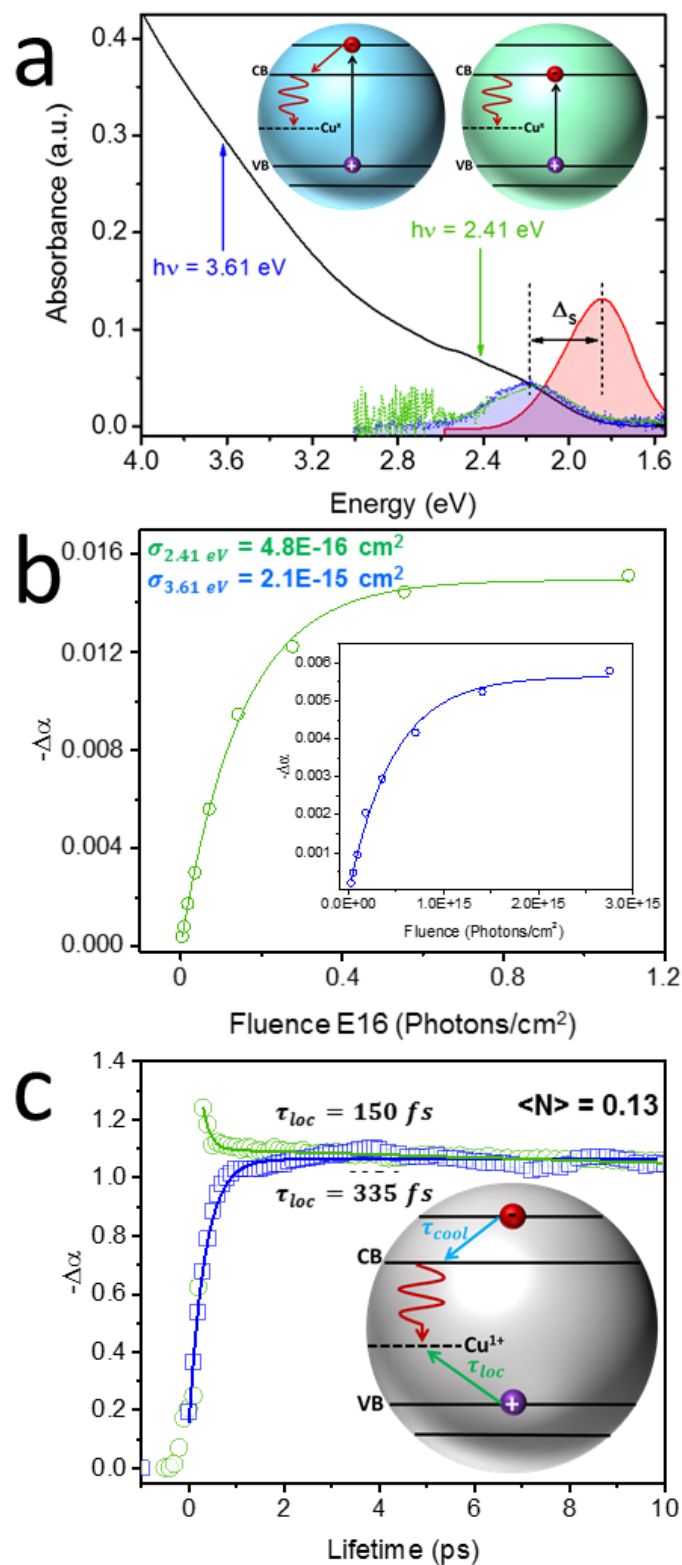


**Figure 4.1.2.2.** (a) Linear absorption (black) and PL (red) for CIS/ZnS core/shell QDs. TA is measured at non-resonant (blue arrow) and (near)-resonant (green arrow) excitation. (b) Measurement of the absorption cross-sections at different excitation energies, which shows that

the ratio of the absorption cross-sections at different excitation energies match the ratios of their optical densities (ODs) in the linear absorption spectra (details in main text). (c) The dynamics at low excitation density for both the non-resonant, and (near)-resonant excitation. Hole localization is faster than carrier cooling, which makes it difficult to resolve hole localization at non-resonant excitation. Hence, later-described Auger dynamics measured at 3.61 eV excitation are expected to be dominated by QD subensembles without hole localizing  $\text{Cu}^{1+}$  defects.

output of an amplified Yb:KGW laser (<190 fs pulse duration, **Figure 4.1.2.2**). As shown in **Figure 4.1.2.2a**, the linear absorption spectrum (solid black line) for the CIS/ZnS core/shell structure is broad and nearly featureless due to the high absorptivity of intra-gap  $\text{Cu}^{1+}$  defects (see Chapter 3 section 3.1.2), which makes determination of the band gap ( $E_g$ ) more complex than for typical II-VI QDs. Hence, we determine  $E_g$  using TA measurements (dotted lines with colored infilling in **Figure 4.1.2.2a**) at 3.61 eV (represented by dotted blue lines with infilling) excitation, which is far higher in energy than the expected BE transition. The peak of the resulting Gaussian-like spectra is ~2.3 eV, and we repeat these measurements with (near)-resonant excitation at 2.41 eV (represented by dotted green lines with infilling), and observe little change in the spectral shape, or peak energy. Hence, we expect that the two measurements represent similar BE excitation processes, but at 3.61 eV excitation there is an excess of hot carriers (optical processes depicted in the blue sphere of the figure inset) whereas the (near)-resonant excitation mostly just excites BE carriers (optical processes depicted in the green sphere of the figure inset). The Stokes shift ( $\Delta_S = 450 \text{ meV}$ ) is then determined as the energy difference between the above mentioned peak and the peak of the PL spectrum (solid red line with red infilling), which is similar to the core-only QDs (see Chapter 3 section 3.1.2), and indicates that overcoating with a ZnS shell improves QY without significantly altering the absorption and emission mechanisms for CIS QDs.

The pump-intensity dependent TA signal at  $t=50$  ps (green circles for 2.41 eV excitation, and blue squares for 3.61 eV excitation) shows trends typically observed for QDs (**Figure 4.1.2.2b**). As the pump-fluence increases in linear increments, the intensity of the TA signal also increases near linearly at ( $\langle N \rangle < 1$ ), but eventually saturates as multi-excitons are created. We use Poisson statistics to fit our experimental fluence-dependent TA signal,<sup>30-31</sup> and obtain the absorption cross-sections ( $\sigma$ ) at non-resonant (3.61 eV) and (near)-resonant (2.41 eV) excitation. The ratio between the absorption cross-section at 3.61 eV and 2.41 eV excitation ( $\frac{\sigma_{3.61\text{ eV}}}{\sigma_{2.41\text{ eV}}} = 4.37$ ) is nearly equal to the ratio of their optical densities (ODs) at the same energies in their linear absorption spectrum ( $\frac{OD_{3.61\text{ eV}}}{OD_{2.41\text{ eV}}} = 5.18$ ). Hence, as mentioned earlier, we expect that there is no significant difference between the non-resonant TA and (near)-resonant TA measurements other than the creation of a high density of ‘hot’ carriers at 3.61 eV excitation that emit phonons before relaxing into the BE states, and are not present in the 2.41 eV excitation measurement. Using the TA dynamics shown in **Figure 4.1.2.2c** ( $\langle N \rangle < 0.1$ ), we determine the rates for carrier cooling and hole localization with mono-exponential fits (solid lines) to the TA measurements (scatter plots). For the carrier cooling rate, we fit the rise for the spectra collected with the non-resonant 3.61 eV excitation (blue squares for original data, and blue solid line for the mono-exponential fit). This yields a cooling rate of  $\sim 335$  fs, which is similar to the expected cooling rates for most (e.g. II-VI) QDs. Interestingly, if we fit the decay of the (near)-resonant excitation (2.41 eV) dynamics (green circles for original data, and green solid line for the mono-exponential fit) we obtain a hole localization rate even faster than the carrier cooling ( $\sim 150$  fs). Notably, this extremely fast localization process is not observed in the non-resonant excitation measurements, which indicates that when we excite the

ensemble at 3.61 eV, and probe the dynamics at the peak of the BE bleach, the population grows in by hot-electron relaxation in parallel with 150 fs localization. This makes localization difficult to resolve from at non-resonant excitation. Hence, the dynamics for later-described high pump-fluence measurements with non-resonant excitation will be mainly used to describe multicarrier interactions for QDs with  $\text{Cu}^{2+}$  defects, or defect-free QDs where sub-picosecond hole localization to the  $\text{Cu}^x$  state does not occur. On the other hand, at (near)-resonant excitation the absence of carrier cooling allows us to measure the dynamics of subensembles with, and without  $\text{Cu}^{1+}$  defects, but we expect that at higher pump-fluences with (near)-resonant excitation an increase in the intensity of this sub-picosecond decay component is merely a reflection of increased hole localization at higher excitation densities, and not indicative of the real multiexciton lifetimes for QD subensembles with  $\text{Cu}^{1+}$  defects.

**Measurement of Auger Dynamics.** We next measure the excitation fluence-dependent population dynamics for the CIS/ZnS core/shell QDs with TA and time-resolved PL spectroscopy using our earlier described SNSPD setup (**Figure 4.1.2.3**). In **Figure 4.1.2.3a**, the TA dynamics collected at (near)-resonant excitation (2.41 eV) are normalized to their intensity at  $t = 50$  ps where the decays are expected to be dominated by single excitons (non-normalized measurements are shown in Figure S6.5.4), and we observe the sub-picosecond hole localization decay component in both the low fluence ( $\langle N \rangle < 1$ ), and high fluence ( $\langle N \rangle > 1$ ) measurements. While the fast, sub-picosecond hole localization is present in all (near)-resonant measurements, at higher fluences, the relative amplitude of hole localization becomes significantly stronger, and there appears to be an additional, fast subnanosecond component in the decay dynamics that we

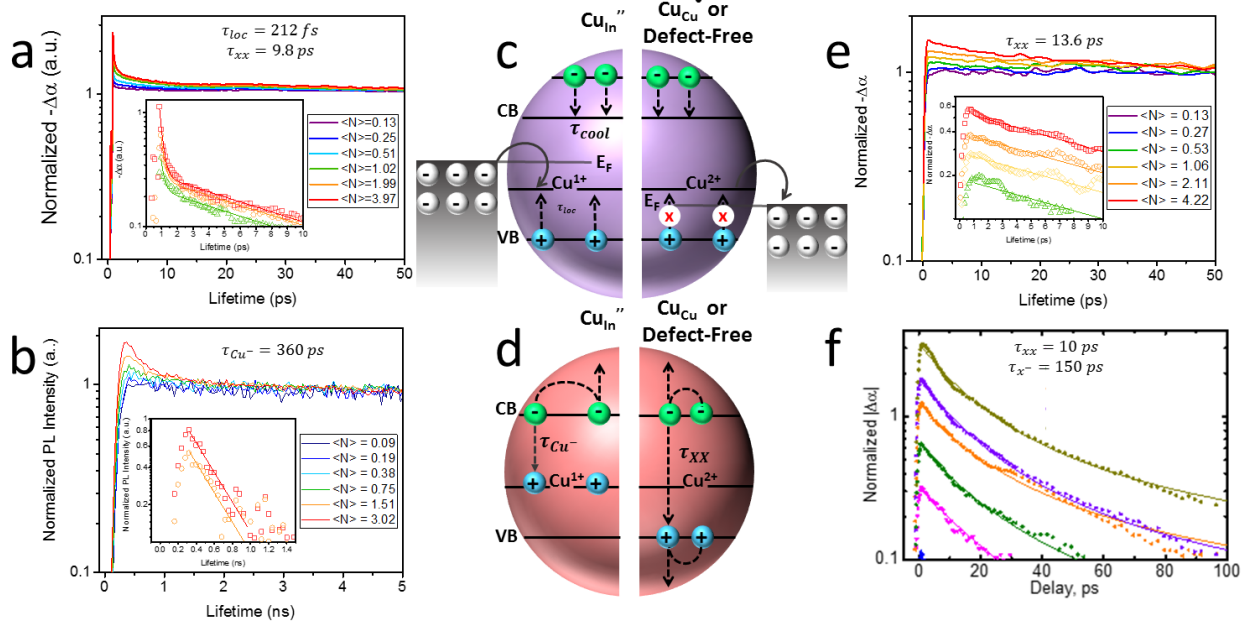


**Figure 4.1.2.3.** (a) TA dynamics (CIS/ZnS core/shells with  $\sim 85\%$  QY) at (near)-resonant excitation is dominated by hole localization for the subensembles with  $\text{Cu}^{1+}$  defects. Hole localization is  $\sim 200$  fs, which is faster than the “normal” biexciton lifetime. The 10 ps biexciton lifetime obtained from the biexponential fit represents the small subensemble of QDs without  $\text{Cu}^{1+}$  defects that undergo “normal” Auger between two delocalized states. (b) After holes are localized, biexcitons occur through delocalized CB and localized  $\text{Cu}^x$  states and have lifetimes more similar to what is expected for 2 trions when measured with SNSPD. (c,d) Hole localization determines whether the subensemble will undergo delocalized, or localized Auger. The left panel for both represents subensembles of QDs with  $\text{Cu}^{1+}$  defects, and explains the optical processes in (a,b). The panels on the right, on the other hand, show Auger properties for QDs without  $\text{Cu}^{1+}$  defects (either defect free or with  $\text{Cu}^{2+}$  defects). In this case, sub-ps hole localization from the VB to the  $\text{Cu}^x$  state does not occur, and TA measurements at non-resonant excitation can be used to obtain the “normal” biexciton lifetime since carrier cooling is slower than hole localization. (e) In this case, mono-exponential fits are used and also show  $\sim 10$  ps biexciton lifetimes. (f) The same measurements are repeated for core-only CIS QDs at high energy excitation. Here, biexponential fits are required due to photocharging, which yields the same biexciton lifetime ( $\sim 10$  ps), but with an additional  $\sim 150$  ps trion lifetime.

preliminarily assign to Auger recombination of biexcitons. Similar to Auger decay in most QDs, the dynamics at time-scales longer than the expected biexciton lifetime ( $>50$  ps) appear to be indistinguishable at different pump-fluences. To determine the precise lifetime of the two decay components, we subtract the low-pump-fluence ( $\langle N \rangle = 0.13$ ) normalized spectra from the higher-pump-fluence measurements (inset of **Figure 4.1.2.3a**), and fit the decays for  $\langle N \rangle > 1$  to a bi-exponential function. By extracting from

the bi-exponential fits two ultra-fast decay time constants (212 fs and 9.8 ps, respectively) we can preliminarily conclude that hole localization dominates high-fluence measurements for QDs with  $\text{Cu}^{1+}$  defects whereas a small subensemble of QDs without  $\text{Cu}^{1+}$  defects (either QDs with  $\text{Cu}^{2+}$  defects, or defect-free QDs) yield near 10 ps biexciton lifetimes. This conclusion is supported by the clear dominance of the 212 fs time constant in the TA dynamics, which has a far greater relative amplitude than the 10 ps decay component. Hence, it appears that for this ensemble the majority of our CIS QDs have  $\text{Cu}^{1+}$  defects, and holes localize faster than the expected biexciton decay. Expectedly, this indicates that biexciton interactions for QDs with  $\text{Cu}^{1+}$  defects do not occur between two delocalized states, and instead holes are localized to  $\text{Cu}^{1+}$  defects, which yield localized-hole, delocalized electron Auger dynamics. If we repeat our procedure for distinguishing the biexciton from single exciton lifetimes using SNSPD measurements of the pump-fluence-dependent PL population dynamics (3.1 eV excitation), we clearly observe that the Auger dynamics for these localized-delocalized biexcitons is far longer than expected for delocalized band-edge carriers ( $\sim 360$  ps as shown in **Figure 4.1.2.3b**).

We explain this phenomena in the schemes presented in **Figure 4.1.2.3c,d**. As stated earlier, subensembles with  $\text{Cu}^{1+}$  defects (**Figure 4.1.2.3c**, left panel) exhibit hole localization faster than the carrier cooling rate ( $\tau_{loc} < \tau_{cool}$ ). Hence, at (near)-resonant excitation VB holes localize to the  $\text{Cu}^{1+}$  defects before CB electrons emit phonons and relax into the CB state, and the growth in the amplitude of the sub-ps time constant indicate that holes localize before “normal,” delocalized Auger or carrier cooling can occur. After holes are localized to  $\text{Cu}^{1+}$  defects, the wavefunction overlap between holes localized to  $\text{Cu}^x$  and delocalized CB electrons is considerably reduced in comparison to

the expected wavefunction overlap of the two delocalized band-edge states. Therefore, the biexciton has a lifetime more than order of magnitude longer than the “typical” tens of ps expected Auger decay rate for delocalized-delocalized carrier interactions, and the transitions are more similar in nature to two negative trions (left panel of **Figure 4.1.2.3d**). However, if CIS QDs do not have  $\text{Cu}^{1+}$  defects, and are instead defect-free or have  $\text{Cu}^{2+}$  defects, VB holes are not removed prior to biexciton decay (right panel of **Figure 4.1.2.3c**). Correspondingly, for a small subensemble of QDs without  $\text{Cu}^{1+}$  defects we observe “normal” delocalized biexciton decay (right panel of **Figure 4.1.2.3d**), which as expected yields  $\sim 10$  ps Auger lifetimes.

We further confirm this hypothesis by repeating our TA measurements at non-resonant excitation (**Figure 4.1.2.3e**). For this case, carrier cooling dominates the sub-picosecond signal of the TA dynamics and we do not distinctly observe the subensemble of QDs with fast hole localizing  $\text{Cu}^{1+}$  defects. Remarkably, after normalizing to  $t=50$  ps and subtracting our spectra collected at  $\langle N \rangle \sim 0.1$ , we observe mono-exponential decay with a 13.6 ps time constant. This is nearly equal to the “slow” decay rate of the biexponential fit for the (near)-resonant excitation measurements (9.8 ps vs. 13.6 ps). We interpret these findings to further indicate that for QDs without  $\text{Cu}^{1+}$  defects, VB holes are not removed prior to multiexciton decay, and delocalized-delocalized Auger interactions yield “normal” biexciton lifetimes. Furthermore, this confirms that CIS QDs *do* form typical delocalized VB states, and that hole localization occurs at  $\text{Cu}^{1+}$  (anti-site) defects, and not from exciton-self trapping. In Figures S6.5.4, S6.5.5 we further show that this finding is rather general, and is reproducible with CISE/ZnS core/shell QDs with  $\sim 75\%$  QY. To eliminate the possibility that Zn alloying in the core/shell structures contributes to the

delocalized VB states, we measure the biexciton lifetimes for core-only CIS QDs at non-resonant excitation in **Figure 4.1.2.3f**. Similar to our (near)-resonant excitation measurements for CIS/ZnS core/shell structures, the decays for these measurements require biexponential fits where one of the two time constants is  $\sim 10$  ps. However, in this case, the second decay component is  $\sim 150$  ps instead of  $\sim 200$  fs, which is similar to the expected negative trion ( $\tau_x^-$ ) lifetime for delocalized BE carriers based on multi-carrier recombination scaling laws.<sup>29-30, 32</sup> Indeed, this is also in agreement with our DFT calculations, which predicted that the square wavefunction for the VB is delocalized in *both* Zn-alloyed, and Zn-free CIS QDs.

The extremely large, over an order of magnitude variation in biexciton lifetimes across the same QD ensemble is further supported by Poisson statistics arguments. In **Figure 4.1.2.4a**, we fit the pump-fluence-dependent intensity of the TA and PL signals for *both* the expected single- and biexciton decay components. Specifically, if we measure the pump-fluence-intensity dependence of the TA signal at non-resonant excitation (3.61 eV, top panel of **Figure 4.1.2.4a**), (near)-resonant excitation (2.41 eV, middle panel of **Figure 4.1.2.4a**), and non-resonant excitation for PL (3.1 eV, bottom panel of **Figure 4.1.2.4a**) we expect that all of the biexcitons have decayed at time  $t \gg \tau_i$  (where  $i$  in  $\tau_i$  can either indicate  $\tau_{xx}$  for delocalized BE “normal” Auger,  $\tau_{loc}$  for the increased localization of VB holes to  $Cu^x$ , or  $Cu^-$  for localized  $Cu^x$  Auger) regardless of the proposed time-scale. Hence, if each of these proposed time-scales ( $\sim 10$  ps for  $\tau_{xx}$ ,  $\sim 200$  fs for  $\tau_{loc}$ , or  $\sim 300$  ps for  $\tau_{Cu^-}$ ) are related to Auger decay than the pump-fluence-intensity for the signal at  $t \gg \tau_i$  (open blue circles for all measurements in **Figure 4.1.2.4a**) should be determined solely by the total number of excited QDs. This should be independent of the

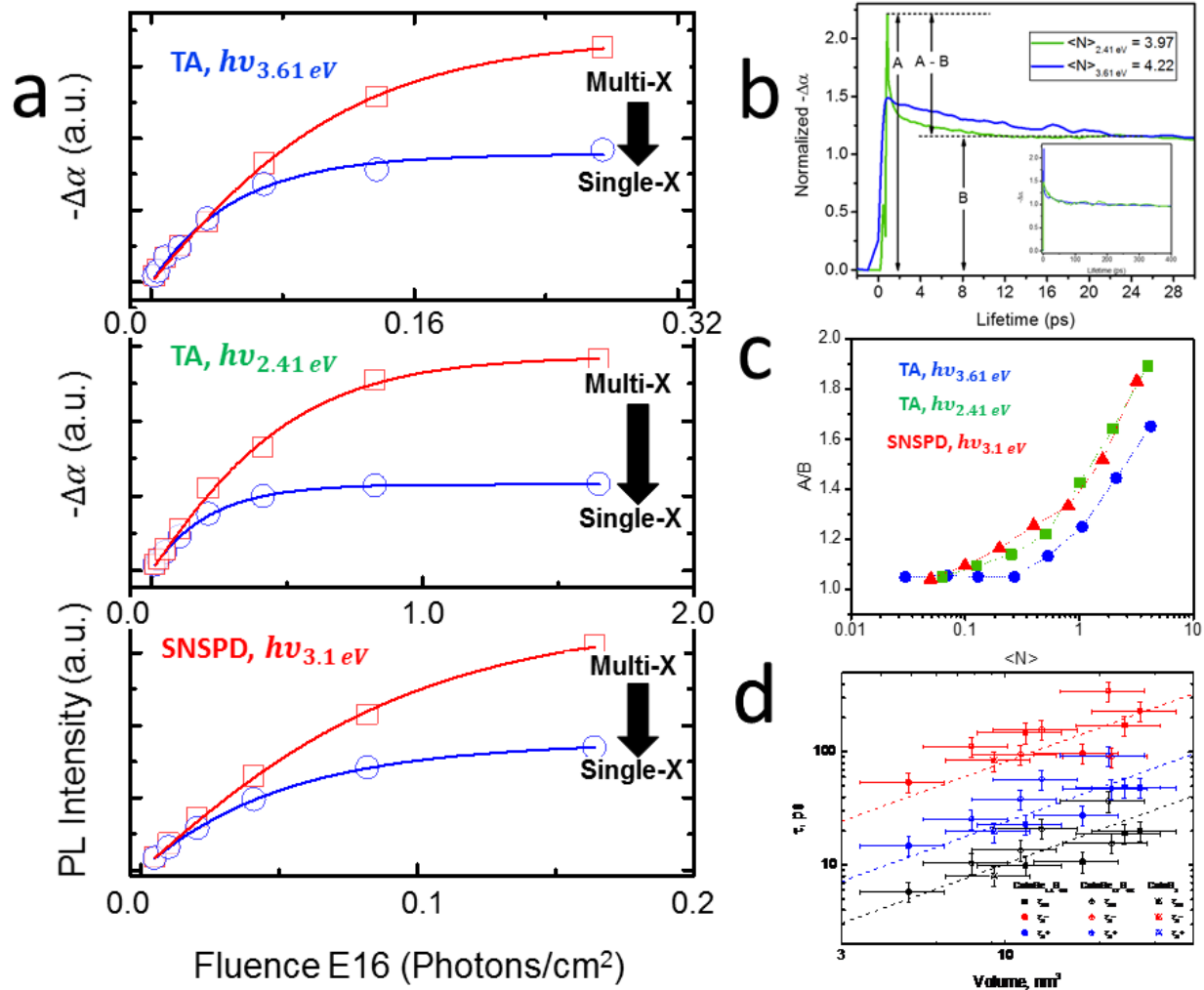


**Figure 4.1.2.4.** (a) Poisson statistics fits to the fluence-dependent early- (red) and late-time (blue) signal for TA measurements at non-resonant excitation (top panel), (near)-resonant excitation (middle panel), and for PL collected at non-resonant excitation (bottom panel). (b) For “normal” Auger in defect-free QDs, or QDs with  $\text{Cu}^{2+}$  defects, CIS exhibits “normal” volume scaling for multicarrier lifetimes due to the delocalized wavefunctions of the band-edge states. (c,d) If we compare the magnitude of the early (A) and late (B) time signal, the relationship between carrier density and the “on-set” of Auger can be compared for all three measurements. (d) The onset for Auger interactions is the same regardless of the measurement method, which indicates that while we have a broad range in lifetimes based on the measurement method, they are all related to multicarrier interactions and Auger dynamics.

early-time signal (open red squares for all measurements in **Figure 4.1.2.4a**), which would be strongly related to multi-exciton decay. Hence, the single- and multi-exciton component of each of these measurements should obey  $P(N) = \langle N_i \rangle^N \exp(-\langle N_i \rangle) / N!$  where  $N$  e-h pairs in a selected QD subensemble have an average population  $\langle N_i \rangle$  in

which  $i$  indicates the time after excitation. In particular, the early-time signal  $\langle N_0 \rangle$  should fit well to Poisson statistics dominated by  $N = 2$ , while at  $t \gg \tau_i$  the data should fit to Poisson statistics of  $N = 1$ . However, for both multi-excitons and single excitons fitting the excitation-fluence ( $J_p$ ) dependence intensity of the TA, or PL signal should yield roughly equivalent absorption cross-sections ( $\sigma$ ) following the relationship  $\langle N_i \rangle = \sigma J_p$ . Hence, if we fit the *early* time signal of the excitation-fluence dependent spectra with  $N = 2$  Poisson statistics (solid red lines in **Figure 4.1.2.4a**), and the *late* time signal with  $N = 1$  Poisson statistics (solid blue lines in **Figure 4.1.2.4a**) we should obtain the same  $\sigma$ , or  $\langle N_0 \rangle = \langle N_{t \gg \tau_i} \rangle$ .

As can be seen in **Figure 4.1.2.4a**, both the early- and late-time signals fit well to the expected Poisson statistics, and we also find that the absorption cross-sections are close to each other between both fits. In addition, as stated earlier, if we compare the ratio of the cross-sections measured with different excitation sources (e.g. 3.61 eV and 2.41 eV excitation) their ratio is comparable to that predicted by their ODs in the linear absorption spectra. This further indicates that while we are observing radically different lifetimes across the ensemble, each decay component obeys the basic Poisson relationships observed as nearly universal to all two-level QD systems. This indicates that the differences in lifetimes merely reflect Auger-related phenomena in different subensembles of the same QD batch. To further prove that the observed differences in lifetimes are indeed related to distinct Auger processes across the different subensembles we verified that they obeyed amplitude scaling laws (**Figure 4.1.2.4b,c**). If we divide the amplitude of the late time signal (B, in **Figure 4.1.2.4b,c**) by the early time signal (A, in **Figure 4.1.2.4b,c**) we should observe the same carrier density dependence

for each measurement, which can be clearly seen in **Figure 4.1.2.4c**. This is because while biexciton lifetimes can vary in QD systems based on excited state wavefunction overlap, the A/B ratio should only reflect the relationship between the carrier density and occupancy of degenerate QD states, which should be universal regardless of the biexciton/exciton lifetimes. Finally, we test volume scaling laws by measuring the biexciton, negative, and positive trion lifetimes for a large-array of CIE, core-only QDs (where E indicates varied Se/S ratios) using our non-resonant TA excitation source. We specifically focus on core-only QDs because the thick ZnS shell prevents photocharging, and makes it difficult to resolve trion lifetimes. Moreover, as stated earlier, the non-resonant TA excitation dynamics represent QDs without  $\text{Cu}^{1+}$  defects due to hole localization being faster than carrier cooling. Resultantly, all multicarrier interactions for these measurements are expected to reflect delocalized BE states, and should therefore obey “universal” volume scaling laws typically used to describe delocalized Auger dynamics in CdSe, and other QDs that exhibit “typical” delocalized excitons. The dashed lines in **Figure 4.1.2.4d** represent the predicted Auger lifetimes for Cl(Se)S QDs based on universal scaling laws, and as can be clearly seen the experimental biexciton, and trion lifetimes match theoretical predictions based on universal volume scaling relationships. Hence, the observance of universal volume scaling where  $\tau_{xx} = 1.02 * Volume$ ,  $\tau_{x-} = 8.2 * Volume$ , and  $\tau_{x+} = 2.4 * Volume$  is in agreement with our earlier assessment that the ~10 ps biexciton lifetime for CIS represents the delocalized biexciton, which occurs in a subensemble of CIS QDs without  $\text{Cu}^{1+}$  defects.

In order to determine the relative population of each subensemble in the CIS/ZnS QD batch, we obtain the excited-state absorption spectrum ( $\alpha$ ) by subtracting the TA

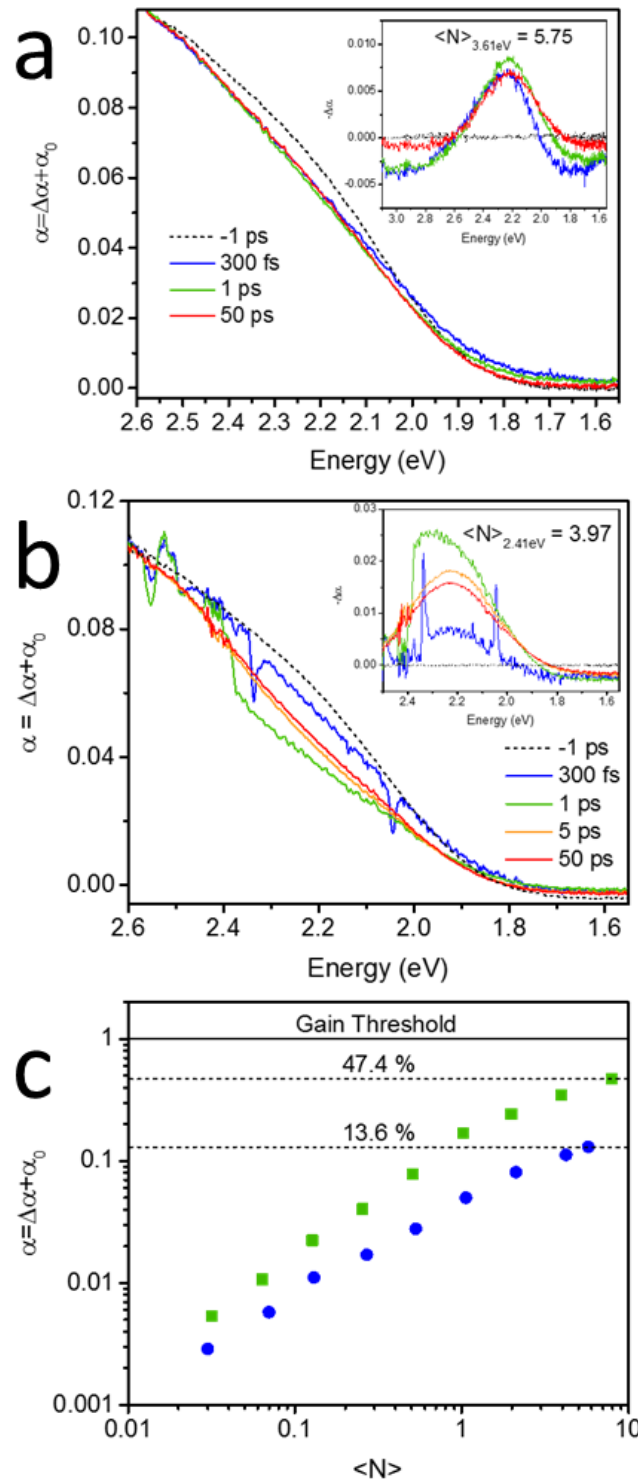


**Figure 4.1.2.5:** (a,b) Measurement of the excited-state absorption spectrum for CIS/ZnS QDs at non-resonant (a) and (near)-resonant (b) excitation. (c) Summary of the data in (a,b) at the 1 ps delay time shows that the magnitude of the bleach is relatively weak in comparison to the linear absorption. However, it is much stronger for (near)-resonant excitation measurements due to the

dominance of hole localization in TA dynamics, which indicates that the majority of the ensemble has  $\text{Cu}^{1+}$  defects.

signal ( $-\Delta\alpha$ ) from the linear absorption ( $\alpha_0$ ), or  $\alpha = \alpha_0 + \Delta\alpha$  (**Figure 4.1.2.5**). This allows us to establish a quantitative relationship between the magnitude of the TA bleach and the average QD population. In “typical” two-level-QD systems (e.g. CdSe) the bleach intensity grows with excitation density before saturating ( $\langle N \rangle > 1$ ) near  $\alpha = 1$ . This condition where  $\alpha_0 = -\Delta\alpha$  indicates that the ensemble absorption is completely bleached, or saturated at the bleach wavelength, and the CB is completely occupied with electrons up to its degeneracy level (2 for CIE QDs). Hence, the bleach dynamics are representative of the entire QD ensemble.<sup>30</sup> In **Figure 4.1.2.5a,b**, we compare  $\alpha$  at non-resonant excitation (3.61 eV, **Figure 4.1.2.5a**), and (near)-resonant excitation (2.41 eV, **Figure 4.1.2.5b**). In each case,  $-\Delta\alpha$  is shown in the figure inset, and  $\alpha_0$  is represented by the spectra at -1 ps delay times (dashed black lines) in the main figure. For the positive delay times, we can clearly observe that even at high carrier densities (e.g. where  $\langle N \rangle = 7.5$ ) the magnitude the TA bleach is significantly weaker than the linear absorption ( $\alpha_0 \gg -\Delta\alpha$ ), and does not represent the entire ensemble.

If we compare the non-resonant (solid blue circles) and (near)-resonant (solid green squares) excited-state absorption spectra in **Figure 4.1.2.5c**, it is readily apparent that the bleach for the (near)-resonant transition (averaged at  $t = 1$  ps for both measurements) is much stronger than for the non-resonant excitation. In fact, while the bleach amplitude reaches  $\sim 50\%$  of the linear absorption for the (near)-resonant excitation measurements, the non-resonant excitation appears to saturate at  $\sim 10\%$  of  $\alpha_0$ . Based on these measurements, we can conclude that the subensemble of QDs that exhibit sub-

picosecond hole localization due to  $\text{Cu}^{1+}$  defects represent a far larger relative population of the experimental ensemble than QDs without hole localization. This smaller subensemble most likely represents QDs with either  $\text{Cu}^{2+}$  defects where VB hole capture at trap states is expected to be slower than hole localization at  $\text{Cu}^{1+}$  defects, and the delocalized biexciton lifetime; or, defect-free QDs where band-to-band transitions are allowed even in the single exciton limit due to the absence of VB hole capture.

### 4.3.3. Conclusions

In conclusion, we have demonstrated that CIE (where E=Se, S) QDs have both delocalized-to-delocalized, and localized-to-delocalized transitions. In the single exciton regime, delocalized exciton decay has tens of ns lifetimes, and only occurs when QDs are defect-free. On the other hand, if the QDs have  $\text{Cu}^x$  defects (where  $x=1+$  or  $2+$ ), VB holes are removed on a faster time-scale than single exciton decay. Correspondingly, emission occurs on the hundreds of ns time-scale due to poor wavefunction overlap of the  $\text{Cu}^x$  localized holes and the delocalized CB electrons. At higher carrier densities, QDs with  $\text{Cu}^{2+}$  defects do not remove VB holes fast enough to block the “normal” band-to-band delocalized Auger transitions. As a result, both defect-free QDs and QDs with  $\text{Cu}^{2+}$  defects exhibit biexciton lifetimes on the tens of ps time-scale, and obey the same scaling laws originally used to describe Auger decay in CdSe QDs. QDs with  $\text{Cu}^{1+}$  defects, conversely localize holes at the sub-ps time-scale and effectively block the “normal” delocalized Auger channel. In this case, Auger dynamics are dominated by delocalized CB electron and  $\text{Cu}^x$  localized hole interactions, and have biexciton lifetimes that are more than an order of magnitude longer than delocalized Auger decay (hundreds of ps instead of tens of ps). Lastly, we determine that the carrier cooling rate is similar to other QD

systems (~300 fs), but hole localization can be even faster than carrier cooling. Therefore, carrier cooling dominates the sub-ps signal in TA measurements at non-resonant excitation whereas hole localization dominates the sub-ps signal in (near)-resonant excitation TA measurements.

#### **4.3.4. Methods**

**Synthesis of Cu(InSe)S QDs.** Typically, 1 mmol of copper iodide and 1 mmol of indium acetate are dissolved in 5 mL of 1-dodecanethiol (DDT) and 1 mL of oleylamine (OLA) in a 50 ml flask, and the mixture is degassed under vacuum at 90 °C for 30 min. The temperature is then raised to 140 °C until all solid precursors are fully dissolved, which usually takes less than 15 min. Separately, a solution of 1 M OLA/DDT-Se is made (e.g., by mixing 79 mg Se powder per 0.75 mL OLA and 0.25 mL DDT) at room temperature under argon. The flask is then heated to 170 – 210 °C, depending on the desired composition, under argon atmosphere, and 0 – 3 mL of the 1 M OLA/DDT-Se solution is added dropwise for coarse control of composition in such a way that the temperature of the reaction mixture does not vary by more than ~3 °C. The temperature is maintained at the injection temperature for ten minutes to allow for nanocrystal nucleation, and then it is set to 230 °C for 1 – 60 min, depending on the desired size of the QDs (typically 10 min for ~3.5 nm face height). After that, the heating element is removed and the QDs are allowed to cool. The resulting CuInSeS QDs are purified by repeated dissolution in chloroform and precipitation with methanol, and then stored in chloroform, octane, hexane, or octadecene under inert conditions (typically argon atmosphere). The reaction is scalable, and typically results in more than 90% chemical yield of QDs (relative to Cu and In precursors). CuInS<sub>2</sub> QDs are prepared the same way, except of the omission of

adding OLA/DDT-Se to the flask. Core/Shell QDs were synthesized by growing ZnS shells onto core-only QDs following the procedure outlined in Chapter 2, Section 2.1.4.

**TR-SEC & Linear Optical Characterization.** An Indium-tin-oxide (ITO) glass slide was used for the working electrode, platinum wire as a counter electrode, and a silver wire as a pseudoreference electrode connected to a potentiostat (CH Instruments). CIS QDs were diluted to 5 mg/ml in air-free chloroform in a Nitrogen glove box. 0.1 M tetrabutylammonium perchlorate (TBAClO<sub>4</sub>) was weighed in the glove box before adding to the QD solution. The CIS:TBAClO<sub>4</sub> molar ratio was roughly 1:5 so that the electrolyte salt can effectively passivate the QD surface. SEC measurements were conducted by holding the potential for each step for 3 minutes, and recording the spectral dynamics with a TCSPC detector probing at the PL peak. This insured that a considerable fraction of the QDs was charged/discharged before each optical measurement. Visible PL spectra were recorded using a Horiba Scientific Fluoromax-4 spectrometer. Absorption spectra were taken with an Agilent 8543 UV-Vis spectrophotometer.

**Transient Absorption Spectroscopy Measurements.** TA spectra were collected using a LabView-controlled home built setup with a standard pump-probe configuration. The excitation source was the frequency tripled (3.61 eV), or frequency doubled (2.41 eV) output of a Pharos amplified Yb:KGW laser (<190 fs pulse duration), and a broad-band, white light supercontinuum probe. For each sample, a pump-fluence-dependent measurement was conducted to determine the absorption cross-section, and all of the spectra shown in the main text reflect the dynamics collected at different carrier densities with  $\langle N \rangle$  determined by the laser fluence and absorption cross-section at the specific excitation energy of the measurement.

**Time-Resolved PL Dynamics Measurements.** The second harmonic of the 800 nm output (400 nm) of a regenerative Ti:sapphire amplifier (Spectra-Physics Spitfire) was used to excite QD solutions. Measurements were conducted at a 1 KHz repetition rate and the dynamics were collected with a superconducting nanowire single photon detector (SNSPD).

**DFT Calculations.** DFT calculations were conducted also using the procedure outlined in Section 2.2.4, but on ZCIS supercells instead of CIS clusters (see main text for details). Supercells were 2X2X2 dimensions (128 atoms) of the CIS unit cell, and the Brillouin Zone was sampled using 2X2X2  $\Gamma$ -centered K-Points. To construct a charge balanced supercell, we replaced 1 Cu and 1 In atoms with Zn in the 16 atom CIS unit cell, before expanding into the supercell. Hence, ~25% of the cations in the structure were Zn.

#### 4.3.5. References

1. Draguta, S.; McDaniel, H.; Klimov, V. I., Tuning Carrier Mobilities and Polarity of Charge Transport in Films of  $\text{CuInSe}_x\text{S}_{2-x}$  Quantum Dots. *Advanced Materials* 2015, 27 (10), 1701-1705.
2. Meinardi, F.; McDaniel, H.; Carulli, F.; Colombo, A.; Velizhanin, K. A.; Makarov, N. S.; Simonutti, R.; Klimov, V. I.; Brovelli, S., Highly efficient large-area colourless luminescent solar concentrators using heavy-metal-free colloidal quantum dots. *Nat Nano* 2015, 10 (10), 878-885.
3. Yun, H. J.; Lim, J.; Fuhr, A. S.; Makarov, N. S.; Keene, S.; Law, M.; Pietryga, J. M.; Klimov, V. I., Charge-Transport Mechanisms in  $\text{CuInSe}_x\text{S}_{2-x}$  Quantum-Dot Films. *ACS Nano* 2018.

4. Jara, D. H.; Yoon, S. J.; Stampelcoskie, K. G.; Kamat, P. V., Size-Dependent Photovoltaic Performance of CuInS<sub>2</sub> Quantum Dot-Sensitized Solar Cells. *Chemistry of Materials* 2014, 26 (24), 7221-7228.
5. Bergren, M. R.; Makarov, N. S.; Ramasamy, K.; Jackson, A.; Guglielmetti, R.; McDaniel, H., High-Performance CuInS<sub>2</sub> Quantum Dot Laminated Glass Luminescent Solar Concentrators for Windows. *ACS Energy Letters* 2018, 3 (3), 520-525.
6. McDaniel, H.; Fuke, N.; Makarov, N. S.; Pietryga, J. M.; Klimov, V. I., An integrated approach to realizing high-performance liquid-junction quantum dot sensitized solar cells. *Nat Commun* 2013, 4.
7. McDaniel, H.; Fuke, N.; Pietryga, J. M.; Klimov, V. I., Engineered CuInSe<sub>x</sub>S<sub>2-x</sub> Quantum Dots for Sensitized Solar Cells. *The Journal of Physical Chemistry Letters* 2013, 4 (3), 355-361.
8. Kim, J.-Y.; Yang, J.; Yu, J. H.; Baek, W.; Lee, C.-H.; Son, H. J.; Hyeon, T.; Ko, M. J., Highly Efficient Copper–Indium–Selenide Quantum Dot Solar Cells: Suppression of Carrier Recombination by Controlled ZnS Overlayers. *ACS Nano* 2015, 9 (11), 11286-11295.
9. Du, J.; Du, Z.; Hu, J.-S.; Pan, Z.; Shen, Q.; Sun, J.; Long, D.; Dong, H.; Sun, L.; Zhong, X.; Wan, L.-J., Zn–Cu–In–Se Quantum Dot Solar Cells with a Certified Power Conversion Efficiency of 11.6%. *Journal of the American Chemical Society* 2016, 138 (12), 4201-4209.
10. Chuang, P.-H.; Lin, C. C.; Liu, R.-S., Emission-Tunable CuInS<sub>2</sub>/ZnS Quantum Dots: Structure, Optical Properties, and Application in White Light-Emitting Diodes with High Color Rendering Index. *ACS Appl. Mater. Interfaces* 2014, 6 (17), 15379-15387.

11. Castro, S. L.; Bailey, S. G.; Raffaele, R. P.; Banger, K. K.; Hepp, A. F., Synthesis and Characterization of Colloidal CuInS<sub>2</sub> Nanoparticles from a Molecular Single-Source Precursor. *The Journal of Physical Chemistry B* 2004, 108 (33), 12429-12435.
12. Allen, P. M.; Bawendi, M. G., Ternary I-III-VI Quantum Dots Luminescent in the Red to Near-Infrared. *Journal of the American Chemical Society* 2008, 130 (29), 9240-9241.
13. Xie, R.; Rutherford, M.; Peng, X., Formation of High-Quality I-III-VI Semiconductor Nanocrystals by Tuning Relative Reactivity of Cationic Precursors. *Journal of the American Chemical Society* 2009, 131 (15), 5691-5697.
14. Bose, R.; Jana, S.; Manna, G.; Chakraborty, S.; Pradhan, N., Rate of Cation Exchange and Change in Optical Properties during Transformation of Ternary to Doped Binary Nanocrystals. *The Journal of Physical Chemistry C* 2013, 117 (30), 15835-15841.
15. Fuhr, A.; Yun, H. J.; Makarov, N. S.; Li, H.; McDaniel, H.; Klimov, V. I., Light-Emission Mechanism in CuInS<sub>2</sub> Quantum Dots Evaluated by Spectral Electrochemistry. *ACS Photonics* 2017.
16. Li, L.; Pandey, A.; Werder, D. J.; Khanal, B. P.; Pietryga, J. M.; Klimov, V. I., Efficient Synthesis of Highly Luminescent Copper Indium Sulfide-Based Core/Shell Nanocrystals with Surprisingly Long-Lived Emission. *Journal of the American Chemical Society* 2011, 133 (5), 1176-1179.
17. Rice, W. D.; McDaniel, H.; Klimov, V. I.; Crooker, S. A., Magneto-Optical Properties of CuInS<sub>2</sub> Nanocrystals. *The Journal of Physical Chemistry Letters* 2014, 5 (23), 4105-4109.

18. Zang, H.; Li, H.; Makarov, N. S.; Velizhanin, K. A.; Wu, K.; Park, Y.-S.; Klimov, V. I., Thick-Shell CuInS<sub>2</sub>/ZnS Quantum Dots with Suppressed “Blinking” and Narrow Single-Particle Emission Line Widths. *Nano Letters* 2017.
19. Jara, D. H.; Stampelcoskie, K. G.; Kamat, P. V., Two Distinct Transitions in Cu<sub>x</sub>InS<sub>2</sub> Quantum Dots. Bandgap versus Sub-Bandgap Excitations in Copper-Deficient Structures. *The Journal of Physical Chemistry Letters* 2016, 7 (8), 1452-1459.
20. Berends, A. C.; Rabouw, F. T.; Spoor, F. C. M.; Bladt, E.; Grozema, F. C.; Houtepen, A. J.; Siebbeles, L. D. A.; de Mello Donegá, C., Radiative and Nonradiative Recombination in CuInS<sub>2</sub> Nanocrystals and CuInS<sub>2</sub>-Based Core/Shell Nanocrystals. *The Journal of Physical Chemistry Letters* 2016, 7 (17), 3503-3509.
21. Knowles, K. E.; Nelson, H. D.; Kilburn, T. B.; Gamelin, D. R., Singlet–Triplet Splittings in the Luminescent Excited States of Colloidal Cu<sup>+</sup>:CdSe, Cu<sup>+</sup>:InP, and CuInS<sub>2</sub> Nanocrystals: Charge-Transfer Configurations and Self-Trapped Excitons. *Journal of the American Chemical Society* 2015, 137 (40), 13138-13147.
22. Fuhr, A. S.; Sautet, P.; Alexandrova, A. N., Heterogeneity in Local Chemical Bonding Explains Spectral Broadening in Quantum Dots with Cu Impurities. *The Journal of Physical Chemistry C* 2019, 123 (9), 5705-5713.
23. van der Stam, W.; de Graaf, M.; Gudjonsdottir, S.; Geuchies, J. J.; Dijkema, J. J.; Kirkwood, N.; Evers, W. H.; Longo, A.; Houtepen, A. J., Tuning and Probing the Distribution of Cu<sup>+</sup> and Cu<sup>2+</sup> Trap States Responsible for Broad-Band Photoluminescence in CuInS<sub>2</sub> Nanocrystals. *ACS Nano* 2018, 12 (11), 11244-11253.

24. Pinchetti, V.; Lorenzon, M.; McDaniel, H.; Lorenzi, R.; Meinardi, F.; Klimov, V. I.; Brovelli, S., Spectro-electrochemical Probing of Intrinsic and Extrinsic Processes in Exciton Recombination in I–III–VI<sub>2</sub> Nanocrystals. *Nano Letters* 2017, 17 (7), 4508-4517.
25. Nelson, H. D.; Gamelin, D. R., Valence-Band Electronic Structures of Cu<sup>+</sup>-Doped ZnS, Alloyed Cu–In–Zn–S, and Ternary CuInS<sub>2</sub> Nanocrystals: A Unified Description of Photoluminescence across Compositions. *The Journal of Physical Chemistry C* 2018, 122 (31), 18124-18133.
26. Brovelli, S.; Galland, C.; Viswanatha, R.; Klimov, V. I., Tuning Radiative Recombination in Cu-Doped Nanocrystals via Electrochemical Control of Surface Trapping. *Nano Letters* 2012, 12 (8), 4372-4379.
27. Viswanatha, R.; Brovelli, S.; Pandey, A.; Crooker, S. A.; Klimov, V. I., Copper-Doped Inverted Core/Shell Nanocrystals with “Permanent” Optically Active Holes. *Nano Letters* 2011, 11 (11), 4753-4758.
28. Hughes, K. E.; Hartstein, K. H.; Gamelin, D. R., Photodoping and Transient Spectroscopies of Copper-Doped CdSe/CdS Nanocrystals. *ACS Nano* 2018, 12 (1), 718-728.
29. Pietryga, J. M.; Park, Y.-S.; Lim, J.; Fidler, A. F.; Bae, W. K.; Brovelli, S.; Klimov, V. I., Spectroscopic and Device Aspects of Nanocrystal Quantum Dots. *Chemical Reviews* 2016, 116 (18), 10513-10622.
30. Klimov, V. I., Optical Nonlinearities and Ultrafast Carrier Dynamics in Semiconductor Nanocrystals. *The Journal of Physical Chemistry B* 2000, 104 (26), 6112-6123.

31. García-Santamaría, F.; Chen, Y.; Vela, J.; Schaller, R. D.; Hollingsworth, J. A.; Klimov, V. I., Suppressed Auger Recombination in “Giant” Nanocrystals Boosts Optical Gain Performance. *Nano Letters* 2009, 9 (10), 3482-3488.
32. Park, Y.-S.; Bae, W. K.; Pietryga, J. M.; Klimov, V. I., Auger Recombination of Biexcitons and Negative and Positive Trions in Individual Quantum Dots. *ACS Nano* 2014, 8 (7), 7288-7296.
33. Sandberg, R. L.; Padilha, L. A.; Qazilbash, M. M.; Bae, W. K.; Schaller, R. D.; Pietryga, J. M.; Stevens, M. J.; Baek, B.; Nam, S. W.; Klimov, V. I., Multiexciton Dynamics in Infrared-Emitting Colloidal Nanostructures Probed by a Superconducting Nanowire Single-Photon Detector. *ACS Nano* 2012, 6 (11), 9532-9540.
34. Pandey, A.; Brovelli, S.; Viswanatha, R.; Li, L.; Pietryga, J. M.; Klimov, V. I.; Crooker, S. A., Long-lived photoinduced magnetization in copper-doped ZnSe-CdSe core-shell nanocrystals. *Nat Nano* 2012, 7 (12), 792-797.
35. Bussian, D. A.; Crooker, S. A.; Yin, M.; Brynda, M.; Efros, A. L.; Klimov, V. I., Tunable magnetic exchange interactions in manganese-doped inverted core-shell ZnSe-CdSe nanocrystals. *Nature Materials* 2008, 8, 35.
36. Kresse, G.; Furthmüller, J., Efficiency of ab-initio total energy calculations for metals and semiconductors using a plane-wave basis set. *Computational Materials Science* 1996, 6 (1), 15-50.
37. Kresse, G.; Furthmüller, J., Efficient iterative schemes for ab initio total-energy calculations using a plane-wave basis set. *Physical Review B* 1996, 54 (16), 11169-11186.

38. Kresse, G.; Hafner, J., *Ab Initio* molecular-dynamics simulation of the liquid-metal-amorphous-semiconductor transition in germanium. *Physical Review B* 1994, 49 (20), 14251-14269.
39. Kresse, G.; Hafner, J., *Ab initio* molecular dynamics for liquid metals. *Physical Review B* 1993, 47 (1), 558-561.
40. Perdew, J. P.; Burke, K.; Ernzerhof, M., Generalized Gradient Approximation Made Simple. *Physical Review Letters* 1996, 77 (18), 3865-3868.
41. Heyd, J.; Scuseria, G. E.; Ernzerhof, M., Hybrid functionals based on a screened Coulomb potential. *The Journal of Chemical Physics* 2003, 118 (18), 8207-8215.
42. Pohl, J.; Albe, K., Thermodynamics and kinetics of the copper vacancy in  $\text{CuInSe}_2$ ,  $\text{CuGaSe}_2$ ,  $\text{CuInS}_2$ , and  $\text{CuGaS}_2$  from screened-exchange hybrid density functional theory. *Journal of Applied Physics* 2010, 108 (2), 023509.
43. Chen, H.; Wang, C.-Y.; Wang, J.-T.; Hu, X.-P.; Zhou, S.-X., First-principles study of point defects in solar cell semiconductor  $\text{CuInS}_2$ . *Journal of Applied Physics* 2012, 112 (8), 084513.
44. Le Bahers, T.; Rérat, M.; Sautet, P., Semiconductors Used in Photovoltaic and Photocatalytic Devices: Assessing Fundamental Properties from DFT. *The Journal of Physical Chemistry C* 2014, 118 (12), 5997-6008.

## CHAPTER 5

### Charge Transport in Quantum Dots with Cu Impurities

## 5.1. Charge Transport Mechanisms in $\text{CuInSe}_x\text{S}_{2-x}$ Quantum Dot Films

### 5.1.1. Introduction

Colloidal quantum dots (QDs) have been used to demonstrate the viability of various QD-based electronic devices such as field-effect transistors (FETs),<sup>1-3</sup> complementary metal-oxide-semiconductor (CMOS) inverters,<sup>4</sup> logic gates,<sup>5</sup> and wearable electronics.<sup>6</sup> One potentially beneficial distinction of QDs from traditional bulk semiconductors is their amenability toward solution-based processing such as spin coating,<sup>2, 6</sup> inkjet printing,<sup>7</sup> and doctor blading,<sup>8</sup> which could enable low-cost, highly flexible (e.g., bendable or foldable) and disposable electronics. Realization of such devices is further simplified by the availability of demonstrated procedures for tuning both transport polarity and carrier mobility *via* relatively simple and noninvasive post-preparation chemical treatments.<sup>2, 4, 8-16</sup>

The majority of published charge-transport studies of QD solids have focused on CdE and PbE QDs (most often, E = S or Se). Due to well-developed methodologies for synthesis and assembly of these materials, they are ideally suited for gaining fundamental insights into mechanisms for charge conductance in QD-based mesoscale solids. However, the presence of highly toxic heavy metals (Pb or Cd) limits their practical utility in prospective real-life electronic devices. Copper indium selenium sulfide ( $\text{CuInSe}_x\text{S}_{2-x}$ ; abbreviated here as CISES) QDs represent an environmentally benign alternative to Pb- and Cd-based QD materials.<sup>17-22</sup> The available literature studies indicate the feasibility of realizing both *p*- and *n*-type transport polarities in films of CISES QDs with fairly high mobilities for both electrons and holes (up to  $\sim 0.02 \text{ cm}^2 \text{ V}^{-1} \text{ s}^{-1}$ )<sup>19, 21</sup> and even ambipolar

conductance.<sup>19</sup> These initial observations suggest the considerable potential of these QDs as electronic materials. However, fully exploiting this potential requires a much deeper understanding of their charge-transport properties.

An important distinction of CISES QDs from PbE and CdE QDs is the presence of two cations and two anions, which makes them prone to a variety of defects that do not occur in binary materials. These defects can affect charge transport by both creating intra-gap traps and acting as electronic dopants. For instance, metal vacancies ( $V_{Cu}^{\cdot}$  and  $V_{In}^{\prime\prime\prime}$ ) and a  $Cu^{1+}$  cation residing on an  $In^{3+}$  site (an anti-site  $Cu_{In}^{\prime\prime}$  defect) represent acceptor states that can enable *p*-type transport.<sup>23, 24</sup> On the other hand, anion vacancies ( $V_S^{\cdot\cdot}$  and  $V_{Se}^{\cdot\cdot}$ ), an  $In^{3+}$  cation occupying a  $Cu^{1+}$  site (an anti-site  $In_{Cu}^{\cdot\cdot}$  defect), or an interstitial In cation (an  $In_i^{\cdot\cdot\cdot}$  defect) create donor states promoting *n*-type transport.<sup>24</sup> If properly controlled, the abundance of these native defects can allow for manipulating doping levels and transport polarity. This method of “defect control” can potentially complement or even replace more traditional approaches involving incorporation of impurities<sup>25-27</sup> and/or various types of surface treatments.<sup>1, 3, 8, 14</sup> It can also allow for the realization of designated transport channels involving engineered defect bands.<sup>28, 29</sup>

Here we investigate carrier transport in films of CISES QDs with a varied Se/(Se+S) ratio ( $f_{Se} = x/2$ ) incorporated into FETs as a conducting channel. We observe that as-prepared QDs exhibit a *p*-type behavior, while moderate-temperature annealing in the presence of indium imparts *n*-type transport characteristics. Further, we find that increasing  $f_{Se}$  leads to improved carrier mobilities in both *n*- and *p*- type QD films, and explain this result using a two-state conductance model, in which charge carriers are transported within a QD solid through a high-mobility band formed by intrinsic band-edge

states and a low-mobility band created by intra-gap defects. The  $f_{\text{Se}}$ -dependent mobility is a result of the  $f_{\text{Se}}$ -dependent energy spacing between the high- and low-mobility bands, which controls thermal distribution of carriers between them. In addition, we demonstrate that carrier mobilities, the contrast between the ON and OFF currents, and the air stability of CISES QD-FETs can be improved by infilling QD films with amorphous  $\text{Al}_2\text{O}_3$  *via* atomic layer deposition (ALD).

### 5.1.2. Results & Discussion

**QD Samples and Spectroscopic Studies.** We synthesize CISES QDs with  $f_{\text{Se}}$  from 0–0.8 following a previously described procedure.<sup>21</sup> According to transmission electron microscopy (TEM) studies (**Figure 5.1.2.1a** and Figure S6.6.1), the QDs have a tetrahedral shape as previously observed.<sup>17, 21, 30</sup> Based on X-ray diffraction (XRD) measurements (Figure S6.6.2), the prepared QDs exhibit a chalcopyrite crystal structure, with the diffraction peaks shifting towards lower angles with increasing  $f_{\text{Se}}$ . This can be explained by the lattice expansion driven by the increased fraction of larger selenium anions. Elemental analysis by inductively coupled plasma optical emission spectroscopy (ICP-OES) indicates that the QDs are anion rich; however, establishing to what degree is complicated by the presence of sulfur in the 1-dodecanethiol (DDT) ligands. The fabricated samples exhibit a Cu:In ratio of 0.95. To focus on the effect of composition without complications due to a varied size, in our studies we use samples with a similar average QD height ( $h$ ) of 5.0 - 5.7 nm (Figure S6.6.1).

As typical for CISES QDs, absorption spectra of the synthesized samples do not exhibit a sharp band-edge peak but instead show a smooth step (blue lines in **Figure**

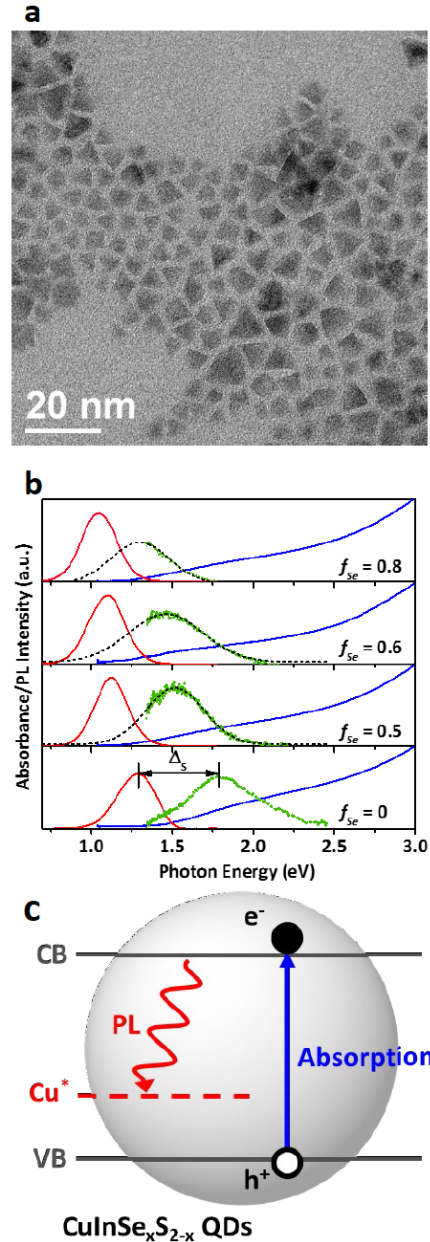


**Figure 5.1.2.1.** Transmission electron microscopy (TEM) images of  $\text{CuInSe}_x\text{S}_{2-x}$  QDs and their optical spectra. (a) TEM images of  $\text{CuInSe}_{1.6}\text{S}_{0.4}$  QDs with a mean height of 5.5 nm and a standard deviation of 1.8 nm. (b) Optical absorption (blue solid lines), photoluminescence (PL; red solid lines), and early-time TA (green circles, 1-ps pump-probe delay; Gaussian fits are shown by black dashed lines) spectra of  $\text{CuInSe}_x\text{S}_{2-x}$  QDs with a varied Se fraction; all samples have approximately the same height of 5.0 - 5.7 nm. (c) Schematic representation of optical transitions responsible for the VB-to-CB absorption (blue arrow) and intragap PL (red wavy arrow); the latter transition involves a native Cu-related defect ( $\text{Cu}^*$ ).

**5.1.2.1b).** Therefore, in order to determine the QD band gap ( $E_g$ ), we apply a transient-absorption (TA) spectroscopy and use the position of the lowest-energy (band-edge),

early-time bleach (green dots in **Figure 5.1.2.1b**; the pump-probe delay is  $\sim 1$  ps) as a measure of  $E_g$ .<sup>31</sup> This yields the band gap of 1.80 to 1.34 eV for  $f_{Se}$  changing from 0 to 0.8. Consistent with previous observations, the observed photoluminescence (PL) (red lines in **Figure 5.1.2.1b**) is characterized by a broad spectral profile ( $\sim 250$  meV full width at half maximum, FWHM)<sup>32, 33</sup> and exhibits a large Stokes shift ( $\Delta_S$ ) of  $\sim 300$  to 500 meV vs.  $E_g$ . As  $f_{Se}$  increases from 0 to 0.8, the PL peak shifts from 1.3 to 1.0 eV.

In literature, the large PL Stokes shift in ClSeS QDs has been explained several ways, including invoking the peculiar electronic structure of chalcopyrite nanocrystals, which features low-oscillator-strength band-edge states,<sup>34</sup> exciton “self-localization”,<sup>35</sup> and finally, the involvement of an emissive intra-gap hole-like state associated with a Cu-related native defect.<sup>23, 24, 36</sup> According to a recently refined Cu-defect model, altering the QD stoichiometry and thereby the amount of  $Cu^{2+}$  vs.  $Cu^{1+}$  defects impacts the dominant emission mechanism.<sup>33</sup> Specifically, in stoichiometric QDs (*i.e.* Cu:In = 1), where the prevailing defect is an anti-site  $In_{Cu}-Cu_{In}$  pair, the copper ion is the  $Cu^{1+}$  state with a fully occupied d-shell ( $d^{10}$ ). In order to become PL active, it must first trap a valence-band (VB) hole, and only after that, it can capture a conduction-band (CB) electron *via* a radiative transition. On the other hand, Cu-deficient QDs (Cu:In < 1) are characterized by a large abundance of  $Cu^{2+}$ -defects created as a means to compensate for copper vacancies. Since the  $d^9$   $Cu^{2+}$  ion can be considered to have a hole in its *d*-shell prior to excitation, such defects are immediately emission ready, and can participate in radiative recombination without capturing a VB hole. As the samples we study here are only slightly Cu-deficient, both of these pathways are likely viable. Accordingly, we simplify our

schematic representation of the emission mechanism in **Figure 5.1.2.1c** by labeling the Cu-related emissive defect as  $\text{Cu}^*$  (where  $*$  can be either 1+ or 2+).

**Cyclic Voltammetry Measurements.** To quantify absolute energies of electronic states in synthesized QDs, we conduct cyclic voltammetry (CV) measurements (see Methods for experimental details). **Figure 5.1.2.2a** shows an example of CV traces taken for the QD sample with  $f_{\text{Se}} = 0.8$ , which exhibits the highest  $p$ -type carrier mobility, as detailed later in this work. Additional CV measurements for samples with varied  $f_{\text{Se}}$  are shown in Figure S6.6.3a. Following the methodology of previous CV studies of QDs,<sup>33, 37, 38</sup> we determine energies of redox-active states from onset potentials of observed CV waves inferred from extrapolations of linear fits (red dotted lines in **Figure 5.1.2.2a**). For a “forward” scan, when the electrochemical potential ( $V_{\text{EC}}$ ) is swept to progressively more oxidative values, we detect two distinct oxidation waves. Based on our previous analysis,<sup>33, 37</sup> the first wave (+0.13 V vs. Ag/Ag<sup>+</sup>) can be ascribed to the  $\text{Cu}^*$  defect ( $E_{\text{Cu}^*}$ ) and the second wave (+0.57 V vs. Ag/Ag<sup>+</sup>) to the VB edge ( $E_{\text{VB}}$ ). In principle, we should be able to determine the CB-edge position ( $E_{\text{CB}}$ ) in a similar manner from the reverse scan. However, as shown in Figure S6.6.3b, the parasitic background current from the electrolyte observed at large reductive potentials masks QD related features. Therefore, we find the CB energy from the sum of the measured VB-edge energy and the optical band gap inferred from the TA spectra (**Figure 5.1.2.1b**, green circles).

In **Figure 5.1.2.2b**, we present a summary of CV and optical measurements of energies of the redox-active intragap state (presumably a  $\text{Cu}^*$  defect) and the VB and CB edges for samples with different Se fractions plotted as a function of  $f_{\text{Se}}$ . The energies are shown vs. both vacuum (left vertical axis) and the Ag/Ag<sup>+</sup> potential (right vertical axis).

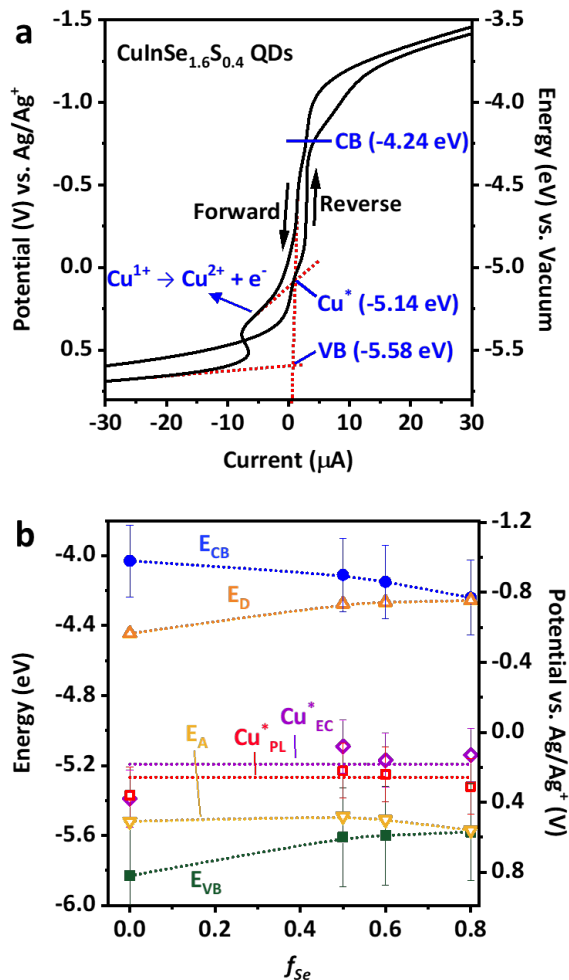


**Figure 5.1.2.2.** Electrochemical studies of  $\text{CuInSe}_x\text{S}_{2-x}$  QDs and energies of optically and electrically active states as a function of a varied Se content ( $f_{\text{Se}}$ ). (a) Cyclic voltammograms (CVs) of  $\text{CuInSe}_{1.6}\text{S}_{0.4}$  QD colloidal solutions; mean QD height is 5.5 nm. The potential is scanned from 0 to 2 V (forward scan), then to -2 V (reverse scan) and finally back to 0 V. An intra-gap wave with onset at -5.14 V (obtained from the intersection of the red dashed lines) observed during the forward scan is ascribed to oxidation of  $\text{Cu}^{1+}$  to  $\text{Cu}^{2+}$ . The second oxidation wave with onset at -5.58 eV is due to hole injection into the QD VB. The position of the CB level is obtained as a sum of the VB energy and the optical band gap. (b) Energies of the CB (blue solid circles) and VB (green solid squares) levels for  $\text{CuInSe}_x\text{S}_{2-x}$  QDs with different  $f_{\text{Se}}$  based on CV and optical measurements. The purple open diamonds ( $\text{Cu}_{\text{EC}}^*$ ) show the redox potential of the intragap feature ascribed to the  $\text{Cu}^*$  defect, and the red open squares ( $\text{Cu}_{\text{PL}}^*$ ) correspond to the energy of the intragap state obtained based on the apparent Stokes shift from the optical measurements (Figure 5.1.2.1b). The energies of native donor and acceptor defect states obtained from transport measurements are shown by orange open up-point triangles and yellow open down-point triangles, respectively.

We observe that increasing  $f_{\text{Se}}$  leads to a drop in  $E_{\text{CB}}$  (blue solid circles), which is accompanied by an increase in  $E_{\text{VB}}$  (green solid squares). The energy of the intragap

state is determined from both CV measurements (purple open diamonds) and the Stokes shift of the PL band (red open squares).<sup>33</sup> The two data sets are in excellent agreement and indicate that  $E_{\text{Cu}^*}$  is nearly independent of  $f_{\text{Se}}$ . Furthermore, the absolute value of  $E_{\text{Cu}^*}$  (ca. -5.22 V; average of the PL and CV measurements) is consistent with the  $\text{Cu}^{1+/2+}$  redox potential,<sup>39-41</sup> confirming the assignment of the intragap state to the Cu-related defect.<sup>33</sup>

**Charge Transport Studies.** To investigate charge transport characteristics of ClSeS QD films, we incorporate them into FETs fabricated on heavily doped *p*-type silicon wafers with a thermally grown silicon oxide (300 nm thickness) using a bottom-gate, bottom-source/drain contact configuration (**Figure 5.1.2.3a**). Source and drain electrodes are applied to the wafer surface *via* thermal evaporation, and colloidal QDs are deposited onto the pre-patterned substrate by spin coating. The typical thickness of the QD layer is ~100 nm. In some cases (as specified below), long native oleylamine and 1-dodecanethiol ligands are replaced with shorter molecules such as 1,2-ethanedithiol (EDT) by solution treatment after deposition. Additionally, for some of the measurements, the FET films have undergone thermal annealing according to protocols described later in this work.

Representative output curves (source-drain current,  $I_{\text{DS}}$ , vs. source-drain voltage,  $V_{\text{DS}}$ ) of FETs fabricated with gold contacts and QDs with  $f_{\text{Se}} = 0.8$  without ligand exchange are presented in **Figure 5.1.2.3b**. Despite a large average interparticle distance of ~1.5 nm defined by long native ligands (**Figure 5.1.2.1a**), the QD films shows fairly good *p*-type conductance that is well modulated by gate voltage ( $V_{\text{GS}}$ ). Based on the measured  $I_{\text{DS}}-V_{\text{DS}}$  characteristics, we obtain that the hole mobility in the linear regime<sup>2</sup> ( $\mu_{\text{h,lin}}$ ) is  $4.33 \times 10^{-5} \text{ cm}^2 \text{ V}^{-1} \text{ s}^{-1}$ . These results are distinct from previously studied FETs based on PbE

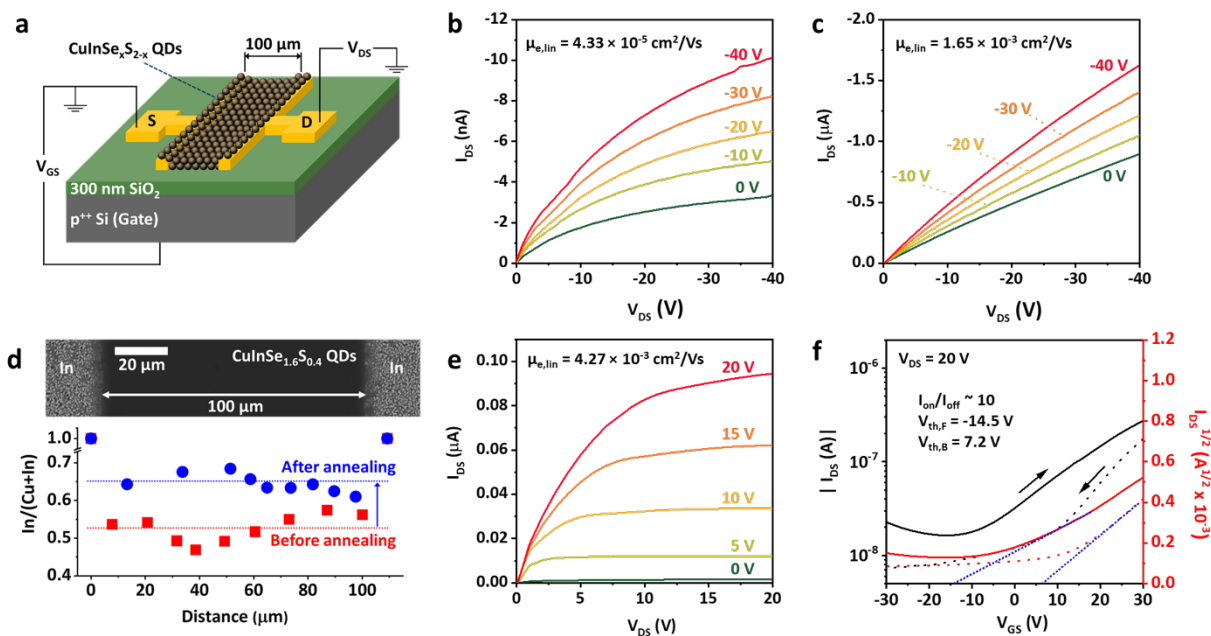


**Figure 5.1.2.3.** Charge transport measurements of CuInSe<sub>1.6</sub>S<sub>0.4</sub> QD films incorporated into FETs. (a) A schematic representation of a bottom-gate, bottom-contact QD-FET. (b) Output characteristics ( $I_{DS}$  vs.  $V_{DS}$ ) of a gold-contact FET made of as-synthesized CuInSe<sub>1.6</sub>S<sub>0.4</sub> QDs with long native ligands (the mean QD height  $h = 5.5$  nm), which shows a  $p$ -channel behavior. (c) Output characteristics for a gold-contact FETs based on QDs treated with EDT ligands. (d) A top-view SEM image of an In-contact CuInSe<sub>1.6</sub>S<sub>0.4</sub> QD-FET along with the plot of the In/(Cu+In) ratio as a function of location along the channel before (red symbols) and after (blue symbols) heat treatment at 250 °C, as determined by EDS. (e) Output characteristics of the In-contact CuInSe<sub>1.6</sub>S<sub>0.4</sub> QD-FET after thermal annealing, which show a nondegenerate  $n$ -channel behavior. (f) Transfer characteristics ( $I_{DS}$  vs.  $V_{GS}$ ) of the device shown in 'e' measured at  $V_{DS} = 20$  V, which corresponds to the saturation regime. Solid and dotted lines are the forward and the reverse scan, respectively. The linear extrapolation of the  $(I_{DS})^{0.5}$  transfer curves measured for large positive voltages are used to determine a threshold voltage,  $V_{th}$  (blue lines); values  $V_{th,F}$  and  $V_{th,B}$  are obtained from the forward and reverse (backward) scans, respectively.

and CdE QDs, wherein the films of as-deposited QDs are insulating and non-gatable prior to ligand exchange. The “gatable” behavior of the as-deposited CISES QDs supports our earlier assertion that native defects inherent to these quaternary materials can serve as electron donors or acceptors. Due to this self-doping effect, the Fermi level shifts closer to high-mobility band-edge states which helps access them by applying gate bias. In this specific case, the observed  $p$ -channel transport can be ascribed to, for example, metal vacancies and/or antisite Cu<sub>In</sub> defects.

After ligand exchange with EDT, the film mobility increases to  $\mu_{h,lin} = 1.65 \times 10^{-3} \text{ cm}^2 \text{ V}^{-1} \text{ s}^{-1}$ ; (**Figure 5.1.2.3c**, gold-contact FET), which is likely a direct result of decreased inter-QD spacing.<sup>11</sup> At the same time, we observe a weakened modulation by  $V_{GS}$ , suggesting an increase in hole concentration caused likely by the increase in the QD density, which translates into increased dopant concentration (by volume) even if a per-dot number of dopants remains constant. Specifically, based on the dimensions of our QDs and the lengths of the original (oleylamine and 1-dodecanethiol) and final (EDT) ligands, the dot concentration can increase by a factor of *ca.* 1.6–2 following surface treatment with EDT. Additionally, the increased hole density can be a result of the “doping effect” of EDT, which is known to impart *p*-type behavior in PbE QD films.<sup>42, 43</sup> Our present observations for ClSeS-QD FETs with gold contacts are in agreement with results of ref. 19 for similar devices, which also revealed *p*-type conduction in both as-prepared and EDT-treated films.

It was previously shown that the use of indium source and drain electrodes, followed by thermal annealing after EDT-ligand exchange, leads to devices that exhibit non-degenerate *n*-type transport.<sup>19</sup> Accordingly, we apply indium contacts to a wafer, then spin-coat QDs and after that, treat the QD film with EDT. Afterwards, we anneal the complete device at 250 °C for 2 hours. **Figure 5.1.2.3d** shows a top-view scanning electron microscopy (SEM) image of the device channel (QDs with  $f_{Se} = 0.8$ ) along with a compositional profile obtained using energy-dispersive X-ray spectroscopy (EDS) before (red squares) and after (blue circles) heat treatment. Before annealing, the average In content (as a fraction of the total number of cations, Cu+In) is 52%, which is in agreement with the ICP-OES results for the QDs themselves. On the other hand, the In content

increases to 65% after annealing, which indicates the diffusion of In throughout the entire device channel. This does not significantly affect the optical absorption of the QD films, and specifically, does not alter the position of the band-edge feature used to quantify the QD band gap (Figure S6.6.4). This suggests that the annealing procedures do not lead to sintering of the ClSeS particles, which thus preserve their quantum-confined nature.

As seen in the representative output and transfer ( $I_{DS}$  vs.  $V_{GS}$ ) characteristics (Figure 5.1.2.3e and f, respectively), thermally annealed, In-contact-based QD-FETs show well-modulated  $n$ -type transport with  $\mu_{e,lin}$  of  $4.27 \times 10^{-3} \text{ cm}^2 \text{ V}^{-1} \text{ s}^{-1}$ . The indium-contact annealed devices exhibit a considerable improvement in the ON/OFF current ratio ( $I_{on}/I_{off} \approx 10$ ; Figure 5.1.2.3f) compared to the  $p$ -type gold-contact based FETs ( $I_{on}/I_{off} \approx 3$ ; Figure S6.6.5). We interpret the switch from  $p$ - to  $n$ -conductance as being due to thermal diffusion of In into the QD solid, resulting in removal of acceptor-type metal-vacancies and/or formation of In-related defects ( $\text{In}_{\text{Cu}}^{2+}$  or  $\text{In}_i^{3+}$ ) acting as donor states.<sup>23, 24</sup> For example, as was suggested earlier, a possible source of  $p$ -doping in as-prepared QDs as well as EDT-treated dots is copper vacancies that trap electrons from the VB leading to generation of VB holes. During annealing in the presence of metallic indium, indium atoms can fill copper vacancies by losing three electrons, one of which reduces the VB hole, while two others are released into the CB. The net result of these processes is the transport polarity switching from  $p$ - to  $n$ -type.

**Charge Transport Model.** Examination of  $p$ - and  $n$ -channel devices based on QDs with a varied Se fraction indicates a dramatic effect of  $f_{\text{Se}}$  on transport characteristics, and in particular, carrier mobilities. Figure S6.6.6 shows output characteristics of the  $n$ -type FETs (indium contacts, annealed) made of QDs with  $f_{\text{Se}} = 0, 0.25, 0.5, 0.6,$  and  $0.7$ .

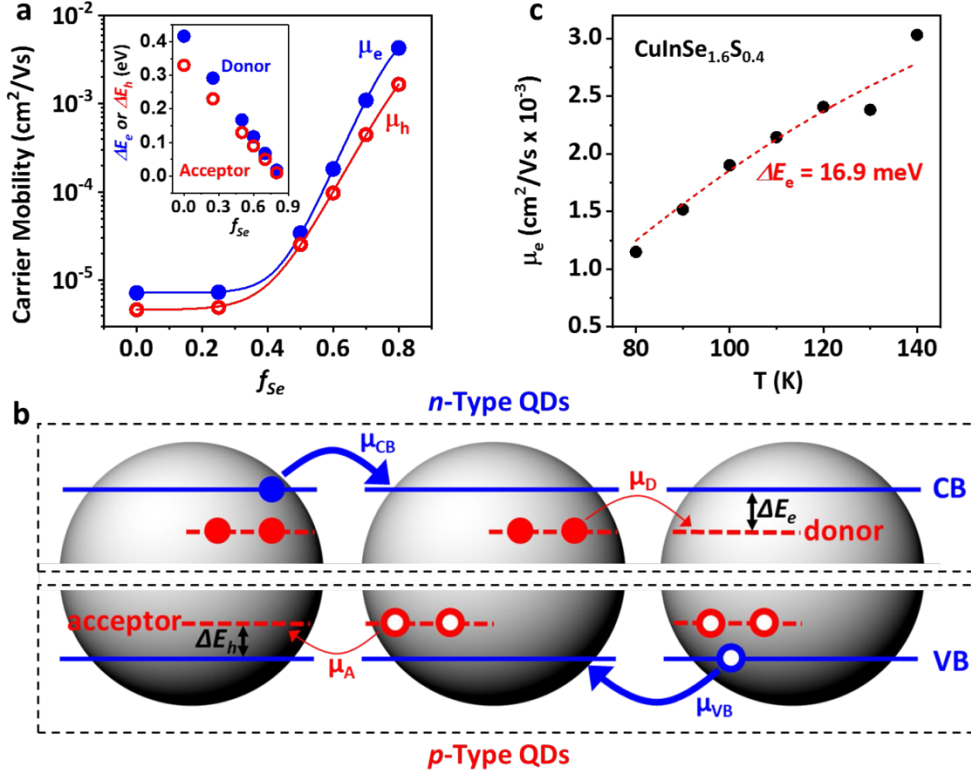


**Figure 5.1.2.4.** The two-state conduction model for explaining the dependence of carrier mobilities in CuInSe<sub>x</sub>S<sub>2-x</sub> QD films on the Se/(Se+S) ratio and temperature. (a) Electron (blue) and hole (red) mobilities obtained from FET measurements of, respectively, *n* (indium contacts; EDT-treated, annealed QD films) and *p* (gold contacts; EDT treated QD films) type devices (symbols) in comparison to fit lines produced by a two-state conduction model (lines). Based on the fits,  $\gamma_{C,D} = 1.76$ ,  $\mu_D = 7.2 \times 10^{-6} \text{ cm}^2 \text{ V}^{-1} \text{ s}^{-1}$ ,  $\mu_{CB} = 9 \times 10^{-3} \text{ cm}^2 \text{ V}^{-1} \text{ s}^{-1}$ ,  $\Delta E_{e,S} = 416 \text{ meV}$ ,  $\Delta E_{e,Se} = 17 \text{ meV}$  (*n*-type films) and  $\gamma_{V,A} = 0.5$ ,  $\mu_A = 4.6 \times 10^{-6} \text{ cm}^2 \text{ V}^{-1} \text{ s}^{-1}$ ,  $\mu_{VB} = 6.4 \times 10^{-3} \text{ cm}^2 \text{ V}^{-1} \text{ s}^{-1}$ ,  $\Delta E_{h,S} = 330 \text{ meV}$ ,  $\Delta E_{h,Se} = 10 \text{ meV}$  (*p*-type films). The energy gap between the band-edge and the defect states as a function of  $f_{Se}$  is displayed in the inset by solid blue (*n*-type films) and open red (*p*-type films) symbols. The absolute energies of defect states derived from charge transport studies are shown in Figure 5.1.2.2b by orange open up-point triangles (donors) and yellow open down-point triangles (acceptors). (b) A schematic depiction of the two-state conduction model for the CuInSe<sub>x</sub>S<sub>2-x</sub> QD films. In this model, carriers are transported *via* two thermally coupled states. A higher-mobility state is ascribed to the intrinsic CB (*n*-type) or VB (*p*-type) levels (blue), and the lower mobility state to the native donor (*n*-type) or acceptor (*p*-type) defects (red). In thermal equilibrium, the relative occupancies of these states and the resulting apparent mobility are defined by the  $f_{Se}$ -dependent inter-state energy gap ( $\Delta E_e$  or  $\Delta E_h$ ) and temperature according to eq 3. (c) Temperature-dependent electron mobility measured in the linear regime for the *n*-type CuInSe<sub>1.6</sub>S<sub>0.4</sub> QD film ( $h = 5.5 \text{ nm}$ ) (symbols) along with a fit (line) using the two-state conduction model. The  $\Delta E_e$  energy produced by this fit (16.9 meV) is virtually identical to that obtained from the room-temperature  $f_{Se}$ -dependent measurements (17 meV; the inset of panel ‘a’).

Electron mobilities derived from these measurements along with the data point for the  $f_{Se} = 0.8$  device (Figure 5.1.2.3e) are plotted in Figure 5.1.2.4a (blue solid circles). These

data reveal a dramatic, three-orders-of-magnitude increase in mobility as  $f_{Se}$  changes from 0 to 0.8. To explain this observation, we propose a two-state conductance model, wherein carrier transport occurs *via* two distinct states with drastically different mobilities that are separated by a  $f_{Se}$ -dependent energy gap (**Figure 5.1.2.4b**). We assume that the higher-energy state is associated with the intrinsic CB-edge level, while the lower energy state is due to a native donor-like defect. This latter state can donate electrons into the CB band *via* thermal excitation. Assuming Maxwell-Boltzmann statistics, we can relate electron occupancies of the CB and donor states ( $n_{CB}$  and  $n_D$ , respectively) by:

$$n_{CB} = n_D \gamma_{C,D} e^{\left(\frac{-\Delta E_e}{k_B T}\right)} \quad (1)$$

where  $\Delta E_e$  is the energy spacing between the CB and the donor level (the donor ionization energy),  $\gamma_{C,D}$  is the ratio of the degeneracy factors of the CB ( $g_{CB}$ ) and the donor ( $g_D$ ) states ( $\gamma_{C,D} = g_{CB}/g_D$ ),  $T$  is temperature, and  $k_B$  is the Boltzmann constant. The intrinsic CB wave function has a considerable extent outside the dot, and as a result the CB state is characterized by a fairly high mobility ( $\mu_{CB}$ ). On the other hand, lower-energy defect-related states are more localized and thus have a poorer mobility ( $\mu_D \ll \mu_{CB}$ ). The effective carrier mobility of this system ( $\mu_e$ ) can be found as a weighted average of the CB- and the defect-state mobilities:

$$\mu_e = \frac{n_{CB}\mu_{CB} + n_D\mu_D}{n_{CB} + n_D} \quad (2)$$

Combining eqns. 1 and 2, we obtain the following expression for the  $T$ -dependent  $\mu_e$ :

$$\mu_e = \frac{1}{\gamma_{C,D} e^{\left(\frac{-\Delta E_e}{k_B T}\right)} + 1} \left[ \gamma_{C,D} \mu_{CB} e^{\left(\frac{-\Delta E_e}{k_B T}\right)} + \mu_D \right] \quad (3)$$

Next, we use eqn. 3 to analyze electron mobility data (**Figure 5.1.2.4a**, blue circles) assuming a linear relationship between  $\Delta E_e$  and  $f_{\text{Se}}$ :  $\Delta E_e = \Delta E_{e,S} + f_{\text{Se}}(\Delta E_{e,\text{Se}} - \Delta E_{e,S})$ , where  $\Delta E_{e,S}$  and  $\Delta E_{e,\text{Se}}$  are the energy separations between the CB and the electron-conducting defect level for purely Se- and S-based QDs, respectively. The saturation of  $\mu_e$  for  $f_{\text{Se}}$  below 0.3 suggests that in this range of compositions,  $\Delta E_e$  is much greater than  $k_B T$ , and hence,  $\mu_e \approx \mu_D = 7.2 \times 10^{-6} \text{ cm}^2 \text{ V}^{-1} \text{ s}^{-1}$  (based on the measured saturated value of  $\mu_e$ ). After quantifying  $\mu_D$ , we are left with four unknown parameters:  $\mu_{\text{CB}}$ ,  $\gamma_{\text{C,D}}$ ,  $\Delta E_{e,S}$  and  $\Delta E_{e,\text{Se}}$ . To find them, we solve the system of four equations obtained by substituting  $\mu_e$  and  $f_{\text{Se}}$  in eq 3 with experimentally measured values. This yields  $\gamma_{\text{C,D}} = 1.76$ ,  $\mu_{\text{CB}} = 9 \times 10^{-3} \text{ cm}^2 \text{ V}^{-1} \text{ s}^{-1}$ ,  $\Delta E_{e,S} = 416 \text{ meV}$ ,  $\Delta E_{e,\text{Se}} = 17 \text{ meV}$ . The dependence of  $\mu_e$  on  $f_{\text{Se}}$  calculated using these values and eqn. 3 is shown in **Figure 5.1.2.4a** (blue solid line), and the  $f_{\text{Se}}$ -dependent donor-state energies are displayed **Figure 5.1.2.2b** (orange open up-point triangles). Given this analysis, a quick increase in  $\mu_e$  with increasing the fraction of Se in the QDs is due to the reduction in the spacing between the CB and the intragap donor states, which leads to the increase in the relative electron occupancy of the high-mobility band-edge state.

To corroborate this model, we have conducted temperature dependent measurements of the output characteristics of the indium-contact  $\text{CuInSe}_{1.6}\text{S}_{0.4}$  QD-FETs (Figure S6.6.7). The mobilities derived from these experiments exhibit a temperature-activated behavior as shown in **Figure 5.1.2.4c**. By fitting these data to eqn. 3, we obtain  $\Delta E_e = 16.9 \text{ meV}$ . This value is close to one obtained from the  $f_{\text{Se}}$ -dependence of the electron mobility (17 meV, inset of **Figure 5.1.2.4a**).

To study hole transport, we use EDT-treated  $\text{CuInSe}_x\text{S}_{2-x}$  QD-FETs with Au contacts that exhibit  $p$ -type channel characteristics (Figure S6.6.8). The measurements of these devices reveal a strong dependence of hole mobility ( $\mu_h$ ) on  $f_{\text{Se}}$  (red open circles in **Figure 5.1.2.4a**), which is similar to that of  $\mu_e$  (blue solid circles in **Figure 5.1.2.4a**). In fact, the observed dependence can be quantitatively described by the same model as that presented by eqn. 3, assuming that the higher-mobility state is associated with a VB-edge hole (mobility  $\mu_{\text{VB}}$ ) while the lower mobility state is ascribed to a native acceptor-type defect (mobility  $\mu_{\text{A}}$ ). We denote the energy separation between these states as  $\Delta E_h$  and the ratio of their degeneracy factors as  $\gamma_{\text{V,A}}$ . Applying the two-state model we can perfectly describe the hole-transport data in **Figure 5.1.2.4** (red line) using the following set of parameters:  $\gamma_{\text{V,A}} = 0.5$ ,  $\mu_{\text{A}} = 4.6 \times 10^{-6} \text{ cm}^2 \text{ V}^{-1} \text{ s}^{-1}$ ,  $\mu_{\text{VB}} = 6.4 \times 10^{-3} \text{ cm}^2 \text{ V}^{-1} \text{ s}^{-1}$ ,  $\Delta E_{\text{h,S}} = 330 \text{ meV}$ , and  $\Delta E_{\text{h,Se}} = 10 \text{ meV}$ . As in the previous analysis of electron mobilities, we determine  $\mu_{\text{A}}$  based on the data for the low-Se-content samples ( $f_{\text{Se}} < 0.4$ ), and then find other parameters ( $\gamma_{\text{V,A}}$ ,  $\mu_{\text{VB}}$ ,  $\Delta E_{\text{h,S}}$ , and  $\Delta E_{\text{h,Se}}$ ) by solving the system of four equations wherein we use four experimental data points for samples with  $f_{\text{Se}} > 0.4$ .

The  $f_{\text{Se}}$ -dependent acceptor-state energies obtained from this analysis are displayed in **Figure 5.1.2.2b** by yellow open down-point triangles. As in the case of electron transport, a decrease in the energy spacing between the hole-donating defect and the band-edge state ( $\Delta E_h$ ) with increasing  $f_{\text{Se}}$  (compare green squares and yellow open down-point triangles in **Figure 5.1.2.2b**) leads to a quick (exponential) increase in the apparent hole mobility.

Interestingly, the  $f_{\text{Se}}$ -dependence of the hole mobility closely follows that of the electron mobility. Furthermore, the  $\mu_e$  and  $\mu_h$  values for a given Se fraction are also very similar to each other. This close correspondence between electron and hole transport characteristics, while stemming from still unclear reasons (or perhaps being even accidental), is useful from the standpoint of practical applications, as a number electronic devices (e.g., inverters) require electron- and hole-transporting materials with closely matched carrier mobilities.

**ALD Infilling.** Previously it was shown that ALD infilling of PbSe QD films with amorphous  $\text{Al}_2\text{O}_3$  could boost carrier mobility and greatly improve air stability of QD samples.<sup>44-46</sup> To test the effect of the ALD treatment on CInSeS QD FET performance, we have infilled them with alumina following published procedures.<sup>44</sup> A cross-sectional scanning electron microscope (SEM) image of one such In-contact device fabricated from  $\text{CuInSe}_{1.6}\text{S}_{0.4}$  QDs and encapsulated with a ca. 20 nm-thick layer of  $\text{Al}_2\text{O}_3$  is displayed in Figure S6.6.9. Following alumina infilling the QD-FET preserves its *n*-type polarity but shows a considerable improvement in both electron mobility ( $2.5 \times 10^{-2} \text{ cm}^2 \text{ V}^{-1} \text{ s}^{-1}$  vs.  $4.27 \times 10^{-3} \text{ cm}^2 \text{ V}^{-1} \text{ s}^{-1}$  before ALD) and the ON/OFF current ratio ( $\sim 100$  vs.  $\sim 10$  before ALD); compare **Figures 5.1.2.3f** and **5.1.2.5b**. Further, we observe an inversion in the sign of the threshold voltage ( $V_{\text{th}}$ ) and a considerable reduction in its absolute value ( $V_{\text{th}} = 0.2 \text{ V}$  for the ALD-treated device vs.  $-14.5 \text{ V}$  before the treatment;  $V_{\text{DS}} = 20 \text{ V}$ ). These results indicate that the ALD procedure enhances the QD film charge transport characteristics in the manner similar to that previously observed for PbSe QD solids.<sup>44, 45</sup> One possible effect of ALD infilling is to facilitate dot-to-dot transport by introducing electronic states in the inter-dot space that are energetically close to the QD band-edge

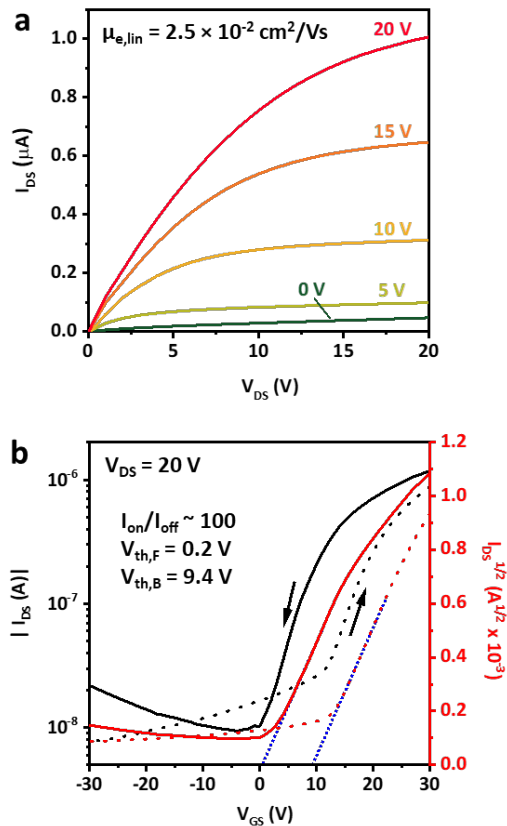


**Figure 5.1.2.5.** Effect of ALD treatment on characteristics of the *n*-type CuInSe<sub>1.6</sub>S<sub>0.4</sub> QD FET. (a) Output characteristics of the ALD-treated indium-contact CuInSe<sub>1.6</sub>S<sub>0.4</sub> QD-FET (*h* = 5.5 nm). (b) Transfer characteristics of the same device. Charge transport parameters are significantly improved upon ALD treatment as discussed in the text.

levels. These states can be associated with intra-gap defects in the Al<sub>2</sub>O<sub>3</sub> matrix and/or an interfacial layer produced by a chemical reaction of alumina precursors with the QD surface ligands. Another effect is passivation of QD surface defects, which allows for a more complete depletion of a conducting channel under the condition of a lowered Fermi level. This leads to the reduced OFF-current (and hence the improved ON/OFF current ratio) and a considerable reduction of  $|V_{th}|$ . The ALD-treated devices also exhibit enhanced air stability compared to non-infilled FETs. The ALD-infilled devices maintain their charge-transport characteristics for at least seven days under ambient conditions

(Figure S6.6.10), which is a considerable improvement vs. non-infilled FETs that undergo similar conditions, which remain stable only for a few minutes.

The ALD infilling also improves the performance of Au-contact QD-FETs (Figure S6.6.11). These devices are originally *p*-type, and interestingly, they maintain their *p*-type characteristics following the ALD procedure. This represents an interesting departure from the case of PbSe QD films, in which Al<sub>2</sub>O<sub>3</sub> infilling changes the polarity of PbSe QD-FETs (from degenerate *p*-type to well-modulated ambipolar), presumably due to passivation of sulfide acceptor states on the QD surfaces.<sup>44</sup> This suggests that the *p*-type transport polarity of CuInSe<sub>1.6</sub>S<sub>0.4</sub> QD films is not due to surface defects, but is instead due to internal acceptor-type states. While not changing transport polarity or the degenerate character of *p*-doping, the ALD treatment boosts hole mobility to 1.55× 10<sup>-2</sup> cm<sup>2</sup>/Vs, which is almost a 10-fold improvement compared to non-ALD devices. As in the case of *n*-type FETs, the improvement in carrier mobility likely results from lowering the inter-dot tunneling barrier.

### 5.1.3. Conclusions

**QD Samples and Spectroscopic Studies.** To summarize, we have studied charge transport characteristics of CISES QDs incorporated into FETs as a function of a varied anion composition (Se-to-S ratio), identity of surface ligands, and device type (gold vs. indium source and drain contacts). Gold-contact FETs made of as-fabricated CISES QDs with long native ligands exhibit degenerate *p*-type transport due to native acceptor-like defects such as metal vacancies and/or anti-site defects (Cu<sup>1+</sup> on an In<sup>3+</sup> site). The transport polarity is not altered by either ligand exchange or ALD infilling, supporting the

assessment that the  $p$ -type doping is not due surface states but rather is due to native lattice defects. The transport type can be switched to nondegenerate  $n$ -type by thermal diffusion of indium throughout the conductive channel realized *via* thermal annealing of indium-contact FETs. This change in transport characteristics likely occurs due to formation of donor-type  $\text{In}_{\text{Cu}}^{\bullet\bullet}$  or  $\text{In}_i^{\bullet\bullet\bullet}$  defects. The electron and hole mobilities of  $\text{CuInSeS}$  QD films show a dramatic, orders-of-magnitude increase with increasing the  $\text{Se}/(\text{S}+\text{Se})$  ratio  $f_{\text{Se}}$ . To explain this behavior, we propose a two-state transport model wherein charge conductance involves two thermally coupled states with strongly different (by *ca.* a factor of  $10^3$ ) mobilities separated by the  $f_{\text{Se}}$ -dependent energy gap ( $\Delta E_e$  and  $\Delta E_h$ ). The higher-energy, higher-mobility state is ascribed to the intrinsic QD CB- or VB-edge levels, while the lower-energy, lower-mobility states are associated with native donor ( $n$ -type films) or acceptor ( $p$ -type films) defects. The increase in the fraction of Se leads to a reduction of  $\Delta E_e$  and  $\Delta E_h$  which increases the occupancy of higher mobility intrinsic band-edge levels and produces the increase in the apparent carrier mobility. We also demonstrate that transport characteristics and environmental stability of both  $p$ - and  $n$ -type films can be enhanced *via*  $\text{Al}_2\text{O}_3$  ALD infilling without altering the transport polarity. The overall conclusion of these studies is that  $\text{CuInSe}_x\text{S}_{2-x}$  QD films represent a viable, environmentally-friendly alternative to films based on Pb- and Cd-containing QDs for applications in solution-processible electronic and optoelectronic devices.

#### 5.1.4. Methods

**Chemicals and Materials.** The following chemicals were purchased and used as received. Anhydrous copper (I) iodide ( $\text{CuI}$ , 99.995 %), 1-dodecanethiol ( $\text{CH}_3(\text{CH}_2)_{11}\text{SH}$ ,

DDT,  $\geq 98\%$ ), selenium (Se, 99.99%), anhydrous octane ( $\text{CH}_3(\text{CH}_2)_6\text{CH}_3$ ,  $\geq 99\%$ ), anhydrous methanol ( $\text{CH}_3\text{OH}$ ,  $\geq 99\%$ ), anhydrous acetonitrile ( $\text{CH}_3\text{CN}$ , ACN, 99.8%), 1,2-ethanedithiol ( $\text{HSCH}_2\text{CH}_2\text{SH}$ , EDT,  $\geq 98\%$ ), tetrabutylammonium perchlorate ( $(\text{CH}_3\text{CH}_2\text{CH}_2\text{CH}_2)_4\text{N}(\text{ClO}_4)$ , TBAClO<sub>4</sub>,  $\geq 99\%$ ), and ((3-Mercaptopropyl)trimethoxysilane ( $\text{HS}(\text{CH}_2)_3\text{Si}(\text{OCH}_3)_3$ , MPTS, 95%) were obtained from Sigma-Aldrich. Anhydrous indium (III) acetate ( $\text{In}(\text{CH}_3\text{COO})_3$ ,  $\text{In}(\text{Ac})_3$ , 99.99%) and oleylamine ( $\text{CH}_3(\text{CH}_2)_7\text{CH}=\text{CH}(\text{CH}_2)_7\text{CH}_2\text{NH}_2$ , OLAm, 80~90%) were purchased from Acros Organics. 2-Propanol ( $(\text{CH}_3)_2\text{CHOH}$ , IPA, 99.5%) and acetone ( $\text{CH}_3\text{COCH}_3$ , 99.5%) were purchased from Fisher Scientific.

Gold (99.99%) and indium (99.99%) evaporation pellets were obtained from Kurt J. Lesker Company. Highly doped  $p^{++}$  Si substrates with thermally grown  $\text{SiO}_2$  (300 nm) were purchased from Ossila Ltd.

**Synthesis of  $\text{CuInSe}_x\text{S}_{2-x}$  QDs.** Typically, 1 mmol of CuI and 1 mmol of  $\text{In}(\text{Ac})_3$  were dissolved in 5 mL of DDT and 1 mL of OLAm in a 50 mL round-bottom flask, and the mixture was degassed under vacuum at 100 °C for 30 min. Separately, a solution of 1 M Se-OLAm/DDT was prepared by dissolving 1.58 g Se powder in mixture of 15 mL of OLAm and 5 mL of DDT at room temperature in a  $\text{N}_2$  glove box. The temperature of the reactants was raised to 140 °C until all solid precursors were fully dissolved, which usually took less than 10 min. Then, the temperature was raised to 170 °C and 1 M Se-OLAm/DDT (0.5 ml for  $\text{CuInSe}_{0.5}\text{S}_{1.5}$ , 1 ml for  $\text{CuInSe}_{1.0}\text{S}_{1.0}$ , 1.3 ml for  $\text{CuInSe}_{1.2}\text{S}_{0.8}$ , 1.7 ml for  $\text{CuInSe}_{1.4}\text{S}_{0.6}$ , and 2 ml for  $\text{CuInSe}_{1.6}\text{S}_{0.4}$  QDs) was added dropwise such that the temperature of the reaction mixture did not vary by more than 3 °C. For nucleation and growth, temperature was set to 230 °C for 60 minutes. The heating element was then

removed and the QDs were allowed to cool. For synthesizing CuInS<sub>2</sub> QDs, the injection of the Se precursor was skipped, and the temperature was raised to 230 °C. The synthesized QDs were purified by iterative dissolution in chloroform and precipitation with methanol and then size-selected by centrifugation at 8000 rpm for 5 minutes. The resulting QDs were stored in octane under an N<sub>2</sub> atmosphere.

**Fabrication of CuInSe<sub>x</sub>S<sub>2-x</sub> QD-FETs.** A heavily *p*-doped silicon wafer with a thermally grown silicon oxide (300 nm thickness) was sonicated in DI water (5 minutes), acetone (5 minutes) and isopropanol (5 minutes), then immersed in the MPTS solution (5% in IPA) and held there for 16 hours. The MPTS-treated substrates were rinsed with toluene and then sonicated in IPA for 5 minutes. Metal (Au for *p*-type and In for *n*-type) source and drain bottom contacts (3 mm channel width and 100 μm channel length) were deposited by thermal evaporation (deposition rate of 1 Å s<sup>-1</sup>) through a shadow mask to achieve a 100 nm thickness. CuInSe<sub>x</sub>S<sub>2-x</sub> QDs dissolved in octane (concentration ~20 mg/ml) were spin-coated onto the pre-patterned substrate at 1200 rpm. The film was then heated to 150 °C for 10 min in a N<sub>2</sub> glove box to evaporate the residual solvent. For the EDT treatment, the QD film was immersed in a 1% (by volume) solution of EDT in ACN for 2 minutes, followed by rinsing with ACN. These QD deposition-ligand-exchange steps were repeated 3 times to yield a total thickness of the QD film of 100 nm. The fabrication of *p*-type FETs was completed by annealing the devices at 100 °C for 30 minutes in an N<sub>2</sub>-filled glove box to remove any organic residuals. To achieve *n*-type transport polarity, the fabricated indium-contact FETs were annealed at 250 °C for 2 hours in an N<sub>2</sub>-filled glove box to facilitate indium diffusion throughout the QD film. For avoiding any deleterious

chemical reactions involving oxygen, the O<sub>2</sub> content in the glove box was thoroughly monitored to ensure it was below 0.1 ppm.

Amorphous Al<sub>2</sub>O<sub>3</sub> was deposited in a homemade, cold-wall, traveling-wave ALD system in a glove box using trimethylaluminum and water as precursors. The substrate temperature was 75 °C and the operating pressure was ~0.1 Torr. The pulse and the purge times were 40 ms and 90–120 s, respectively. With these parameters, the preparation of a 20 nm ALD film required ~10 hours.

**Characterization.** Transmission electron microscopy (TEM) images were recorded using a JEOL 2010 TEM equipped with a SC1000 ORIUS CCD camera operating at 120 kV. A top-view scanning electron microscopy (SEM) and an energy-dispersive X-ray spectroscopy (EDS) measurements of CuInSe<sub>x</sub>S<sub>2-x</sub> QD-FETs were performed using a JEOL JSM-IT100 TEM. Cross-sectional SEM studies of ALD-infilled films were conducted on a FEI Magellan 400 XHR SEM. The crystal structure of the QDs was examined by high resolution X-ray diffraction (XRD, Bede D1 System) with the CuKα X-ray source (1.54 Å wavelength) operating at 40 kV and 40 mA. Optical absorption spectra were recorded using a UV/Vis/NIR spectrophotometer (Lambda 950, Perkin Elmer). Near-IR PL spectra were collected using a custom-built apparatus comprising a mechanically chopped 808 nm laser, a grating monochromator, and a liquid N<sub>2</sub>-cooled InSb detector coupled to a lock-in amplifier. Elemental analysis was carried out using a Shimadzu ICPE-9000 inductively-coupled plasma optical emission spectrometer (ICP-OES).

FET characterization was conducted in an N<sub>2</sub>-filled glove box at room temperature using a semiconductor device parameter analyzer (B1500A, Agilent). The probes were placed on top of FET electrodes using a DC probe positioner.

TA spectra and dynamics were measured in a standard pump-probe configuration using a LabView-controlled home-build setup. The measurements were conducted using 515-nm, 200-fs pump pulses at a 500-Hz repetition rate (second harmonic output of an amplified Yb:KGW laser, Light Conversion Pharos) and a broad-band, white-light supercontinuum probe. The excited-spot diameter was  $\sim 200 \mu\text{m}$  at the  $1/e^2$  level, and the excitation flux was  $(1.5\text{--}9)\times 10^{14}$  photons/cm<sup>2</sup>s, which corresponded to an average per-dot excitonic occupancy of 0.02 – 0.1. All measurements were conducted under oxygen-free and moisture-free conditions using airtight quartz cuvettes with vigorous stirring of the sample to minimize photocharging. Samples were prepared in an inert atmosphere in a glove box.

For electrochemical analyses, an indium-tin-oxide (ITO)-coated glass slide was used as a working electrode, platinum wire as a counter electrode, and a silver wire as a pseudoreference electrode. CuInSe<sub>x</sub>S<sub>2-x</sub> QDs were diluted to 5 mg/ml in air-free chloroform in a N<sub>2</sub> glove box. 0.1 M of TBAClO<sub>4</sub> was weighed in the glove box before adding to the QD solution. The QDs:TBAClO<sub>4</sub> molar ratio was *ca.* 1:5 so that the electrolyte salt could effectively passivate the QD surface. Cyclic voltammetry (CV) measurements were conducted by loading a QD/electrolyte solution into a quartz cuvette and placing inside it electrodes connected to a computer-controlled potentiostat (CH Instruments). The cuvette was masked with a black tape to eliminate exposure to ambient light. The scan rate was 0.1 V s<sup>-1</sup> and data were collected for every 0.001 V for the scan range of 2 V to -2 V.

### 5.1.5. References

1. Oh, S. J.; Berry, N. E.; Choi, J.-H.; Gauling, E. A.; Lin, H.; Paik, T.; Diroll, B. T.; Muramoto, S.; Murray, C. B.; Kagan, C. R. Designing High-Performance PbS and PbSe Nanocrystal Electronic Devices through Stepwise, Post-Synthesis, Colloidal Atomic Layer Deposition. *Nano Lett.* 2014, 14, 1559-1566.
2. Hetsch, F.; Zhao, N.; Kershaw, S. V.; Rogach, A. L. Quantum Dot Field Effect Transistors. *Mater. Today* 2013, 16, 312-325.
3. Dolzhenkov, D. S.; Zhang, H.; Jang, J.; Son, J. S.; Panthani, M. G.; Shibata, T.; Chattopadhyay, S.; Talapin, D. V. Composition-Matched Molecular “Soldiers” for Semiconductors. *Science* 2015, 347, 425-428.
4. Oh, S. J.; Wang, Z.; Berry, N. E.; Choi, J.-H.; Zhao, T.; Gauling, E. A.; Paik, T.; Lai, Y.; Murray, C. B.; Kagan, C. R. Engineering Charge Injection and Charge Transport for High Performance PbSe Nanocrystal Thin Film Devices and Circuits. *Nano Lett.* 2014, 14, 6210-6216.
5. Stinner, F. S.; Lai, Y.; Straus, D. B.; Diroll, B. T.; Kim, D. K.; Murray, C. B.; Kagan, C. R. Flexible, High-Speed CdSe Nanocrystal Integrated Circuits. *Nano Lett.* 2015, 15, 7155-7160.
6. Choi, J.-H.; Wang, H.; Oh, S. J.; Paik, T.; Sung, P.; Sung, J.; Ye, X.; Zhao, T.; Diroll, B. T.; Murray, C. B.; Kagan, C. R. Exploiting the Colloidal Nanocrystal Library to Construct Electronic Devices. *Science* 2016, 352, 205-208.
7. Haverinen, H. M.; Myllylä, R. A.; Jabbour, G. E. Inkjet Printing of Light Emitting Quantum Dots. *Appl. Phys. Lett.* 2009, 94, 073108.

8. Lin, Q.; Yun, H. J.; Liu, W.; Song, H.-J.; Makarov, N. S.; Isaienko, O.; Nakotte, T.; Chen, G.; Luo, H.; Klimov, V. I.; Pietryga, J. M. Phase-Transfer Ligand Exchange of Lead Chalcogenide Quantum Dots for Direct Deposition of Thick, Highly Conductive Films. *J. Am. Chem. Soc.* 2017, 139, 6644-6653.
9. Talapin, D. V.; Murray, C. B. PbSe Nanocrystal Solids for n- and p-Channel Thin Film Field-Effect Transistors. *Science* 2005, 310, 86-89.
10. Nag, A.; Kovalenko, M. V.; Lee, J. S.; Liu, W.; Spokoyny, B.; Talapin, D. V. Metal-Free Inorganic Ligands for Colloidal Nanocrystals:  $S^{2-}$ ,  $HS^-$ ,  $Se^{2-}$ ,  $HSe^-$ ,  $Te^{2-}$ ,  $HTe^-$ ,  $TeS_3^{2-}$ ,  $OH^-$ , and  $NH_2^-$  as Surface Ligands. *J. Am. Chem. Soc.* 2011, 133, 10612-10620.
11. Liu, Y.; Gibbs, M.; Puthussery, J.; Gaik, S.; Ihly, R.; Hillhouse, H. W.; Law, M. Dependence of Carrier Mobility on Nanocrystal Size and Ligand Length in PbSe Nanocrystal Solids. *Nano Lett.* 2010, 10, 1960-1969.
12. Fafarman, A. T.; Koh, W. K.; Diroll, B. T.; Kim, D. K.; Ko, D. K.; Oh, S. J.; Ye, X.; Doan-Nguyen, V.; Crump, M. R.; Reifsnnyder, D. C.; Murray, C. B.; Kagan, C. R. Thiocyanate-Capped Nanocrystal Colloids: Vibrational Reporter of Surface Chemistry and Solution-Based Route to Enhanced Coupling in Nanocrystal Solids. *J. Am. Chem. Soc.* 2011, 133, 15753-15761.
13. Boles, M. A.; Ling, D.; Hyeon, T.; Talapin, D. V. The Surface Science of Nanocrystals. *Nat. Mater.* 2016, 15, 141-153.

14. Lee, J.-S.; Kovalenko, M. V.; Huang, J.; Chung, D. S.; Talapin, D. V. Band-Like Transport, High Electron Mobility and High Photoconductivity in All-Inorganic Nanocrystal Arrays. *Nat. Nanotechnol.* 2011, 6, 348.
15. Brown, P. R.; Kim, D.; Lunt, R. R.; Zhao, N.; Bawendi, M. G.; Grossman, J. C.; Bulović, V. Energy Level Modification in Lead Sulfide Quantum Dot Thin Films through Ligand Exchange. *ACS Nano* 2014, 8, 5863-5872.
16. Kroupa, D. M.; Vörös, M.; Brawand, N. P.; McNichols, B. W.; Miller, E. M.; Gu, J.; Nozik, A. J.; Sellinger, A.; Galli, G.; Beard, M. C. Tuning Colloidal Quantum Dot Band Edge Positions through Solution-Phase Surface Chemistry Modification. *Nat. Commun.* 2017, 8, 15257.
17. McDaniel, H.; Fuke, N.; Pietryga, J. M.; Klimov, V. I. Engineered  $\text{CuInSe}_x\text{S}_{2-x}$  Quantum Dots for Sensitized Solar Cells. *J. Phys. Chem. Lett.* 2013, 4, 355-361.
18. McDaniel, H.; Fuke, N.; Makarov, N. S.; Pietryga, J. M.; Klimov, V. I. An Integrated Approach to Realizing High-Performance Liquid-Junction Quantum Dot Sensitized Solar Cells. *Nat. Commun.* 2013, 4.
19. Draguta, S.; McDaniel, H.; Klimov, V. I. Tuning Carrier Mobilities and Polarity of Charge Transport in Films of  $\text{CuInSe}_x\text{S}_{2-x}$  Quantum Dots. *Adv. Mater.* 2015, 27, 1701-1705.
20. Kim, J.-Y.; Yang, J.; Yu, J. H.; Baek, W.; Lee, C.-H.; Son, H. J.; Hyeon, T.; Ko, M. J. Highly Efficient Copper–Indium–Selenide Quantum Dot Solar Cells: Suppression of Carrier Recombination by Controlled ZnS Overlayers. *ACS Nano* 2015, 9, 11286-11295.

21. McDaniel, H.; Kuposov, A. Y.; Draguta, S.; Makarov, N. S.; Pietryga, J. M.; Klimov, V. I. Simple yet Versatile Synthesis of  $\text{CuInSe}_x\text{S}_{2-x}$  Quantum Dots for Sunlight Harvesting. *J. Phys. Chem. C* 2014, 118, 16987-16994.
22. Lim, Y. S.; Kwon, H.-S.; Jeong, J.; Kim, J. Y.; Kim, H.; Ko, M. J.; Jeong, U.; Lee, D.-K. Colloidal Solution-Processed  $\text{CuInSe}_2$  Solar Cells with Significantly Improved Efficiency up to 9% by Morphological Improvement. *ACS Appl. Mater. Interfaces* 2014, 6, 259-267.
23. Ueng, H. Y.; Hwang, H. L. The Defect Structure of  $\text{CuInS}_2$ . Part I: Intrinsic Defects. *J. Phys. Chem. Solids* 1989, 50, 1297-1305.
24. Dagan, G.; Abou-Elfotouh, F.; Dunlavy, D. J.; Matson, R. J.; Cahen, D. Defect Level Identification in Copper Indium Selenide ( $\text{CuInSe}_2$ ) from Photoluminescence Studies. *Chem. Mater.* 1990, 2, 286-293.
25. Choi, J.-H.; Fafarman, A. T.; Oh, S. J.; Ko, D.-K.; Kim, D. K.; Diroll, B. T.; Muramoto, S.; Gillen, J. G.; Murray, C. B.; Kagan, C. R. Bandlike Transport in Strongly Coupled and Doped Quantum Dot Solids: A Route to High-Performance Thin-Film Electronics. *Nano Lett.* 2012, 12, 2631-2638.
26. Talapin, D. V.; Lee, J.-S.; Kovalenko, M. V.; Shevchenko, E. V. Prospects of Colloidal Nanocrystals for Electronic and Optoelectronic Applications. *Chem. Rev.* 2010, 110, 389-458.

27. Gresback, R.; Kramer, N. J.; Ding, Y.; Chen, T.; Kortshagen, U. R.; Nozaki, T. Controlled Doping of Silicon Nanocrystals Investigated by Solution-Processed Field Effect Transistors. *ACS Nano* 2014, 8, 5650-5656.
28. Mycielski, J. Mechanism of Impurity Conduction in Semiconductors. *Phys. Rev.* 1961, 123, 99-103.
29. Brawand, N. P.; Goldey, M. B.; Vörös, M.; Galli, G. Defect States and Charge Transport in Quantum Dot Solids. *Chem. Mater.* 2017, 29, 1255-1262.
30. Zang, H.; Li, H.; Makarov, N. S.; Velizhanin, K. A.; Wu, K.; Park, Y.-S.; Klimov, V. I. Thick-Shell CuInS<sub>2</sub>/ZnS Quantum Dots with Suppressed “Blinking” and Narrow Single-Particle Emission Line Widths. *Nano Lett.* 2017, 17, 1787-1795.
31. Li, L.; Pandey, A.; Werder, D. J.; Khanal, B. P.; Pietryga, J. M.; Klimov, V. I., Efficient Synthesis of Highly Luminescent Copper Indium Sulfide-Based Core/Shell Nanocrystals with Surprisingly Long-Lived Emission. *J. Am. Chem. Soc.* 2011, 13, 1176-1179.
32. Meinardi, F.; McDaniel, H.; Carulli, F.; Colombo, A.; Velizhanin, K. A.; Makarov, N. S.; Simonutti, R.; Klimov, V. I.; Brovelli, S. Highly Efficient Large-Area Colourless Luminescent Solar Concentrators Using Heavy-Metal-Free Colloidal Quantum Dots. *Nat. Nanotechnol.* 2015, 10, 878-885.
33. Fuhr, A. S.; Yun, H. J.; Makarov, N. S.; Li, H.; McDaniel, H.; Klimov, V. I. Light Emission Mechanisms in CuInS<sub>2</sub> Quantum Dots Evaluated by Spectral Electrochemistry. *ACS Photonics* 2017, 4, 2425-2435.

34. Shabaev, A.; Mehl, M. J.; Efros, A. L. Energy Band Structure of CuInS<sub>2</sub> and Optical Spectra of CuInS<sub>2</sub> Nanocrystals. *Phys. Rev. B* 2015, 92, 035431.
35. Knowles, K. E.; Nelson, H. D.; Kilburn, T. B.; Gamelin, D. R. Singlet–Triplet Splittings in the Luminescent Excited States of Colloidal Cu<sup>+</sup>:CdSe, Cu<sup>+</sup>:InP, and CuInS<sub>2</sub> Nanocrystals: Charge-Transfer Configurations and Self-Trapped Excitons. *J. Am. Chem. Soc.* 2015, 137, 13138-13147.
36. Krustok, J.; Schön, J. H.; Collan, H.; Yakushev, M.; Mädasson, J.; Bucher, E. Origin of the Deep Center Photoluminescence in CuGaSe<sub>2</sub> and CuInS<sub>2</sub> Crystals. *J. Appl. Phys.* 1999, 86, 364-369.
37. Zhong, H.; Lo, S. S.; Mirkovic, T.; Li, Y.; Ding, Y.; Li, Y.; Scholes, G. D. Noninjection Gram-Scale Synthesis of Monodisperse Pyramidal CuInS<sub>2</sub> Nanocrystals and Their Size-Dependent Properties. *ACS Nano* 2010, 4, 5253-5262.
38. Akkerman, Q. A.; Genovese, A.; George, C.; Prato, M.; Moreels, I.; Casu, A.; Marras, S.; Curcio, A.; Scarpellini, A.; Pellegrino, T.; Manna, L.; Lesnyak, V. From Binary Cu<sub>2</sub>S to Ternary Cu–In–S and Quaternary Cu–In–Zn–S Nanocrystals with Tunable Composition via Partial Cation Exchange. *ACS Nano* 2015, 9, 521-531.
39. Sanz, L.; Palma, J.; García-Quismondo, E.; Anderson, M. The Effect of Chloride Ion Complexation on Reversibility and Redox Potential of the Cu(II)/Cu(I) Couple for Use in Redox Flow Batteries. *J. Power Sources* 2013, 224, 278-284.
40. Bard, A. J.; Faulkner, L. R. *Electrochemical Methods*. Wiley: New York, 2001.

41. Hoffeditz, W. L.; Katz, M. J.; Deria, P.; Cutsail Iii, G. E.; Pellin, M. J.; Farha, O. K.; Hupp, J. T. One Electron Changes Everything. A Multispecies Copper Redox Shuttle for Dye-Sensitized Solar Cells. *J. Phys. Chem. C* 2016, 120, 3731-3740.
42. Nagpal, P.; Klimov, V. I. Role of Mid-Gap States in Charge Transport and Photoconductivity in Semiconductor Nanocrystal Films. *Nat. Commun.* 2011, 2, 486.
43. Klem, E. J. D.; Shukla, H.; Hinds, S.; MacNeil, D. D.; Levina, L.; Sargent, E. H. Impact of Dithiol Treatment and Air Annealing on the Conductivity, Mobility, and Hole Density in PbS Colloidal Quantum Dot Solids. *Appl. Phys. Lett.* 2008, 92, 212105.
44. Liu, Y.; Tolentino, J.; Gibbs, M.; Ihly, R.; Perkins, C. L.; Liu, Y.; Crawford, N.; Hemminger, J. C.; Law, M. PbSe Quantum Dot Field-Effect Transistors with Air-Stable Electron Mobilities above  $7 \text{ cm}^2 \text{ V}^{-1} \text{ s}^{-1}$ . *Nano Lett.* 2013, 13, 1578-1587.
45. Liu, Y.; Gibbs, M.; Perkins, C. L.; Tolentino, J.; Zarghami, M. H.; Bustamante, J.; Law, M. Robust, Functional Nanocrystal Solids by Infilling with Atomic Layer Deposition. *Nano Lett.* 2011, 11, 5349-5355.
46. Zhao, Q.; Zhao, T.; Guo, J.; Chen, W.; Zhang, M.; Kagan, C. R. The Effect of Dielectric Environment on Doping Efficiency in Colloidal PbSe Nanostructures. *ACS Nano* 2018, 12, 1313-1320.

## 6. Appendix

### 6.1 Supporting Information for Chapter 2, Section 2.1

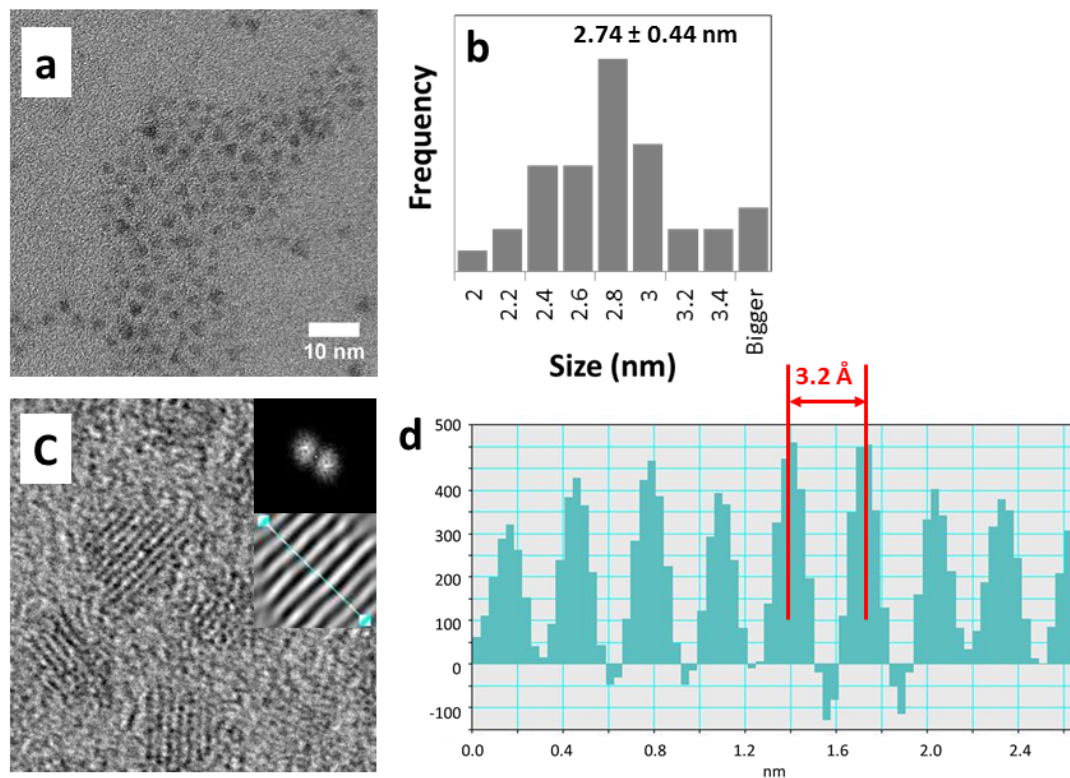


**Figure S6.1.1.** (a) An example of a transmission electron microscopy (TEM) image for intermediately-sized core-only stoichiometric CuInS<sub>2</sub> (CIS) quantum dots (QDs). As observed previously, CIS QDs are characterized by tetrahedral shapes. (b) The distribution of QD sizes (apex-to-apex side length) from the TEM images. The average size is  $2.74 \pm 0.44$  nm. (c) The QD crystalline structure investigated by high-resolution (HR) TEM imaging and selected-area electron diffraction (SAED). The top and bottom insets are, respectively, the fast Fourier transform (FFT) taken for the HR-TEM image of a QD and the inverse FFT. (d) The line-profiling of the inverse FFT indicates the  $3.82 \text{ \AA}$  lattice constant, which corresponds to the (112) direction in the chalcopyrite structure.

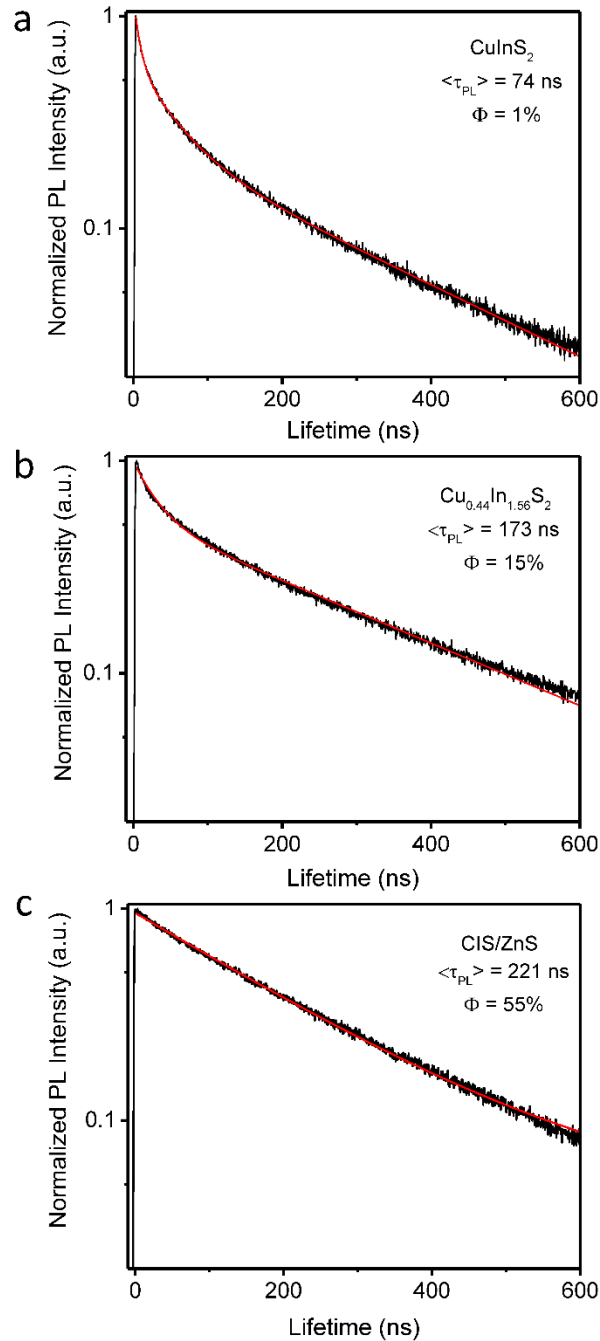


**Figure S6.1.2.** Time-resolved photoluminescence (PL) measurements (solid black lines) for core-only stoichiometric (a) and Cu-deficient (b) QDs, as well as the stoichiometric core/shell CIS/ZnS sample (c); low intensity excitation (sub-single-exciton regime) at 445 nm, 50 ps pulse duration, 1.5 ns temporal resolution of the detection system. Fits are shown by solid red lines. Stoichiometric QDs were fitted to a tri-exponential decay, Cu-poor QDs to a bi-exponential decay, and CIS/ZnS core/shell QDs to a single-exponential function. Labels in the panels show average PL lifetimes ( $\langle \tau_{PL} \rangle$ ) and PL quantum yields ( $\Phi$ ).

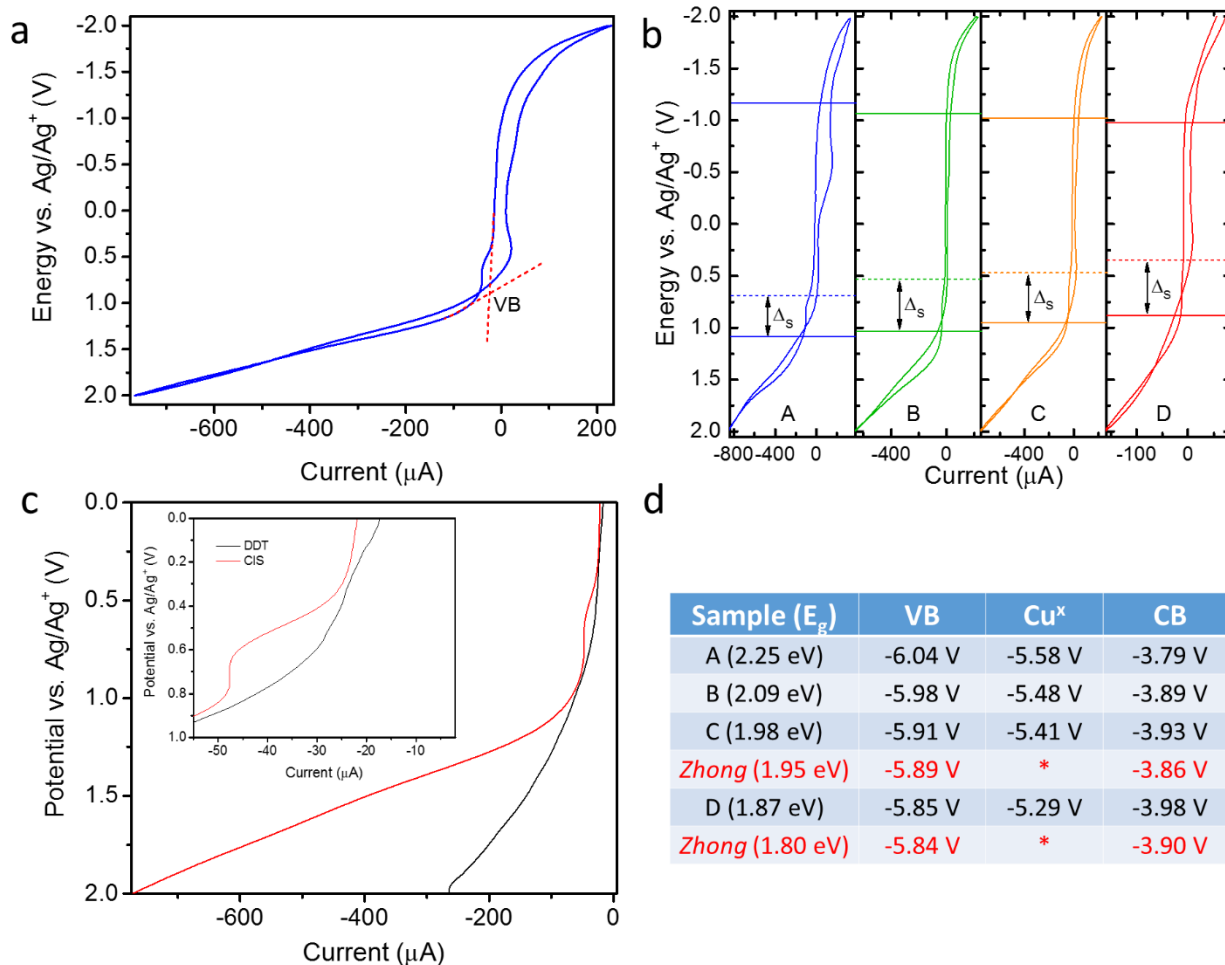


**Figure S6.1.3.** (a) The full scan range for the cyclic voltammetry (CV) measurements of sample C from the main text. The dashed red lines represent the linear fits (described in the main text) used to determine the onset potential for oxidation *via* hole injection into the QD valence band (VB). (b) The full scan range for the CV measurements for samples of varied sizes (denoted A-D in the main text). The band edges are marked by the solid colored lines and the  $\text{Cu}^x$  state is marked by the dashed color lines. The electrochemical (EC) Stokes shift is denoted as  $\Delta_s$ . (c) The linear-sweep voltammetry (LSV) measurements at positive potentials for sample C is compared to a solution of the electrolyte and 1-dodecanethiols (DDT) without the QDs. A small, relatively weak shoulder appears for DDT at  $\sim 0.2$  V, which is almost indistinguishable from the background electrolyte in the case of the CIS QD measurements. The considerably larger current obtained for  $\sim 0.65$  V for the QDs is absent in the DDT measurements. This indicates that this feature is from the  $\text{Cu}^x$  state and not DDT. (d) The positions of the VB,  $\text{Cu}^x$ , and CB energy levels described in the main text. All voltages are reported *versus* vacuum. Measurements by Zhong *et al.*<sup>1</sup> for CIS QDs with band gaps (as determined from optical absorption spectra) are shown in red; an asterisk is used in the  $\text{Cu}^x$  column as this publication did not report the observation of the  $\text{Cu}^x$  feature.

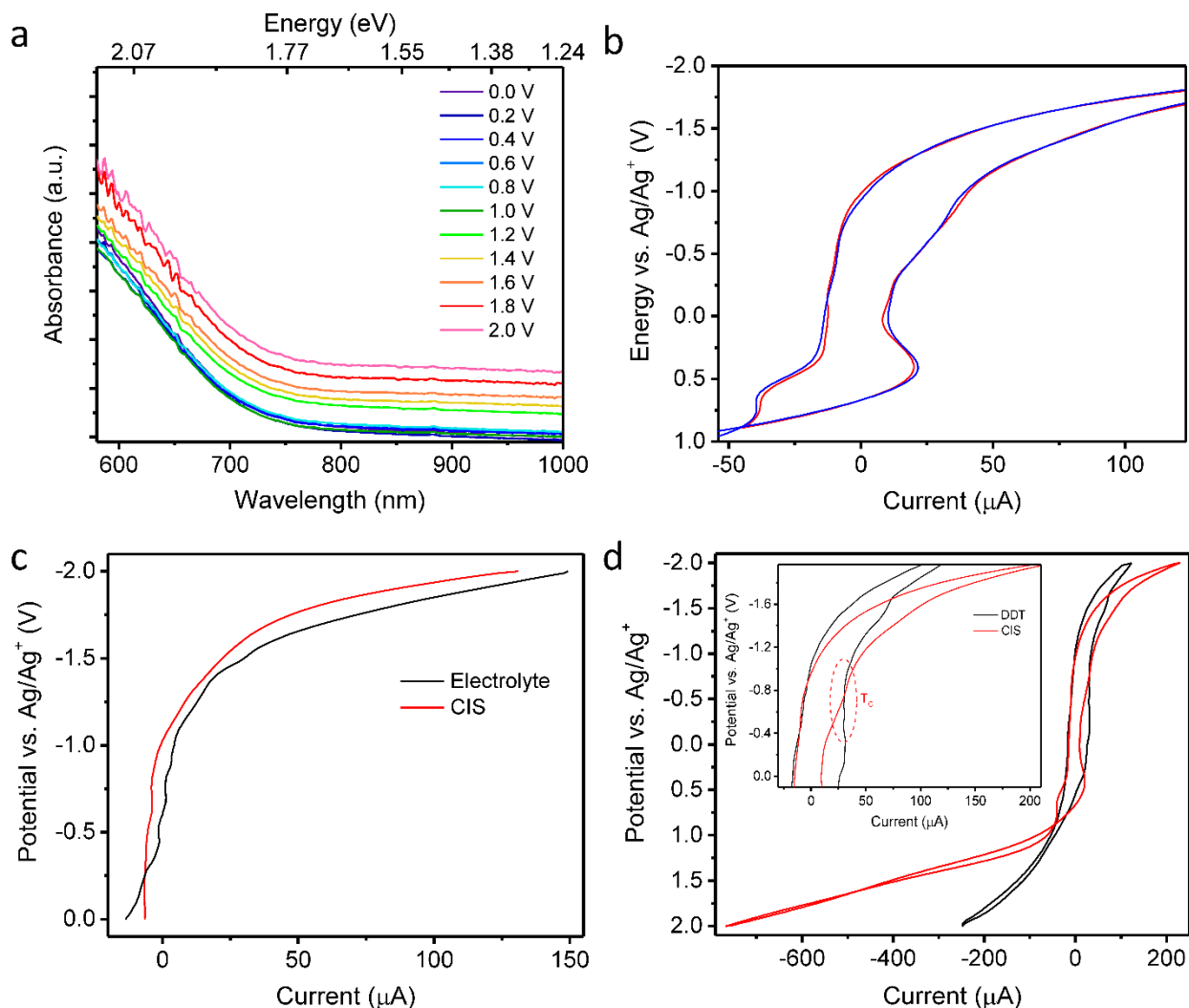


**Figure S6.1.4.** (a) Absorbance as a function of EC potential ( $V_{EC}$ ) versus the Ag wire pseudoreference electrode. Notably, no significant changes are observed from 0 V to +1 V (intra-gap to VB-edge regime). However, optical scattering sharply increases once the Fermi level is pushed just below the VB edge (+1.2 V and higher) and continually increases up to +2 V. (b) A comparison between the  $\text{Cu}^x$  redox waves from the large scan window (blue lines) and after repeating the experiment (red lines) where the positive scan range is limited to the VB-edge (+0.96 V for sample C). Clearly, no significant changes occur. (c) LSV measurements on CIS QDs are then compared to the background electrolyte at negative potentials. These traces are also nearly indistinguishable. Thus, the current increase at -1.2 V is not due to the CB of the QDs. (d) CV measurement on CIS QDs (red line) are compared to measurements on DDT (black line). The shoulder at -0.3 V described in the main text for the CIS QDs is absent in the LSV measurements, and only appears on the reverse scans in the CV measurements as shown in the inset. This suggests that the feature is from an intra-gap trap state  $T_c$  (dashed red circles in the figure inset), which is further supported by *in situ* SEC measurements discussed in the main text.

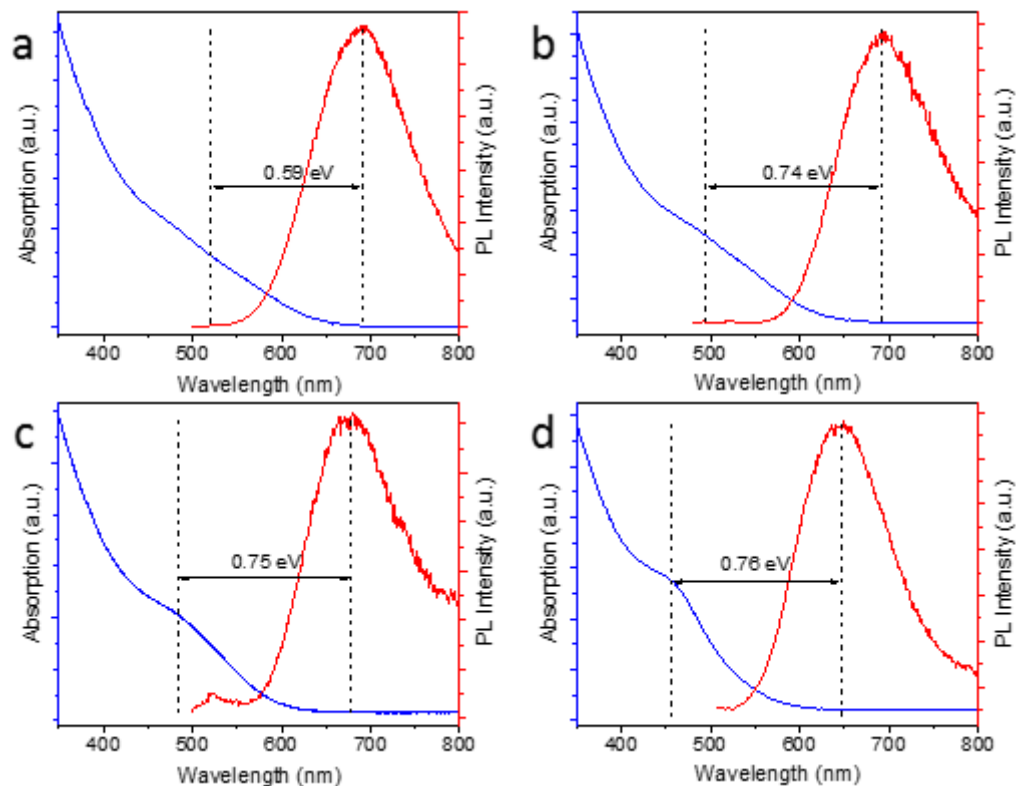


**Figure S6.1.5.** Absorption (blue) and emission (red) spectra of Cu-deficient core-only CIS QDs with different sizes. The emission peak position ranged from 640 nm to 690 nm and the position of the lowest-energy absorption feature varies from 478 nm to 520 nm. The Stokes shift ( $\Delta_S$ ) varies from 590 to 760 meV.

## References

1. Zhong, H.; Lo, S. S.; Mirkovic, T.; Li, Y.; Ding, Y.; Li, Y.; Scholes, G. D., Noninjection Gram-Scale Synthesis of Monodisperse Pyramidal  $\text{CuInS}_2$  Nanocrystals and Their Size-Dependent Properties. *ACS Nano* 2010, 4, 5253-5262.

## 6.2 Supporting Information for Chapter 2, Section 2.2

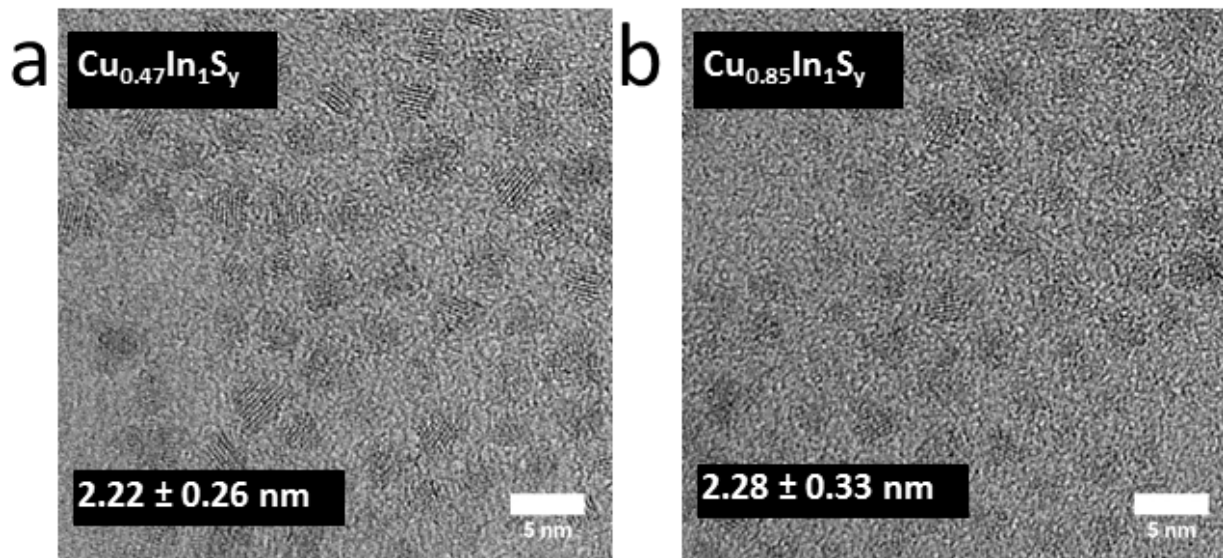


**Figure S6.2.1.** TEM images for CIS QDs with different copper to indium ratios. As observed previously, QDs have a tetrahedral shape based on (112) facets.

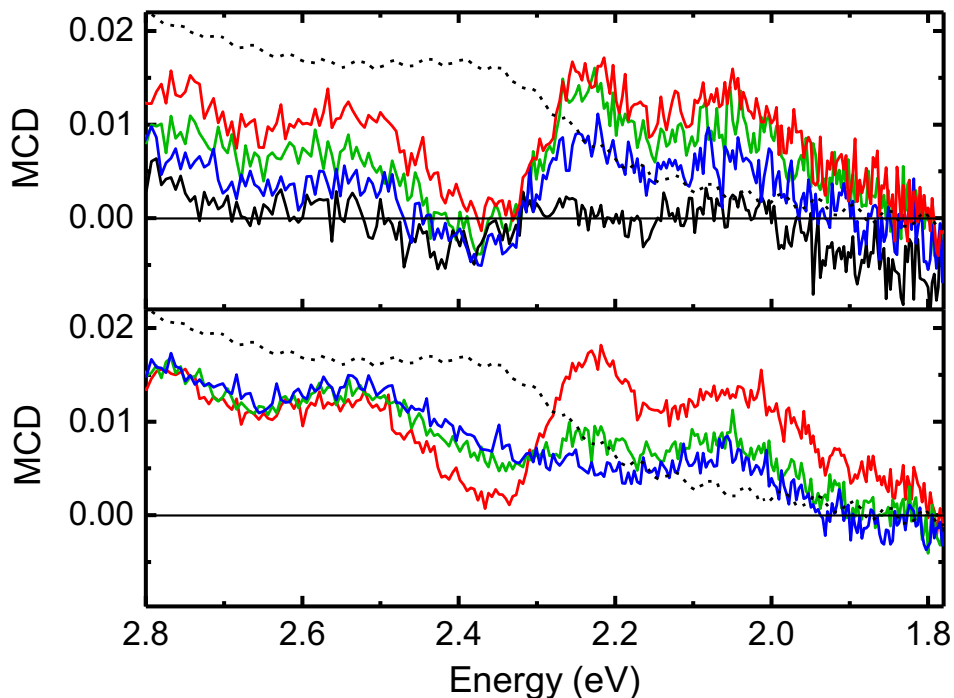


**Figure S6.2.2.** MCD measurements for Cu<sub>0.85</sub>In<sub>1</sub>S<sub>y</sub> QDs. The top panel shows the magnetic field dependence (solid black lines represent 0 T, blue 2 T, green 4 T, and red 6 T) at 3 K. The bottom panel shows the temperature dependence (blue represents 20 K, green 10 K, and red 3 K) at 6 T. For both panels, the linear absorption spectra is shown as dashed black lines.

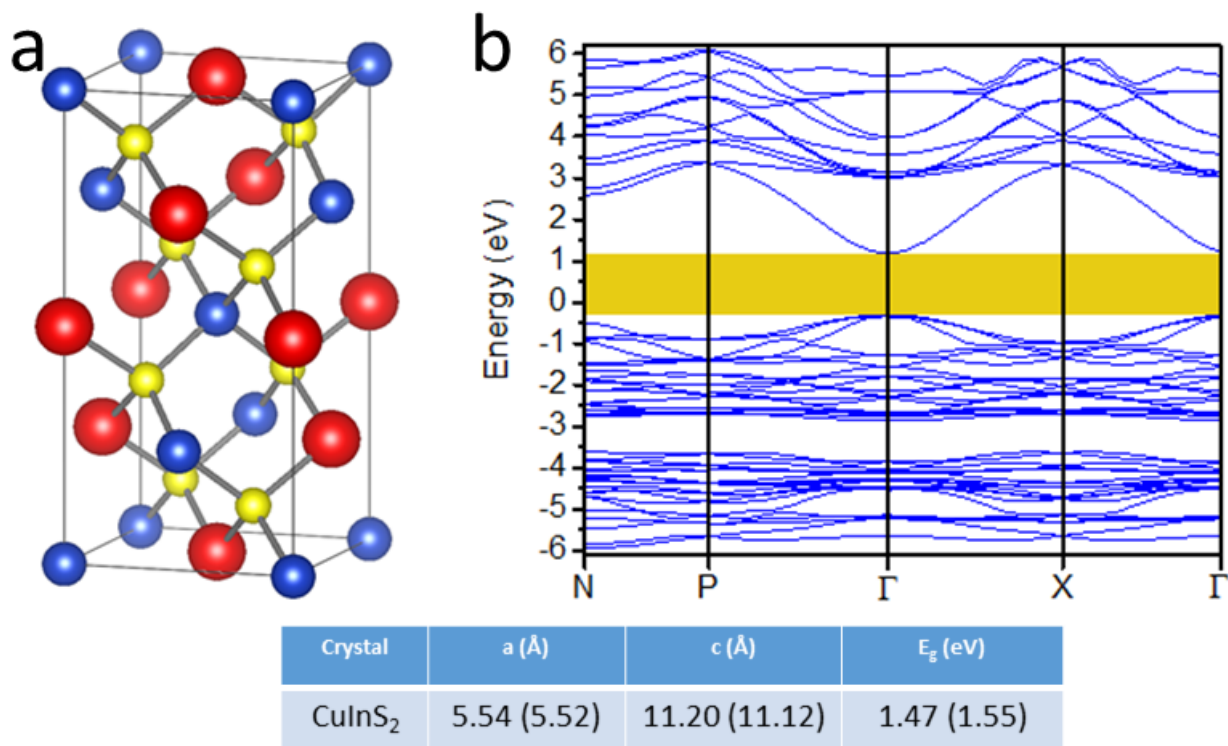


**Figure S6.2.3.** DFT calculation on a bulk CIS unit-cell. (a) shows the optimized cell, while (b) represents the electronic structure. The band gap in (b) is marked in yellow. The table below shows the optimized lattice parameters determined by PBE, and the calculated band gap using HSE06. In all cases, experimental values are represented in parentheses.

### 6.3 Supporting Information for Chapter 3, Section 3.1

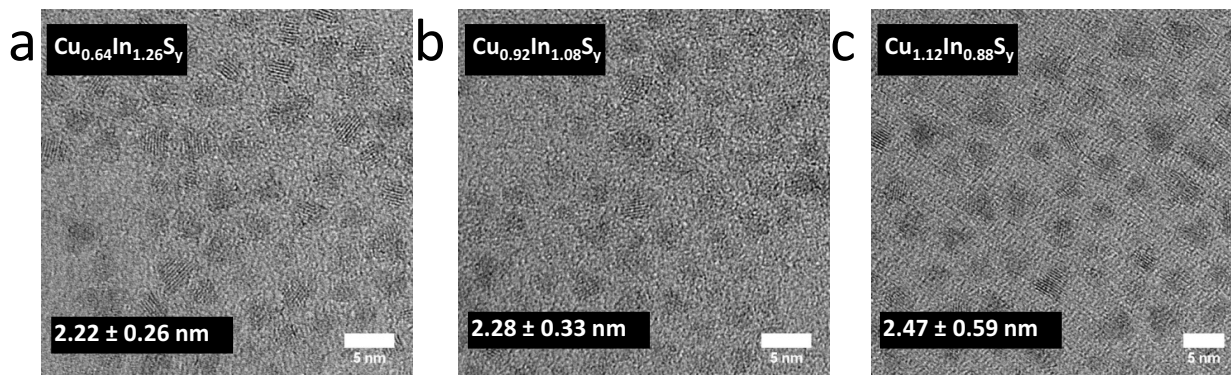


**Figure S6.3.1.** TEM images for CIS QDs with different copper to indium ratios. As observed in section 6.2, QDs have a tetrahedral shape based on (112) facets.

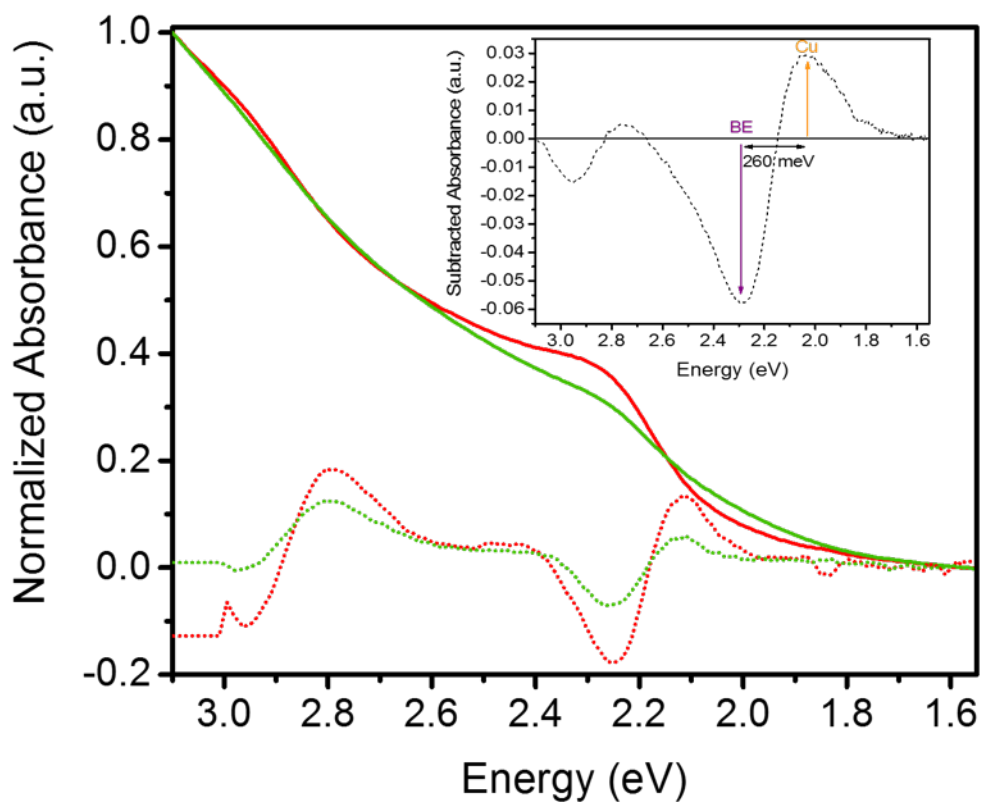


**Figure S6.3.2.** Linear absorption spectra for  $\text{Cu}_{0.85}\text{In}_1\text{S}_y$  (solid green line) and  $\text{Cu}_{0.47}\text{In}_1\text{S}_y$  (solid red line), and their second derivatives (dotted lines with corresponding colors). The figure inset shows the “subtraction spectrum” where the linear absorption spectrum of  $\text{Cu}_{0.85}\text{In}_1\text{S}_y$  is subtracted from  $\text{Cu}_{0.47}\text{In}_1\text{S}_y$ . The negative peak represents a decrease in the relative intensity of the band-edge transition whereas the positive peak represents an increase in the intensity of Cu-

defect absorption as QDs become closer to stoichiometric, or Cu-rich. The energy separation between the two transitions ( $\sim 260$  meV) is near identical to the separation predicted by transient absorption and 3D-PLE measurements discussed in the main text.

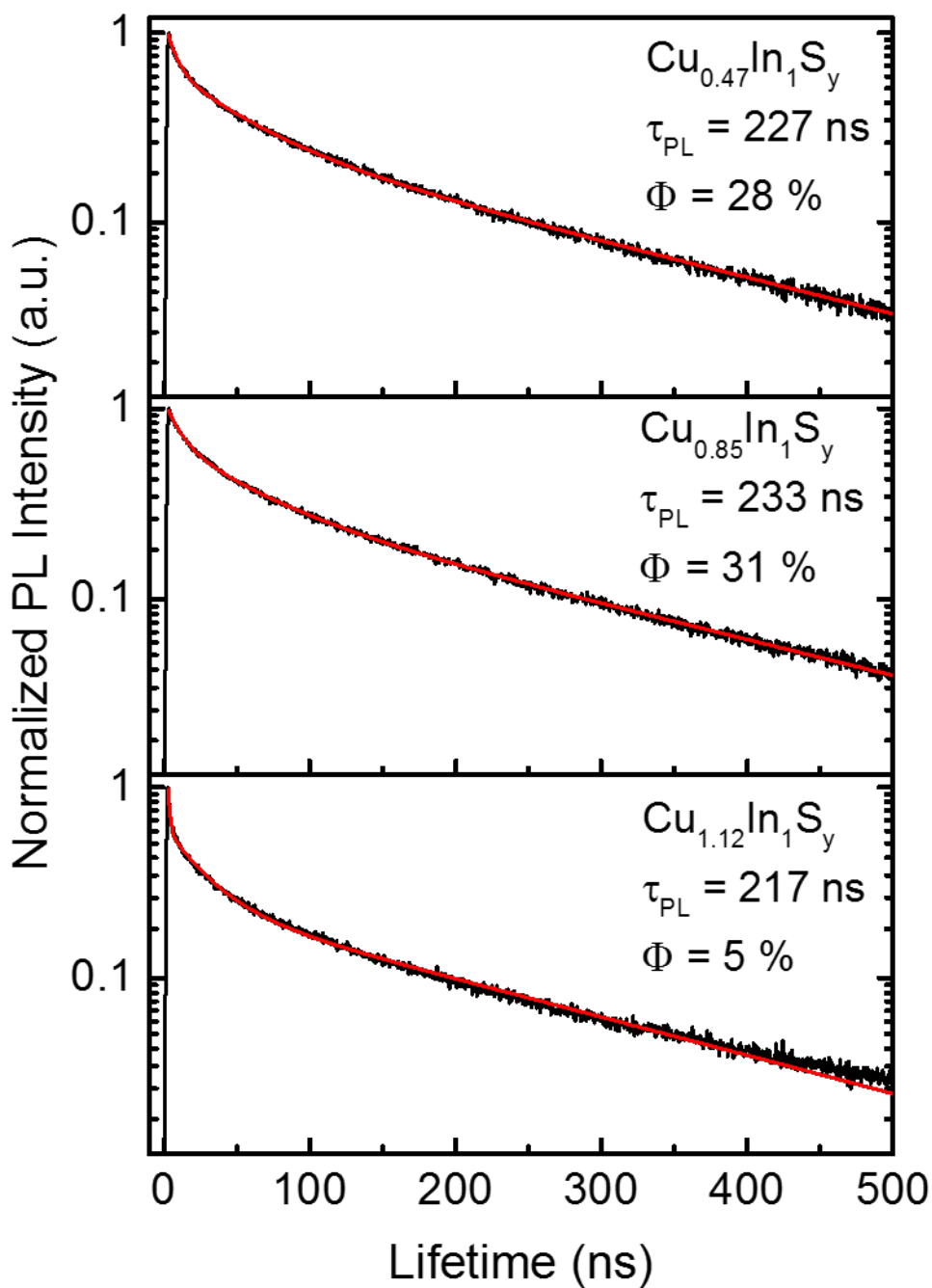


**Figure S6.3.3.** Time-correlated single photon counting (TCSPC) measurements of the PL dynamics for the samples described in the main text. Solid black lines represent the data collected

from the spectrometer, and the solid red lines represent triexponential fits to the data. The long component ( $\sim 230$  ns) corresponds with the PL lifetime, and is listed in the figure inset for each sample along with its respective QY.

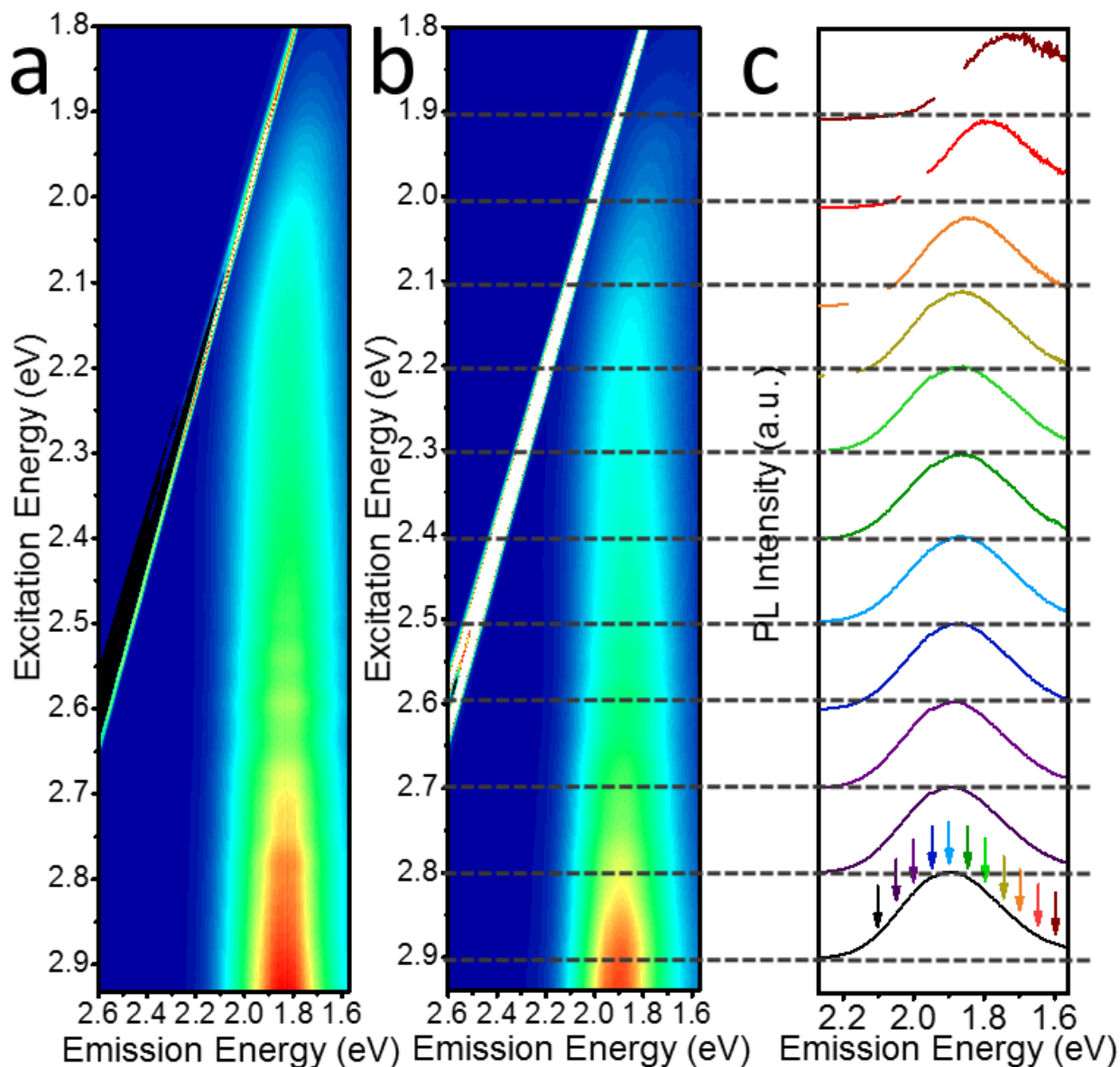


**Figure S6.3.4.** The raw data for the 3D-PL measurements described in the main text are shown as contour plots for  $\text{Cu}_{0.85}\text{In}_1\text{S}_y$  in (a), and  $\text{Cu}_{0.47}\text{In}_1\text{S}_y$  in (b). The y-axis represents the PLE for the sample, and the x-axis represents the PL resonant with the PLE. (c) The PL spectra at different excitation energies for  $\text{Cu}_{0.47}\text{In}_1\text{S}_y$  is extracted from the data in (b) in 0.1 eV increments. The bottom panel shows colored arrows corresponding to the probe energies for the PLE spectra shown in the main text.

## 6.4 Supporting Information for Chapter 3, Section 3.2

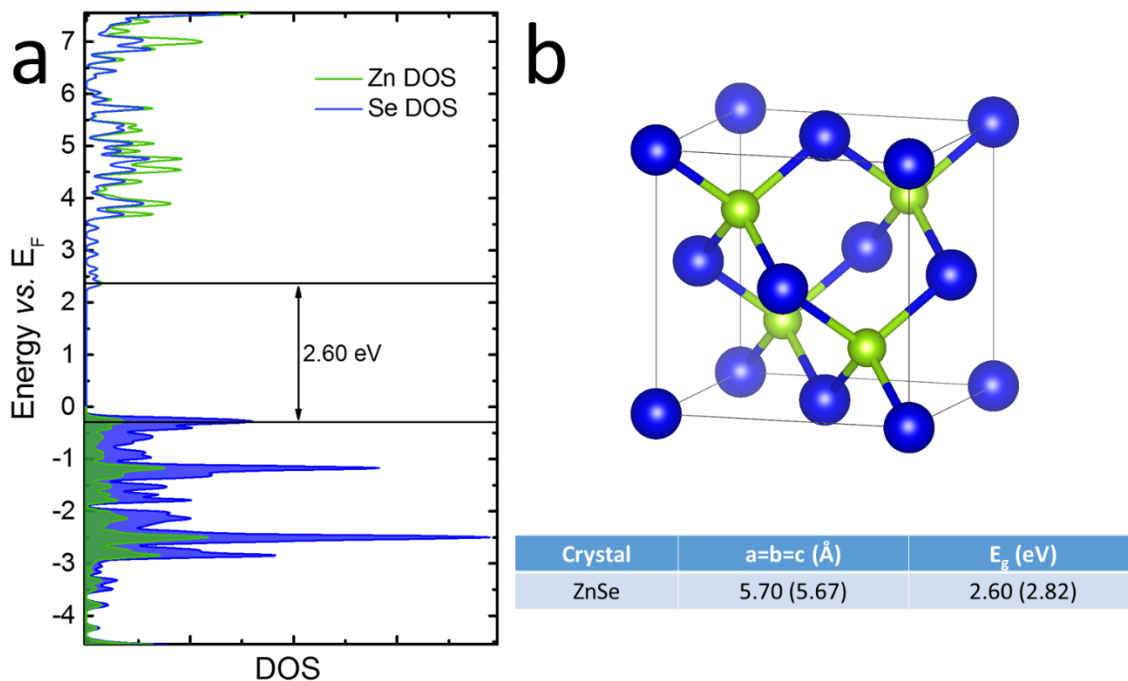


**Figure S6.4.1.** (a) The density of states (DOS) for a ZnSe unit cell calculated at the HSE06 level. The corresponding band gap is listed in (b) next to the lattice parameters determined by the PBE functional. Experimental values for the lattice parameters and band gap are listed in parentheses.<sup>1</sup>

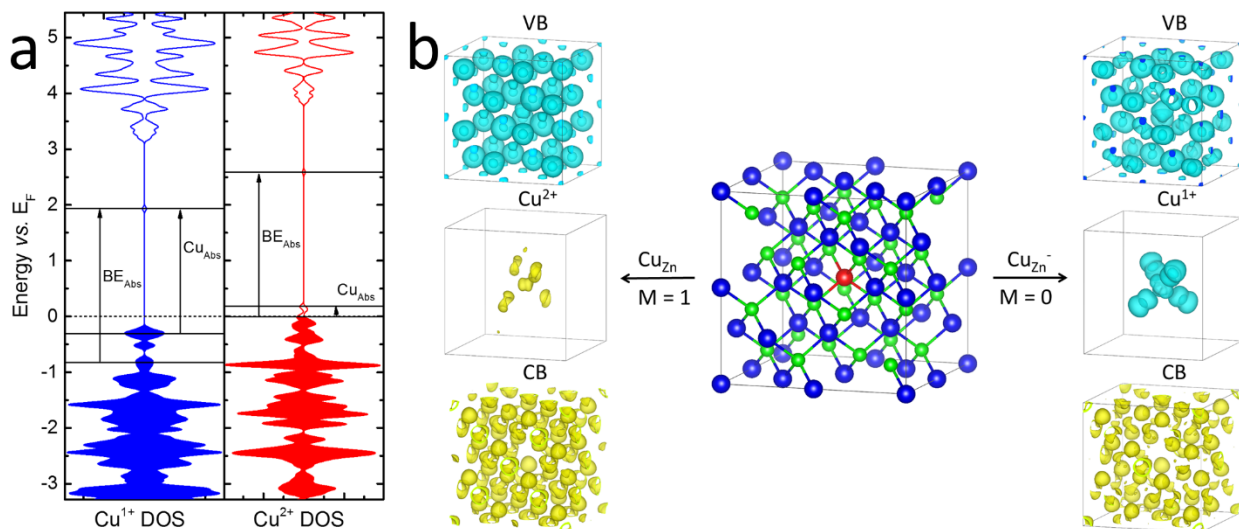


**Figure S6.4.2.** (a) DOS for a ZnSe supercell doped with  $\text{Cu}^{1+}$  (blue) and  $\text{Cu}^{2+}$  (red) impurities. (b) The charge density distribution is shown for each state with turquoise corresponding with occupied, and yellow with unoccupied states. M refers to the magnetization of the system.

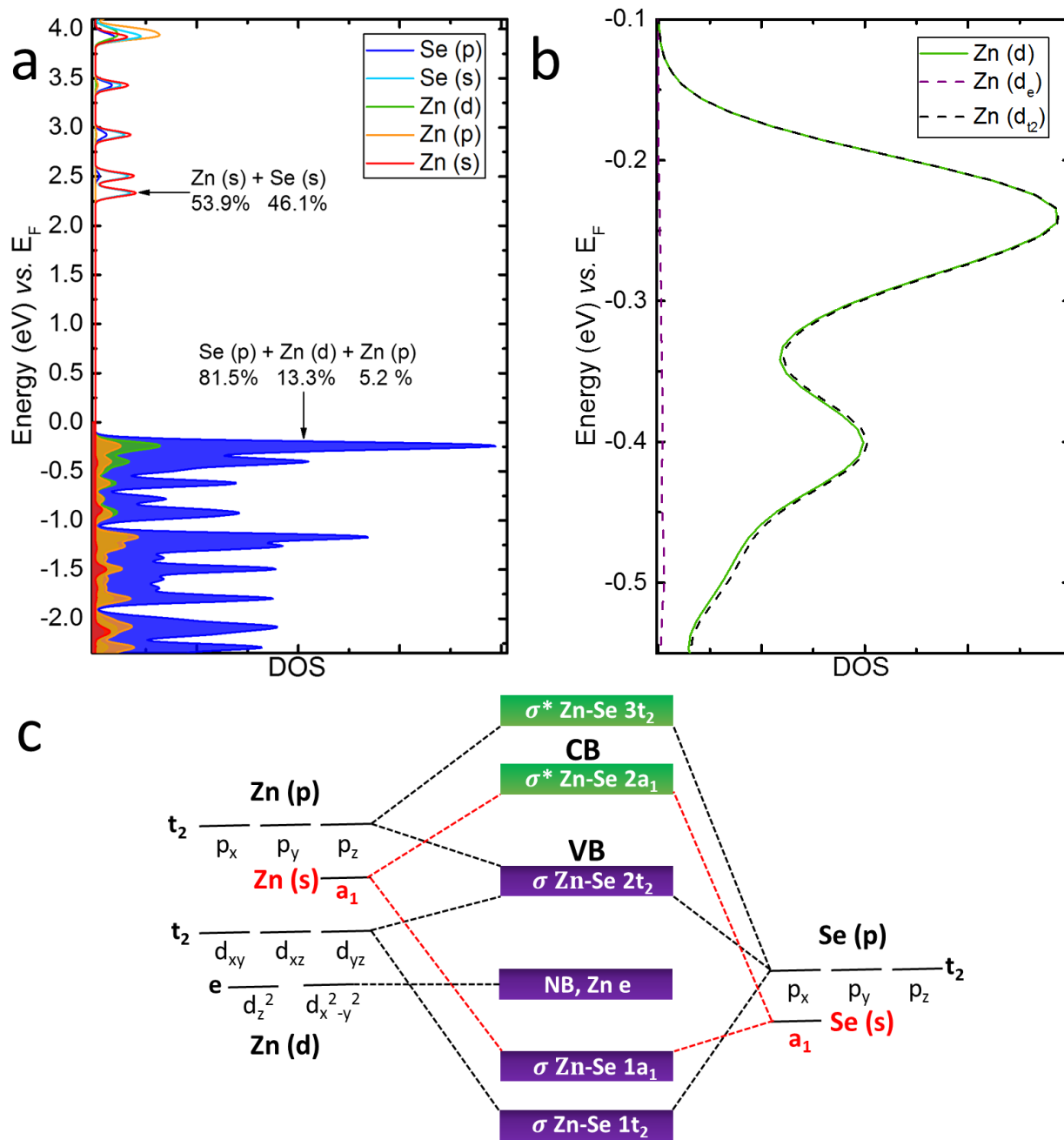


**Figure S6.4.3.** The PDOS for a ZnSe unit-cell is shown in (a). The Zn (d) DOS is replotted in (b) on a smaller energy scale to highlight the VB features. There is a near perfect match between the overall Zn (d) DOS and the DOS for (d) orbitals with  $t_2$  symmetry ( $d_{xy}$ ,  $d_{xz}$ , and  $d_{yz}$ ), and nearly zero contribution from the other two (d) orbitals. The corresponding MO diagram is shown in (c) with all bonds from hybridized (d) and (p) orbitals, and non-bonding Zn (d) orbitals marked with dashed black lines, while (s) orbitals with  $a_1$  symmetry are marked with dashed red lines.

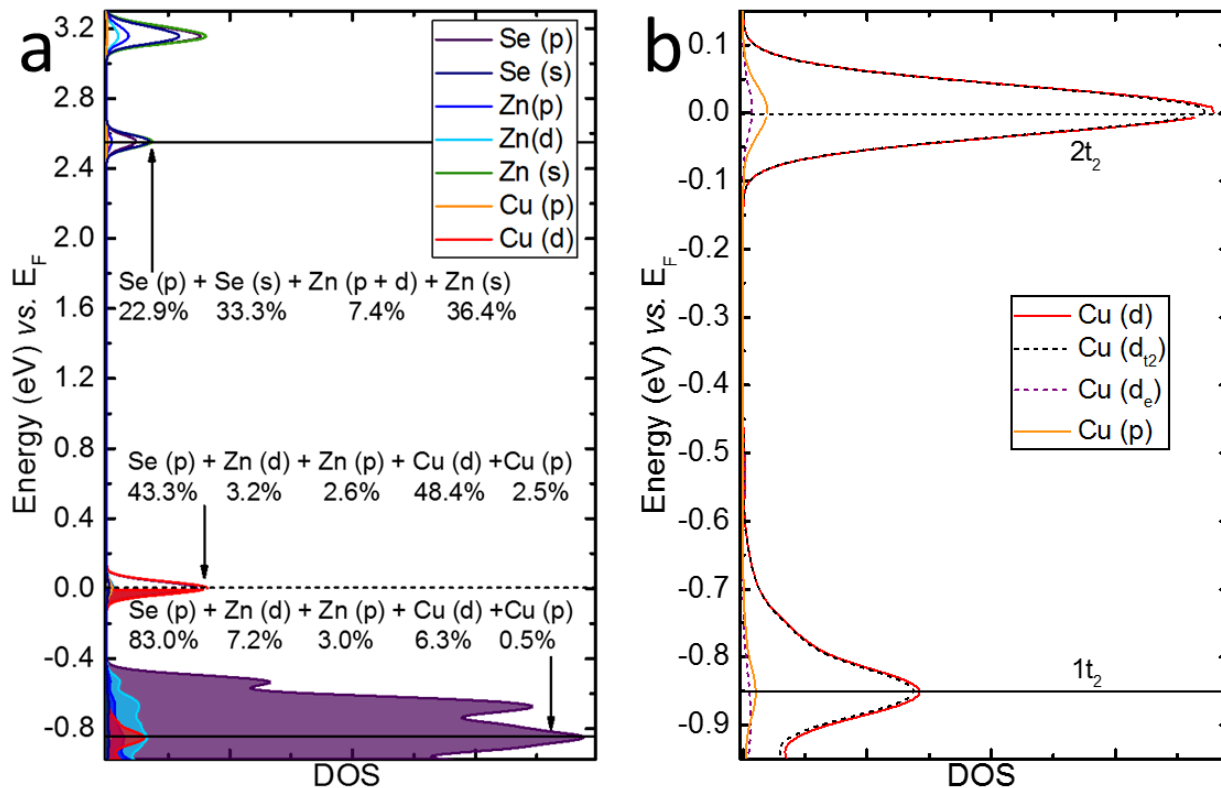


**Figure S6.4.4.** (a) The orbital PDOS for the Sub QD described in the main text. The contribution of the Cu (d) orbitals with  $t_2$  and  $e$  symmetry are shown in (b).

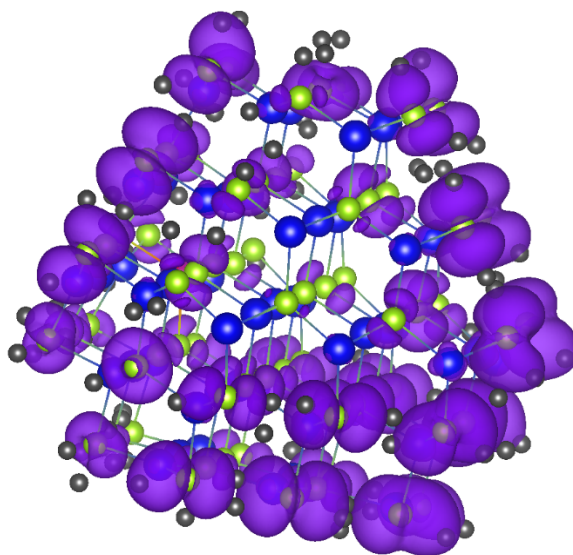


**Figure S6.4.5.** Spatial distribution of the square wave function for the Sub DOS between the VB and IG (for full DOS, see the main text). The charge density is mostly distributed on the surface, and is indicative of “trap-like” states.

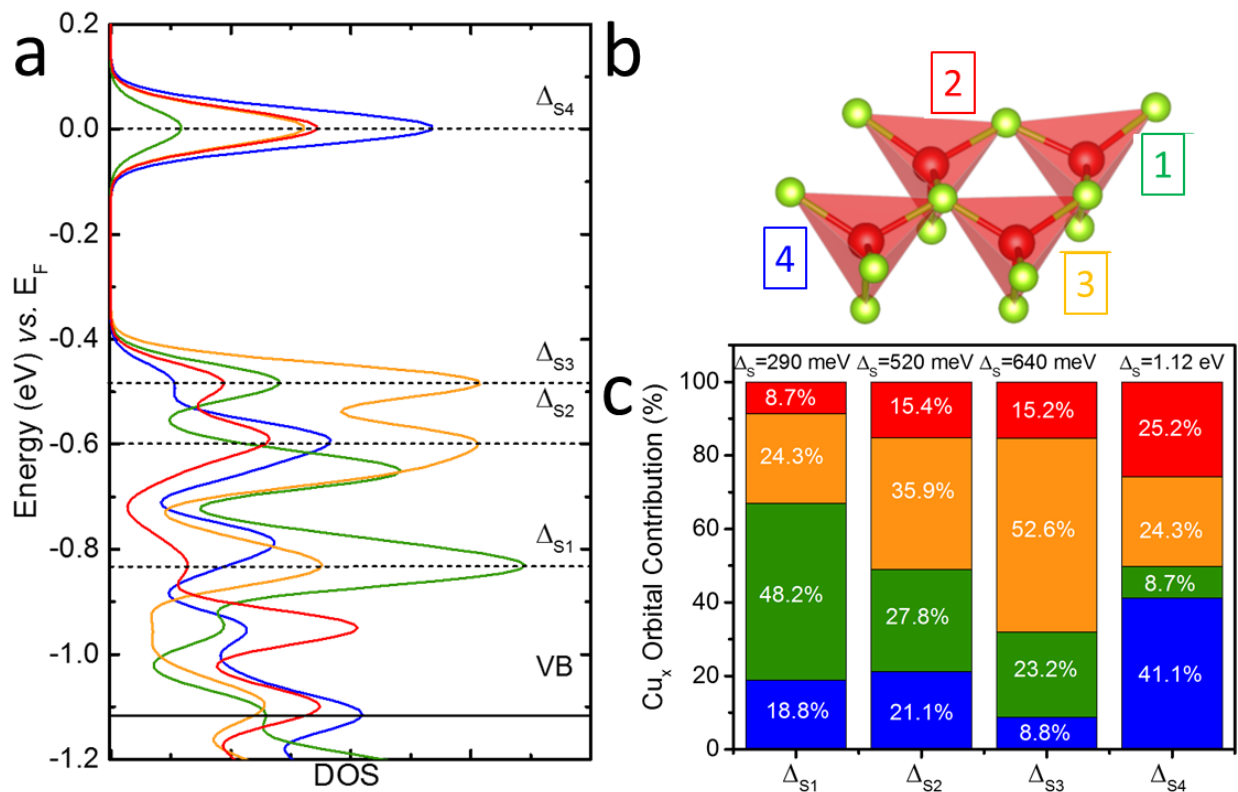


**Figure S6.4.6.** (a) Split-DOS for the different Cu atoms in  $\text{Cu}_4$ . The colors represent the Cu atoms labelled in (b) where 1-3 are “Sub” Cu impurities, and 4 indicates the only surface Cu (Surf4 configuration). In (c) we plot the orbital contribution of each Cu to the total Cu DOS marked in (a) with each color corresponding to the labels in (b).

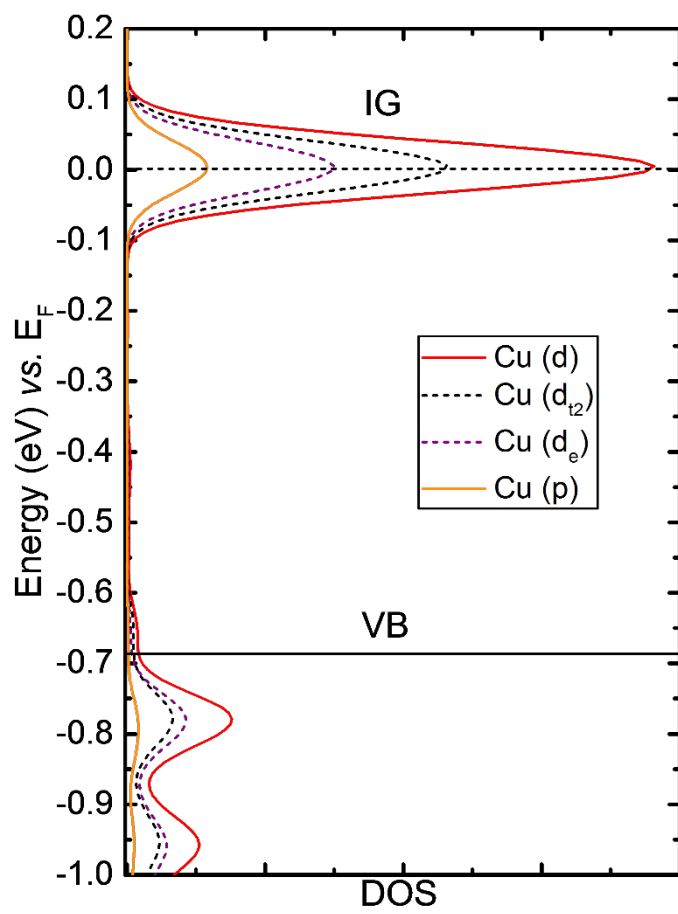
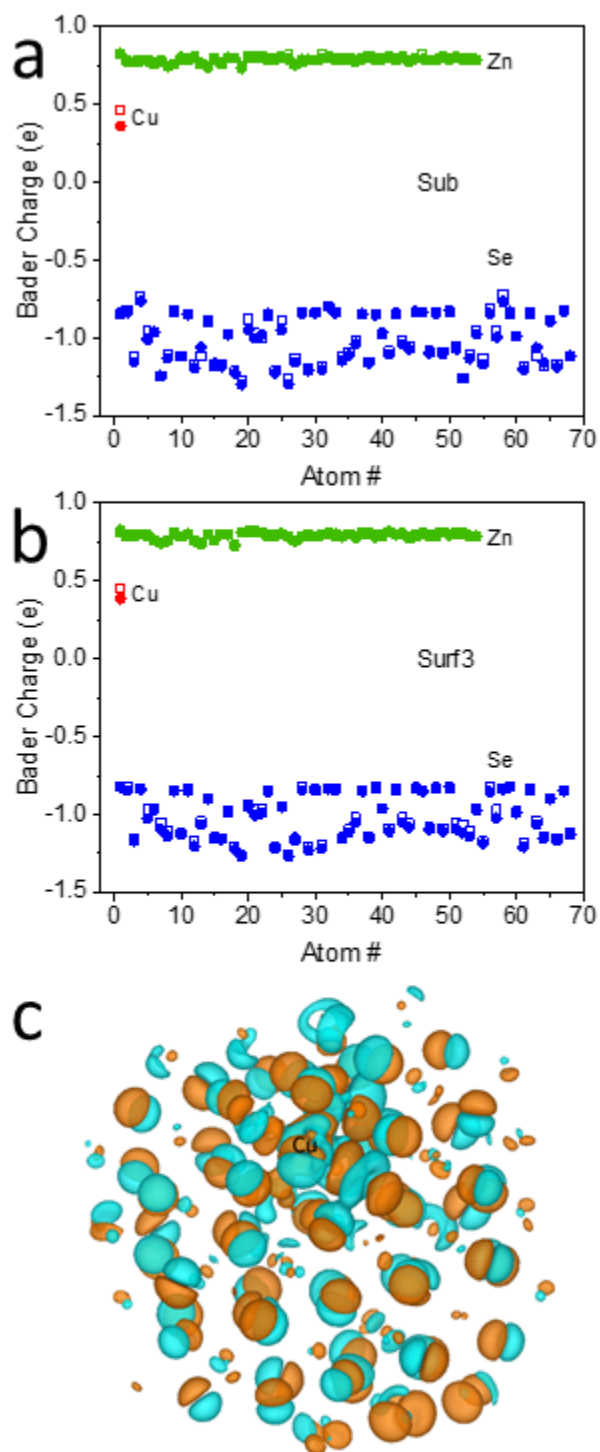


Figure S6.4.7 PDOS for Surf3 with Cu<sup>1+</sup> impurities.



**Figure S6.4.8** Bader charges for Sub (shown in (a) and Surf3 (shown in (b)) QDs. Closed (open) symbols represent QDs with (without) an electron added into the system. There is no significant change in the charge of Zn or Se. (c) Charge density difference plot for Sub with  $\text{Cu}^{2+}$ .

Chemical Bond	$q_x$
Cu <sup>+</sup> -Se (Sub)	-2.20
Cu <sup>+</sup> -Se (Surf4)	-2.91
Cu <sup>+</sup> -Se (Surf3)	-2.67
Cu <sup>2+</sup> -Se (Sub)	-1.67
Cu <sup>2+</sup> -Se (Surf3)	-2.13
Zn <sup>2+</sup> -Se (Avg., Sub)	-1.04
Zn <sup>2+</sup> -Se (Avg., Surf)	-1.54

**Table S6.4.1** Bader charges for different chemical bonds where  $q_x$  indicates the charge ratio of Selenium (Se) and the metal (M), or Se/M.

## References

1. Theis, D., Wavelength-modulated reflectivity spectra of ZnSe and ZnS from 2.5 to 8 eV. *Status Solidi b* 1977, 79, 125-130.

## 6.5 Supporting Information for Chapter 4

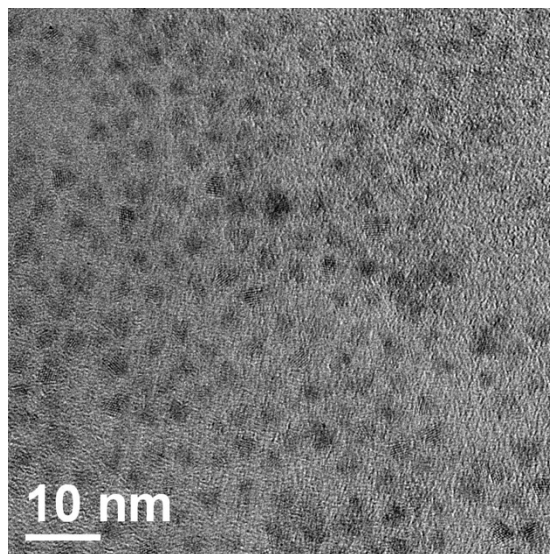


**Figure S6.5.1.** TEM images for CIS/ZnS core/shell QDs with 85% QY. The average size of the tetrahedral nanocrystals is  $\sim 2.94 \pm 7.7\%$  with a Cu:In ratio of 0.94:1.

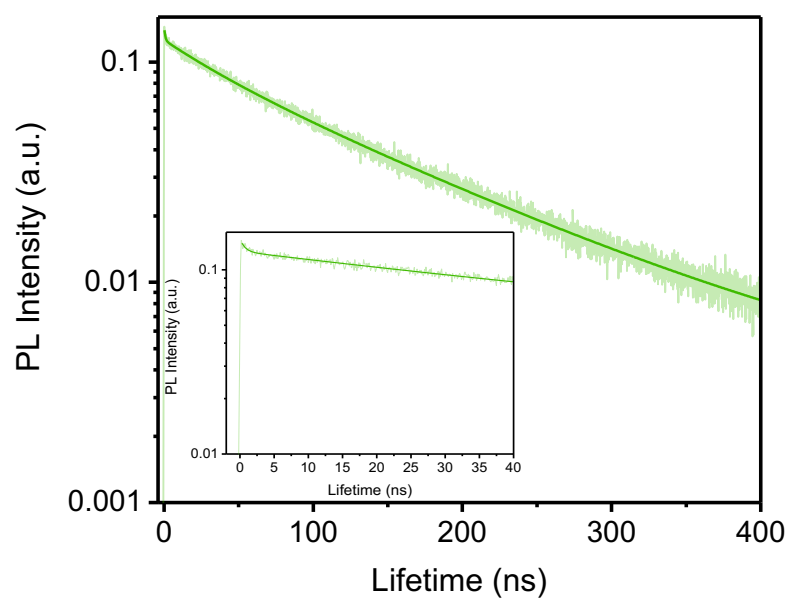


**Figure S6.5.2.** Time-resolved PL measurements of CISe/ZnS core/shell QDs with 75% QY using an SNSPD detector at low excitation density ( $\langle N \rangle = 0.15$ ).

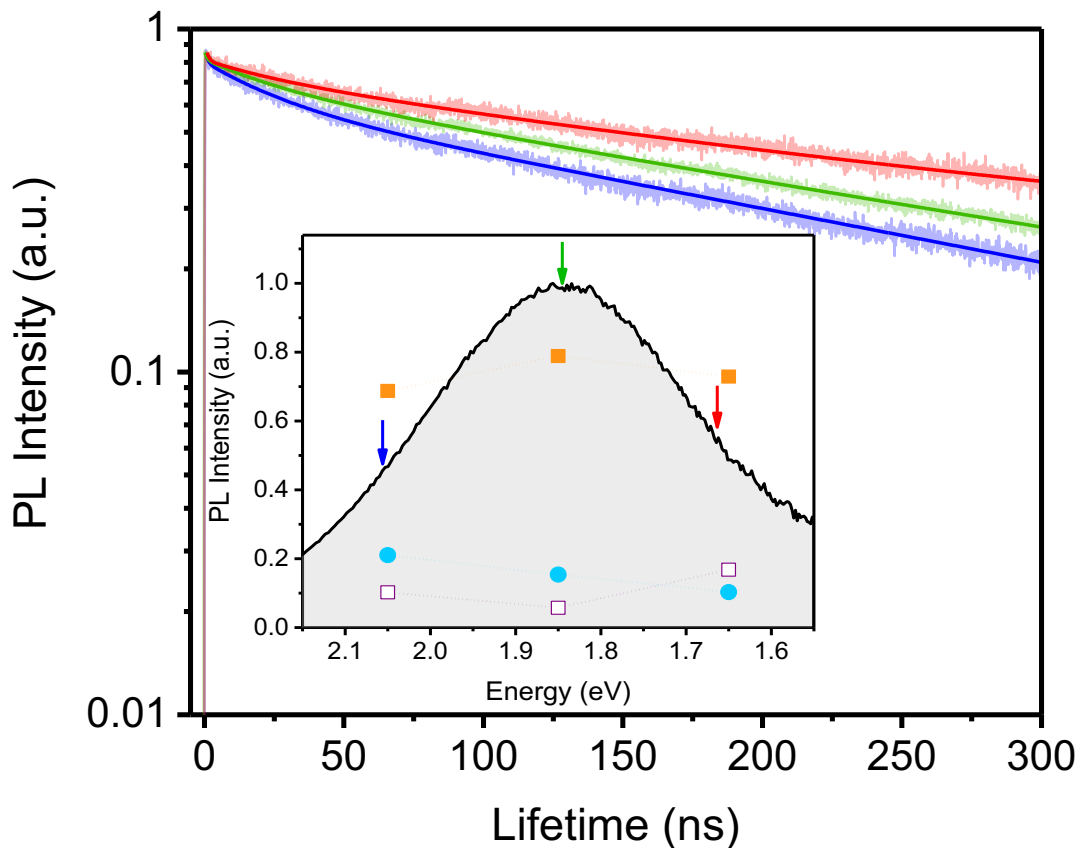


**Figure S6.5.3.** Probe energy dependent PL decay dynamics at low fluence ( $\langle N \rangle = 0.15$ ) using an SNSPD detector. The color of the lines used in the normalized decays represent the probe energies marked in the figure inset, and the 3 decay components are 920 ps ( $\tau_T$ ), 27 ns ( $\tau_{BE}$ ), and 281 ns ( $\tau_{Cu}$ ) as determined by a global tri-exponential fit. Similar to the probe energy-dependent decay of the core-only QDs, the amplitude of the BE decay (turquoise closed circle in figure inset) decreases from  $\sim 21\%$  to 10% as the probe is shifted from the blue (2.05 eV) to red (1.65 eV). This is distinct from the trapping and  $Cu^x$  PL (purple open squares and orange closed squares, respectively) where trapping is strongest on both the red and blue side of the spectra, and weakest at the PL peak. On the other hand,  $Cu^x$  PL exhibits the opposite relationship with probe energy where it is strongest at the peak, and weakest on the red and blue side of the spectra.

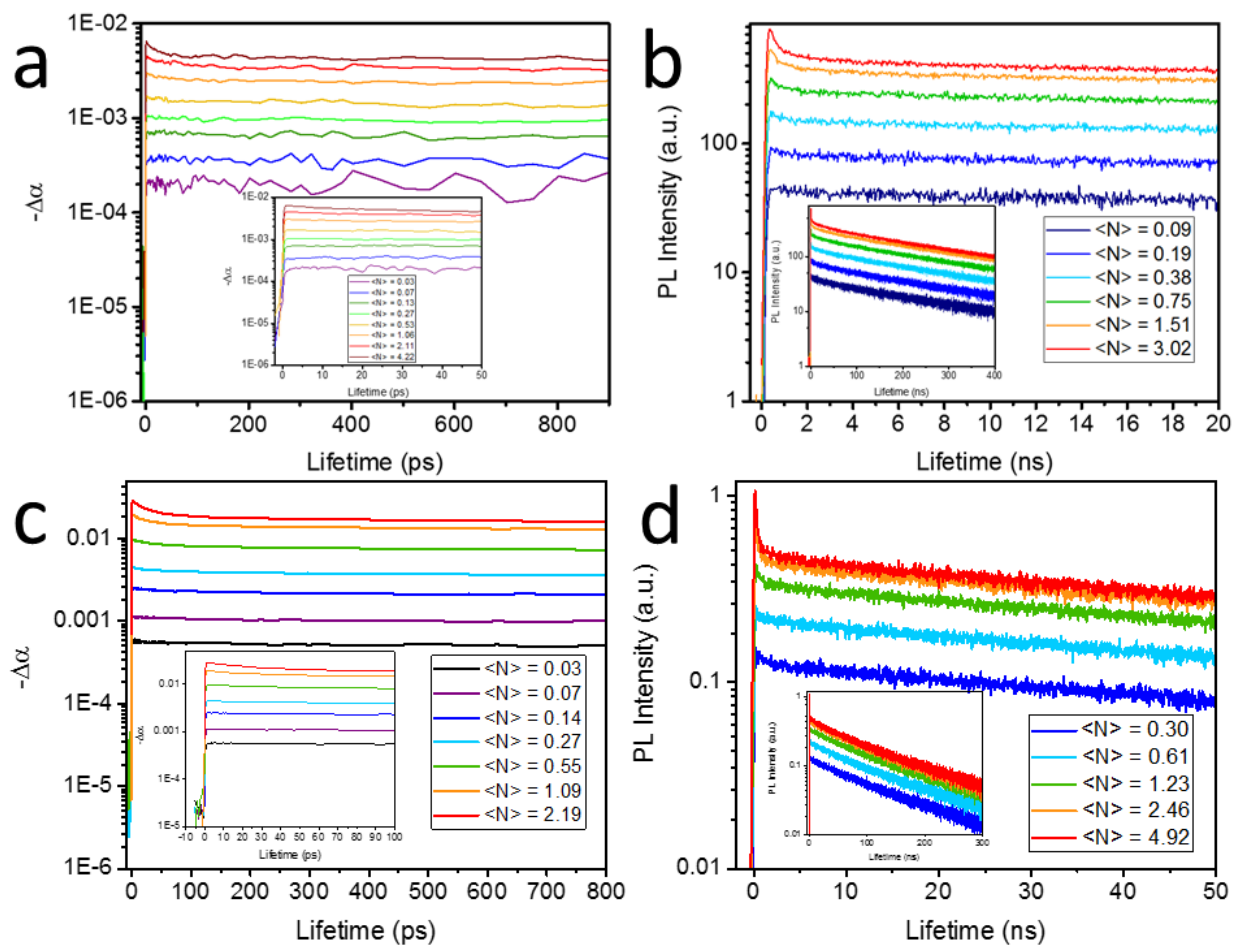


**Figure S6.5.4.** Non-normalized, pump-fluence-dependent time-resolved spectra of high QY CIS/ZnS (a,b) and CISE/ZnS (c,d) core/shell QDs. (a) TA measurements at 3.61 eV excitation for CIS/ZnS QDs. (b) SNSPD measurements at 3.1 eV excitation also for CIS/ZnS QDs. (c) TA measurements at 3.61 eV excitation for CISE/ZnS. (d) SNSPD measurements at 3.1 eV excitation also for CISE/ZnS.

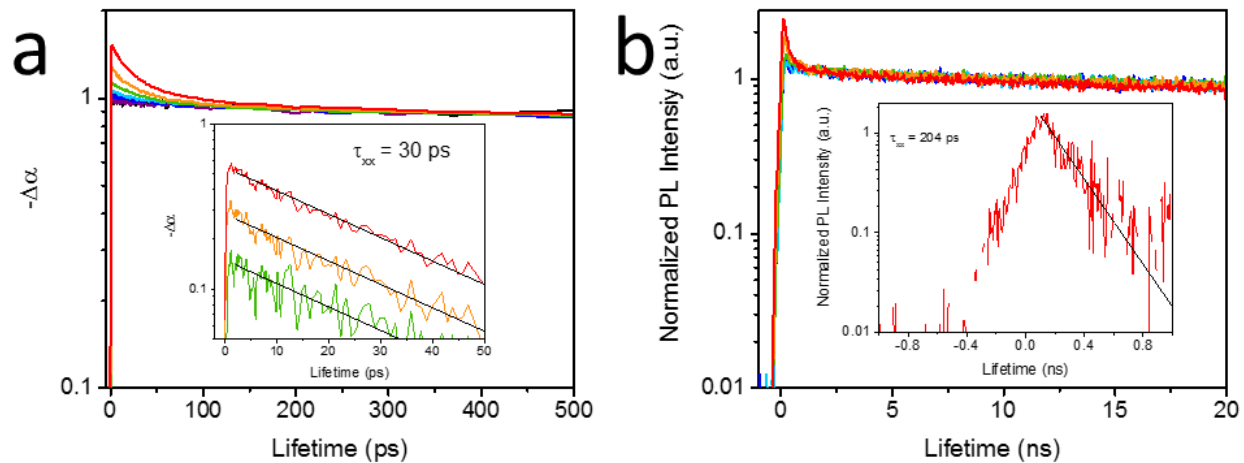


**Figure S6.5.5.** (a) Normalized TA spectra at 2.41 eV excitation for CISE/ZnS QDs. The inset shows the subtracted spectra and the 30 ps biexciton. Notably, in this case 2.41 eV is non-resonant excitation due to the smaller band gap for Se-alloyed structures. (b) The same procedure for determining multicarrier lifetimes is repeated, but by measuring PL dynamics with an SNSPSD.

## 6.6 Supporting Information for Chapter 5

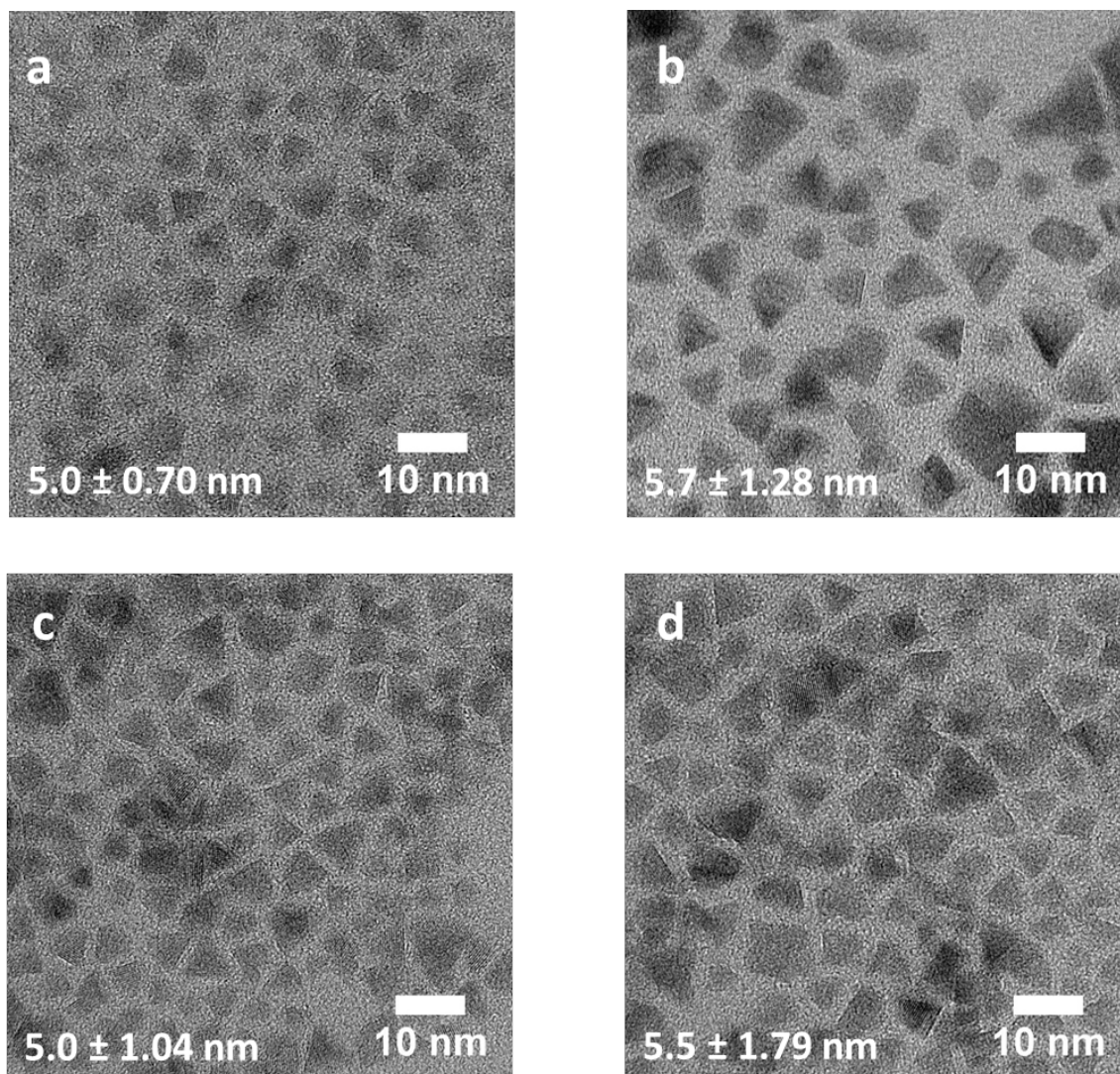


**Figure S6.6.1.** Representative transmission electron microscopy (TEM) images of (a)  $\text{CuInS}_2$ , (b)  $\text{CuInSe}_{1.0}\text{S}_{1.0}$ , (c)  $\text{CuInSe}_{1.2}\text{S}_{0.8}$ , and (d)  $\text{CuInSe}_{1.4}\text{S}_{0.6}$  QDs. The average QD height for each sample along with the corresponding standard deviation are shown in the figure.

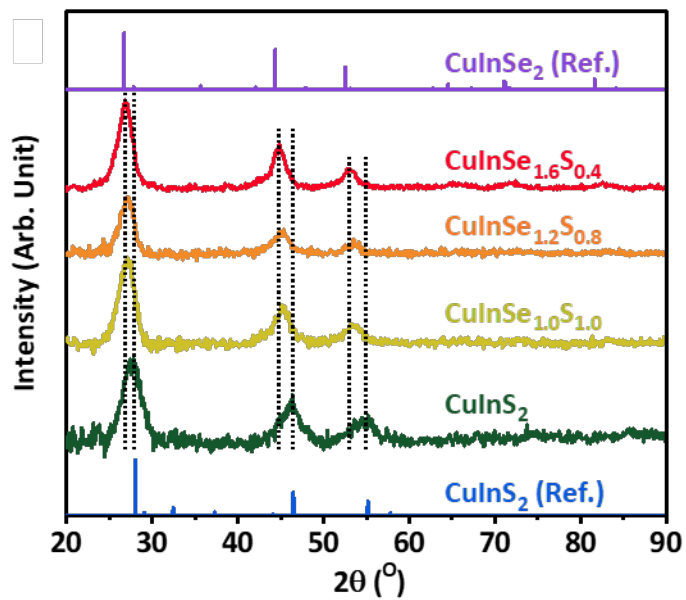


**Figure S6.6.2.** X-ray diffraction (XRD) patterns of CuInSe<sub>x</sub>S<sub>2-x</sub> QDs with a varied fraction of Se ( $f_{\text{Se}} = x/2$ ). They show a chalcopyrite crystal structure typical of I-III-VI<sub>2</sub> semiconductors. The diffraction peaks shift to smaller angles ( $2\theta$ ) with increasing  $f_{\text{Se}}$  indicating lattice expansion.

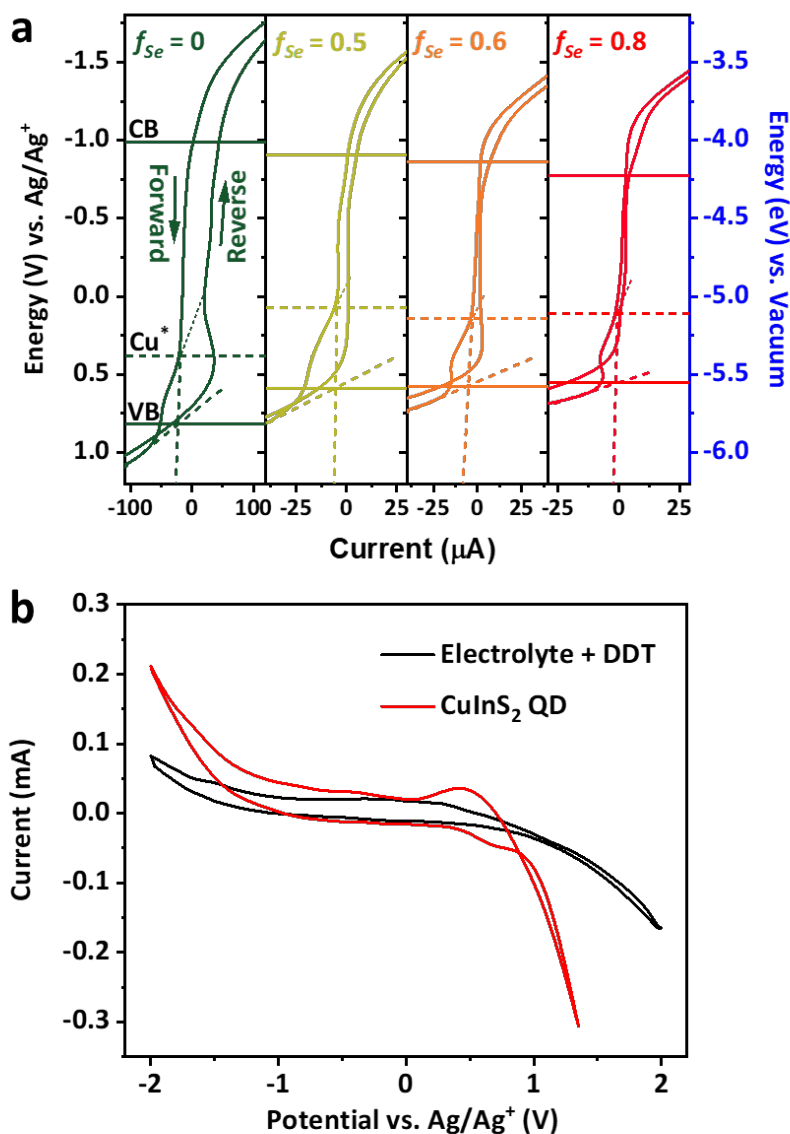


**Figure S6.6.3.** (a) Cyclic voltammograms (CVs) of  $\text{CuInSe}_x\text{S}_{2-x}$  QDs with different Se fractions. The horizontal solid lines mark the positions of the conduction and valence bands (CB and VB, respectively). The horizontal dashed line shows the energy of the Cu-related defect ( $\text{Cu}^*$ ). (b) The CV scan of DDT in an electrolyte (black) in comparison to that of  $\text{CuInS}_2$  QDs (red).

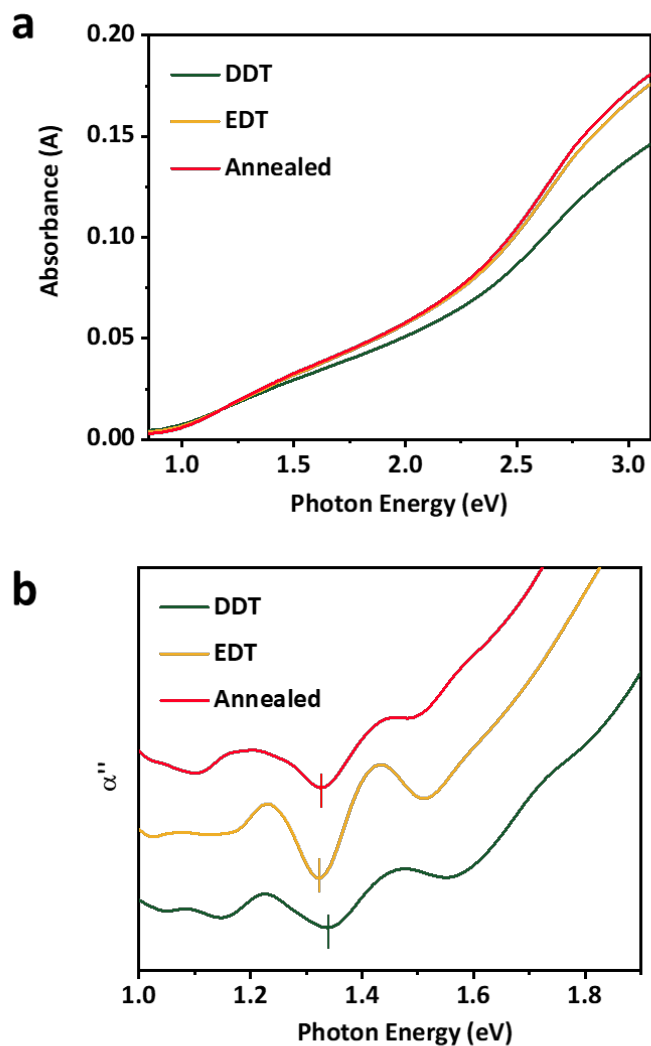


**Figure S6.6.4.** (a) The absorption spectra and (b) the spectra of the absorption second derivative of the as-prepared  $\text{CuInSe}_{1.6}\text{S}_{0.4}$  QD film (green) and the same film after treatment with EDT (yellow) and then annealing (red). The positions of the minima in the second derivative spectra (marked by vertical bars) are used to quantify the QD band gap ( $E_g$ ).

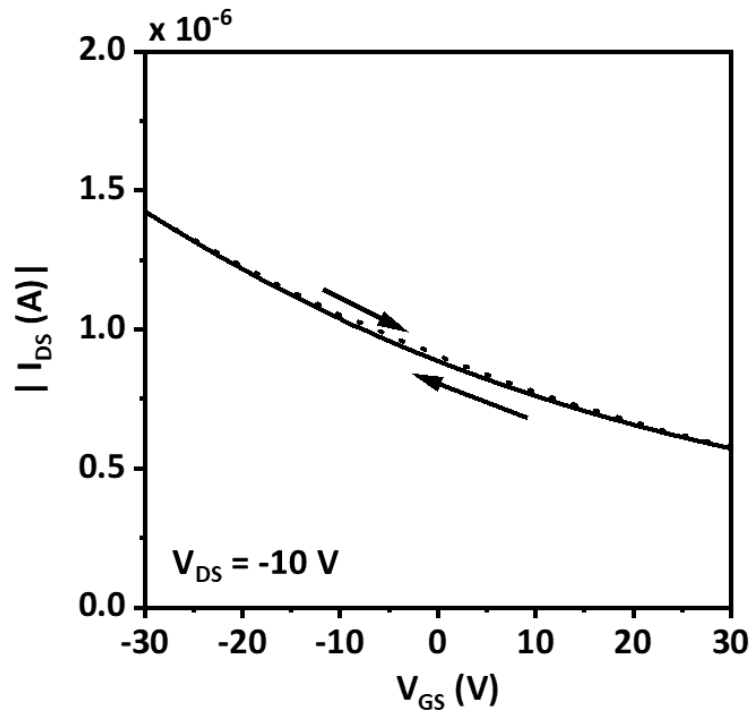


**Figure S6.6.5.** Transfer characteristics of the CuInSe<sub>1.6</sub>S<sub>0.4</sub> QD-FET with gold contacts.

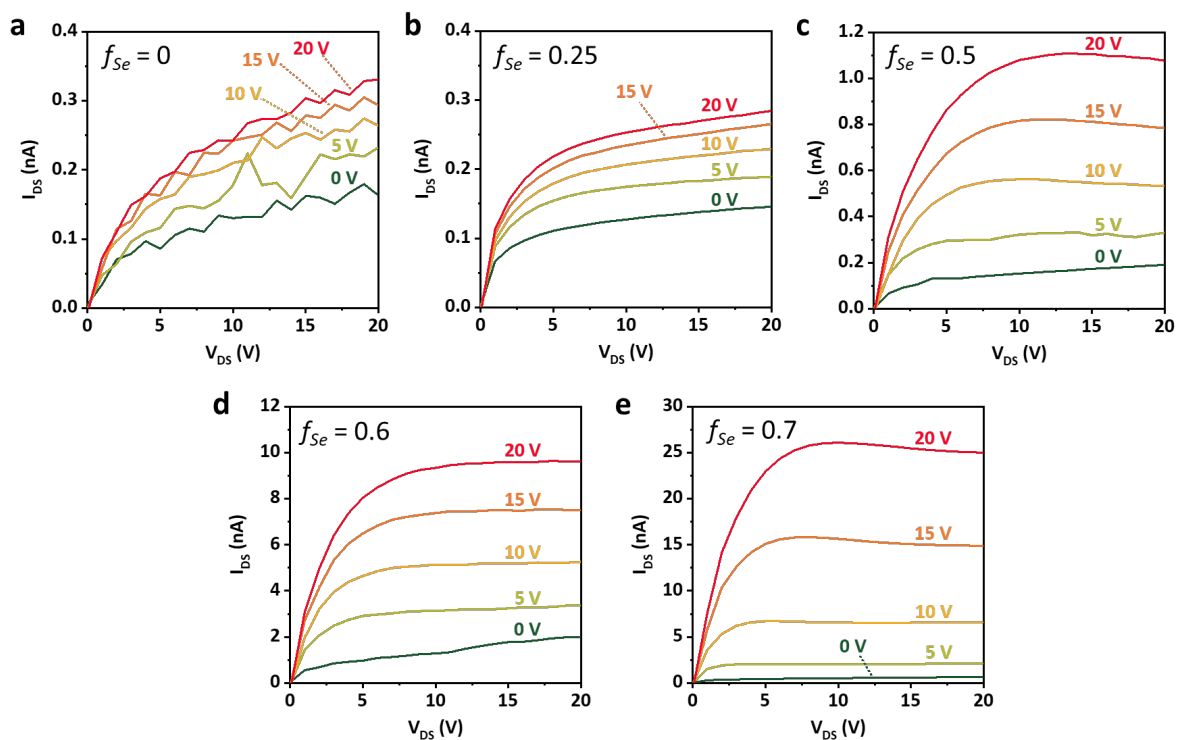


**Figure S6.6.6.** Output characteristics of the indium-contact FETs made of QDs of (a) CuInS<sub>2</sub>, (b) CuInSe<sub>0.5</sub>S<sub>1.5</sub> (c) CuInSe<sub>1.0</sub>S<sub>1.0</sub>, (d) CuInSe<sub>1.2</sub>S<sub>0.8</sub>, and (e) CuInSe<sub>1.4</sub>S<sub>0.6</sub>.

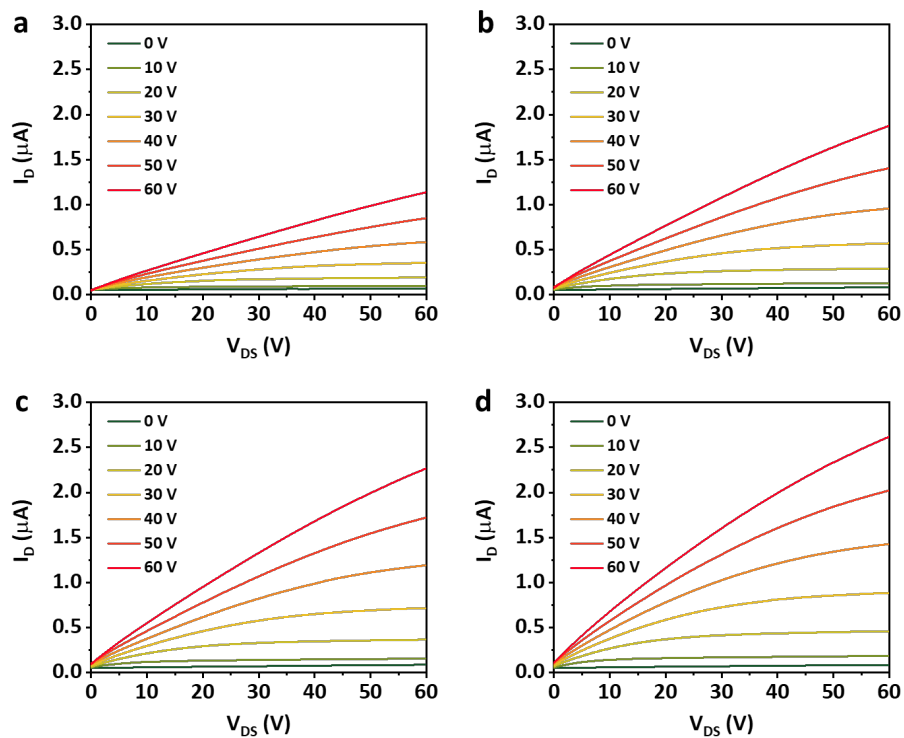


**Figure S6.6.7.** Output characteristics of the indium-contact  $\text{CuInSe}_{1.6}\text{S}_{0.4}$  QD-FET cooled down to (a) 80 K, (b) 100 K, (c) 120 K, and (d) 140 K.

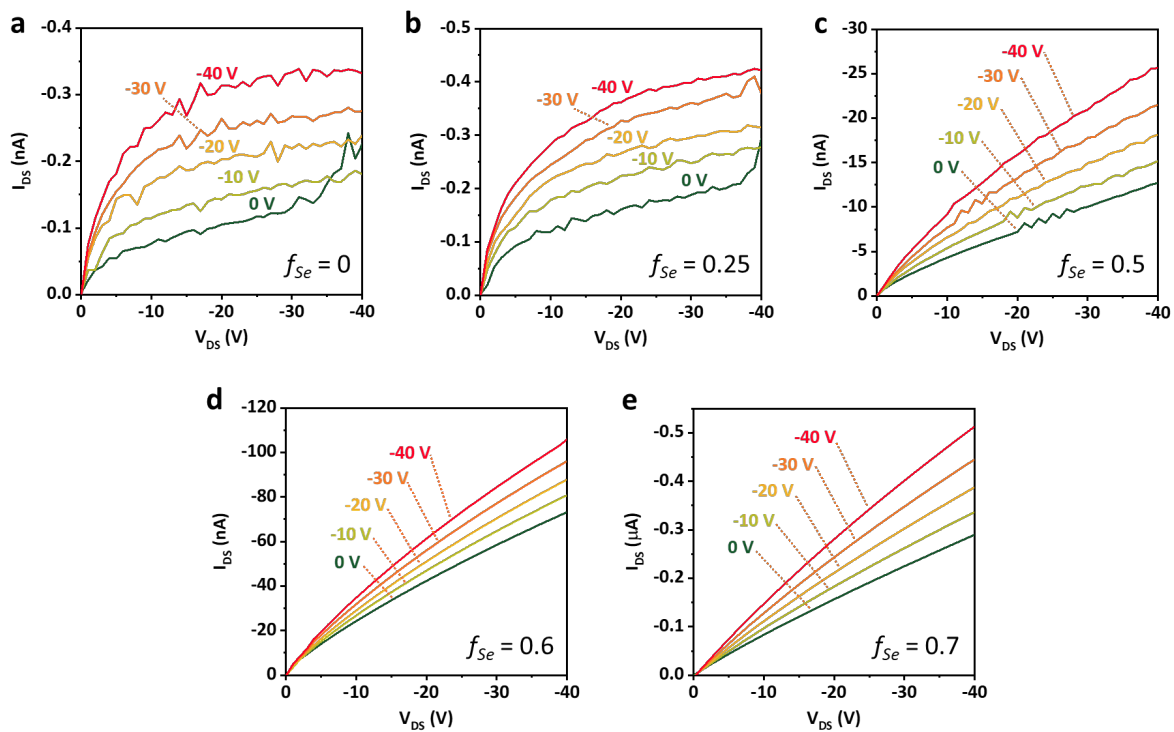


**Figure S6.6.8.** Output characteristics of the gold-contact FETs made of QDs of (a)  $\text{CuInS}_2$ , (b)  $\text{CuInSe}_{0.5}\text{S}_{1.5}$  (c)  $\text{CuInSe}_{1.0}\text{S}_{1.0}$ , (d)  $\text{CuInSe}_{1.2}\text{S}_{0.8}$ , and (e)  $\text{CuInSe}_{1.4}\text{S}_{0.6}$ .

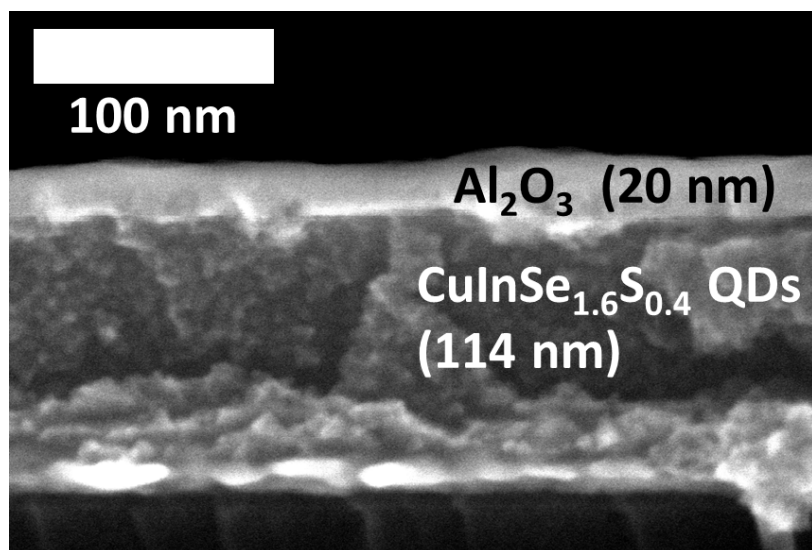


**Figure S6.6.9.** The cross-sectional SEM image of the ALD-infilled  $\text{CuInSe}_{1.6}\text{S}_{0.4}$  QD film.

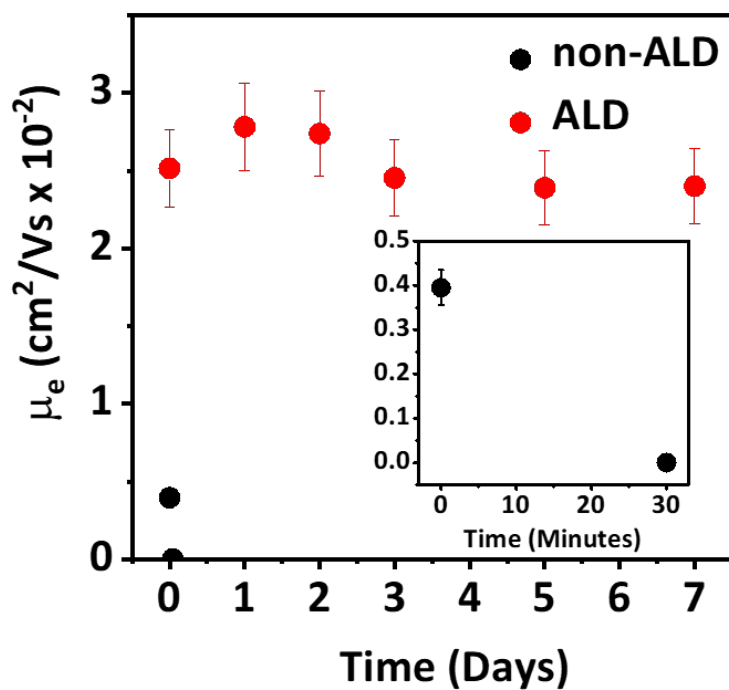


**Figure S6.6.10.** Air-stability studies of the non-ALD and the ALD-infilled QD-FETs. The inset illustrates very fast degradation of the non-ALD QD-FET in air.

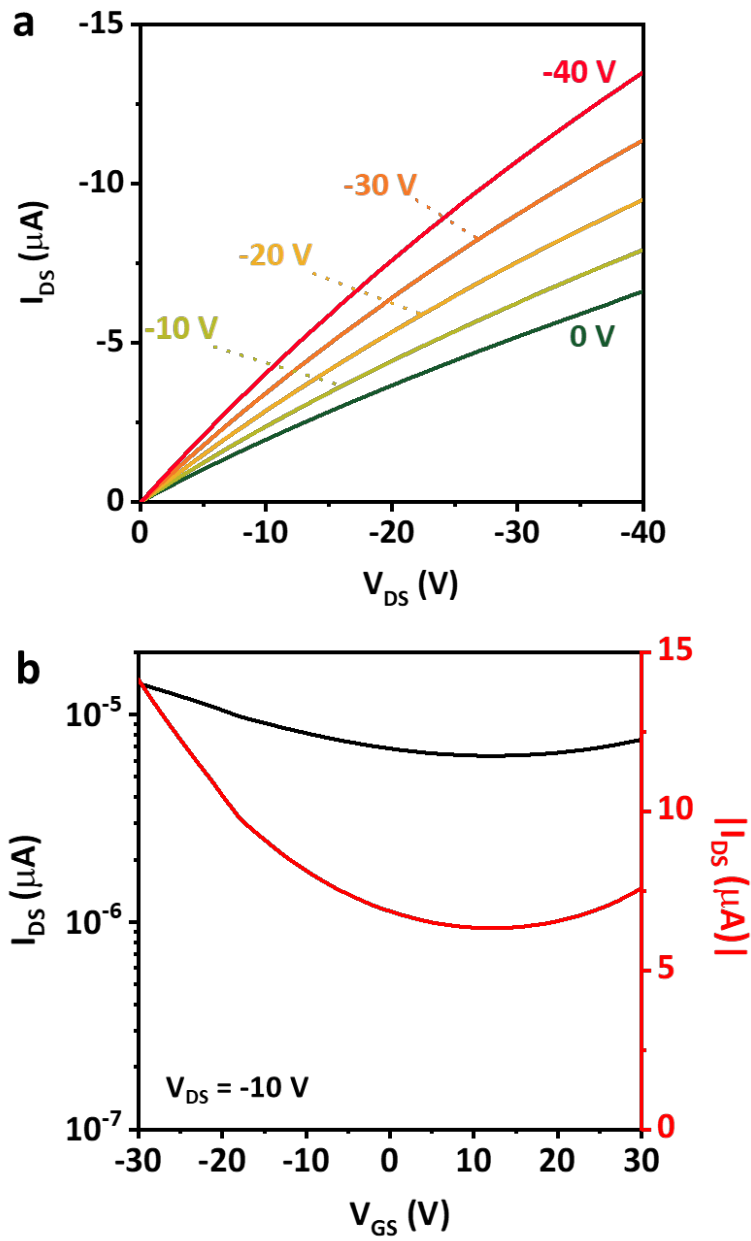


**Figure S6.6.11.** (a) Output and (b) transfer characteristics of the gold-contact ALD-infilled FETs based on EDT-treated  $\text{CuInSe}_{1.6}\text{S}_{0.4}$  QDs.